In situ and *Ex situ* TEM Studies of Fluoride Ion Batteries

TECHNISCHE UNIVERSITÄT DARMSTADT

Dissertation approved by the department of
Materials and Earth Sciences
in fulfilment of the requirements for the degree of
Doctor-Engineer
(Dr.-Ing.)

by

Mohammed Hammad Mohammed Fawey

M.Sc. Physics, Sohag University, Egypt
Born on October 01, 1980 at Sohag, Egypt

Referee:	Prof. Dr.-Ing. H. Hahn
Co-referee:	Prof. Dr. rer. nat. H.-J. Kleebe
Date of submission:	22/05/2017
Date of oral exam:	29/09/2017

Darmstadt 2017

D17

Ehrenwörtliche Erklärung

Ich erkläre hiermit ehrenwörtlich, dass ich die vorliegende Arbeit selbstständig angefertigt habe. Sämtliche aus fremden Quellen direkt oder indirekt übernommenen Gedanken sind als solche kenntlich gemacht.
Die Arbeit wurde bisher keiner anderen Prüfungsbehörde vorgelegt und noch nicht veröffentlicht.

Darmstadt, den 22 May 2017

(**Mohammed H. Fawey**)

Acknowledgements

All the praises and thanks be to Allah, who has given me the guidance and the power to finish this work.

I would like to express my gratitude and thanks to my parents, my wife "T. Awad" and my family for their love, understanding and support throughout my work, without their support I could not have done anything.

I would like to express my sincere gratitude and appreciation to my research supervisors, Prof. Horst Hahn, Dr. Christian Kübel and Dr. VS Kiran Chakravadhanula for their guidance, beneficial discussions, support and patience towards the completion of this work. This thesis would not have been possible without their support.

I express my sincere thanks to Dr. Di Wang, Dr. Houari Amari, Dr. Xiaoke Mu and Dr. Torsten Scherer for their valuable suggestions and advice during my research work. My sincere appreciations also extend to Mr. Robby Prang for useful discussions about FIB sample preparation. I thank Dr. D. Vinga Szabo, Dr. Andrey Mazilkin, Dr. Sabine Schlabach, Saleh Gorji, Shyam Chethala Neelakandhan, and all of electron microscopy & spectroscopy (EMS) group members; they have always been friendly and helpful during my research period.

My sincere appreciations also extend to Prof. Maximilian Fichtner, Dr. Munnangi Anji Reddy, Dr. Carine Rongeat, Dr. Thieu Duc and Harshita Bhatia for their kind cooperation and scientific discussions, which were extremely helpful at various stages of my research. I express my sincere thanks to Dr. Julia Ivanisenko and Dr. Mohsen Panah for their help to compress the battery pellets.

I would like to express my grateful acknowledgements to the secretaries and all technicians at the Institute of Nanotechnology (INT). Special thanks and appreciation to the Islamic Development Bank (IDB) and the Institute of Nanotechnology (INT) of the Karlsruhe Institute of Technology (KIT) for the financial support.

Lastly, my sincere thanks to one and all who have helped me, directly or indirectly, to successfully complete my doctoral research.

Mohammed H. Fawey

Abstract

Lithium ion batteries (LIBs) are widely used for portable electronics. However, their application is limited because of energy density, safety issues, and the high cost. This necessitates a search for alternative battery technologies. Many alternative battery systems are currently investigated based on different chemistries, which include sodium, magnesium, chloride, aluminum, and potassium based batteries. Rechargeable batteries based on a fluoride anion shuttle are a promising alternative to Li-ion batteries with theoretical energy densities of more than 5000 WhL^{-1}. However, detailed chemical and structural investigations are necessary to understand the structural changes and the degradation mechanisms to improve the performance of fluoride ion batteries. In the present thesis, TEM has been used to study all-solid-state fluoride ion batteries *in situ* and *ex situ*.

For *in situ* TEM studies, two all-solid-state fluoride ion battery systems were used; a half-cell consisting of a Bi composite as electrode and $La_{0.9}Ba_{0.1}F_{2.9}$ as a solid electrolyte; and a full cell consisting of a Cu composite as cathode, a MgF_2 composite as anode, and $La_{0.9}Ba_{0.1}F_{2.9}$ as a solid electrolyte. Optimization of sample preparation was an essential step to enable reliable *in situ* TEM studies during electrochemical biasing. Challenges during sample preparation, such as re-deposition/metal contamination, contact resistance, porosity of the battery materials and leakage current were resolved using an optimized FIB based approach. The successful preparation has been demonstrated for two fluoride ion battery systems. The *in situ* TEM studies of the half-cell revealed the fluorination of Bi and Bi_2O_3 forming BiF_3 and $BiO_{0.1}F_{2.8}$, and the simultaneous reduction of $La_{0.9}Ba_{0.1}F_{2.9}$ to La and Ba during charging. During discharging, most of the BiF_3 was reduced to Bi metal. Comparing the structural changes with the electrochemical charging curve, the main phase formed was the irreversible phase $BiO_{0.1}F_{2.8}$, leading to the poor reversibility of the half-cell. On the other hand, the TEM studies of the cathode-electrolyte interface of the full cell revealed fluoride migration into the composite cathode during charging resulting in the formation of CuF_2, which was absent in the as-prepared state. Due to the high volumetric changes associated with the CuF_2 formation, the cell fractured at the cathode-electrolyte interface during the second charging. However, a detailed electrochemical study during discharging was problematic, as a short circuit between cathode and anode dominated the current.

In addition, a fluoride ion battery system consisting of a CuF_2 composite as cathode, $La_{0.9}Ba_{0.1}F_{2.9}$ as a solid electrolyte, and a La sheet as anode was studied *ex situ* in the as-prepared, discharged, and recharged states. The interfacial studies were performed by lifting-out two

lamellae from each pellet at the electrodes-electrolyte interfaces using FIB. The TEM studies of the cathode confirmed the defluorination/fluorination during cycling of CuF_2/Cu. However, the TEM studies revealed a high oxygen content in the cathode composite explaining the difference between the theoretical capacity of Cu/CuF_2 (528 mAh g^{-1}) and the observed capacity during the first discharge (360 mAh g^{-1}). On the anode side, the presence of La_2O_3 on the surface led to a side reaction by LaOF formation during recharging, which acts as a significant fluoride trap. Therefore, the capacity faded upon cycling to only 165 mAh g^{-1} in the second discharge. Moreover, The STEM-EDX maps revealed Cu diffusion from the cathode into the electrolyte due to the high volumetric change in the cathode, partially explain the capacity fading.

Table of Contents

List of Figures

List of Tables

List of symbols and abbreviations

3D	Three-dimensional
ADF-STEM	Annular dark field scanning transmission electron microscopy
AE	Auger electrons
AFM	Atomic force microscopy
BF-STEM	Bright field scanning transmission electron microscopy
BF-TEM	Bright field transmission electron microscopy
BSE	Backscattered electron
CCD	Charged coupled device
CL	Cathodoluminescence
CNT	Carbon nanotube
CRT	Cathode ray tube
CV	Cyclic voltammetry
d	Interplanar distance
D	Path length difference between scattered X-rays
DC	Direct current
DF-TEM	Dark field transmission electron microscopy
DMC	Dimethyl carbonate
e^-	Electron
e	Euler's number (≈ 2.71828183)
E_p^a	Anodic potential peak
E_p^c	Cathodic potential peak
EBSD	Electron backscatter diffraction
EC	Ethylene carbonate
EDID	Electron beam induced deposition
EDX	Energy dispersive X-ray spectroscopy
EELS	Electron energy loss spectroscopy
EFTEM	Energy filtered transmission electron microscopy
E-TEM	Environmental transmission electron microscopy

EV	Electric vehicle
F^-	Fluoride anion
FEG	Field emission gun
FFT	Fast Fourier transform
FIB	Focused ion beam
FIB-SEM	Focused ion beam scanning electron microscopy
GIF	Gatan imaging filter
GIS	Gas injection system
Gy	Gray „a measure of the radiation dose“
HAADF-STEM	High angle annular dark field scanning transmission electron microscopy
HPT	High pressure torsion
HR-STEM	High resolution scanning transmission electron microscopy
HRTEM	High resolution transmission electron microscopy
HV	Hybrid vehicle
i_p^a	Anodic current peak
i_p^c	Cathodic current peak
IBID	Ion beam induced deposition
ICSD	Inorganic crystal structure database
KIT	Karlsruhe institute of technology
ILE	Ionic liquid electrolyte
INLO	*In situ* lift-out
LIB	Lithium ion battery
LSV	Linear sweep voltammetry
M′	Metal electrode
MAS-NMR	Magic angle spinning nuclear magnetic resonance spectroscopy
MEMS	Micro-electromechanical system
MF_x	Metal fluoride electrode
n	Reflectance order
NED	Nano electron beam diffraction
NMR	Nuclear magnetic resonance spectroscopy

OCV	Open circuit voltage
OM	Optical microscope
PLD	Pulsed laser deposition
RT	Room temperature
SAED	Selected area electron diffraction
SE	Secondary electron
SEI	Solid electrolyte interphase
SEM	Scanning electron microscopy
SHE	Standard hydrogen electrode
SIB	Sodium ion battery
STEM	Scanning transmission electron microscopy
STM-TEM	Scanning tunneling microscopy transmission electron microscopy
TEM	Transmission electron microscopy
TERS	Tip enhanced Raman spectroscopy
TOF-SIMS	Time of flight secondary ion mass spectrometry
TXM	Transmission X-ray microscopy
UPS	Uninterruptible power supply
XPS	X-ray photoelectron spectroscopy
XRD	X-ray diffraction
β	Semi-angle of collection of the magnifying lens
δ	Resolution of microscopy
θ	Incident angle of X-ray
λ	Radiation wavelength
μ	Refractive index of the viewing medium
τ	Transition time
ΔE	Difference between oxidation and reduction peaks

1 Introduction

1.1 Introduction

During the last decades, researchers exerted great efforts to develop efficient approaches to produce electricity from renewable sources and to develop energy storage systems to back up this energy. Many types of energy storage systems such as chemical energy storage [1], electrical energy storage [2], thermal energy storage [3], mechanical energy storage [4] and electrochemical energy storage [5] are in use. Rechargeable batteries, i.e. electrochemical power sources that directly and efficiently convert chemical energy into electrical energy, are currently the most common energy storage solutions.

In addition to the well-established applications in consumer electronics, reliable reversible energy storage systems are investigated for a wide variety of applications such as hybrid vehicles (HVs) and electric vehicles (EVs) [6], uninterruptible power supply (UPS) systems [7], grid stabilization [8], notebook computers [9], portable electronics [10], and spacecraft [11]. In general, high gravimetric or volumetric energy density, high cycling efficiency, fast charging, environmental safety, and materials and production costs are important issues for batteries [12, 13]. Depending on the specific application for a battery, different performance aspects have to be optimized, e.g. energy density for mobile applications and in addition power density for transportation, elevated operating temperature for smart cards and during sterilization of surgical instruments, and micron-sized battery for smart cards and medical electronics. In addition, many performance aspects are universal for all applications such as safety, cycle life, self-discharge rate, and cost.

A battery consists of anode, cathode and electrolyte, where the two electrodes are separated by an electrolyte as shown schematically in Figure 1.1 with $LiCoO_2$ as an example for a positive electrode (cathode) and graphite as a negative electrode (anode). During charging, (lithium) ions migrate to the negative electrode through the electrolyte, while electrons are provided through the external circuit to the cathode. The potential of the cathode will rise as a result of the corresponding redox reaction (intercalation or redox conversion), while the anode potential will decrease in the corresponding reaction. In sum, the cell voltage increases during charging. This process is reversible during discharging through an electrical connection between cathode and anode. This mechanism allows to store DC electrical energy during the charging process and to deliver (a large fraction of) it during the discharging process. To generate the necessary voltage and capacity, several electrochemical cells can be connected in series and/or

parallel. The redox equations that describe the charging process for a $LiCoO_2$/graphite battery are as follows (Equations 1.1 & 1.2):

$$6\,C + x\,Li^+ + x\,e^- \rightarrow Li_xC_6 \quad \text{(Negative electrode reaction)} \qquad 1.1$$

$$LiCoO_2 \rightarrow Li_{1-x}CoO_2 + x\,Li^+ + x\,e^- \quad \text{(Positive electrode reaction)} \qquad 1.2$$

The electrode materials of batteries should be stable, reversible, cheap, have high electronic and ionic conductivity, and be environmentally friendly. Moreover, they must be insoluble in the electrolyte and chemically inert with respect to the electrolyte [14]. On the other hand, the electrolyte, which acts as a medium to transfer ions between anode and cathode during cycling, should have high ionic conductivity for fast cycling and low electrical conductivity to prevent unwanted electrical short circuits inside the battery [15]. Furthermore, the electrolyte should not participate in the redox reactions and needs to be chemically stable in contact with the electrodes during cycling and over long storage times.

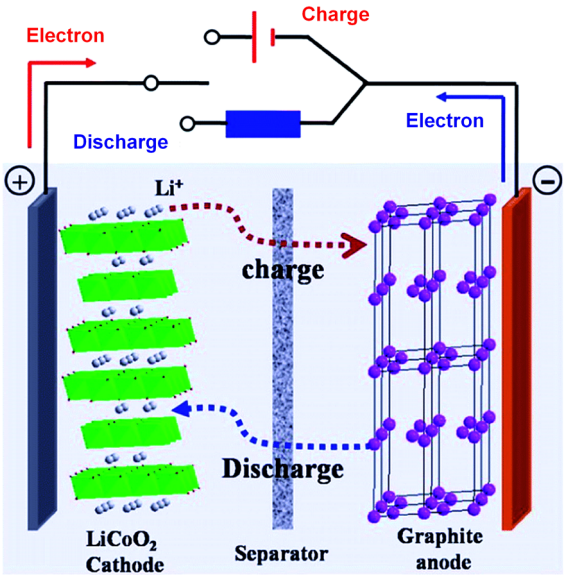

Figure 1.1: Schematic diagram of a rechargeable lithium ion battery [16].

1.2 Lithium ion batteries

The first attempt to develop rechargeable lithium ion batteries (LIBs) started in the 1970's [17]. They were first commercialized by Sony in the early 1990s [18] using layered $LiCoO_2$ as positive electrode (cathode) and carbon as the negative electrode (anode). They have a high energy density arising from a high working potential and good capacity [19]. This makes them attractive energy storage systems, satisfying the basic needs for mobile applications and

consumer electronics. Since then researchers exerted great efforts to develop different types of lithium-based batteries and different designs to improve their performance. Many different kinds of Li-ion batteries are available based on various cathode, anode, and electrolyte materials [20–22]. At present, lithium ion batteries are the most advanced batteries on the market for portable electronic devices. The improvement in both gravimetric and volumetric densities of the different types of commercial battery systems are shown in Figure 1.2.

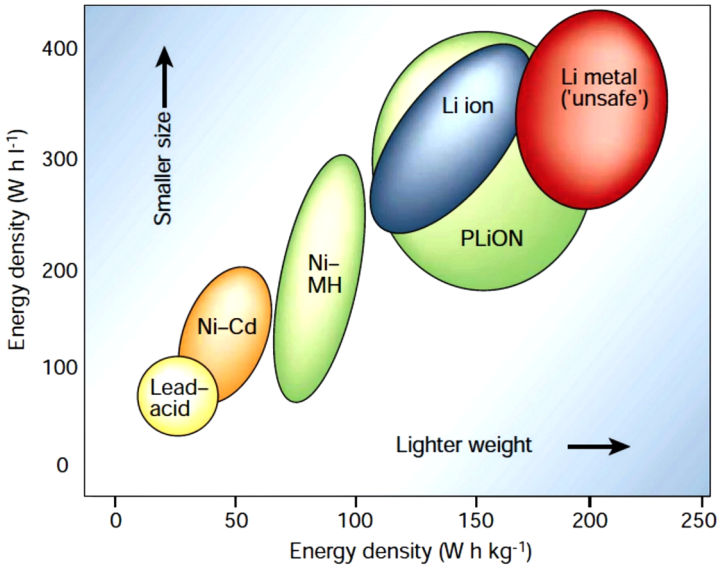

Figure 1.2: Comparison of the energy density (Wh kg^{-1}) and energy density (WhL^{-1}) for Ni-MH, Ni-Cd, and Lead-acid commercial batteries [23].

Besides the aforementioned properties of electrode materials, the ideal anode material for LIBs should have a large amount of moveable Li per formula unit and its potential must be close to that of metallic Li [14]. Graphite as an anode material satisfies most of these requirements [14, 24] and, therefore, is the preferred choice for current commercial Li-ion batteries [21]. However, the number of Li ions, which can be intercalated in carbon, is small (the stoichiometry is LiC_6) resulting in a reversible capacity of 372 mAh g^{-1} [24]. Moreover, the lithium diffusion rate into graphite is between 10^{-9} and 10^{-7} cm^2 s^{-1} resulting in a low power density [25].

Metallic lithium would provide a very high theoretical capacity (3860 mAh g^{-1}) [26]. However, lithium dendrite formation on the anode surface during charging has prevented the reliable use of lithium metal as an anode. Lithium dendrite formation is also a problem on other anode materials. Many factors influence the dendrite formation, such as high charging rates [27] or the degree of random orientation of the particles in the anode material that leads to an inhomogeneous charge distribution and hence non-uniform current distribution [28]. These

factors affect the diffusion rate of lithium ions into the anode so that Li plating takes place instead of intercalation in the electrode lattice [29]. The dendrites grow into the electrolyte with the repeated cycling and can penetrate the separator forming a short circuit in the LIB [30], so that the complete chemical energy stored in the battery will be converted to heat resulting in smoke, fire, or explosion [14]. Therefore, new anode materials such as carbon nanotubes (1100 mAh g^{-1}) [31], graphene (960 mAh g^{-1}) [32], SiO (1600 mAh g^{-1}) [33], silicon (4200 mAh g^{-1}) [34], germanium (1600 mAh g^{-1}) [35], and tin (994 mAh g^{-1}) [36] are under development.

Efforts to develop better anode materials and improve the electrochemistry of LIBs will further enhance the battery performance. However, more critical are cathode materials, which currently have lower specific capacity [23] and higher cost [37]. Cathode materials have been intensely investigated over the years to improve battery performance and increasingly also environmental issues. As a result, there are a number of promising cathode materials such as $Li(Ni_{0.8}Co_{0.15}Al_{0.05})O_2$ [38] and $Li(Ni_{1/3}Co_{1/3}Mn_{1/3})O_2$ [39] with reduced Co-content compared to $LiCoO_2$ [40], as well as $LiMn_2O4$ [41], $LiFePO_4$ [42], $LiVPO_4F$ [43] and $Li_3V_2P_3O_{12}$ [44].

1.3 Beyond lithium

Application of LIBs is limited because of their energy density, the required environmental conditions, safety risks, their aging (even if not in use), needs for circuit protection, and the high cost. High power density, longer lifetime, a wide operation temperature and high operating voltage would be allowing battery pack designs with only one cell for most the portable electronics. The automobile industry has been focusing on EVs as an alternative to the traditional vehicles based on gasoline engines. EVs require longer battery lifetimes and higher power and energy densities than offered by the present lithium ion batteries [45]. For example, the EV needs a battery pack that can deliver a total energy content in the order of 100 kWh to match the internal combustion engine [46].

Huge efforts have been exerted over the last two decades to find alternative batteries such as chloride ion batteries [47], fluoride ion batteries [48], magnesium ion batteries [49], and sodium ion batteries [50] to reach the required energy density. Theoretically, Mg-ion batteries has a high volumetric capacity of 3833 mAh cm^{-3} (compared to 2046 mAh cm^{-3} for Li metal) [49]. Also, chloride ion batteries can provide a high theoretical energy density of 2500 WhL^{-1} [51], close to the theoretical volumetric energy density of Li/S battery, 2199 WhL^{-1} [52]. The theoretical energy density of the fluoride system can be more than

5000 WhL^{-1}, 50% above the theoretical capacity of the Li air cell [53]. Optimizing the electrode materials for these new battery types could lead to very good alternative batteries to satisfy more of the requirements of the different applications, such as the energy density discussed above.

Another critical aspect for current lithium ion batteries is the electrolytes, which typically consist of an organic liquid with an inorganic ion conducting salt. Close to the freezing point of the electrolyte solution (around -20 ˚C in typical commercial systems) the performance is strongly reduced because of the limited lithium mobility in the frozen solution [54]. Even more critical, flammability and volatility of the organic liquid result in a limitation for the operating temperature and can become a safety limitation [55, 56]. In most commercial lithium ion batteries, the electrolyte solution starts to deteriorate at temperatures above 60 ˚C [54]. As a result, irreversible reactions between the dissolved lithium salts and the solvent can take place, which affects the performance. If the battery temperature is increasing further, typically above 80 ˚C [57], vaporization will lead to a pressure build-up inside the battery, which can eventually lead to a rupture of container resulting in a fire and in some cases even to an explosion [56]. In some cases, thermal decomposition of $LiPF_6$ at temperatures above 50 ˚C in the presence of water could result in the formation of highly toxic HF compounds [58].

A wide range of different battery materials and cell setups has been developed or is currently under investigation to fulfil specific performance requirements. For instance, sodium is more abundant and less expensive than lithium, so sodium ion batteries (SIBs) could be an attractive replacement for LIBs [50]. SIBs have some advantages over LIBs such as higher safety, a higher half-reaction potential for sodium (-2.71 V vs. standard hydrogen electrode (SHE)) compared to lithium (-3.04 V vs. SHE) and, hence, the possibility to utilize water-based electrolytes of lower decomposition potential [59]. Furthermore, Na ion is less Lewis-acidic compared to Li ion and, hence, fast transfer of Na ions at the electrode-electrolyte interface could be achieved in SIBs [50]. However, the energy density of SIBs is typically lower compared to LIBs [60]. Nevertheless, for large-scale stationary systems a high energy density is less critical [61], so SIBs might become economically competitive for grid energy storage of renewable energy sources like solar and wind power [60].

Rechargeable magnesium batteries have been long considered as a highly promising technology for energy storage [49, 62]. Mg has several advantages that rank it as one of the most promising metal anodes for batteries with high energy density. Mg is divalent with a density lower than Li, so carrying two electrons per ion offers a theoretical volumetric capacity of 3833 mAh cm^{-3} versus 2046 mAh cm^{-3} of Li [49]. Mg anodes do no show dendrite formation

during charging, which is a major safety concern when using metallic lithium as anode [62]. Moreover, it provides a chance for cost reduction because of its high natural abundance in the earth crust (the 5th most abundant element) [49] and most Mg compounds are nontoxic [62]. Furthermore, Mg has a higher reduction potential of -2.37 V (vs. SHE) than Li (-3.04 V vs. SHE) and, hence, the possibility to utilize electrolytes of lower decomposition potential. Therefore, magnesium ion batteries have attracted increased attention. However, the absence of good electrolytes and cathodes for magnesium ion batteries makes the currently achieved energy density and rate capability of prototypes not attractive enough for commercializing [49, 63].

In addition to Na- and Mg-ion batteries, chloride ion batteries [47, 51], fluoride ion batteries [48], potassium ion batteries [64] and aluminium ion batteries [65] have been introduced as new electrochemical systems. However, currently, the most utilized battery systems are LIBs as they provide a good overall compromise for mobile applications and consumer electronics.

1.4 All-solid-state ion batteries

An increasingly investigated class of batteries are all-solid-state ion batteries as they provide a potential solution to the aforementioned problems. All-solid-state ion batteries combine a higher energy density, low volatility, higher safety with the absence of the corrosive solvent leakage or harmful gas production, and a wider operating temperature range in comparison to commercial ion batteries with liquid organic electrolyte [66, 67]. The schematic setup is analogous to a liquid battery, but a thin solid-state ionic conductor is used as electrolyte. However, solid electrolytes have not been used much in bulk batteries until recently because of the lower ionic conductivity of solid electrolytes at room temperature (RT) compare to the organic liquid electrolytes [68]. This can partially be overcome by working with a very thin solid electrolyte layer, but production of larger batteries without short circuits is then challenging. Therefore, the key material under development for all-solid-state batteries is a solid electrolyte with high ionic conductivity at RT, low electrical conductivity and good processability.

Moreover, solid-state electrolytes demonstrate superior stability against lithium dendrite growth [69] and there is no need for a separator, simplifying the battery design. Furthermore, high operating voltages and high volumetric density can be achieved by stacking the solid-state cells in one package, which are favourable for vehicle applications [70]. In addition to overcoming safety issues, solid electrolytes provide a possibility to use attractive high capacity

electrode materials, which are difficult to use in conventional liquid electrolyte batteries, such as lithium metal as negative electrode and sulphur as positive electrode [71].

With the recent advances in solid-state electrolytes, increasing efforts to develop solid-state electrolytes with high ionic conductivity, approaching the conductivity of liquid electrolytes are currently pursued. For example, $La_{0.9}Ba_{0.1}F_{2.9}$ with an ionic conductivity of 2.8×10^{-4} S cm^{-1} at 150 °C [48], or for lithium transport $Li_{1.3}Al_{0.3}Ti_{1.7}(PO_4)_3$ (7×10^{-4} S cm^{-1}) [72], $Li_{1.5}Al_{0.5}Ge_{1.5}(PO_4)_3$ (4×10^{-4} S cm^{-1}) [73], $La_{0.51}Li_{0.34}TiO_{2.94}$ (1.4×10^{-3} S cm^{-1}) [74], $Li_{2.9}PO_{3.3}N_{0.46}$ (3.3×10^{-6} S cm^{-1}) [75] and $Li_7La_3Zr_2O_{12}$ (3×10^{-4} S cm^{-1}) [76]. However, the conductivities of these solid electrolytes are still low compared to organic liquid electrolytes used in commercial lithium ion batteries (10^{-2} S cm^{-1}) [71]. On the other hand, sulphide glass-ceramic electrolytes have higher ionic conductivity than oxides due to the large ionic radius of sulphur ions [77], e.g. $Li_{10}GeP_2S_{12}$ and $Li_7P_3S_{11}$ have a high ionic conductivity of 1.2×10^{-2} S cm^{-1} [78] and 1.1×10^{-2} S cm^{-1} [79], respectively. However, sulphides are chemically unstable. The sulphide glass-ceramic electrolytes can react with ambient moisture to produce H_2S gas [80], and hence, extra attention is required in handling and packaging of sulphide electrolytes.

1.5 Fluoride ion batteries

As discussed above, alternative ion shuttles provide much higher theoretical capacities compared to lithium. One example is rechargeable batteries based on a fluoride ion shuttle [48] currently developed in the group of Prof. Fichtner at Karlsruhe institute of technology (KIT). They are a promising alternative to Li-ion batteries with energy densities of more than 5000 WhL^{-1} [53]. Figure 1.3 shows a schematic of a fluoride ion battery, illustrating the cycling process. This cell consists of a metal (M′) electrode as anode and a metal fluoride (MF_x) electrode as cathode in the charged state. During discharging, fluoride anions (F^-) will migrate from the cathode (MF_x) to the anode (M′) through the electrolyte forming a metal fluoride $M'F_x$ at the anode. At the same time, the electrons provide the work in the external circuit moving from anode to cathode. The equations of the corresponding cathodic and anodic reactions that describe the discharging process are as follows (Equations 1.3 & 1.4):

$$xe^- + MF_x \rightarrow M + xF^- \quad \text{(at cathode)} \qquad 1.3$$

$$xF^- + M' \rightarrow M'F_x + xe^- \quad \text{(at anode)} \qquad 1.4$$

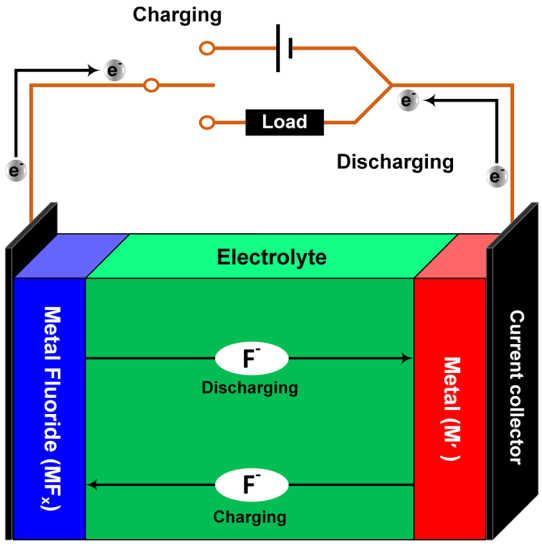

Figure 1.3: Schematic diagram of a rechargeable fluoride ion battery.

The high capacity is due to the large change in free energy during the formation of the different metal fluorides yielding high theoretical potentials [48, 53]. Moreover, more than one electron can be transferred per metal atom when the reaction of bivalent or trivalent metals with several anions takes place [81]. Metal combinations that were initially investigated are CuF_2 composites, BiF_3 composites, SnF_2 and $KBiF_4$ as cathode materials in the charged state versus Ce metal as anode and $La_{0.9}Ba_{0.1}F_{2.9}$ as solid electrolyte to validate the concept mentioned above [48]. All these full battery systems were cycled at a temperature of 150 °C to ensure sufficient ionic conductivity of the solid electrolyte. The results show that the first discharge of all cathodes is lower than the theoretical values (42-77% depending on the specific material). The partial discharging was attributed to isolated agglomerates of active material that were not connected to either ion or electron transfer. In parallel to the work in this thesis, further tests were performed on Bi composites or Cu as a cathode, and CeF_3, CaF_2, MgF_2, or Mg/MgF_2 composites as an anode [82]. During charging, all cells exhibited capacities higher than the theoretical values, indicating that side reaction(s) occurred, e.g. the formation of β-BiO_xF_{3-2x} in addition to BiF_3 was observed. This phase is assumed to be the result of fluorination of Bi_2O_3 present in the starting Bi powder. Moreover, BiF_5 is formed after charging to 4 V, which contributed to the high capacity obtained during first charging. After discharging, X-ray diffraction (XRD) showed the presence of β-BiO_xF_{3-2x} in addition to Bi, indicating an irreversible reaction of the oxyfluoride, which (partially) explained the low capacities during first discharging. No further cycling was possible for these systems even at 150 °C.

To develop a functional fluoride ion battery, a good fluoride ion conducting electrolyte is critical. The electrolyte currently used is a polycrystalline $La_{0.9}Ba_{0.1}F_{2.9}$ solid solution. At high

temperatures, it has a good conductivity, i.e. 2.8×10^{-4} S cm^{-1} at 150 °C [48], but at RT the conductivity is rather low with 2×10^{-6} S cm^{-1}. There is a continuous research effort at Helmholtz Institute Ulm (HIU) (group of Prof. Fichtner) to develop improved fluoride ion conductors.

Another important development aspect is the electrode composites used and their morphology. The pure metal fluorides are electrically insulating and exhibit poor fluoride ion conductivity. Therefore, it is essential to use composites adding components for electrical and ionic conductivity, intermixed at the nanoscale for intimate contact of all components. In the published work, carbon and $La_{0.9}Ba_{0.1}F_{2.9}$ have been added by ball milling [48, 83]. However, prior to the start of this thesis, no information on the morphology of these composites was available. Furthermore, for the optimization of solid-state fluoride ion batteries, information on the role of interface structures, the influence of crystal orientation and defects as well as the structural/morphological stability are critical.

1.6 *Ex situ* characterization of battery materials and systems

Ex situ characterization of battery materials before and after cycling is necessary to understand the fundamental behavior of the materials in the electrochemical reaction, interphase phenomena, mechanisms by which the ions interact with electrode materials, and mechanisms of cell degradation based on the micro- and nanostructure. The ability to achieve that and, hence, create advanced electrical storage systems relies critically on the characterization tools with high spatial and energy resolution. Scanning electron microscopy (SEM), (scanning) transmission electron microscopy (S)TEM, XRD, nuclear magnetic resonance spectroscopy (NMR), X-ray absorption spectroscopy (XAS), Raman spectroscopy, and atomic force microscopy (AFM) have contributed tremendously to a fundamental understanding of electrical storage systems.

X-ray scattering techniques as non-destructive analytical techniques can provide information about the crystal structure [84] and chemical composition [85] of the materials as well as the three-dimensional (3D) morphology using tomography technique [86]. For example, the 3D morphological evolution of $LiVO_2$ negative electrode during oxidation was studied by X-ray tomography to investigate the degradation mechanisms [86]. The 3D microstructure of the $LiVO_2$ was visualized and quantified using a transmission X-ray microscopy (TXM) before and after exposure to air. Pre-existing cracks were observed because of the stress induced during electrode processing. After exposing to air, an oxide layer (Li-rich oxidants) of 120-240 nm thickness was observed on the surface of $LiVO_2$ particles. Moreover, the distribution of the

particle size showed an overall shift towards smaller particles, while the volume remained relatively constant after oxidation. This attributed to the crack growth due to the local exothermal oxidation reactions resulting in a phase transition with an alteration of lattice constants.

^{7}Li NMR spectroscopy is another important characterization tool, which is used to characterize different electrodes of Li-ion cells. For example, ^{7}Li-MAS-NMR (magic angle spinning NMR) of an inverse spinel cathode material ($LiNi_{1/3}Co_{1/3}Mn_{1/3}VO_4$) revealed a small paramagnetic effect and small side bands compared to $LiNi_{1/2}Co_{1/2}VO_4$ [87]. This was attributed to lattice expansion upon Mn substitution making the lithium nucleus more distant from the lattice transition metal ions. Furthermore, focussed ion beam scanning electron microscopes (FIB-SEM) tomography has proven suitable for the reconstruction and characterization of the porous battery materials. For example, FIB-SEM tomography was used to reconstruct the carbon-binder domain of a $LiCoO_2$ battery cathode [88] and the results revealed that the porosity inside the carbon-binder domain is 57%. Moreover, the results showed that the clustering in the carbon-binder domain decreased its electronic conductivity and increased the ionic diffusivity.

In addition, the combination of different techniques provides a multi-modal analysis, which allows to reveal complex and interdependent processes in electrodes and at interfaces. For instance, neutron diffraction and NMR spectroscopy were used to study the size influence on the phase morphology and the mobility of Li ions in nanosized lithiated anatase (Li_xTiO_2) [89]. Neutron diffraction provides information on atomic structure and phase transition, while NMR spectroscopy provides information on the dynamics and the local environment of the Li ions. Therefore, detailed structural and mobility information for Li can be extracted from these combined methods. As a result, it was shown that, e.g. crystalline anatase particles of 40 nm size are lithiated and changes in phase behavior and morphology were observed. In addition, a reduction of the conduction-electron density at the Li ions sites was observed by NMR, which was accompanied by a reduced spontaneous Li ion mobility. As another example, correlative microscope combining focussed ion beam (FIB) and SEM with Time-of-Flight Secondary Ion Mass Spectrometry (TOF-SIMS) was used to achieve nanoscale-mapping of mixed oxide Li-ion battery cathodes (Li-rich nickel-manganese-cobalt oxide) [90]. The maps of Li, Mn and Co revealed the microstructural consequences of the electrochemical reaction during charging and discharging. Increased local concentration of Li near grain boundaries and at particle interfaces was observed, which may has an important effect in the structural degradation by inducing stress concentration and leading to a reduction in ionic conductivity and capacity fading [90].

1.6.1 *Ex situ* TEM of battery materials and systems

While the aforementioned examples illustrate the use of advanced analytical techniques to understand the performance of batteries, these techniques have a relatively low spatial resolution. In order to reveal structural features down to the atomic scale, TEM is a very powerful tool that can provide structural information through high resolution imaging in TEM or STEM mode [91], selected area electron diffraction (SAED) [92] as well as local compositional information through energy dispersive X-ray spectroscopy (EDX) [93] and chemical and electronic structure information through electron energy loss spectroscopy (EELS) [94].

Traditionally, TEM characterization is performed *ex situ* at selected states during cycling. For example, the effect of the upper potential limit on the structure and electrochemical properties of layered $LiNi_{1/3}Mn_{1/3}Co_{1/3}O_2$ (NMC) as a cathode material for LIBs was studied using TEM [95]. Cycling up to 4.2 V resulted in stable performance of the electrode, but higher voltages caused capacity fading. TEM studies of the cathode cycled to 4.2 V revealed only the rhombohedral NMC phase in the electrode (Figure 1.4a), whereas after 50 cycles to 4.3 V the rhombohedral and the spinel-like phase coexist in some of the particles (Figure 1.4b). After 50 cycles to 4.6 V also pure spinel-like particles could be detected by TEM (Figure 1.4c, d). This transformation from rhombohedral to spinel-like structure was attributed to the capacity loss. The study illustrates the importance of different TEM analyses for materials characterization.

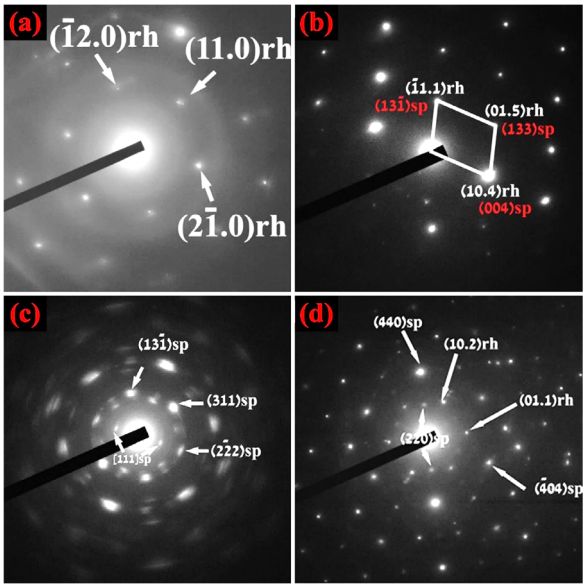

Figure 1.4: SAED patterns of $LiNi_{1/3}Mn_{1/3}Co_{1/3}O_2$ (NMC) electrodes after 50 cycles at (a) 2.5-4.2V, revealing only rhombohedral NMC phase; (b) 2.5-4.3V, revealing a mixture of both spinel-like and rhombohedral NMC phases; (c, d) 2.5–4.6 V, revealing some particles of only spinel-like phase and other particles of a mixture of both spinel-like and rhombohedral NMC phases [95].

In another example, the first cross-section observation of an all-solid-state Li-ion battery by TEM was reported in 2008 by Brazier et. al. [96]. In the study, an all-solid-state ion battery ($LiCoO_2$/solid electrolyte/SnO) was prepared using pulsed laser deposition (PLD) and a FIB system was used to cut and lift-out a cross-section (Figure 1.5). TEM was used to analyse the pristine and cycled states of a set of batteries. The results reveal a rapid deterioration at the SnO-electrode/electrolyte interface during cycling as a result of electromigration between the stacked layers (Figure 1.6).

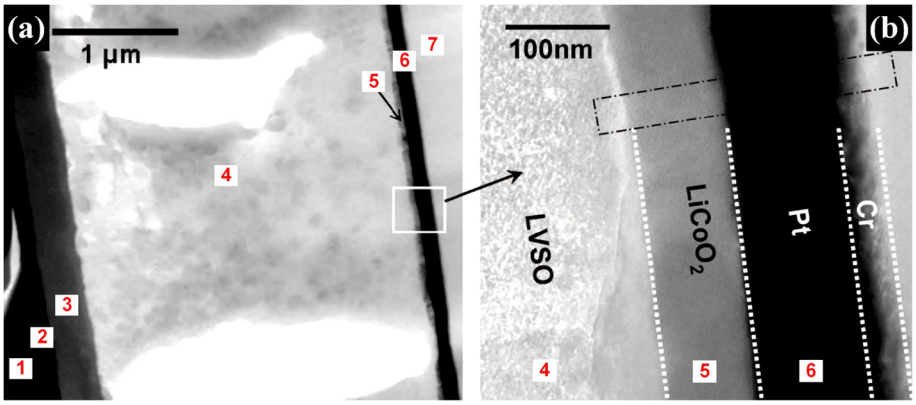

Figure 1.5: (a) TEM image of the entire structure of a pristine micron-sized battery showing the following sequence: (1) FIB deposited platinum, (2) PLD platinum, (3) SnO negative electrode, (4) Li_2O-V_2O_5-SiO_2 electrolyte, (5) $LiCoO_2$ positive electrode, (6) PLD chromium and platinum, and (7) glass substrate. (b) TEM image at higher magnification of the region close to the $LiCoO_2$ [96].

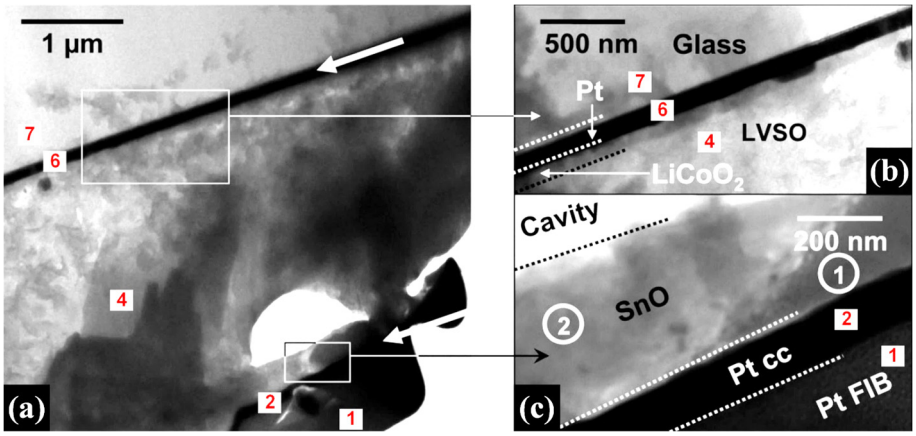

Figure 1.6: (a) TEM image of the cycled micron-sized battery, the arrows indicate the positive (top) and the negative (bottom) Pt current collectors' layers; (b, c) Higher magnification images of the $LiCoO_2$ positive electrode region and SnO negative electrode region [96].

While *ex situ* characterization of battery materials is important to understand electrochemical reactions, it only allows to characterize specific individual states, whereas real-time observation of the structural evolution during electrochemical cycling is missing. This

becomes critical to identify metastable phases and to prevent relaxation effects/reactions during transfer and analysis, that do not appropriately reflect what happens during cycling [97]. In particular, removing/inserting the cell materials from/to the characterization tool has a great effect for air and moisture sensitive materials. Most materials used in Li-ion batteries are air and moisture sensitive, which may lead to spontaneous redox reactions during the characterizations [97]. Moreover, the *ex situ* studies leave many open questions about kinetics, mechanisms of interactions, and mechanism of cell degradation. Currently, attempts to perform studies *in situ* to overcome some of these problems are very popular.

1.7 *In situ* electrochemical studies

During the past few years, there has been a growing interest to develop various *in situ* characterization tools to study structural changes during cycling by optical microscopy (OM) [30, 98], scanning electron microscopy [99], transmission electron microscopy [100], X-ray diffraction [101], nuclear magnetic resonance spectroscopy [102], and Raman spectroscopy [103]. These *in situ* studies provide direct information about the phase transformation, morphological changes and material degradation mechanisms during cycling. For example, the lattice parameters and strain of the layered lithium excess compound $Li[Li_{0.2}Ni_{0.2}Mn_{0.6}]O_2$ during the first electrochemical charge/discharge cycle were studied by *in situ* X-ray diffraction [101]. Rietveld refinement revealed dynamically changing lattice parameters during the first electrochemical cycle. The lattice parameter *c* increased in the sloping region of the charging curve associating with a slight decrease in the lattice parameter *a*, when Ni was oxidized from Ni^{2+} to Ni^{4+} as Li was removed from the layered structure and, hence, the ionic radius decreased. Then both lattice parameters *c* and *a* decreased through the plateau region. After discharge, the lattice parameters *a* and *c* increased to values larger than observed from the pristine material and the lattice ratio *c/a* expanded showing irreversible changes. Moreover, the results revealed large changes in strain, which was attributed to non-uniformly distributed lithium and oxygen vacancies. During discharging, the strain increased because of the intercalation of Li ions into the structure filling the lattice vacancies and causing lattice expansion.

The advantages and limitations of some techniques used to study batteries *in situ* are summarized in the next Table 1-1.

Table 1-1: Advantages and limitations of some microscopy/spectroscopy techniques used in the *in situ* study of batteries.

Technique	Advantages	Limitations
▪ **Optical microscopy**	• Studying macro structure changes	• Not appropriate to monitor microstructural changes as the spatial resolution is low.
▪ **Scanning electron microscopy**	• Good spatial resolution (~1 nm) • 3D and topographical imaging • Large depth of focus	• Mostly morphology information • No information about the oxidation state and electronic structure. • Mostly surface information
▪ **X-ray absorption spectroscopy**	• Information about electronic structure and oxidation state [104, 105] • Amorphous samples can be analysed [105] • Low X-ray dose (low radiation damage) [104]	• Inability to distinguish atoms of similar atomic number [104, 105] • Signal is average from a large area/or volume of the battery
▪ **Atomic force microscopy**	• Information about volume changes • Studying mechanical properties [106] • Good spatial resolution (nm range) • Very sensitive to surface changes	• No information about the oxidation state and electronic structure • Only surface structure
▪ **Raman spectroscopy**	• Determine Raman active structural changes • Not limited by sample state [107] • Amorphous samples can be analysed [107] • High spatial resolution using tip enhanced Raman spectroscopy (TERS) [108]	• Thermal degradation because of intense laser radiation [107] • Typically, difficult to obtain quantitative information [107]
▪ **Nuclear magnetic resonance spectroscopy**	• Detailed information about chemical and physical properties • Detailed information about the local electronic environment around nucleus	• The applied magnetic fields can be shield by the metal parts present in the battery (casings, current collectors) [109] • Cathodes of paramagnetic nature can produce a signal broadening and peak shifting [110] • Signal is average from a large area of the battery

While the aforementioned *in situ* techniques are powerful, TEM is the only characterization tool that can provide directly structural, compositional and morphological information at the nanometre and atomic scale.

1.7.1 *In situ* TEM electrochemical studies

The vacuum in the column of the electron microscope is the main obstacle to image liquid specimens, as most liquids evaporate and destroy the high vacuum. There are different strategies to overcome this problem for *in situ* electrochemical studies in the TEM. One approach is to introduce an environmental chamber in the electron microscope (E-TEM) [111], where additional apertures are placed in the pole pieces of the objective lens to enable a poor vacuum in the sample region, while the main part of a column can maintain high vacuum. Early *in situ* TEM experiments have been documented by E. Ruska in 1942 [111] and H. Hashimoto et al. in 1968 [112] using this approach. More recent alternative approaches are to replace the volatile liquid by ionic liquid or solid electrolytes and by introducing a closed cell better resembling a typical *ex situ* battery setup. These two strategies will be explained in detail in the next two sections.

1.7.1.1 Closed cell approach

The closed cell approach, in which a liquid is enclosed between thin membranes forming an encapsulated environment for the TEM measurements, was first proposed by Abrams & McBain in 1944, [113]. The thin membranes should have high permeability for electrons, mechanical strength to withstand the pressure differences and be resistant to the medium [113]. F. M. Ross and co-workers performed early *in situ* electrochemistry in the TEM, where the electrodeposition of nanoscale copper clusters was characterized in real-time [114]. In the closed cell approach, organic (or in general volatile) electrolytes can be used. This enables a cell more closely resembling the operation conditions in actual batteries. To study the liquids and volatile substances inside a TEM, two silicon micro-electromechanical systems (MEMS) consisting of thin electron transparent silicon nitride membranes at the centre are assembled face-to-face with a thin spacer to seal the liquid (Figure 1.7) [114, 115]. If the liquid layer and the membrane windows are sufficiently thin, this setup allows imaging with a spatial resolution of ~0.2 nA at 200 kV [116]. For *in situ* cycling using external electrical current, current collectors (typically Pt or Au) are fabricated on the silicon chips. In the past decade, the rapid development of new TEM sample holders and liquid cell platforms [114, 117, 118] is enabling a quantitative analysis of electrochemical processes such as nanoparticle growth from solution [119] or direct observation of beam sensitive materials [120]. For instance, the dynamic growth of Pt_3Fe nanorods in solution was imaged in real-time using TEM (Figure 1.8A & B) [121]. In this study, small nanoparticles were formed at the beginning due to the reduction of Pt and Fe

precursors by the electron beam. These nanoparticles interacted, forming nanoparticle chains. It was observed that the preferred addition of new nanoparticles to the chains is at the end rather than the formation of a side chain, suggesting the predominance of dipolar forces for the growth. These chains finally straightened forming smooth single crystal nanorods, presumably reducing the total system energy by reducing the surface energy and eliminating the crystal defects. High resolution transmission electron microscopy (HRTEM) images obtained during growth revealed different orientations of the nanoparticles, indicating that lattice rotation occurred during formation of a straight single crystal nanorod (Figure 1.8C).

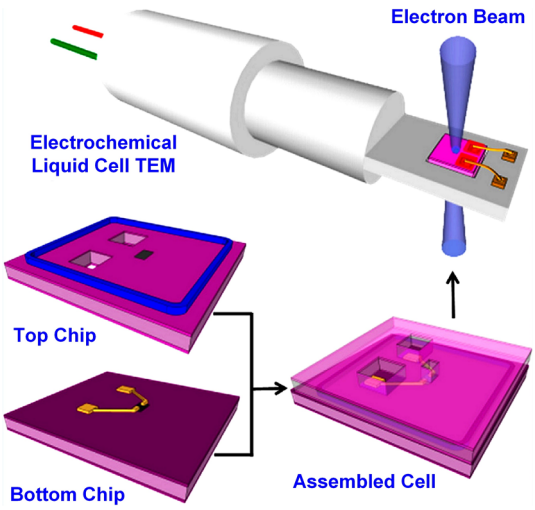

Figure 1.7: Schematic of an *in situ* TEM holder using a liquid cell for observation of electrochemical reactions [122].

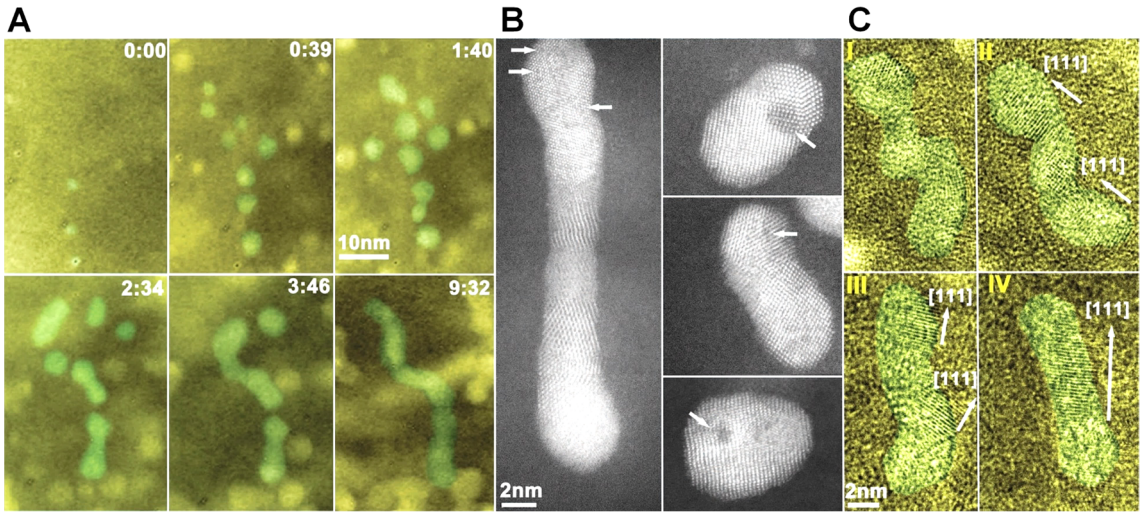

Figure 1.8: (A) Sequential coloured TEM images showing the growth of Pt_3Fe nanowires in a liquid cell during exposure to the electron beam. Time is displayed as minutes:seconds, (B) HR-STEM images of a polycrystalline Pt_3Fe nanorod, dimers, and nanoparticles obtained in a liquid cell. The dark spots (highlighted by arrows) indicate the iron rich regions, (C) Sequential HRTEM images showing both crystal orientation and shape changes during the straightening of a twisted nanoparticle chain [121].

A similar approach has also been applied in Li-ion battery research in order to visualize the lithiation-delithiation processes and to study the effect of electron beam on battery materials [122, 123]. For example, M. E. Holtz and co-workers visualized the Li ion distribution during charging and discharging of an electrode prepared of $LiFePO_4$ nanoparticles in a liquid cell using *in situ* energy filtered transmission electron microscopy (EFTEM) [123]. The phase transformations and different delithiation mechanisms in neighbouring particles were imaged. Moreover, core-shell structures and anisotropic growth in different particles were observed within the same agglomerated nanoparticles. In another study, P. Abellan et al. studied the stability of different electrolytes against electron beam illumination by *in situ* liquid STEM [120]. The electron beam caused localized electrochemical reactions allowing to estimate the electrolyte breakdown by imaging the decomposition products (Figure 1.9). It was observed that apart from lithium triflate in dimethyl sulfoxide, all the other tested salt containing solutions showed evidence for degradation, although the specific rates, products, and mechanisms varied and depended on the salt solvent combination. The degradation of $LiAsF_6$ in 1,3-dioxolane started by forming particles, which evolved into nanorods that continuously grew suggesting no degradation in the organic solvent (Figure 1.9a). The growth of rounded nanoparticles was observed instead of nanorods in both $LiAsF_6$ in dimethyl carbonate (DMC) (Figure 1.9b) and $LiAsF_6$ in ethylene carbonate (EC)/DMC (Figure 1.9c). The particle growth appeared to be slower by mixing EC with DMC (Figure 1.9c). To study the effect of the salt, the stability of $LiPF_6$ in EC/DMC was tested under the same dose conditions used for $LiAsF_6$ in EC/DMC (Figure 1.9d). The $LiPF_6$ mixture appeared to be more stable compared to $LiAsF_6$. Finally, a mixture of EC/DMC was tested to study the effect of electron beam on the solvent in the absence of salt (Figure 1.9f) and no obvious particle formation was observed.

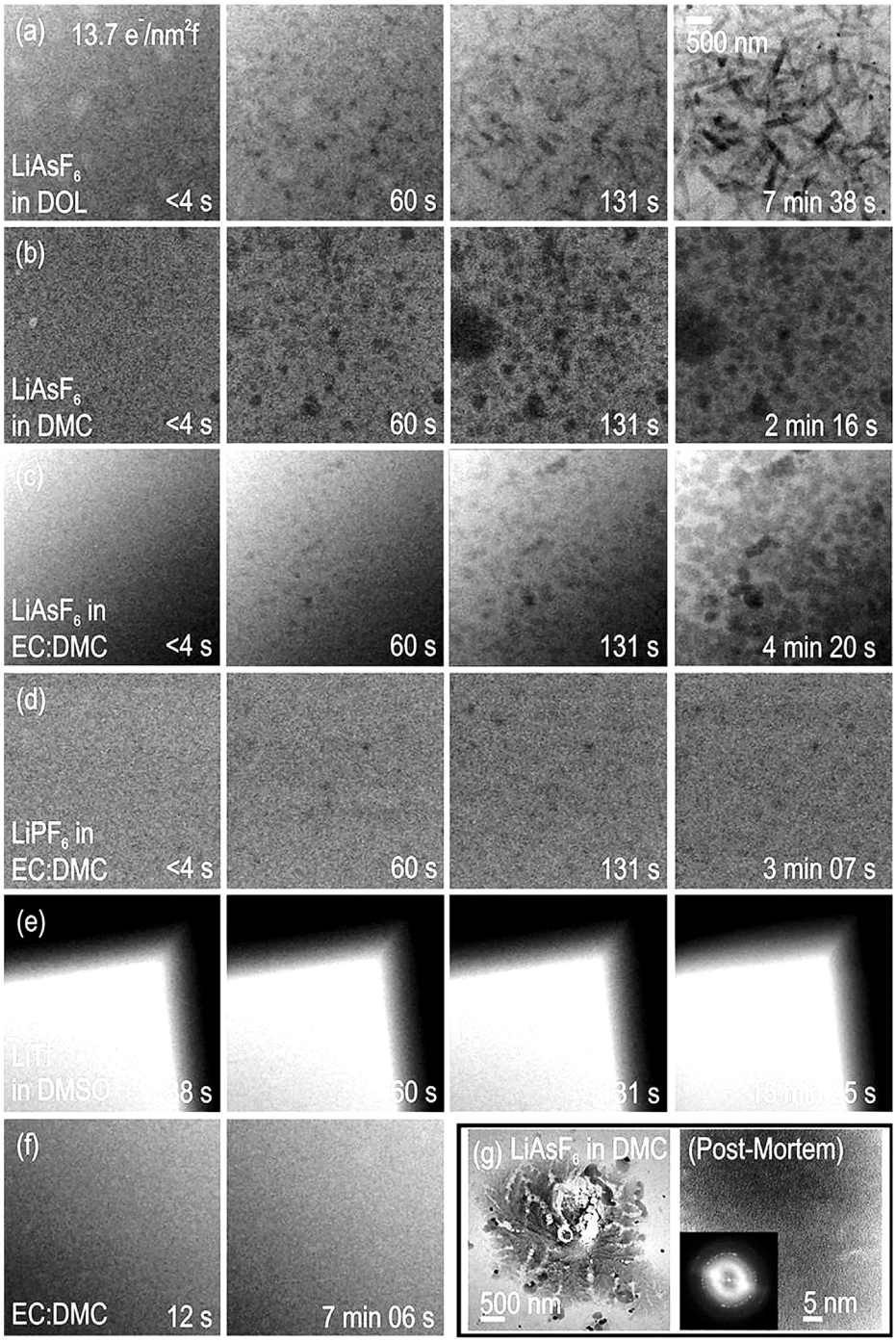

Figure 1.9: Electron beam induced breakdown of different electrolytes upon irradiation. (a-e) BF-STEM images showing the time evolution of different electrolytes during an exposure series and (f) frames from an exposure series of the pure EC/DMC solvent. (g) TEM images of an irradiated area of the $LiAsF_6$ in DMC mixture after separating and washing the Si chips for performing postmortem analysis. Low magnification (left) and HRTEM and consequent fast Fourier transform (FFT) of the irradiated area shows the presence of LiF nanocrystals [120].

As shown above, the high-energy electrons have a significant effect on the solution during imaging with the radicals and ions generated by the electron beam, which can participate in further electrochemical reactions [124]. Moreover, the electron beam acts as a

reduction agent for dissolved salts resulting in the growth of (metallic) nanoparticles [125]. Therefore, the electron beam–liquid interactions (e-beam damage) represent a major limitation for imaging liquid samples inside electron microscope. In addition, bubble formation from degradation products, heating, electrostatic charging and hydrocarbon contamination are common problems during *in situ* TEM [126, 127]. Consequently, radiation damage has to be critically considered when interpreting the results obtained for electron beam sensitive materials like Li containing materials or organics.

1.7.1.2 Open cell approach

In the "open cell" approach, a nanobattery is assembled either by using an ionic liquid electrolyte (ILE) to avoid evaporation in the high vacuum of the TEM column [128] or by using an all-solid-state battery [129]. Construction of a nanobattery using an ionic liquid electrolyte can be achieved using a STM-TEM (scanning tunnelling microscopy combined with transmission electron microscopy) holder with the active material under investigation in form of nanorods, nanotubes or nanoparticles. These electrode materials are attached by the simple adhesion forces to a clean current collector surface at the tip of the STM-TEM holder. On the other side, a tungsten tip is used to carry the counter electrode, which is covered by an ILE as electrolyte [128]. Alternatively, Li_2O, which forms on a Li surface in air during transfer into the TEM can also be used as solid electrolyte [129]. The positions of the nanowires on the STM-TEM tip can be adjusted with a high accuracy towards the counter electrode to establish contact between the electrodes through the electrolyte. Figure 1.10 shows schematic illustrations of these approaches for an open cell configuration.

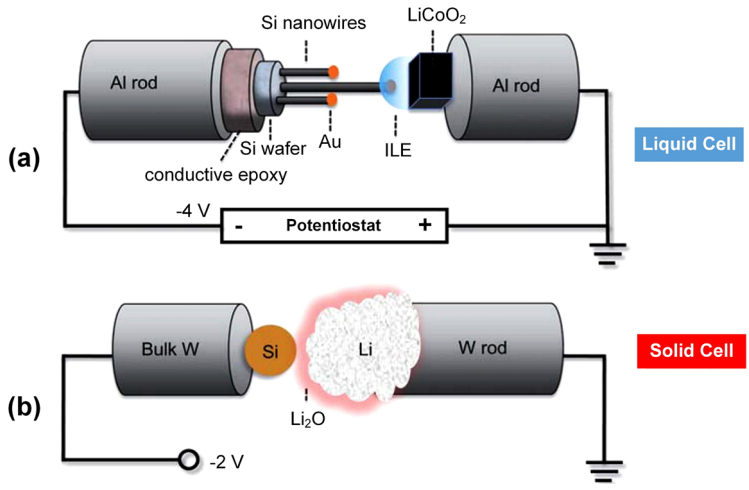

Figure 1.10: Schematic illustrations of the open cell nanobattery setup inside a TEM using (a) ionic liquid electrolyte, (b) solid-state electrolyte (the thin Li_2O layer formed on the Li metal) [100].

As an example for a TEM study with an open cell approach, Jian Yu Huang et al. investigated a single SnO_2 nanowire anode with an ionic liquid electrolyte and a $LiCoO_2$ cathode [130]. The *in situ* TEM observation of the lithiation of the SnO_2 nanowire during electrochemical charging revealed the propagation of the reaction along the nanowire causing swelling, elongation, and spiral. TEM analysis showed a transformation of the nanowire from single crystalline before the reaction and small nanocrystals (Li_xSn and Sn) dispersed in an amorphous matrix (Li_2O) after prolonged charging. Moreover, the reaction front consists of a cloud of dislocations driven by the high stresses induced by the electrochemical reaction. It was suggested that these dislocations disturb the structural order of the crystal leading to amorphization. Furthermore, it was noted that the dislocation cores are highly effective Li transport channels facilitating the insertion of Li ions into the crystalline interior. Similarly, *in situ* TEM studies using ionic liquid electrolyte based open cells have been performed to understand fundamental aspects of the lithiation of silicon nanowires [131], SnO_2 nanowires [132], and amorphous silicon coated carbon nanofiber [133]. For example, Xiao and Jian [131] imaged the lithiation of a single crystalline Si nanowire in real-time while the tip of the nanowire was immersed in an ionic liquid electrolyte. During lithiation, the single crystalline silicon (*c*-Si) nanowire was partially converted to an amorphous lithium silicon (*a*-Li_xSi). In addition, they observed that the reaction proceeded from the surface to the centre of the nanowire while a residual *c*-Si core was usually observed even after extended charging. To improve the electrical conductivity of the nanowire, heavily doped Si nanowires, carbon coated and carbon-coated doped Si nanowires were studied. The microstructural evolution of the C-coated and the doped Si nanowires showed fast charging, large volumetric expansion and full lithiation to the crystalline $Li_{15}Si_4$ (*c*-$Li_{15}Si_4$) phase during the first charging process rather than the partial conversion to the a-Li_xSi alloy observed previously. During discharging, the *c*-$Li_{15}Si_4$ nanowire was delithiated to amorphous silicon (a-Si). An increased charging rate was observed for the doped Si nanowire coated with carbon causing spiral and twisting motion of the lithiated nanowire (Figure 1.11a-j). This nanowire was first lithiated forming an *a*-Li_xSi phase, followed by a transition to c-$Li_{15}Si_4$ phase (Figure 1.11k). The fast charging rate was attributed to the improved electron and ion transport. The authors found that the only crystalline phase formed as a fully lithiated phase was $Li_{15}Si_4$ rather than the $Li_{22}Si_5$ or $Li_{21}Si_5$ phases as widely believed. This means that the maximum lithium storage in Si is 3.75 Li/Si atoms corresponding to a maximum energy storage capacity for Li in Si of 3579 mAh g^{-1} rather than the widely believed 4200 mAh g^{-1}. However, this study could not determine the exact Li/Si ratio in the amorphous Li_xSi phase.

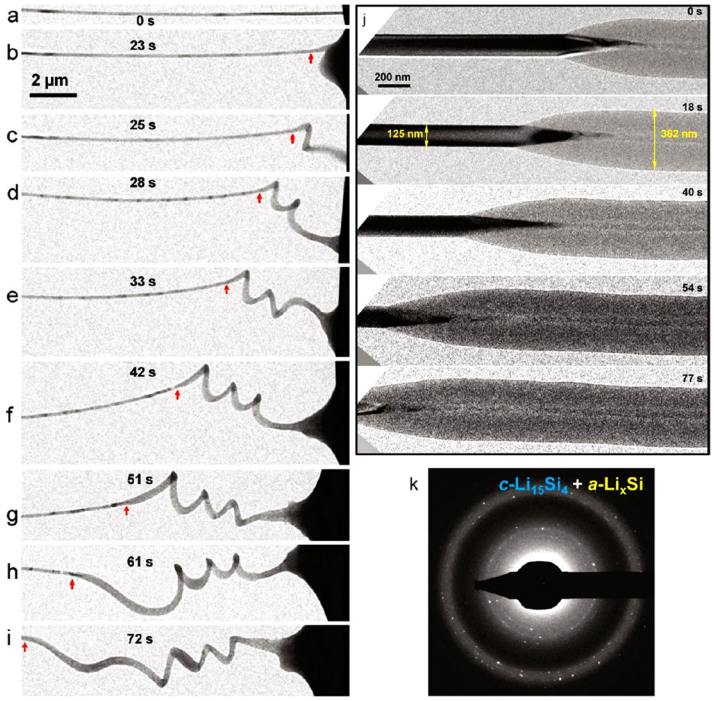

Figure 1.11: (a-i) TEM images of carbon-coated and phosphorus-doped Si nanowires during charging, (j) high magnification time-lapse TEM images showing the expansion and the core-shell lithiation behaviour, (k) SAED pattern showing coexistence of the *c*-$Li_{15}Si_4$ and *a*-Li_xSi phases [131].

All-solid-state nano-LIBs have been prepared inside a TEM using lithium with a thin Li_2O layer on the surface as one electrode and e.g. individual Co_9S_8/Co nanowire-filled carbon nanotube (CNT) as a working electrode [129]. Two types of nanowire-filled CNTs have been studied, filled CNTs with an open end and another with closed ends. For the filled CNTs with closed ends, the lithiation produced an axial elongation of 4.5% and a major radial expansion of 32.4% while the lithiated core of nanowire was confined inside the CNT. SAED results confirmed the phase transformation from a single crystalline Co_9S_8 nanowire to a polycrystalline nanowire of Co nanograins and Li_2S after lithiation. On the other hand, the full lithiation of Co_9S_8/Co-filled CNTs with an open end caused a radial expansion of 4% due to Li intercalation within the graphite layer while no axial elongation was detectable. However, the Co_9S_8 inside the nanowire showed an axial elongation of 94.2% while maintaining its diameter. Because of the large volume expansion during lithiation, the lithiated core was extruded out of the CNT (Figure 1.12). Moreover, a conical shape of the reaction front was always observed during lithiation (Figure 1.12c), which indicates diffusion of Li ions through the CNT shell. Therefore, the complete encapsulation of metal sulphides by CNTs is advantageous for anode material in LIBs to maintain the structural stability during the lithiation-delithiation process. Many other studies have been based on the same approach, e.g. for SiO_2 electrodes [134], silicon nanowires [135], Al nanowires [136], Ge nanowires [137], SnO_2 nanowires [134], InAs nanowires [138],

Si nanoparticles [139], an individual Co_3O_4/graphene nano-sheet [140], $MnFe_2O_4$/graphene nano-sheet [141], PbSe/reduced graphene oxide nano-sheet [142] and Fe_2O_3/graphene [143]. Similarly, the sodiation and desodiation in sodium ion batteries were recently studied *in situ* using nanowires with an open cell design, where Na metal is used as a source of Na ions with the oxide layer formed on the metal surface (Na_2O) acting as a solid electrolyte. For example, single crystalline alpha-MnO_2 nanowires [144], ZnO nanowires [145], and α-MoO_3 nanobelts [146] were studied inside the TEM. Other solid electrolytes have also been used in solid-state open cells such as $LiAlSiO_x$ [147]. All these different studies have made significant progresses in understanding the electrochemical reactions in batteries.

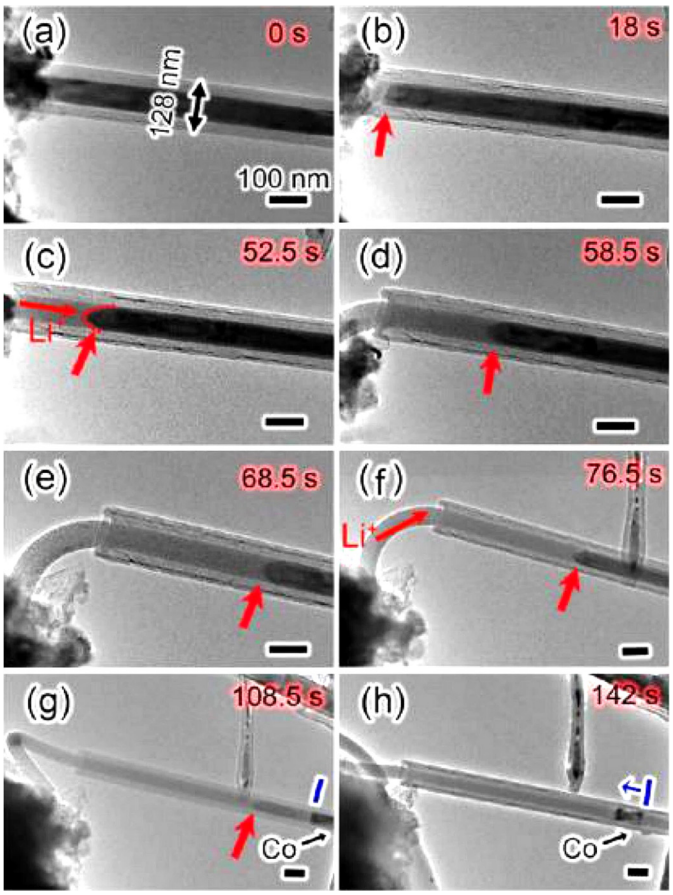

Figure 1.12: TEM images of an individual Co_9S_8/Co-filled CNT with an open end: (a) the selected Co_9S_8/Co-filled CNT, (b-h) time sequence of lithiation process showing the gradual extrusion through the open end of CNT [129].

Although the open cell configuration has been used extensively to study LIBs *in situ*, this system can only be considered as a simplified model as the ionic liquid electrolyte is only in point contact with the electrode so the diffusion patterns of Li ions in the electrode may differ from a real battery where the electrode is fully immersed in the electrolyte [124]. Moreover,

the results might not be directly transferable to other liquid electrolytes with solid electrolyte interphase (SEI) formation. In case of Li_2O as electrolyte, a large overpotential is normally applied to drive the Li ions into the electrode, so the kinetics and phase behaviour of lithiation may change [124]. Preparation of thin-film all-solid-state batteries and cutting a micron-sized battery from it to perform *in situ* electrochemical studies in the TEM is significantly closer to analysing a real battery. To prepare micron-sized all-solid-state ion batteries, a FIB system can be used to lift-out a lamella consisting of anode, cathode and electrolyte in between. A first *in situ* TEM study of an all-solid-state Li-ion battery prepared by FIB was performed by Y. S. Meng et al. in 2011 [148]. They used FIB to prepare micron-sized battery from an all-solid-state LIB consisting of an amorphous $Li_{3.4}V_{0.6}Si_{0.4}O_4$ (LVSO) as electrolyte, SnO_2 as an anode, and $LiCoO_2$ as a cathode. The thinned lamella of the battery still connected to the bulk battery was cycled within the FIB and the Li distribution in the cathode mapped afterwards. However, attempts for *in situ* cycling of an isolated micron-sized battery in the TEM resulted in an 'explosion' of the battery.

1.8 Motivation and outline of the present work

All-solid-state fluoride ion batteries were selected as a model system for *in situ* TEM investigation of their electrochemical processes as they are a new class of promising high capacity battery systems. However, the state-of-the-art nanocomposites prepared in the group of Prof. Fichtner as cathode, anode and electrolyte materials resulted in fluoride ion batteries with capacities far below the theoretical values and rapidly fading during cycling. Chemical and structural information for the fluoride ion batteries are needed to understand the basic processes, the degradation mechanisms, and the structural changes in the electrodes to develop a better understanding of the structure-property relationships for this type of battery. This understanding will help to improve the all-solid-state fluoride ion batteries.

The electrodes and electrolyte materials used in the fluoride ion battery are mostly stable under the electron beam, further making this a good model system for *in situ* TEM electrochemistry, not suffering from the typical beam damage and the problems present in most previous *in situ* TEM investigations. In addition, *ex situ* TEM studies at different stages of the electrochemical process were performed to understand the structural changes in batteries cycled at the envisioned elevated temperatures, which was not possible for our *in situ* MEMS devices. Furthermore, this is critical as reference to evaluate the *in situ* TEM results.

For the *in situ* TEM studies, all-solid-state micron-sized batteries were fabricated from fluoride ion batteries by using FIB. The fluoride ion batteries used in this thesis are:

1- A half-cell consisting of Bi/$La_{0.9}Ba_{0.1}F_{2.9}$/C as an electrode and $La_{0.9}Ba_{0.1}F_{2.9}$ as a solid electrolyte.
2- A full cell consisting of Cu/C as a cathode, Mg/MgF_2/$La_{0.9}Ba_{0.1}F_{2.9}$/C as an anode, and $La_{0.9}Ba_{0.1}F_{2.9}$ as a solid electrolyte.

As part of this thesis, the sample preparation for the *in situ* TEM studies was developed and optimized. The preparation started from an all-solid-state fluoride ion battery based on a compressed powder cell using conventional FIB TEM lamella preparation methods. Challenges that had to be overcome for the successful FIB preparation of a working battery include contamination during metal deposition, porosity of the battery materials, resistance of the metal contacts, MEMS leakage currents, and the cohesion and adhesion of/between the electrodes at the nanoscale. However, ultimately, it was possible to prepare a micron-sized battery closely resembling the bulk cell. The miniaturized cathode half-cell and full cell fluoride ion batteries were charged/discharged inside an aberration corrected TEM for the *in situ* studies to follow the structural changes.

In addition, *ex situ* TEM studies were performed for a full cell consisting of CuF_2/$La_{0.9}Ba_{0.1}F_{2.9}$/C as cathode, a La sheet as anode, and $La_{0.9}Ba_{0.1}F_{2.9}$ as a solid electrolyte. The system was cycled to different charging states for the investigation. The aim was to follow morphological and chemical changes as well as the various phases formed during cycling to understand the capacity fading.

1.9 Structure of thesis

This thesis consists of seven chapters with the following structure:

Chapter 1 covers the basic background of battery technology, the working principle, some history, and current limitations. In addition, the chapter introduces characterization techniques for batteries, in particular TEM studies of LIBs as reference for the current work.

Chapter 2 introduces the background and working principles of the analytical techniques used for understanding the electrochemical reactions such as XRD, SEM, FIB system and the different TEM techniques. In addition, electron-matter interaction and radiation damage in the electron microscope are discussed. Furthermore, the chapter presents the working principle of electrochemistry techniques (potentiometric and galvanometric methods).

Chapter 3 addresses how the materials for the fluoride ion batteries and the bulk batteries are prepared and their electrochemical characterization is introduced. Furthermore, FIB fabrication and mounting of micron-sized fluoride ion batteries are presented.

Chapter 4 presents the challenges in sample preparation for *in situ* studies such as porosity of the battery materials, contamination during metal deposition, resistance of the metal contacts, MEMS leakage currents, and interfaces smoothness.

Chapter 5 presents the results obtained during *in situ* TEM studies of the Bi/$La_{0.9}Ba_{0.1}F_{2.9}$ half-cell and the Cu/$La_{0.9}Ba_{0.1}F_{2.9}$/MgF_2 full cell. Furthermore, the electrochemistry result of a micron-sized Cu/$La_{0.9}Ba_{0.1}F_{2.9}$/MgF_2 full cell, which was cycled *ex situ*, is presented.

Chapter 6 presents the results of the *ex situ* TEM studies of the CuF_2/$La_{2.9}Ba_{0.1}F_{2.9}$/La full cell at different charging states.

Chapter 7 provides up the conclusions of the thesis and gives an outlook on future work.

2 Methods and characterization techniques

2.1 Introduction

For good materials understanding the knowledge of the morphology, crystal and electronic structure and their correlation with processing parameters, properties, and performance is mandatory for the development of battery materials. Characterization tools enable us to establish links between these aspects and hence understand the performance of materials. For that purpose, a large variety of characterization techniques are available such as SEM, TEM, AFM, XRD, energy dispersive X-ray spectroscopy (EDX), EELS, and X-ray photoelectron spectroscopy (XPS).

TEM is one of the major characterization tools to directly image the structure of a material down to the atomic scale, opening the door to synthesize new materials with exciting properties [149]. In order to interpret the (atomic) structure observed in TEM, understanding the interaction of the electron beam with the specimen is essential as well as understanding the effects of the microscope on the image formation. Therefore, this chapter will start with the interaction of the electron beam with bulk and thin film samples. In particular, the effect of the electron beam on battery materials will be discussed. Furthermore, the principles of X-ray powder diffraction, FIB microscope and TEM will be presented and its operation modes explained. Finally, potentiostatic and galvanostatic cycling techniques as tools for the electrochemical characterization will be presented.

2.2 Electron-matter interaction

2.2.1 Interaction of an electron beam with matter

The interaction of an electron beam with the specimen is the base for any electron microscopic characterization providing a wealth of information in the form of different types of signals that can be detected. Figure 2.1 shows the interaction of an electron beam with a thick sample, which can be classified into two main categories [150–152]:

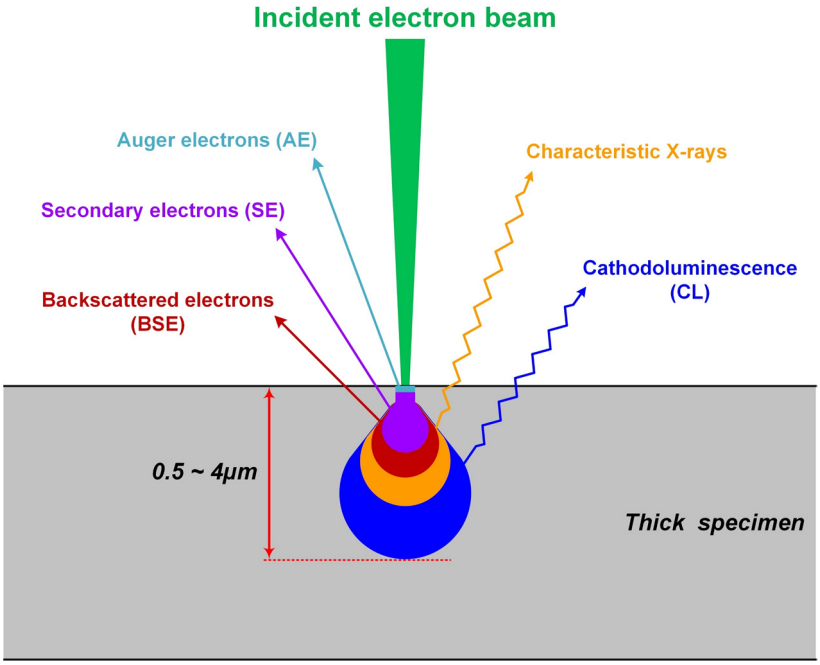

Figure 2.1: Interaction of high-energy electrons with a material (bulk specimen).

2.2.1.1 Elastic interactions

During an elastic interaction, no energy is transferred from the incident electrons to the specimen. Some of the electrons of the original high-energy beam are scattered/diffracted elastically by the atoms of the sample so that they are reflected from the sample surface forming the so-called backscattered electrons (BSE) providing information about atomic number differences in the material and for electron backscatter diffraction (EBSD) about the crystal structure/orientation.

2.2.1.2 Inelastic interactions

During an inelastic interaction, energy is transferred from the incident electrons to the specimen leading to a reduced energy of the electrons. Depending on the process causing the energy transfer, this will result in a range of signals emitted from the sample such as characteristic X-rays, Auger electrons (AE), secondary electrons (SEs) and cathodoluminescence (CL). These signals contain information about the specimen that can be collected in an (analytical) electron microscope to characterize the morphology and chemistry of the specimen.

- **Secondary electrons (SEs):**

SEs are ejected from an atom by transferring sufficient energy from an incident electron to overcome the work function. SEs have energies below 50 eV and therefore they can only

escape from regions near the surface. These electrons provide information about the morphology and surface topography in the SEM. In SE images, sharp edges appear bright compared to flat regions, which can be explained by the greater surface area of edges and hence a higher yield of SEs.

- **Characteristic X-rays:**

The atoms in a sample can be excited by the primary electron beam knocking an electron from an inner shell leaving behind a hole in the inner shell. For that, the primary electron must possess sufficient energy, which is higher than the energy difference to the next unoccupied electronic state. In this excited state, an electron from a higher energy level can fill the hole in the inner shell. The corresponding energy difference is then emitted in the form of electromagnetic radiation (X-ray) (Figure 2.2), which has a characteristic energy depending on the energy difference between the two states. The energy of X-rays is characteristic for the different elements as is explained in more detail in section 2.5.3.

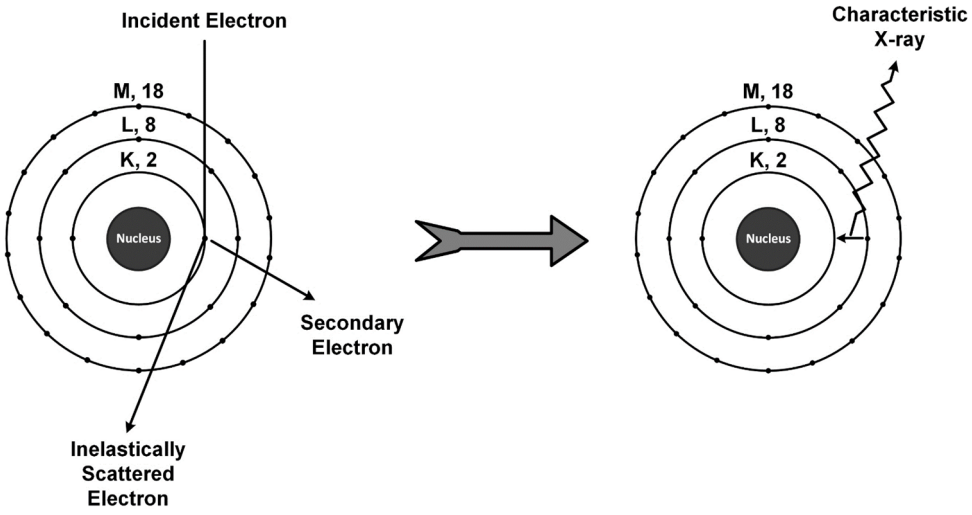

Figure 2.2: Origin of characteristic X-rays constituting the basis for EDX spectroscopy in the simplified framework of Bohr's atom model.

- **Auger electrons:**

An alternative relaxation of an excited atom is described by the Auger process. Instead of directly emitting the energy as a single characteristic X-ray, the energy difference of the transition will be transferred to another electron in the same atom that, in turn, gets sufficient energy to be emitted as an Auger electron. The energy of Auger electrons is characteristic for the different elements similar the characteristic X-rays. Their detection probability is highest for light elements. Auger electrons have low energies and interact strongly with the specimen

resulting in a strong absorption. Therefore, detectable Auger electrons come from a thin region close to the sample surface (~1-2 nm).

- **Backscattered electrons (BSE):**

Rutherford backscattering is an elastic scattering process as the result of the Coulomb interaction between the incident electrons and the nucleus of an atom. The backscattered electrons are high-energy electrons with the same energy as the incident electrons and can originate from up to a few microns in the specimen. The probability that an electron is backscattered from the sample depends on the average atomic number of the material. Atoms with high atomic number have large nuclei and their backscattering probability is high. This results in more backscattered electrons from phases with high average atomic number, so that these phases appear brighter than phases with low average atomic number in BSE images.

- **Cathodoluminescence (CL):**

Electron-hole pairs can be generated when a primary electron excites an electron from the valence band of the specimen to the conduction band. This excited state is energetically unstable and hence an electron from the conduction band can relax and fill the hole in the valence band. As a result of this recombination process, a photon carrying the energy difference will be emitted (CL). This difference in energy is small and hence the frequency of the emitted characteristic radiation is low, typically in the visible range. Measuring the wavelength of the CL is useful, e.g. in semiconductors to determine the band gap.

- **Transmitted electrons:**

If a sample is sufficiently thin, a large fraction of the incident electron beam will pass through the sample and can thus be detected in transmission as the basis for TEM analysis. The basic principles for the interaction of an electron beam with a thin sample are the same as for a thick sample leading to both elastically and inelastically scattered electrons in transmission in addition to the previously discussed signals as shown in Figure 2.3. While transmitted electrons can be detected for micron thick sample in case of high-energy electrons, a thin sample in transmission electron microscope refers to a sample where the majority of the electrons passes unscattered. Details on the information that can be obtained from the transmitted signals will be discussed in section 2.5.

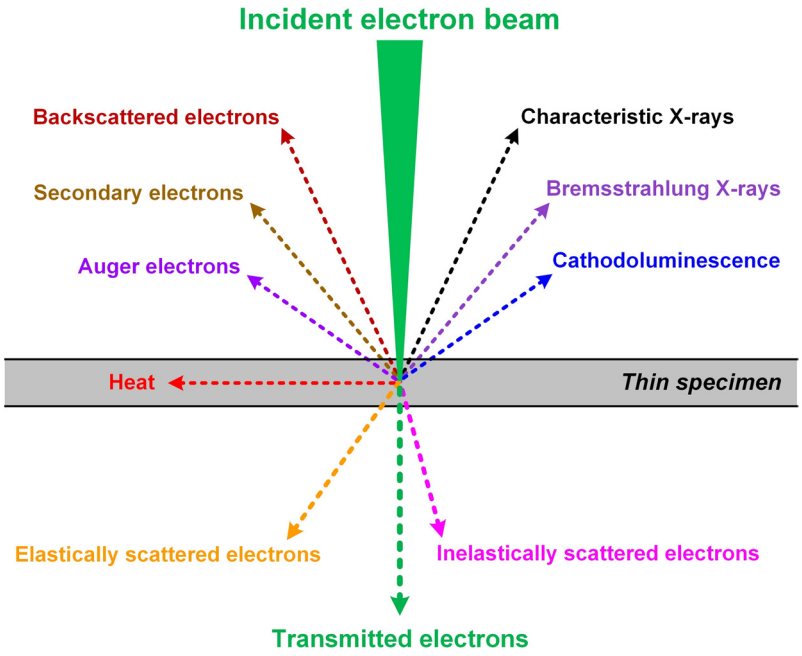

Figure 2.3: Interaction of high-energy electrons with materials (ultra-thin specimen).

2.2.2 Radiation damage in electron microscopy

Electron microscopic imaging and spectroscopy provide important information about the chemical composition and micro/nano structure of materials with high spatial resolution. However, the electron beam may also cause undesirable changes in the surface or the bulk structure of the specimen investigated. Especially for studying battery materials, electron beam damage remains a critical obstacle for the application of electron microscopy techniques. The mechanisms responsible for the electron beam damage are [153, 154]:

1- Knock-on damage where the kinetic energy and momentum of an incident electron will be transferred to an atom. If the transferred kinetic energy is higher than the displacement threshold or higher than the surface binding energy, the atom will be kicked out from its regular site to an interstitial or vacancy position or sputtered from the surface. This can result in an amorphization of the material and sputtering can lead to compositional changes. The damage rate will increase with increasing operation voltage.

2- Radiolysis is due to the Coulomb interaction between the incident electrons and the electron shell of an atom/molecule raising one of the electrons to an exited state or leading to ionization (in the same basic process giving rise to the signals for analytical TEM). The resulting ions and radicals can react further leading to fragmentation of the molecule or the formation of new chemical species. This process is also the primary cause for hydrocarbon contamination build-up by cracking/reaction of mobile hydrocarbons on the sample surface

during TEM or SEM imaging. The damage rate for radiolysis decreases with increasing operation voltage.

In X-ray and medical applications, the unit “Gray” (Gy) is used as a measure for the radiation dose and defined as “absorption of one joule of energy introduced by ionizing radiation to one kilogram of matter (1 Gy=1 J/kg)” [154]. A more common measure for the irradiation dose in electron microscopy is the “electron dose” as the number of the incident electrons hitting an exposed unit area (C/cm^2 or e/nm^2). It is assumed that every material has a dose threshold below which, beam damage is not strongly noticeable in TEM [155, 156]. Typically, the critical dose is quoted for specific imaging conditions in static TEM analysis, where the strength of a specific signal is reduced to $1/e$. This is typically tolerable for static imaging of the structure, but means that ~2/3 of the material is already damaged. However, beam damage effects are even more critical in *in situ* TEM as small amounts of excited atoms/molecules could lead to different side reactions. As an example of radiation damage, the effect of electron dose on one compound in Li-ion battery electrolytes (Li_2CO_3) [157] was studied, where a gradual degradation (decomposition) after repeated EELS measurements of the same area was observed. This degradation has been attributed to knock-on, ionization, and thermal effects of the electron beam that lead to structural and compositional changes [126, 157, 158].

In general, electron beam induced damage is decreased by reducing the dose per area, reducing the sample temperature (freezing the structure of interest) and the operating voltage can be optimized depending on the damage mechanism. Moreover, it was found that the critical dose can be dependent on the dose rate (e/nm/sec), e.g. decreasing the dose rate reduced the radiation damage of a CaF_2–Al_2O_3–SiO_2 glass [154]. To perform *in situ* electrochemical measurements or even just to study battery materials in the electron microscope, caution is required to consider electron beam irradiation effects during analysis as well as during sample preparation. Electron dose effects on the battery components must be understood and quantified, and imaging conditions adjusted to reduce the electron beam dose below the critical values to prevent significant artefacts [159]. In addition to the active battery materials, electron beam irradiation strongly affects organic electrolytes and thus the exchange of ions at the electrode-electrolyte interfaces as well as the transport of ions within the electrolyte [120]. With the combined effects on the electrode materials and the electrolyte it is therefore difficult to distinguish chemical and structural changes due to electrochemical cycling from those arising from electron beam effects in *in situ* TEM investigations.

2.3 X-ray diffraction (XRD)

XRD is a common analytical technique used for determining crystal structure, crystallite size, phase analysis and texture [160]. A typical X-ray diffractometer consists of a cathode ray tube (CRT) where a filament can be heated to emit electrons. By applying a high voltage, these electrons will be accelerated towards a water-cooled target. Characteristic X-ray spectra are emitted due to interaction between the incident energetic electrons and inner shell electrons of the target material. The generated X-ray spectrum is polychromatic and is typically filtered by a crystal monochromator to produce monochromatic radiation directed towards the specimen. As the X-ray wavelength is comparable to the spacing of the planes in a crystal lattice, crystalline materials act as three-dimensional diffraction gratings for the X-rays. Constructive interference of the X-rays is obtained when the path length difference **D** between X-rays scattered at different atoms is a multiple of the wavelength. From simple geometric considerations shown in Figure 2.4, the path length difference **D** can be calculated for lattices with distance **d** by equation 2.1 depending on the incident angle of the X-rays **θ**:

$$\mathbf{D = 2.d \sin \theta} \qquad 2.1$$

Consequently, constructive interference is achieved when **D** is equal to an integer number of the X-ray wavelength **λ.** Thus, diffraction peaks can only be observed if Bragg's law [161] is satisfied (equation 2.2), where **n** is the reflectance order:

$$\mathbf{n\lambda = 2.d \sin \theta}\ ; \mathrm{n} = 1, 2, 3, \ldots \ldots \qquad 2.2$$

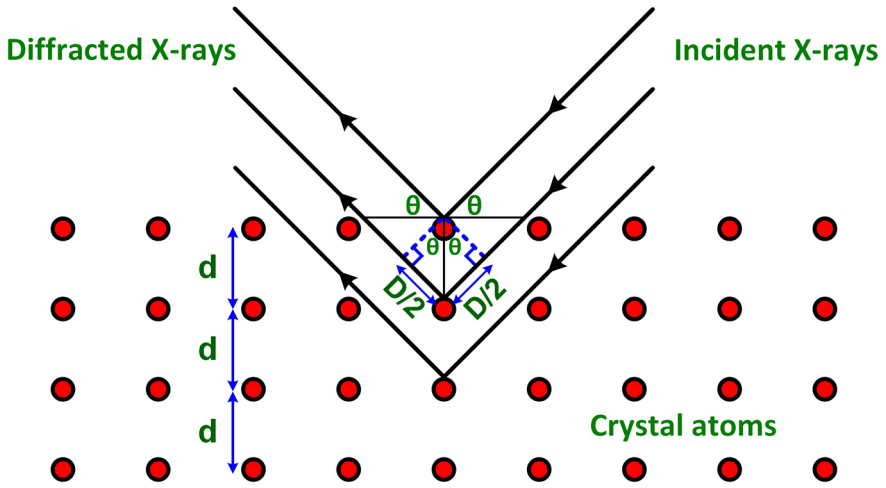

Figure 2.4: Schematic illustration of scattering at a regular lattice leading to Bragg's law for diffraction.

In a case of powder, all possible diffraction directions of the lattice planes are observed as a result of the random orientation of the power. Thus, the unit cell parameters and symmetry of the sample can be determined from the observed diffraction angles. Moreover, X-ray diffraction can be used to obtain further information such as [162]: strain, structural distortions, crystallite size, dislocation density, texture, and phase purity.

2.4 Scanning electron microscopy (SEM)

SEM is one of the most commonly used electron microscopy techniques. In a SEM, a focused electron beam is scanned across a selected area of a sample surface, where the electrons interact with the specimen generating different signals discussed in section 2.2.1. These signals contain information about the specimen morphology, topology, composition, crystal structure, and orientation. A typical SEM microscope comprises a column, which consists of an electron gun, two condenser lenses, an objective lens, the corresponding apertures, and the electronics to generate the required acceleration voltage. Moreover, the detectors and the sample stage are located in an evacuated chamber to reduce scattering of the electrons by the atmosphere. Figure 2.5 shows a schematic view of a scanning electron microscope.

The most commonly utilized signal is due to secondary electrons, which can be detected by an Everhart-Thornley detector or more recently using various types of in-lens detectors. Synchronized with the scanning electron beam, the secondary electron detector counts the number of electrons per unit time and transforms these counts to an electronic current. SE images are dominated by the surface topology as edges and convex surfaces of the sample appear brighter than flat surfaces because of the higher probability of secondary electron emission. This allows imaging the morphology and topology with a high resolution of $\sim$1 nm in state-of-the-art SEMs. In addition to SE detectors, BSE detectors are commonly employed in SEM analysis. As discussed in section 2.2.1, BSE imaging provides the atomic number or material contrast. The combination of both detection schemes allows to obtain topographical and compositional information of the sample surface. Furthermore, the combination with EDX analysis (discussed in more detail in section 2.5.3) can provide direct chemical information on a sub-micron level.

To prevent charging of non-conductive samples by the electron beam, a conductive coating, e.g. Au or Cr, is often deposited on the sample prior to the analysis [163]. Alternatively, low vacuum modes can be employed in specialized SEMs to reduce surface charging and to work with wet samples.

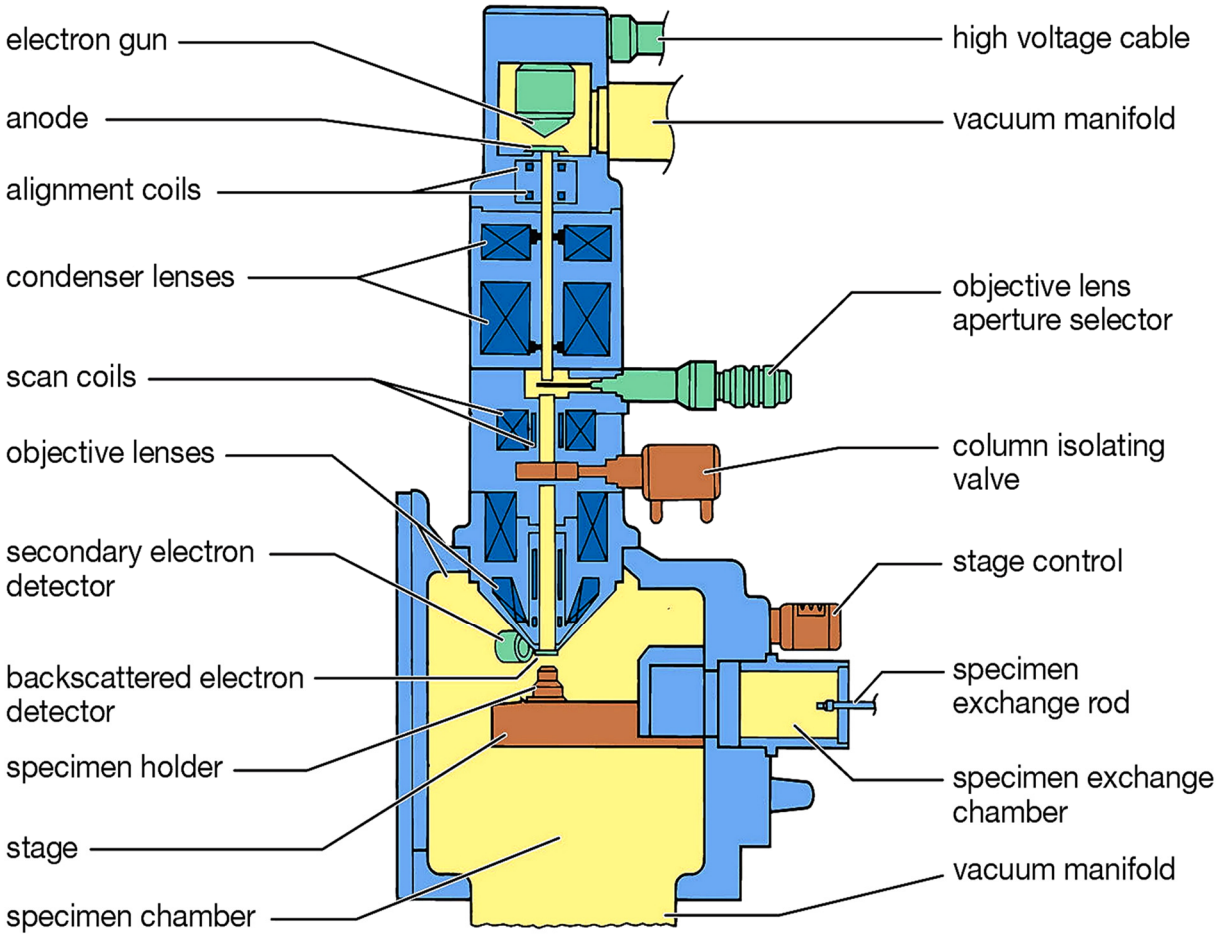

Figure 2.5: Schematic cross-sectional view of a scanning electron microscope [164].

2.5 Transmission electron microscopy (TEM)

TEM comprises a variety of different techniques that provide information on morphology, structure and composition of a sample. In general, the optical setup in a transmission electron microscope is similar to optical microscope. In a classical optical microscope, the resolution is limited by the wavelength of the light used for imaging. The resolution (**δ**) is typically given by the Rayleigh diffraction limit, see equation 2.3 [152]:

$$\delta = \frac{0.61\,\boldsymbol{\lambda}}{\boldsymbol{\mu}\sin\boldsymbol{\beta}} \qquad 2.3$$

where, **λ** is the wavelength of the incident electron, μ is the refractive index of the viewing medium, and **β** is the semi-angle of collection of the magnifying lens. The term "μ sin β" is also called numerical aperture and is around 1.4 in modern optical microscopes [165]. For green light with a wave length of 5100 Å, the resolution is thus limited to ~2200 Å. The De Broglie wavelength of electrons depends on the acceleration voltage and is between 4.18×10^{-2} Å and

1.97×10^{-2} Å for the typical voltages between 80 and 300 kV [166] used nowadays. This provides the potential for a huge resolution improvement into the far sub-Ångström range by using electrons for imaging [167]. The resolution in state-of-the-art electron microscopy is not diffraction limited, but limited by the energy spread and the microscope stability (information limit) and the ability to correct residual lens aberrations (point resolution). Recently, the information limit in TEMs has been improved to 50×10^{-2} Å with the development of highly stable aberration corrected TEMs [168], making it an excellent tool for nanostructure characterization.

Figure 2.6 shows a schematic cross-sectional drawing of a TEM. The electrons are extracted from the tip of the electron gun (located at the top of the TEM column) and are accelerated in high vacuum conditions by an applied potential typically of 80-300 kV to reach a speed of approx. 0.502-0.776 the speed of light [152]. The electron beam is shaped by a two or three condenser lens system (electromagnetic lenses controlling intensity, beam diameter and convergence angle) before illuminating the electron transparent specimen. The electron beam interacts with the specimen generating different scattered electrons and hence the signals for analysis (as discussed in section 2.2.1). A first intermediate image is formed by the objective lens. A four-stage projection system is used to magnify the electron intensity distribution of the first intermediate image for viewing/recording on a fluorescent screen, film or a charged coupled device (CCD) camera. [167].

The electromagnetic lens system in a TEM provides a much higher flexibility compared to classical glass lenses in an optical microscope and allows operating the TEM in a large variety of different modes such as STEM or SAED in addition to bright and dark field imaging (BF/DF-TEM). All of these modes can be combined with e.g. EELS and EDX spectroscopy for compositional analysis as well be discussed in the following sections.

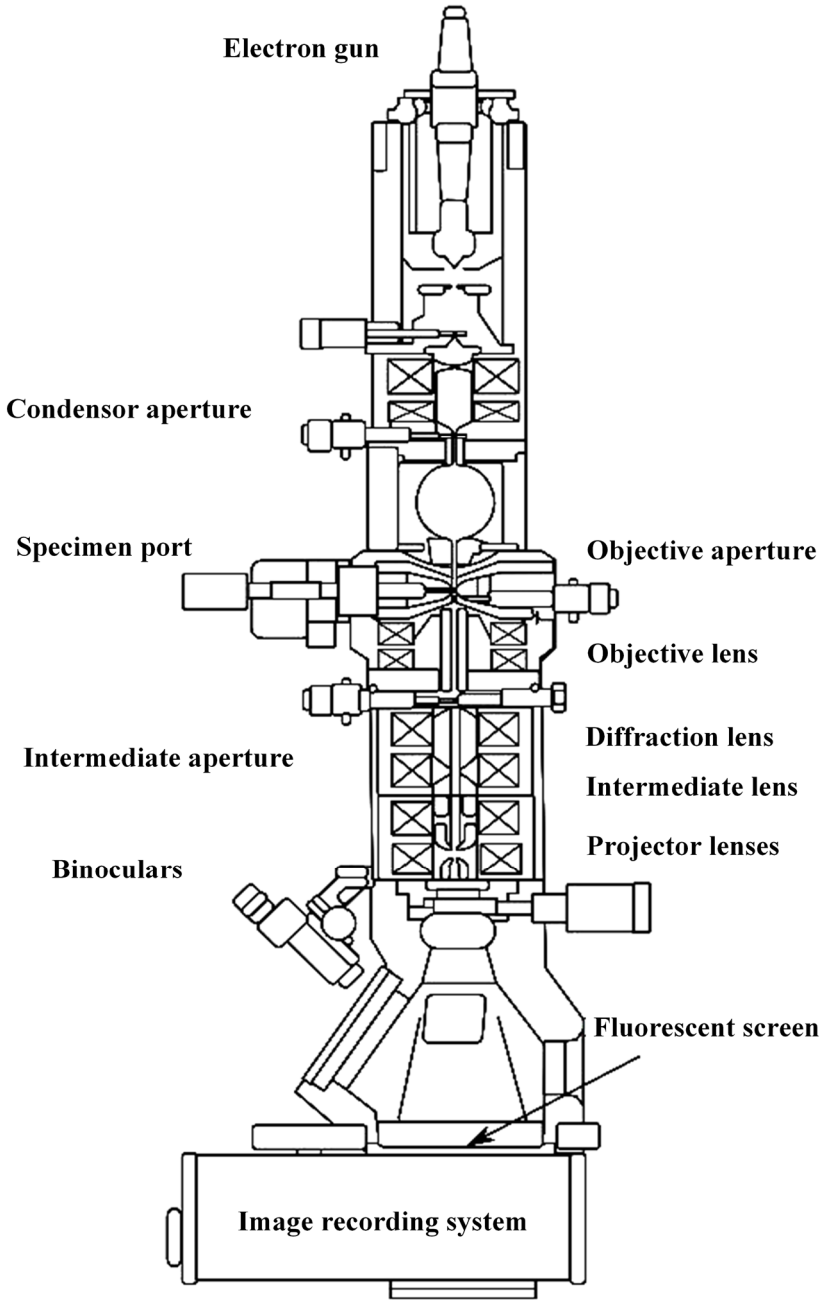

Figure 2.6: Schematic outlining the internal components of a basic TEM system [169].

2.5.1 Imaging and diffraction modes

A TEM can be operated either in imaging mode (BF- or DF-TEM) or in diffraction mode. As discussed before, the electron beam illuminates and interacts with the thin specimen, after shaping it using the condenser lens systems. The major part of the electron beam is forward scattered through the sample. An objective lens is used to focus the forward scattered electrons forming a primary image in the intermediate image plane, while the diffracted electrons are focused in the back-focal plane of the objective lens leading to the formation of a diffraction

pattern there (Figure 2.7). In TEM imaging mode, the diffraction lens is set to transfer the intermediate image onto the image plane of the projection system, which will then produce a magnified image on the screen (Figure 2.7b). In diffraction mode, the strength of the diffraction lens is changed to image the diffraction pattern in the back-focal plane onto the image plane of the projection system, so that a magnified diffraction pattern is imaged on the screen or CCD camera (Figure 2.7a).

For BF-TEM imaging (Figure 2.7b), an objective aperture is inserted in the back-focal plane of the objective lens limiting the acceptance angle of the beam and thus blocking some of the diffracted or highly scattered electrons. As a result, the areas strongly contributing to the blocked diffracted or scattered beams will have low intensity in the intermediate image plane and thus appear dark in the projected image. BF-TEM images therefore exhibit a mixture of mass-thickness and diffraction contrast. With increasing sample thickness and increasing density, the average scattering angle is increasing, thus resulting in a bigger fraction of the electron beam that is blocked by the objective aperture for thicker and/or more dense parts of the sample. This contrast is dominating BF-TEM images of amorphous samples. In addition, in crystalline samples some of the strong diffraction spots satisfying Bragg's law will be blocked by the objective aperture and the corresponding crystals will appear dark. This diffraction contrast is typically much stronger compared to the mass-thickness contrast and dominates BF-TEM images of crystalline samples.

For DF-TEM imaging, the incident beam can be tilted, so that one or more of the diffracted beams pass through the objective aperture, whereas all other diffracted beams and the directly transmitted beam are blocked. As a result, a DF-TEM image is formed, which shows all parts of the sample strongly contributing to the diffracted beams passing through the objective aperture as bright areas.

In the diffraction mode (Figure 2.7a) a diffraction pattern corresponding to the full area illuminated by the electron is formed in the back-focal plane and imaged on the screen. A selected area aperture can be inserted in the intermediate image plane to choose a region of interest resulting in a so-called selected area electron diffraction (SAED) pattern. Information about the crystal structure and orientation of the specimen can be obtained from the diffraction pattern analogous to X-ray diffraction. As an alternative to selected area electron diffraction, the illuminated area can be adjusted using the condenser system, which can be used to generate nano electron beam diffraction patterns (NED) from areas as small as a few nanometers [170]. Thus, it is possible to obtain individual single crystalline diffraction patterns even for nanostructured materials.

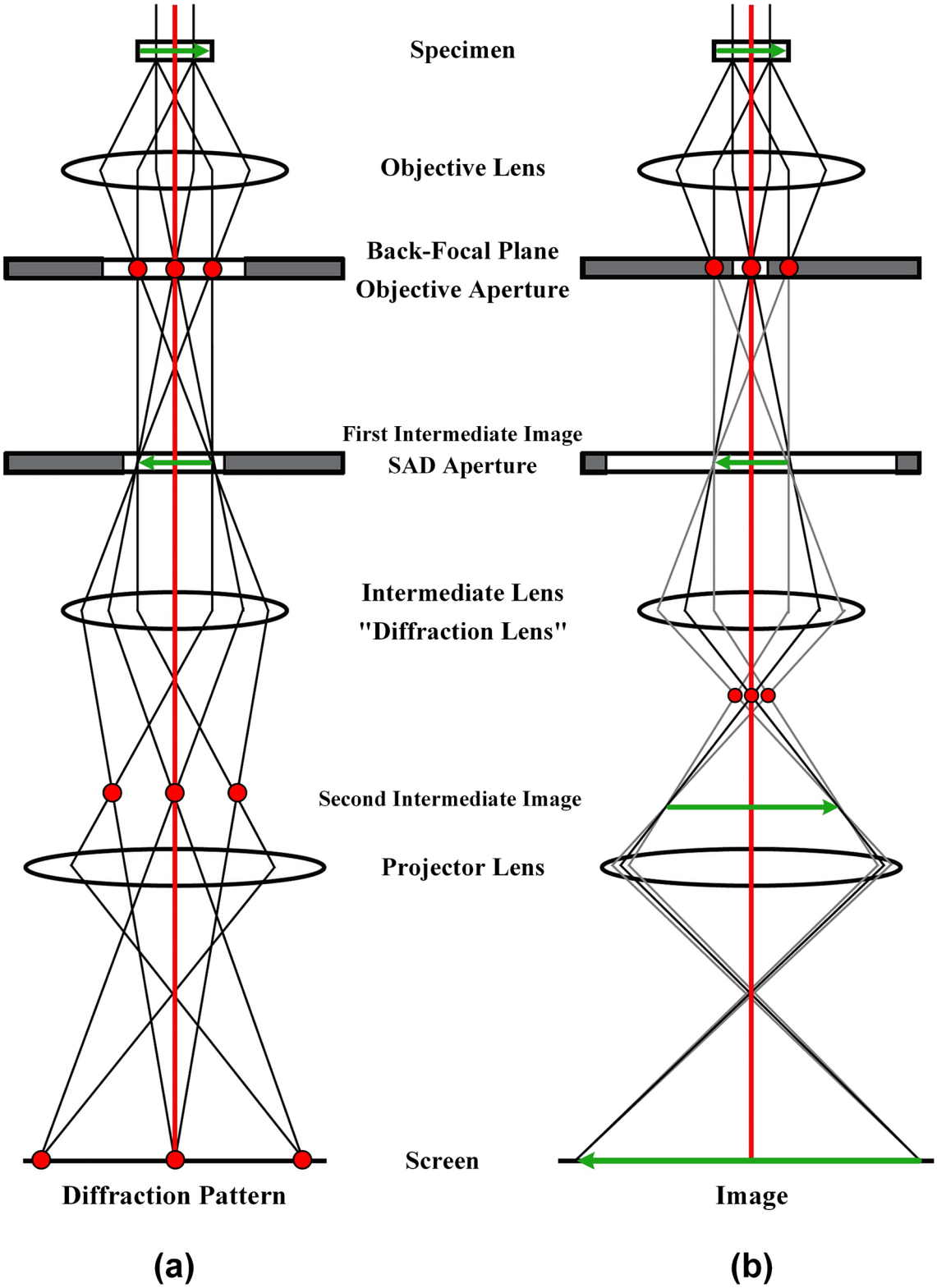

Figure 2.7: Schematic diagram showing the two basic operations of TEM (a) diffraction mode: projection of the diffraction pattern onto the viewing screen (b) imaging mode: projection of the image onto the viewing screen (modified from [151]).

2.5.2 Scanning transmission electron microscopy (STEM)

Scanning transmission electron microscopy is another TEM operation mode. In STEM, the electron beam is focused to a small spot (probe) on the sample and the probe is scanned across the specimen analogous to the SEM. The projection system is operated in diffraction mode and for each position of the probe, the intensity of part of the diffraction pattern is recorded. Depending on the part of the electron diffraction pattern used for the image formation, one differentiates between the bright field (BF), annular dark field (ADF) and high angle annular dark field (HAADF) STEM. A BF image is formed from the electrons that have not been diffracted, while DF images are formed by detecting the electrons scattered to low angles (ADF) or high angles (HAADF) as shown in Figure 2.8. By tuning the camera length in STEM, the scattering angle can by optimized and hence, the different scattering contributions can be tuned from more coherent scattering (diffraction contrast) to mostly Rutherford scattering (Z-contrast).

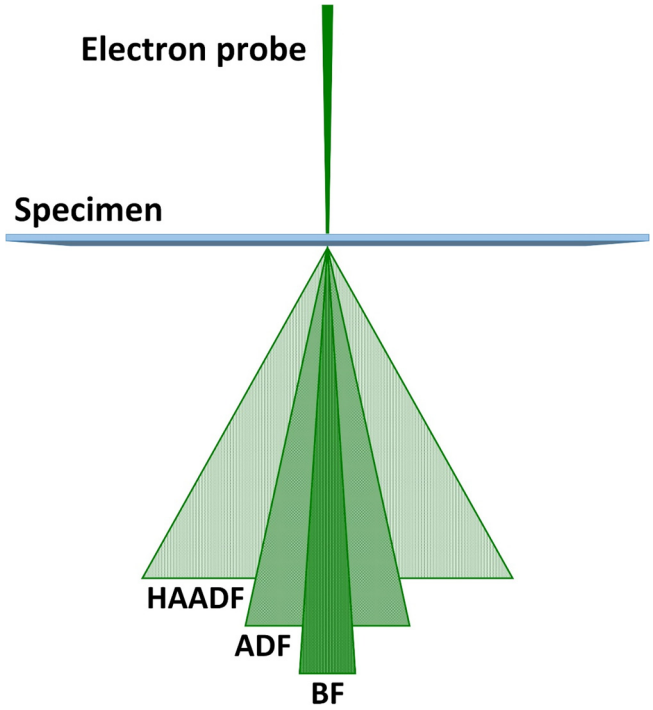

Figure 2.8: Schematic drawing of BF-, ADF-, and HAADF detectors for STEM imaging.

Most commonly, STEM images are recorded using the HAADF signal from electrons scatter to high angles. This is dominated by Rutherford scattering where the scattering power mostly depends on the average atomic number as well as the total amount of material [171], whereas coherent diffraction is weak at such high angles. Therefore, HAADF-STEM images are

dominated by the sample thickness and the average atomic number [167]. As a result, STEM-HAADF images can be easily interpreted in terms of Z-contrast with bright regions (more scattered electrons) corresponding to thicker regions or regions with a high average atomic number. Furthermore, STEM imaging can be easily combined with spectroscopy, where the local analytical signal can be recorded using EDX and/or EELS detectors. This provides direct information on composition, bonding and thickness for each data point with down to sub-nanometer resolution.

2.5.3 Electron dispersive X-ray analysis (EDX)

The X-rays generated during the interaction of the electron beam with the specimen (section 2.2.1) can be detected and their energy analysed by electron dispersive X-ray spectroscopy (EDX). Every element has a characteristic set of allowed transitions for electronic excitations satisfying the quantum mechanical selection rules (Figure 2.9). These transitions have a characteristic energy difference, resulting in a discrete set of X-ray energies for each element, which can be used to uniquely identify that element [172]. By combining STEM imaging and EDX analysis to acquire 2D arrays with full EDX spectra at each point, mapping of compositional differences in the specimen is possible.

With the known X-ray emission efficiency of the different elements, it is further possible to quantify the chemical composition of the specimen. However, for an accurate quantification reabsorption of X-rays within the specimen and at the detector entrance have to be considered as well as X-ray fluorescence, where a high-energy X-rays can excite a lower energy X-ray emission in another part of the sample [150]. This effect becomes especially relevant for two elements with similar emission/absorption energies. Furthermore, the bremsstrahlung background has to be properly subtracted for quantification, which can be difficult for losses less than 1 keV.

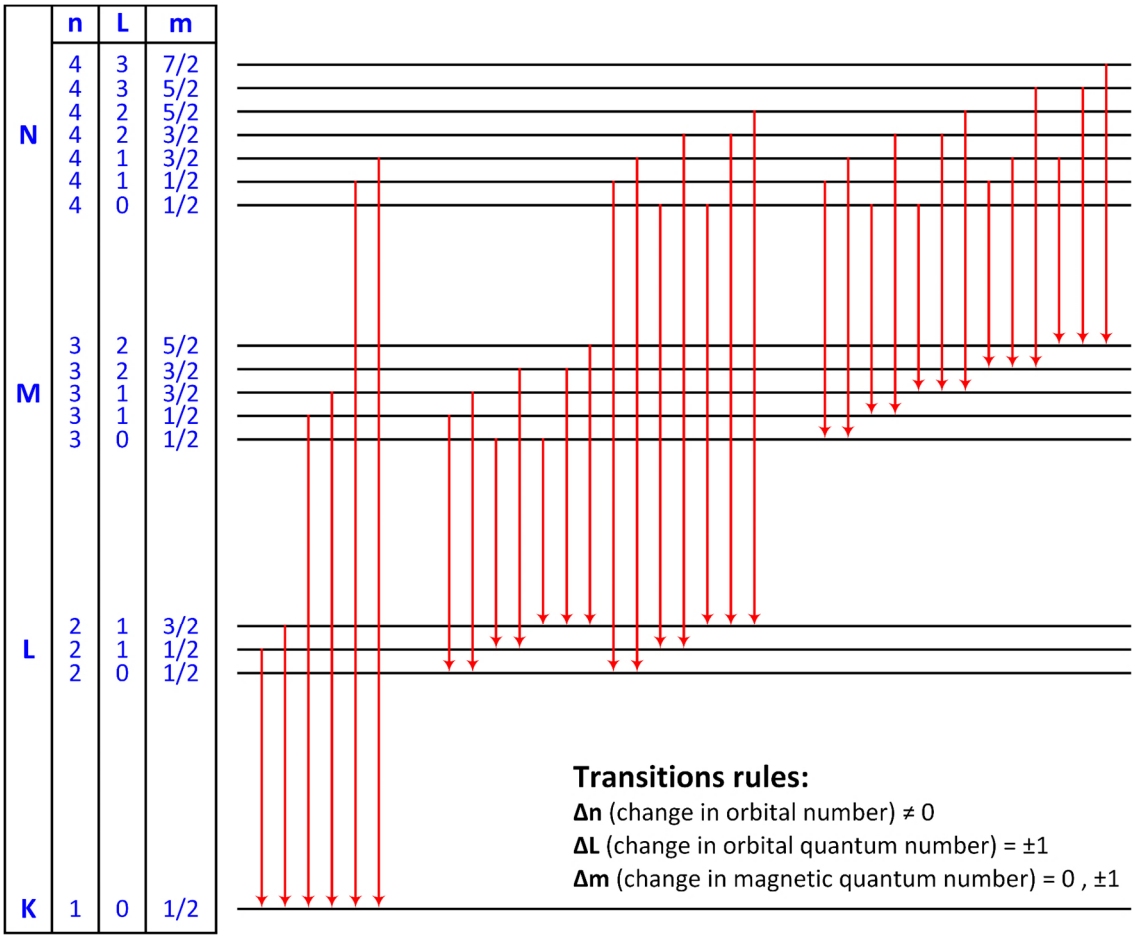

Figure 2.9: All allowed transitions between the K, L, M, and N shells of an atom.

2.5.4 Electron energy loss spectroscopy (EELS)

EELS is an important analytical technique that measures the change in kinetic energy of electrons after they passed through the sample. Energy loss measurements give a lot of information about the electronic structure of the sample such as chemical bonding, valence state, band gap and as well elemental composition. In EELS, the sample is exposed to a monochromatic electron beam. Because of inelastic scattering, some of the electrons will lose energy. By applying a perpendicular magnetic field, the electrons are deflected depending on their energy, which can be used to record the energy distribution of the electron beam. Figure 2.10(a & b) shows a schematic and cross-section of the EELS setup with a Gatan imaging filter (GIF), which is mounted below the TEM column. A magnetic sector-field (magnetic prism) is used to disperse the forward scattered electrons and hence record an electron energy loss (EEL) spectrum. Moreover, an energy selecting slit can be inserted in the dispersion plane and a series of lenses can be used for forming a real space image from these electrons – an EFTEM image with a defined energy loss. CCD camera records the image/spectrum. EELS on a field

emission gun (FEG) system provides an energy resolution of about 0.3-0.4 eV, which can be improved to 0.1 eV by using a monochromator [173].

For EEL spectroscopy, generally two regions are considered: the low loss region up to around 50 eV and characteristic inner shell excitation edges. The low loss region consists of a sharp peak (zero-loss peak), which correspond to the elastically scattered electrons and a number of broad peaks corresponding to plasmon losses [174]. The low loss region can give information related to the dielectric function, band gap and as well the sample thickness. The core-loss region with the characteristic inner shell excitation edges provides information about the composition (edge intensity) as well as on the oxidation state/local atomic environment (near edge fine structure). EELS has a high sensitivity for analysis of light elements and, in general, edges with an energy loss between 100 and 1000 eV. Here, EELS is significantly more sensitive compared to classical EDX detectors [175]. However, EDX is typically more sensitive for heavy elements. Furthermore, in form of EFTEM imaging, it is very powerful for large area element specific imaging, whereas STEM-EDX/EELS mapping is quite time consuming.

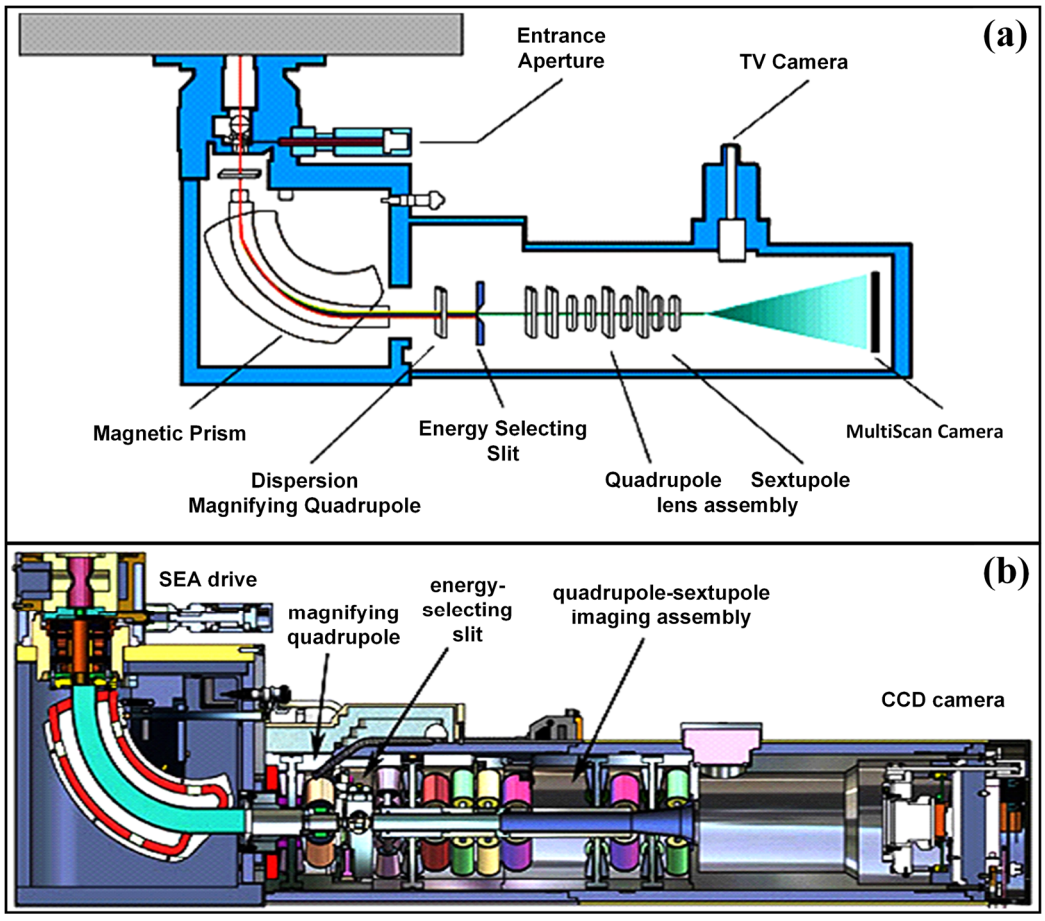

Figure 2.10: EELS experimental setup for a GIF (a) schematic [176], (b) cross-section of a GIF Tridiem spectrometer (model 863) [177].

2.6 Focused ion beam microscopy (FIB)

The basic setup of a focused ion beam microscope is very similar to an SEM: a finely focused beam of charged particles (typically Ga^+) is scanned across the sample surface and the resulting secondary ions or electrons are detected to image the structure. Because of the higher mass, the ion beam can not only be used for imaging, but the primary use in most FIB systems is for site-selective sputtering or milling using the impact of the high-energy ions on the sample surface (Figure 2.11). This can be used to structure specimens on micrometers sized areas with ~10 nm precision. To increase the sputtering speed during ion beam milling, a higher beam current is used compared to typical imaging conditions or etch-enhancing gases can be introduced. Furthermore, gas-assisted deposition (Figure 2.12) of metals or insulator in specific areas is a very versatile extension of the FIB for nanostructuring.

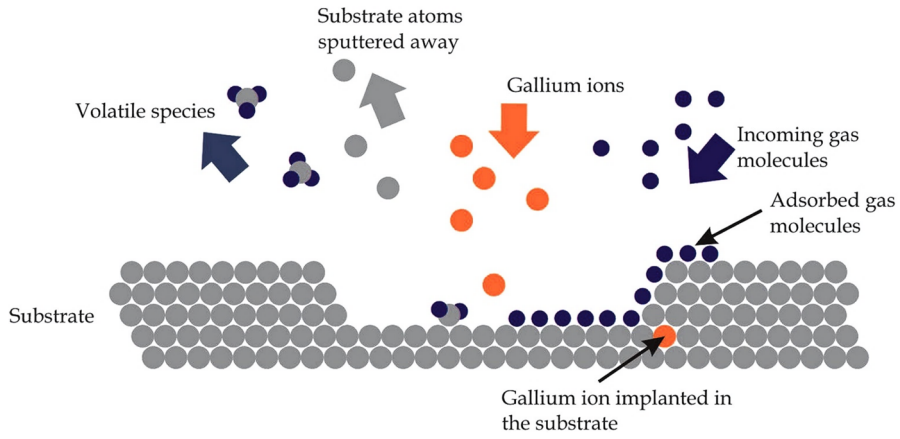

Figure 2.11: Schematic describing processes during ion beam milling [178].

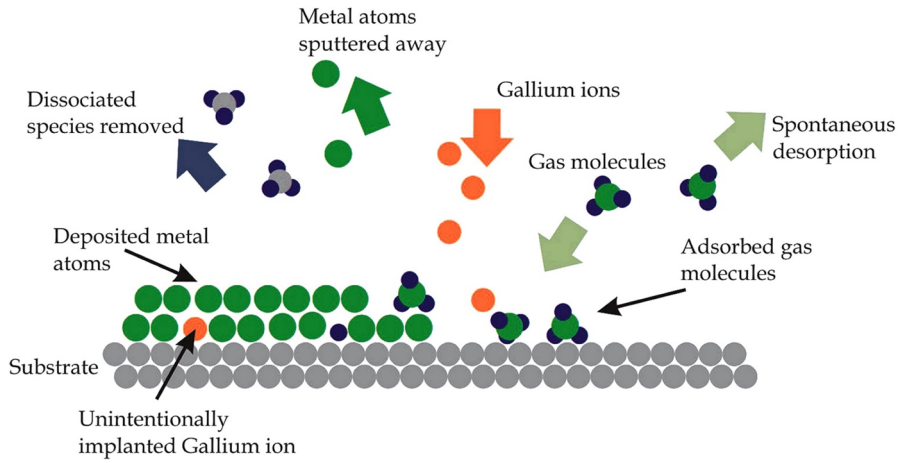

Figure 2.12: Schematic describing atomic processes during ion beam gas-assisted deposition [178].

The flexible combination of analytical SEM and nanostructuring with the ion beam (Figure 2.13), makes modern FIB systems essential tools in many laboratories for high resolution imaging in plane-view and cross-section and for micro/nano machining, in particular for TEM sample preparation. FIB has many advantages for preparing TEM specimens compared to traditional methods [179]:

- Target preparation with high spatial accuracy,
- Complex materials combinations can be processed, which are difficult for traditional mechanical or broad beam polishing techniques, e.g. from the combination of hard and soft matter.
- Faster than traditional polishing methods.

However, FIB sample preparation also has some disadvantages such as Ga implantation and surface damage during the milling process. This is minimized by performing the final thinning at low voltages (5 kV in our case, down to 500 V in state-of-the-art FIBs) and the long machine times need for large area sample preparation. Furthermore, re-deposition and contamination with deposited metals (Pt and W) can be a big problem for electrical measurement (see chapter 4).

TEM sample preparation is typically performed by *in situ* lift-out (INLO) [180]. For INLO, a small lamella is cut free from the bulk specimen with trenches on both sides. The lamella is contacted by the tip of a micromanipulator and is fully cut free to transfer it to a TEM half-grid inside the FIB chamber. Afterwards, final milling to TEM transparency is performed with the lamella mounted on a TEM half-grid [179]. Figure 2.14 illustrates the steps of the INLO technique.

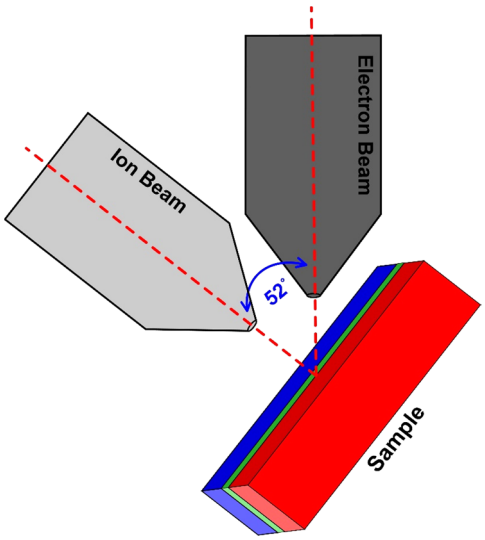

Figure 2.13: Schematic of FIB cross-section preparation for micron-sized operational batteries.

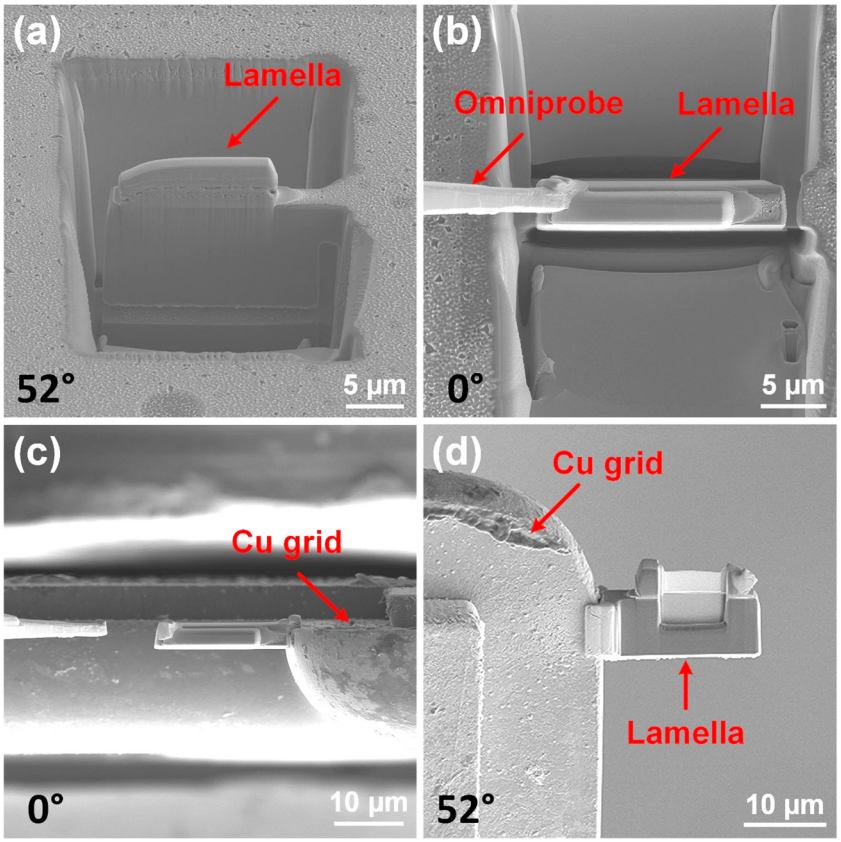

Figure 2.14: SEM images of INLO technique, (a) overview of the lamella after milling off two trenches, and mill it from the bottom and one side, (b) extracting the lamella from the bulk sample using nanomanipulator, (c) attaching the lamella to the Cu TEM grid, (d) Lamella after thinning.

2.7 Electrochemical characterization

The fundamental performance of a battery system can be characterized using electrochemical techniques to learn more about the redox reactions involved, overpotentials as well as degradation processes. For the electrochemical characterization, the techniques are differentiated as potentiometry (voltage controlled) and amperometry (current controlled) as well as for discharging test open and close circuit testing.

2.7.1 Potentiometric techniques

Potentiometric techniques are electrochemical analysis techniques where the potential of the working electrode of the electrochemical cell is controlled and the resulting current during charging/discharging of the battery is measured. The potential of the working electrode is measured against a reference electrode with constant potential. Various potentiometry methods have been implemented [181–183]:

2.7.1.1 Potential step (or Chronoamperometry)

In this technique, the applied voltage is abruptly changed from one value (V_1), where the electrode is in the equilibrium to another value (V_2). As a result, the current rises suddenly and then decrease gradually (Figure 2.15). This resulting current is measured as a function of time.

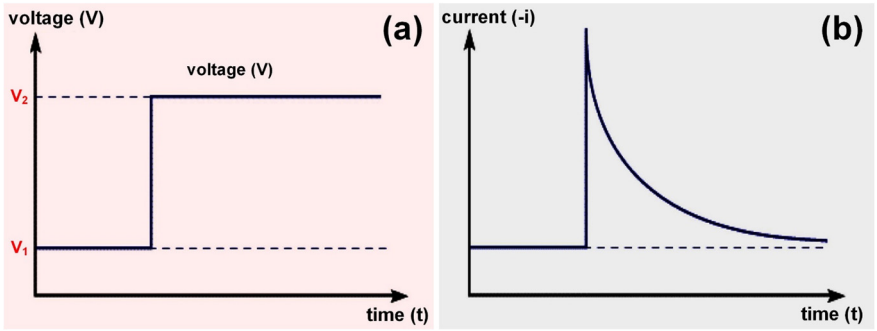

Figure 2.15: Potential step voltammetry: (a) voltage vs. time, (b) current vs. time [183].

2.7.1.2 Linear sweep voltammetry (LSV or LV)

In LSV, the working electrode potential is linearly swept with time. The potential scan is either in positive or negative direction. As the voltage sweep starts a current begin to flow, which corresponds to the oxidation/reduction reactions taking place at the electrodes. There are many factors that have an effect on the characteristics of the recorded linear sweep voltammogram such as the rate of the electron transfer, chemical reactivity of the electroactive species and voltage scan rate [184]. Figure 2.16 shows the voltammogram of a single linear sweep voltage.

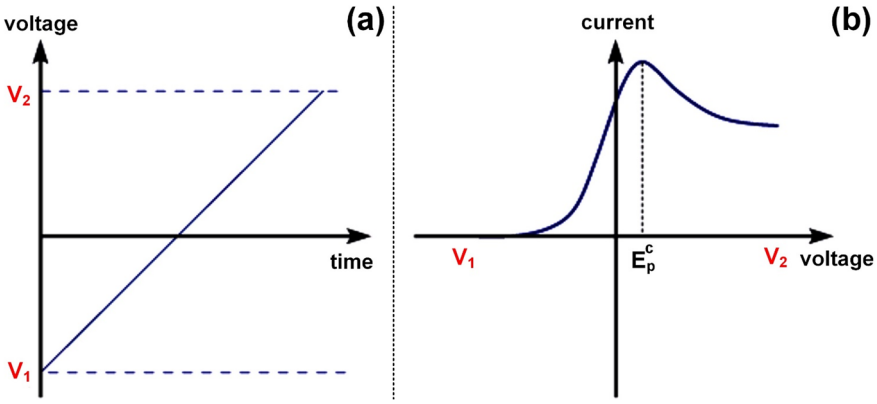

Figure 2.16: (a) Linear sweep voltage as a function of time, (b) resulting current as a function of voltage [184].

2.7.1.3 Cyclic voltammetry (CV)

CV is one of the most used potentiodynamic electroanalytical techniques for studying the electrochemical performance of batteries [181]. CV can be considered as linear sweep voltammetry (LSV) repeated continuously between two values (V_1 & V_2) at a fixed rate, where the sweep direction is reversed at the end of each scan. CV can be used over a wide potential range to observe redox reactions. The cyclic voltammogram displays current vs. potential and can be obtained by measuring the current at the working electrode during the potential sweep. Schematically shown in Figure 2.17 is a typical cyclic voltammogram consisting of two redox peaks opposite to each other.

Kinetic information about the redox potential and the electrochemical reaction rates of the electrode materials can be obtained from the CV curve. Reversibility and redox potentials of the battery system can be estimated by analysing the anodic current ($\mathbf{i_p^a}$), cathodic current ($\mathbf{i_p^c}$), the anodic potential ($\mathbf{E_p^a}$) and the cathodic potential ($\mathbf{E_p^c}$) peaks in CV curve. An offset between the oxidation and reduction peaks ($\Delta\mathbf{E} = \mathbf{E_p^c} - \mathbf{E_p^a}$) is often present and gives an indication for polarization and overpotentials. Polarization takes place when the reactant species/or the product species do not arrive at/or do not leave the surface of the electrode fast enough to maintain the resulting current. Polarization may affect either or both of the battery electrodes, and often depends on the voltage scan rate and the diffusion rates of the reactants.

Moreover, the effect of scan rate on the intensity of the responding currents for a reversible electron transfer reaction is shown in Figure 2.18a. This can be explained in the framework of the diffusion layer thickness at the electrode surface and the time of recording [184]. The diffusion layer on the electrode surface will grow much further at the slow voltage scan rate compared to a fast scan rate. Consequently, the current is smaller at lower rates than at faster rates, where the current is directly proportional to the flux towards the electrode. Therefore, the voltage scan rate strongly affects the behaviour seen of the recorded voltammogram.

Furthermore, the position of the peak maximum as a function of the scan rate gives an indication of the electron transfer rate. As long as the electron transfer processes are fast relative to the voltage scan rate, the redox system remains in equilibrium during the potential scan and the peak maximum occurs at the same voltage (Figure 2.18a). In contrast, if the kinetics of the electron transfer processes are slow compared to the voltage scan, an equilibrium at the surface cannot be established. As a result, the position of the current maximum shifts depending on the scan rate and the oxidation/reduction rate (Figure 2.18b).

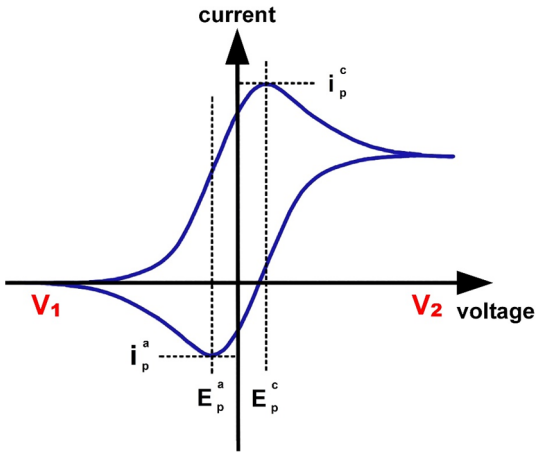

Figure 2.17: Ideal shape of CV recorded for a reversible single electrode transfer reaction [184].

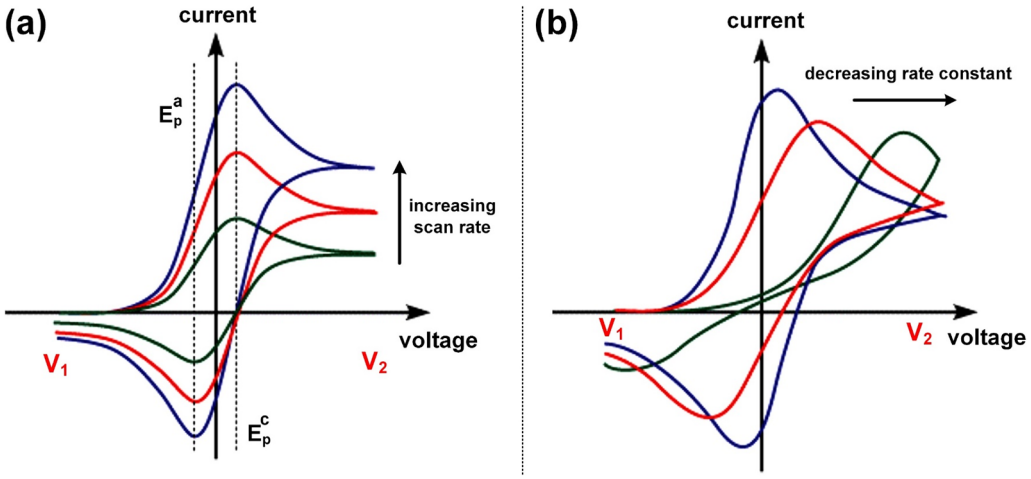

Figure 2.18: Series of cyclic voltammograms recorded for (a) a fast reversible electron transfer reaction at different scan rates, (b) a slow (partially reversible) electron transfer reaction at different scan rates [184].

2.7.2 Amperometric (galvanometric) technique

In amperometric (galvanometric) techniques, a current is applied to the counter and working electrodes and the potential of the working electrode relative to a reference electrode is measured. For the applied current to flow, a redox reaction (electron transfer) at the electrode has to occur. Various amperometric technique are used such as [181]:

2.7.2.1 Constant current chronopotentiometry

It is an amperometry technique where a constant current is applied to the working electrode of the electrochemical cell, causing redox reactions of the electroactive species. The concentration ratio (product to reactant) will vary with time on the electrode surface and

accordingly the electrode potential will change. The electrode potential will rapidly shift to higher values when the concentration of the reactant on the electrode drops to zero and a new redox process has to start. The time needed to apply this constant current until the potential transition occurs called *the transition time (**τ**)*. This time depends on concentration, diffusion coefficient, and applied current. The reversibility of the electrode reaction governs the curve shape. Moreover, it is possible to apply more than one current step during the same experiment (multiple current steps) to characterize the electrode reactions. As the applied current can be varied with time, rather than being kept constant, so there are other forms for the amperometry such as:

2.7.2.2 Linearly rising current chronopotentiometry

Where the current can be linearly increased or decreased (counterpart to LSV measurements).

2.7.2.3 Current reversal chronopotentiometry

Where the current can be reversed after a specific time.

2.7.2.4 Cyclic chronopotentiometry

Where the current is continuously reversed, repeats the reversal technique many times (counterpart to CV measurements).

In particular, the current reversal chronopotentiometry and cyclic chronopotentiometry techniques are frequently used to evaluate the specific capacity and the cycling stability of a battery. The potential response vs. the current of the different amperometry techniques is shown in Figure 2.19 as a function of time.

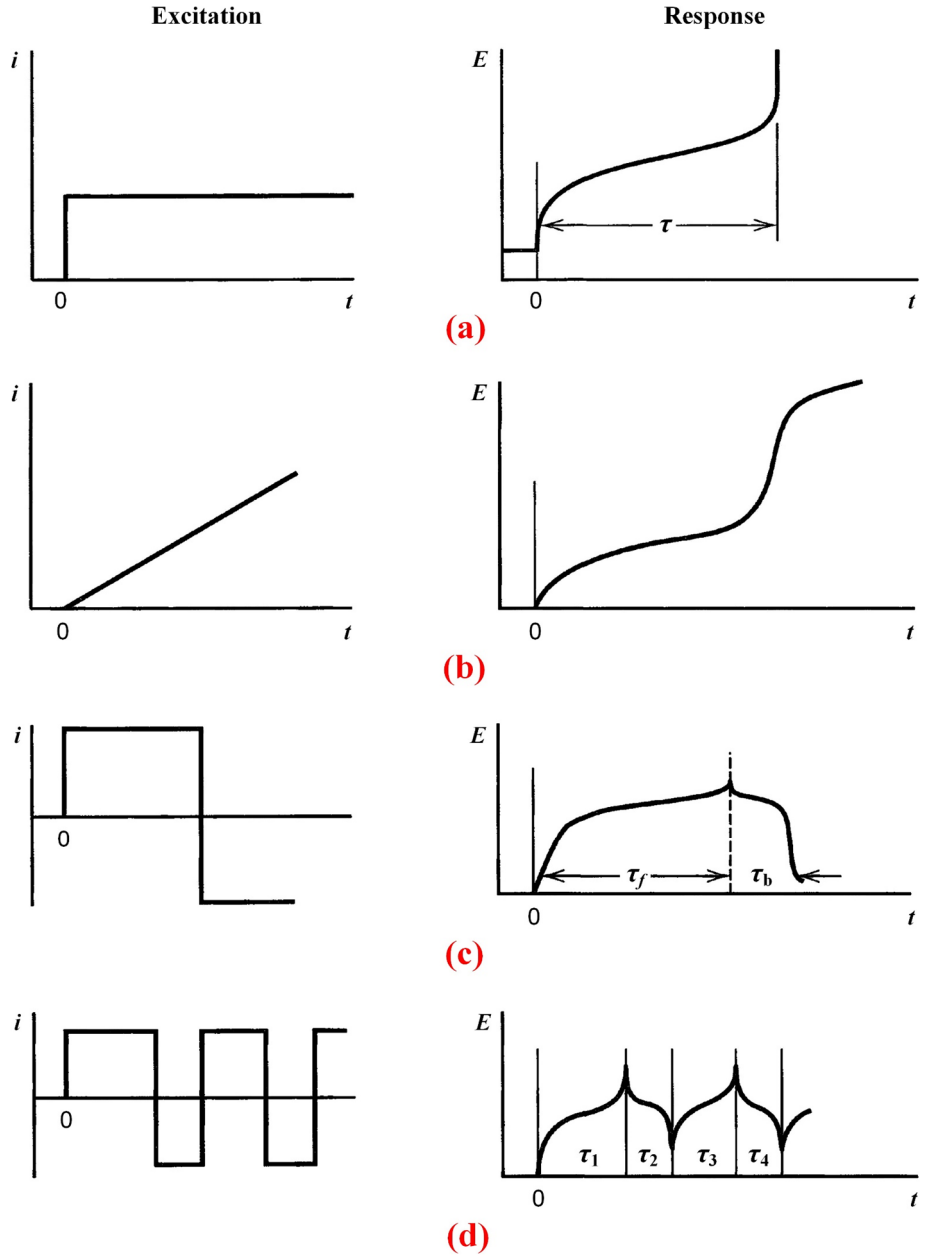

Figure 2.19: Different types of chronopotentiometric experiments. (a) constant current, (b) linearly rising current, (c) current reversal, (d) cyclic chronopotentiometry [181].

3 Experimental

3.1 Introduction

Transmission electron microscope provides the highest spatial resolution among the various types of microscope exploited to date. Therefore, TEM is the technique of choice to study details of battery systems at the atomic scale. The understanding of the electrochemical reactions occurring at the electrodes can eventually lead to fundamental improvements of the battery design and performance. As discussed in the previous chapter, the quality of a TEM analysis is greatly influenced by the lamella thickness, artefacts and the formation of damage at surface layers (amorphous layers) during preparation. Consequently, the preparation of TEM samples plays an important role in the quality of the analysis. The TEM samples under investigation must be electron transparent (~100 nm or less in thickness) to enable a quantitative analysis of the structure. FIB techniques have become the most common method for preparing TEM samples from bulk materials. This method has been modified to fabricate micron-sized batteries from all-solid-state fluoride ion battery, which were fixed on an electro-contacting MEMS device to enable *in situ* electrochemical cycling in the TEM. The bulk fluoride ion batteries were prepared by pressing the raw powders for the cathode, electrolyte and anode under high pressure. The preparation of the battery materials and the procedures for TEM sample preparation using FEI Strata 400S Dual Beam FIB system are explained in this chapter.

3.2 Bulk material preparation

The group of Prof. Maximilian Fichtner at the Helmholtz Institute Ulm for Electrochemical Energy Storage at KIT has pioneered the fluoride ion battery systems used in this thesis and prepared the raw materials for the cathode, anode and electrolyte used in our studies. Carine Rongeat et al. [185] and M. Anji Reddy et al. [48] prepared $La_{1-y}Ba_yF_{3-y}$ electrolytes with different compositions (y=0, 0.05, 0.1 and 0.15) by ball milling the corresponding LaF_3 and BaF_2 mixtures. Powder XRD was used to study the structure of the samples after 12 h ball milling and confirmed a tysonite-type structure for the $La_{0.9}Ba_{0.1}F_{2.9}$ electrolyte [48]. The ionic conductivity measured for $La_{0.9}Ba_{0.1}F_{2.9}$ was the highest among the $La_{1-y}Ba_yF_{3-y}$ electrolytes and increased with increasing temperature. At 150 °C a conductivity of 2.8×10^{-4} S cm^{-1} was measured for the $La_{0.9}Ba_{0.1}F_{2.9}$ electrolyte. At RT, the conductivity was much lower in the range of 2×10^{-6} S cm^{-1} [186]. Nevertheless, $La_{0.9}Ba_{0.1}F_{2.9}$ was chosen as a

reasonable fluoride ion conductor for the electrochemical studies of fluoride ion batteries in this thesis.

Different fluoride ion battery systems were studied as part of this PhD work. In all cases, $La_{0.9}Ba_{0.1}F_{2.9}$ was used as electrolyte, but different anode and cathode materials were tested. A Bi composite cathode was used for initial studies of a half-cell. The cathode consisted of a mixture of 30 wt% Bi (purity 99%), 60 wt% of the tysonite-type $La_{0.9}Ba_{0.1}F_{2.9}$ electrolyte, and 10 wt% carbon black, all ball milled together for 12 h. The addition of the electrolyte and carbon to the electrode was necessary to ensure both ionic and electronic conductivity as the pure metal fluorides are insulators and poor ion conductors.

For the case of full cells, two different cathodes were prepared for two different battery systems. One composite cathode was prepared from a mixture of 90 wt% Cu nanoparticles (purity 99.9%) and 10 wt% carbon black. For this, Cu and carbon black were mixed and mechanically milled for 12 h. This cathode was used for the *in situ* studies.

The second composite cathode was prepared from a mixture of CuF_2, $La_{0.9}Ba_{0.1}F_{2.9}$ electrolyte and carbon black by mechanical milling for 12 h. The weight ratio of the materials was 30% CuF_2, 60% tysonite-type $La_{0.9}Ba_{0.1}F_{2.9}$ electrolyte, and 10% carbon black. This cathode used for the *ex situ* studies.

Two different anodes were used for two different battery systems, a MgF_2 composite anode for the $Cu/La_{0.9}Ba_{0.1}F_{2.9}/MgF_2$ full battery and a pure metallic La sheet for the $CuF_2/La_{0.9}Ba_{0.1}F_{2.9}/La$ full battery. The MgF_2 composite anode was prepared by ball milling a mixture of 20 wt% Mg (99.6%), 20 wt% MgF_2 (99.9%), 50 wt% $La_{0.9}Ba_{0.1}F_{2.9}$ and 10 wt% carbon black. This MgF_2 composite anode was prepared in the discharged state by adding MgF_2 to the Mg metal to avoid rapid degradation of its performance as Mg is sensitive to surface oxidation [82]. Moreover, more reactive interfaces can be obtained by mixing the discharge and charge products in one electrode [187].

3.3 Cell assembly

The electrochemical cells were assembled by compacting the powders for anode, electrolyte and cathode. For bulk measurements, the electrolyte thickness is typically around 750 μm and the cells are compacted using a hand-press. The resulting battery pellets have a diameter of 7 mm and a thickness of approx. 2 mm (Figure 3.1a). These samples were used for the *ex situ* TEM analysis. For *in situ* TEM investigations, the battery setup has to be sufficiently small to enable FIB cross-section preparation covering anode/electrolyte/cathode within one

TEM lamella. Therefore, the thickness of the electrolyte has been reduced significantly to around 20-30 μm for these battery samples (Figure 3.1b). Furthermore, the high porosity, which is advantageous in the bulk batteries to allow for the volumetric changes of the electrode during cycling, is problematic when preparing thin TEM lamella. In order to ensure proper electrical contacts and mechanical stability of the electron transparent regions of the TEM sample, the battery pellets were further compacted at high pressure of 2-5 GPa for ~5 min using an 8 mm die in a custom-built computer controlled high pressure torsion (HPT) device (W. Klement GmbH, Lang, Austria) without applying any torsion. This resulted in a dense battery system with a total thickness of approx. 1 mm. From this pellet, the micron-sized battery for *in situ* testing was prepared as a cross-section across the electrodes.

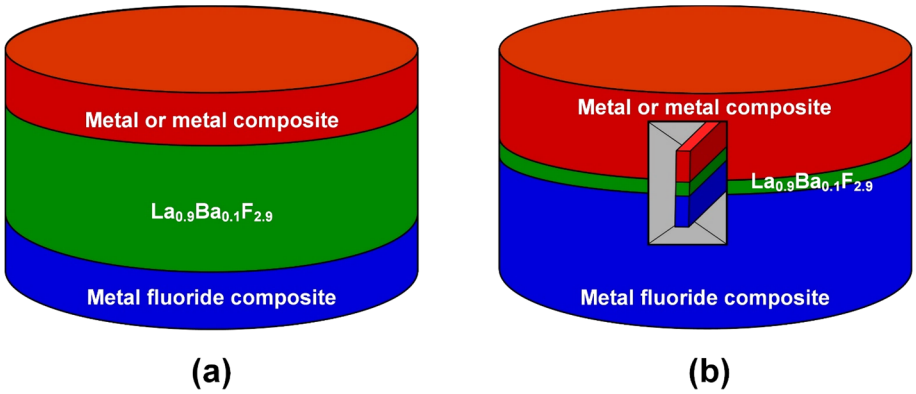

Figure 3.1: Schematic of the pellet used as electrochemical cell for (a) *ex situ* studies, (b) *in situ* studies.

3.4 FIB fabrication of micron-sized battery systems

Fabrication of a micron-sized battery from an all-solid-state battery is possible using FIB techniques. The micro battery is first cut by FIB as a cross-section from the bulk battery. This is then fixed on an electrical MEMS device [188] with electrical contacts on a SiN membrane. Finally, the micron-sized battery is contacted by local Pt-deposition between the electrical contacts and the anode/cathode to enable electrochemical cycling. The details of the fabrication process using a FEI Strata 400S Dual Beam FIB system equipped with Omniprobe 200 micromanipulator and a flip stage (Figure 3.2) are explained in the following.

Figure 3.2: FEI Strata 400S Dual Beam FIB.

3.4.1 FIB cross-section preparation

Large TEM lamellae with dimensions of approx. 70×35×10 μm were milled incorporating all interfaces (anode-electrolyte and electrolyte-cathode in case of the full cell and cathode-electrolyte in case of the half-cell) using conventional FIB TEM lamella preparation methods [179, 189, 190]. The preparation was initially performed at 30 kV with an ion beam current of 20 nA, followed by cleaning using an ion beam current of 6.5 nA (Figure 3.3a, b). Because of the large dimensions of the lamella, the preparation of the sample for lift-out took around 10h. The milled battery lamella was then mounted on a Cu lift-out grid on a flip stage using an Omniprobe 200 system (Figure 3.3c). The areas of interest around the interfaces were thinned to about 100 nm thickness (Figure 3.3d). The final thinning steps were performed at 5 kV with an ion beam current of 0.15 nA.

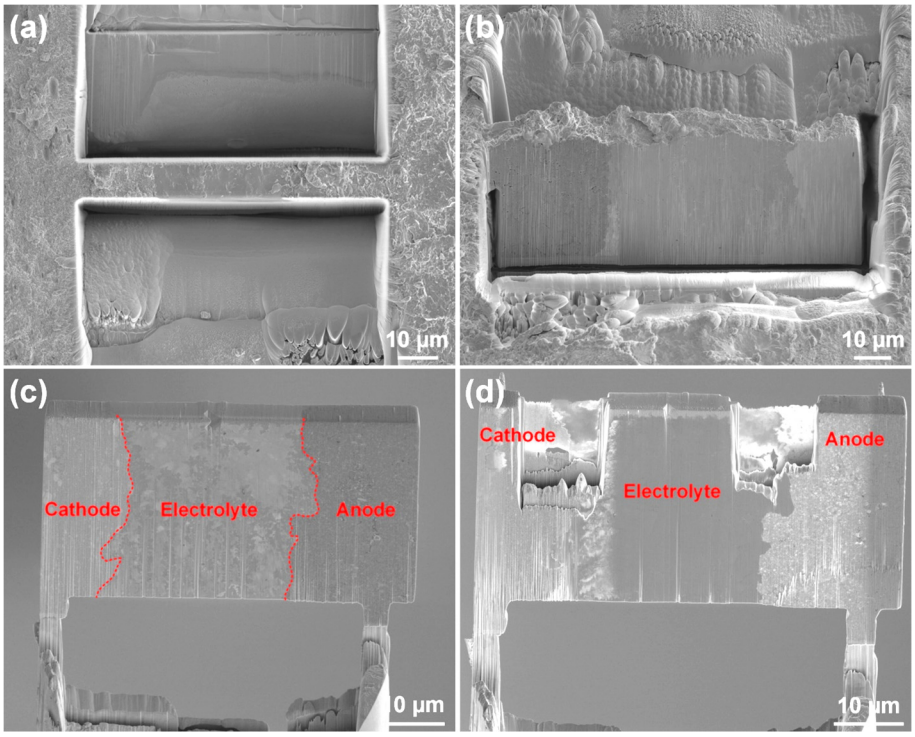

Figure 3.3: Cross-sectional TEM lamella preparation by *in situ* lift-out: (a) milling trenches around the area of interest; (b) cutting the area of interest free for lift-out; (c) micron-sized battery on the Cu support, and (d) thinning TEM transparent section at the areas of interest.

3.4.2 Mounting and electrical contacting of the micron-sized battery

To characterize the structural and chemical modifications of the thinned area of interest using *in situ* TEM, the micron-sized battery was mounted on a MEMS device (Protochips E-AEK11). The MEMS device has to be modified before mounting the micron-sized battery. To ensure proper contacts between the MEMS device and the battery electrodes even if the sample is slightly tilted, two Pt columns with dimensions of approx. $1.5 \times 1.5 \times 4$ μm were deposited on the electrical contacts of the MEMS device using ion beam induced deposition (IBID) (Figure 3.4a). The IBID parameters were 30 kV acceleration voltage, 48 pA current and 200 ns dwell time. The distance between these two columns should be slightly more than the length of the micron-sized battery itself, so that the micron-sized battery can be mounted in between (Figure 3.4b & Figure 3.5b). In addition, to prevent the metal deposition around the two columns (bright halos around the two columns, Figure 3.4a) that can create a short circuit, the SiN membrane between the contacts was removed (Figure 3.4b) [191].

For mounting the micron-sized battery, the flip stage was initially tilted to 90° allowing the micron-sized battery to come parallel to the MEMS device. Subsequently, the Omniprobe micromanipulator was used to transfer the micron-sized battery to the MEMS device

(Figure 3.5a). Finally, the micron-sized battery was contacted by local Pt-deposition between the electrical contacts of the MEMS device and the electrodes (cathode & anode) of the cell to enable electrochemical biasing for *in situ* TEM (Figure 3.4b & Figure 3.5b).

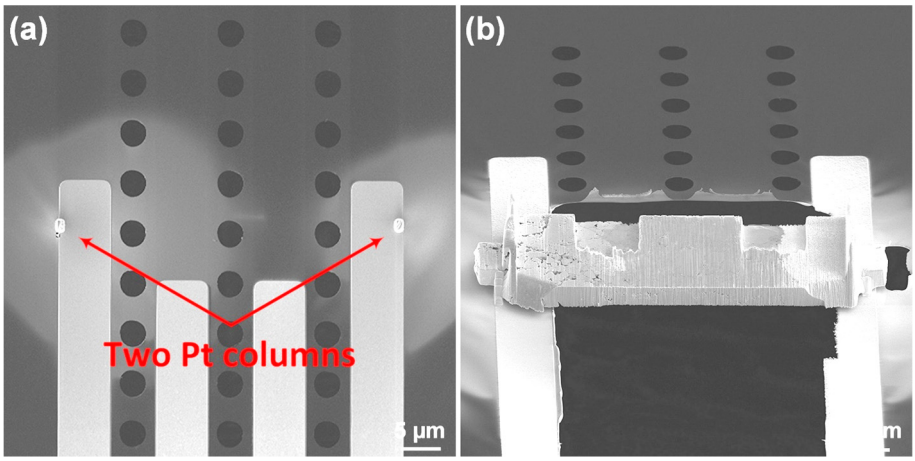

Figure 3.4: (a) Two Pt columns deposited on MEMS for supporting, and (b) lamella after mounting.

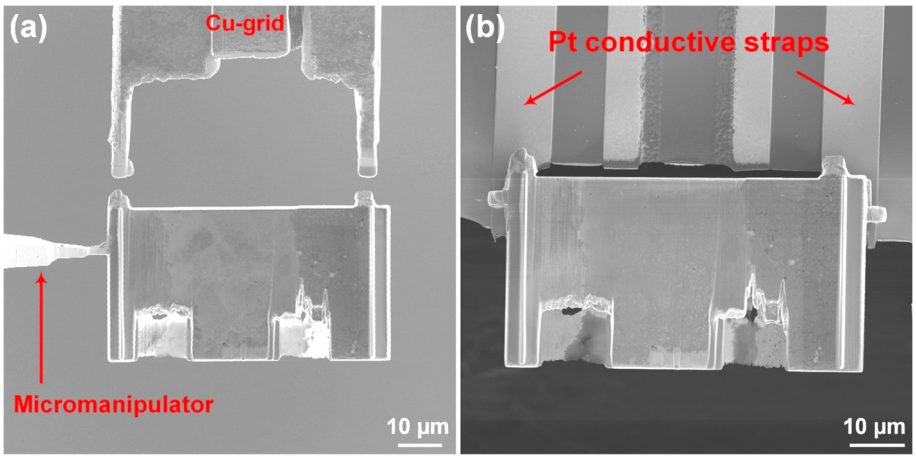

Figure 3.5: The lamella (a) on the micromanipulator before mounting, and (b) after mounting on MEMS device.

3.5 Electrochemical measurements

The group of Prof. Maximilian Fichtner performed the *ex situ* electrochemical studies. Preparation of the electrode materials and the subsequent construction of the electrochemical cell were done inside an argon-filled glove box. The full battery in form of a pellet was introduced in a modified Swagelok-type cell designed to perform the electrochemical studies at a high temperature. To enhance the ionic conductivity of the electrolyte, the cells were heated to a working temperature of 150 ˚C using a temperature programmed band heater for cycling

experiments. A multichannel battery tester Arbin BT 2000 was used to perform galvanostatic charge and discharge studies. The density of the applied current for charging of the $Cu/La_{0.9}Ba_{0.1}F_{2.9}/MgF_2$ full cell was +4 mA g^{-1} (10 mA cm^{-2}) until a cut off potential of 3.5 V, and after that -4 mA g^{-1} for discharging until 1.5 V [192]. For the $CuF_2/La_{0.9}Ba_{0.1}F_{2.9}/La$ full cell, the applied current density for discharging was -4 mA g^{-1} (10 mA cm^{-2}) until 1 V cut off potential, and then +4 mA g^{-1} for charging until 3.5 V. As the weight of the active material in the anode was in excess compared to the cathode, the cell capacity was calculated based on the weight of active material in the cathode.

Cyclic voltammetry has been used to charge and discharge the micron-sized fluoride ion batteries inside the TEM. For that, the MEMS devices with the micron-sized battery described in section 3.4 were mounted in a Protochips Aduro electrical TEM holder (Figure 3.6). The cycling was performed inside an aberration corrected FEI Titan 80-300 TEM using a Keithley 2611A source meter. The cathode half-cell (Bi composite/$La_{0.9}Ba_{0.1}F_{2.9}$) was charged from 0 V to 3 V in 1 h (0.833 mV/s scan rate), and the voltage held at 3 V for 15 min for TEM analysis. Afterwards, the cathode half-cell was discharged to 0 V in 1 h. The full $Cu/La_{0.9}Ba_{0.1}F_{2.9}/MgF_2$ battery was charged from 0 V to 3.5 V in 2 h with a scan rate of 0.486 mV/s. After charging, the structural and chemical modifications of the cathode, electrolyte, and anode were characterized using BF-TEM, SAED and STEM by holding the voltage at 3.5 V for 30 min. Then the system discharged to 0 V in 2 h.

Figure 3.6: Keithley 2611A power supply and components/details of the Aduro electrical TEM sample holder.

4 Optimized sample preparation

4.1 Introduction

An ideal model system for *in situ* TEM battery studies is insensitive to air/moisture and the electron beam, enabling to study only the dynamic processes due to the electrochemical cycling without having to worry about environmental artefacts. The recently developed fluoride ion battery [48] has been shown to be such a model system, where the individual components are not particularly air sensitive and are mostly stable under the electron beam. Therefore, a micron-sized all-solid-state fluoride ion cell can be fabricated using FIB techniques with a geometry close to the bulk cell compared to the more typical *in situ* TEM setups based on individual nanowires contacted by an ionic liquid [100, 193–198].

However, preparation of samples for *in situ* biasing experiments is challenging because of the required geometry with electron transparent areas for the analysis while maintaining good electrical contacts without short circuits. In this chapter, we discuss these challenges and solutions for the preparation of micron-sized all-solid-state batteries using FIB techniques.

4.2 Challenges and solutions

The basic sample preparation steps are explained in more detail in chapter 3 for a cell in pellet form consisting of cathode, anode and solid electrolyte. The thickness of the solid electrolyte was chosen to be around 20-30 μm to prevent local short circuits (Figure 4.1). Initially, a battery section with dimensions of approx. $70\times35\times10$ μm was milled by FIB from the bulk battery using conventional FIB TEM lamella preparation methods [179, 189, 190] (Figure 4.2 & Figure 4.3). Subsequently, the micron-sized battery was mounted on a MEMS device with electrical contacts on a SiN membrane [188]. Finally, local Pt-deposition was used to contact the anode/cathode materials to enable electrochemical biasing.

During the various stages of the sample preparation, several challenges arise due to, e.g., the porous nature of the pellets, the contamination during metal deposition, the contact resistance, the leakage currents and the roughness/smoothness of the different interfaces. Addressing these aspects is pivotal for the success of an *in situ* biasing experiment and are discussed in detail for the electrochemical biasing studies on the fluoride battery.

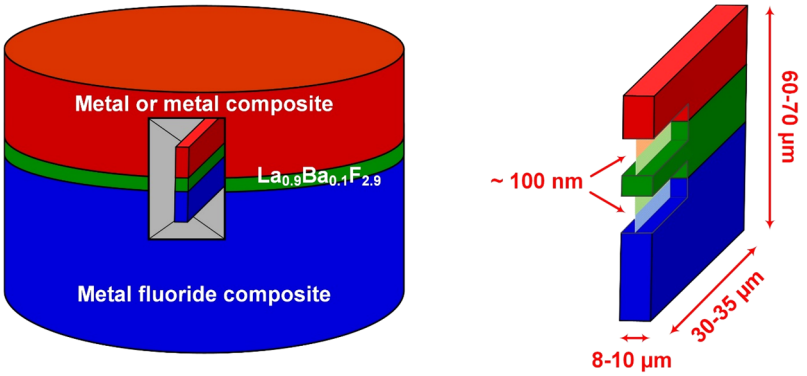

Figure 4.1: Schematic of the all-solid-state battery and FIB preparation of a cross-section.

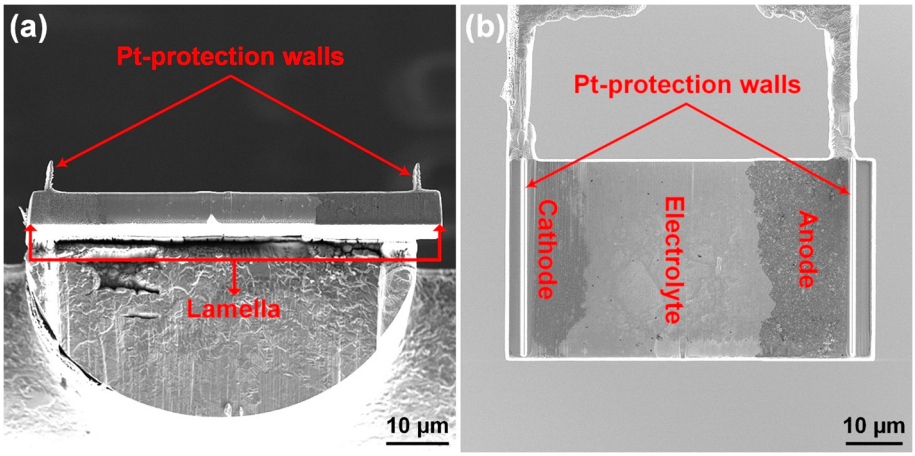

Figure 4.2: Battery lamella on the copper TEM grid, (a) side view after deposition the two Pt-protection walls, (b) top view after initial thinning.

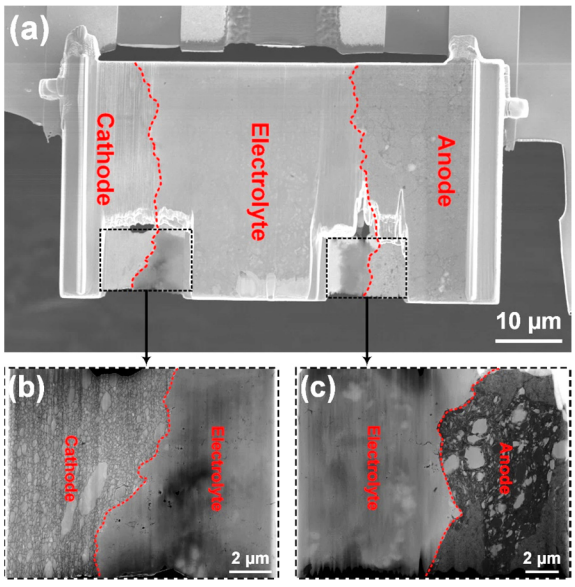

Figure 4.3: (a) SEM image of the full micron-sized battery mounted on an electrical MEMS device, (b, c) STEM images of the thin areas at the electrolyte-cathode and anode-electrolyte interfaces, respectively.

4.2.1 Porosity of the battery materials

In general, in bulk batteries, the composite components for anode and cathode require an optimum porosity to allow for volumetric changes during electrochemical cycling. However, for *in situ* TEM measurements, which require a thin lamella, porosity poses a huge problem affecting both the mechanical stability and the connectivity in the thin electron transparent region of the battery. Therefore, a compromise between porosity and mechanical stability/conductivity of the battery is required for successful *in situ* TEM studies. To reduce the porosity compared to typical bulk batteries, the initially assembled and hand-pressed powder-based batteries were further compacted at a pressure of ~5 GPa for ~5 min to produce a stable, fairly dense battery with good contact between neighbouring grains as well as between the electrodes and electrolyte (Figure 4.4).

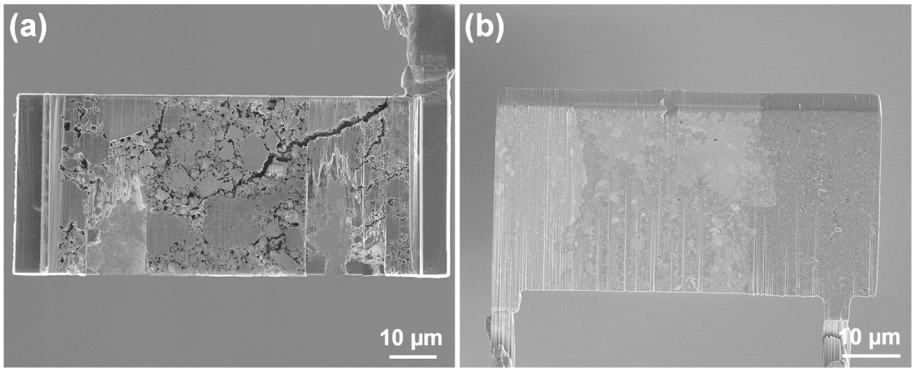

Figure 4.4: (a) pores and cracks visible during lifting-out and thinning of a TEM lamella from a porous battery, (b) lamella prepared after pressing at of ~5 GPa for ~5 min.

4.2.2 Contamination due to metal deposition

Contamination of the battery lamella during electrical contacting by Pt (or also W) deposition is a major problem during FIB preparation [191, 199]. Figure 4.5(a-d) shows the deposition of Pt and W 'wires' with nominal dimensions of 25 μm (length) × 1 μm (width) × 1 μm (height) using ion beam induced deposition (IBID) and electron beam induced deposition (EDID) inside the FIB. Both the Pt and the W wires were deposited using the following parameters: current 1.6 nA, acceleration voltage 5 kV and dwell time 1.4 ms (EBID) and current 46 pA, acceleration voltage 30 kV and dwell time 200 ns (IBID). In addition to the predefined areas for the wire, deposition outside the wire is visible as bright halos. For both the Pt and the W-deposition, the contamination area around the wires was smaller for EBID (~1 μm) compared to IBID (~17 μm Pt, ~3.5 μm W). This slight contamination is not critical for

conventional TEM sample preparation; but for the *in situ* sample preparation, the metal deposition might create an electrical contact between the electrodes resulting in a short circuit of the micron-sized battery. The probability of this to happen is much higher, if the size of the battery is small. Preventing this is a prerequisite to obtain a functional battery. Consequently, a MEMS device (Protochips E-AEK11) with a wide separation of 50 μm between the Pt contacts has to be used (Figure 4.6).

As an additional approach to reduce the metal contamination during electrical contacting of the battery, two Pt-protection walls were deposited on the cathode and the anode before performing the initial thinning. This should reduce the flow across the active area of the battery and thus contamination and re-deposition. The Pt-protection walls were deposited vertically on the lamella (Figure 4.2a) and are about 300 nm wide and 7 μm high. After the deposition of the Pt-protection walls, the area between the two Pt-protection walls was cleaned using the Ga ion beam to remove metal deposition on the entire battery. This was done before thinning the area of interest at the interfaces between the electrodes (Figure 4.2b). With this process, we reduce metal contamination and re-deposition during the later sample preparation stages. Despite the large distance, in a few cases problems with short circuits were present without the Pt-protection walls. In addition, removing the SiN membrane between the contacts also helped to reduce contamination by allowing free gas flow from the gas injection system (GIS) around the sample [191], Figure 4.7.

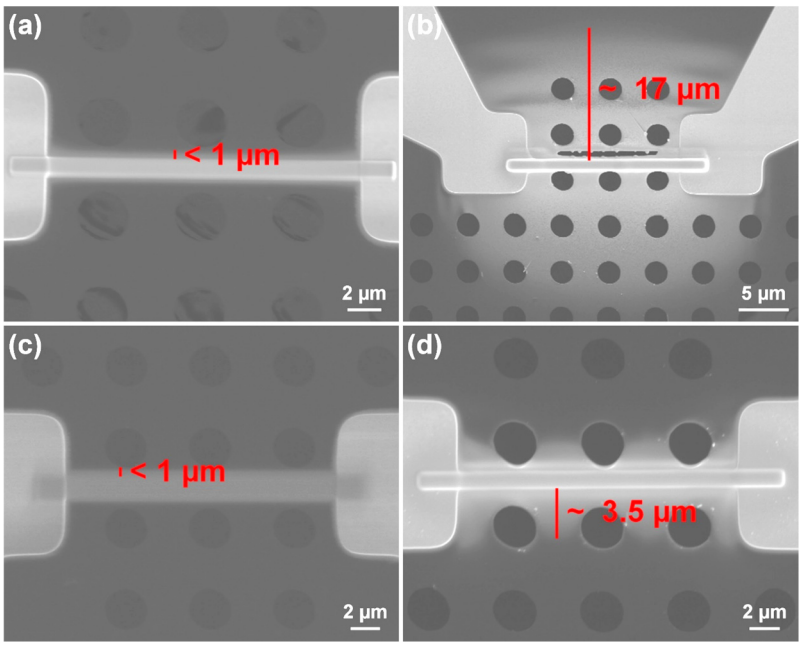

Figure 4.5: (a) Pt deposited by e-beam, (b) Pt deposited by ion beam, (c) W deposited by e-beam, (d) W deposited by ion beam.

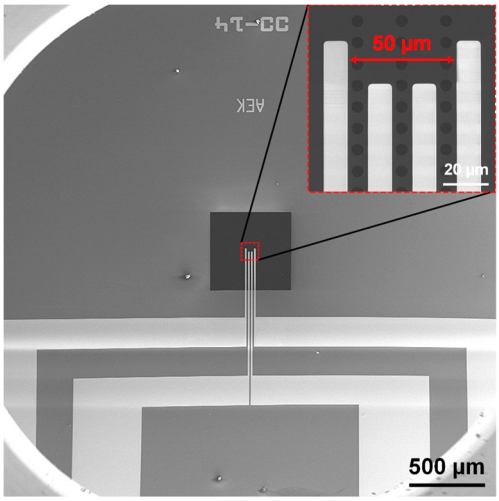

Figure 4.6: SEM image of the new MEMS device with a 50 μm wide separation between Pt contacts.

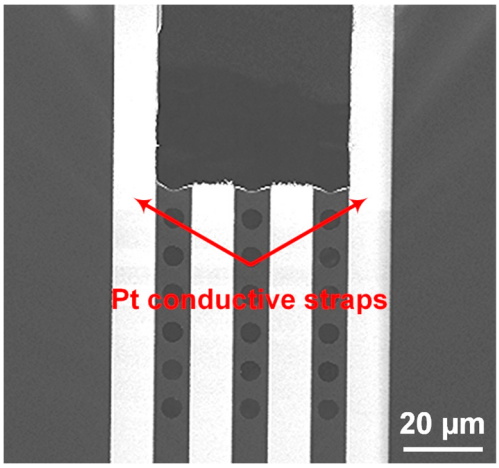

Figure 4.7: SEM image of the MEMS device after removing the SiN membrane between the contacts.

4.2.3 Contact resistance

The conductivity of the metal contacts has to be sufficiently high to prevent significant losses at the contacts during the charging/discharging process of the micro battery. Therefore, it is important to know the resistivity of the metal used for contacting. The aforementioned Pt and W structures deposited by IBID and EBID were used to measure and compare the resistivity of the resulting metal wires (Figure 4.8). A Keithley 2611A power supply with a Protochips Aduro 200 *in situ* electrical TEM sample holder was used running a voltage sweep of 100/150 mV and measuring the corresponding current. The resistance of Pt deposited by EBID is 6 orders of magnitude higher compared to that deposited by IBID (1.88 MΩ and 156 Ω, Figure 4.8a, b). A similar difference was observed for W, where the resistance was 0.135 MΩ and 95 Ω for EBID and IBID respectively (Figure 4.8c, d).

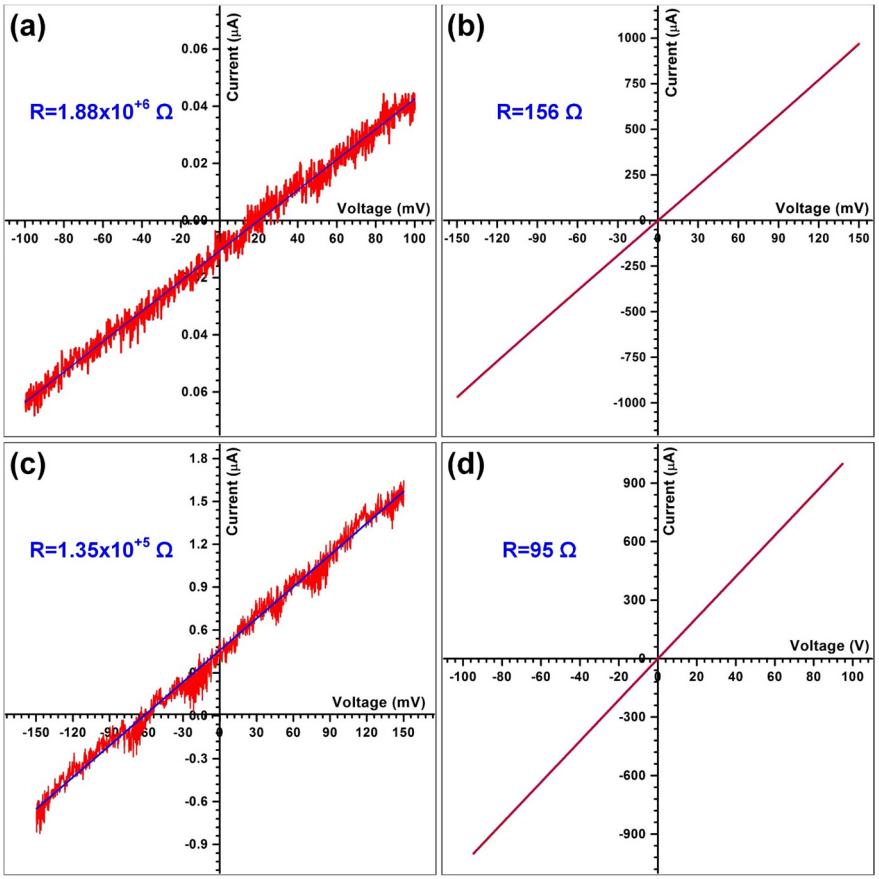

Figure 4.8: I-V curves and the resistivity for (a) Pt deposited by e-beam, (b) Pt deposited by ion beam, (c) W deposited by e-beam, (d) W deposited by ion beam.

Based on the nominal wire geometry, the resistivity of deposited Pt is calculated to be 7.5×10^{-2} Ω.m (EBID) and 6.2×10^{-6} Ω.m (IBID), in agreement with previously reported results [200–207]. The resistivity of the deposited W is 5.4×10^{-3} Ω.m (EBID) and 3.8×10^{-6} Ω.m (IBID), also in agreement with previously reported results [200, 208–213]. The resistance difference between the IBID and EBID techniques can be partially attributed to differences in the carbon content incorporated from the precursor system into the wires in addition to some gallium incorporation [214–218]. Other potential effects that influence the conductivity are the density (the IBID wires are denser than those deposited by EBID [219]), and the cross-linkage/carbonization level of the residual carbon. However, it is expected that the high carbon content is the main factor changing the wire structure from a percolating Pt or W network to isolated metal nanoparticles, so that the conductivity switches from a metallic conductivity to a 'hopping' process [220, 221].

Based on SEM-EDX analysis (Figure 4.9a-d), the Pt-IBID wire consists of ~64 at% Pt and ~36 at% Ga with carbon below the detection limit (ignoring Al & Si from the substrate), while the Pt-EBID wire consists of ~36 at% Pt and ~64 at% C. The Pt content reported in this

thesis is higher than values reported previously by other authors [207, 215, 222]. As the electrical and structural properties of the IBID or EBID deposited wires depend on a number of factors such as beam current and energy [223, 224], scanning conditions [225, 226], vacuum conditions [227] and the precursor compound [227], it is not surprising that the composition varies somewhat between different setups. For the W-IBID wire we measured ~44 at% W, ~18 at% Ga and ~38 at% O with carbon below the detection limit, while the W-EBID wire consists of ~23 at% W, ~33 at% C and ~43 at% O. The oxygen content in the W wires can be attributed either to the residual gas in the vacuum system [214], insufficient decomposition of the $W(CO)_6$ precursor [216], or oxidation when removing the test structure from the FIB.

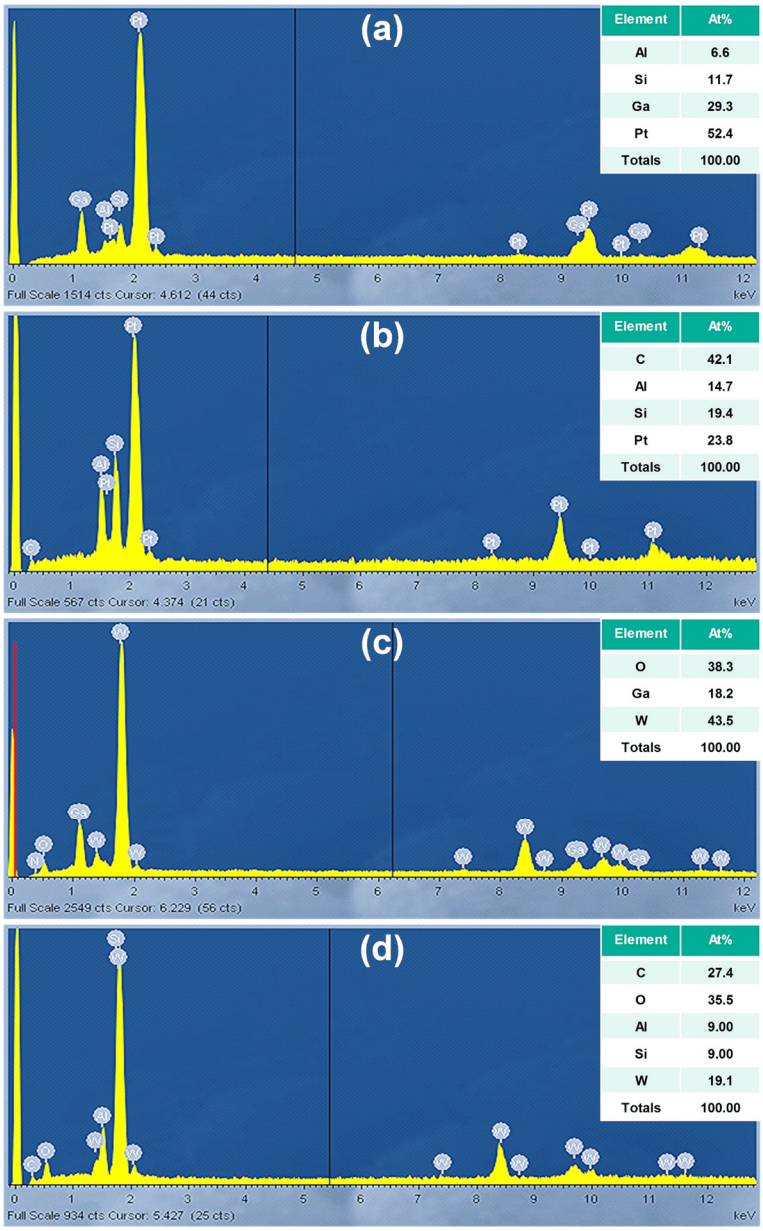

Figure 4.9: EDX of (a) Pt-IBID, (b) Pt-EBID, (c) W-IBID, (d) W-EBID.

In order to contact the lamella to the MEMS device, two Pt contacts with dimensions of 5 μm (length) $\times$ 2 μm (width) $\times$ 1 μm (height) were used. The resistance of two contacting Pt-EBID wires would be 375 kΩ, while it is only 31 Ω in the case of Pt-IBID. This resistance from the Pt-IBID structure is negligible compared to the resistance of the whole micron-sized battery ($\sim$1 MΩ), whereas the Pt-EBID wires would have added noticeably to the resistivity. Therefore, we used IBID for contacting the sample, even though the metal contamination area is larger.

4.2.4 Leakage current

Any leakage current through the MEMS device leads to a higher charging current and a gradual loss of energy stored in the charged battery and thus to a faster discharge than expected. This leads to varying results of charging currents in the *in situ* experiments. Therefore, it is important to have low leakage currents, especially for characterizing the charged state where it provides more time to perform an in depth TEM characterization. The I-V curves of the standard MEMS (Protochips E-AEL11) devices and the new high resistance MEMS (Protochips E-AEK11) devices have been acquired using blank devices mounted in the Aduro TEM holder at a vacuum level of 10^{-7} mbar. A Keithley 2611A source meter and the Keithley control software has been used to perform voltage sweeps between -5 V and 5 V. The standard MEMS devices from Protochips have resistances of $\sim$30 MΩ (Figure 4.10a), while the new high resistance MEMS devices have a resistance of $\sim$1.5 GΩ leading to leakage currents of $\sim$1.75 nA at 3 V (Figure 4.10b). When calculating the charge stored in the fully charged state based on the theoretical specific capacity and the weight of limiting active material (Cu/CuF_2 for the full cell) this is around 44 μC. Thus, the leakage current would discharge the battery in only $\sim$13 min in case of the standard MEMS devices, while it would take around 6 h in case of the new high resistance MEMS devices.

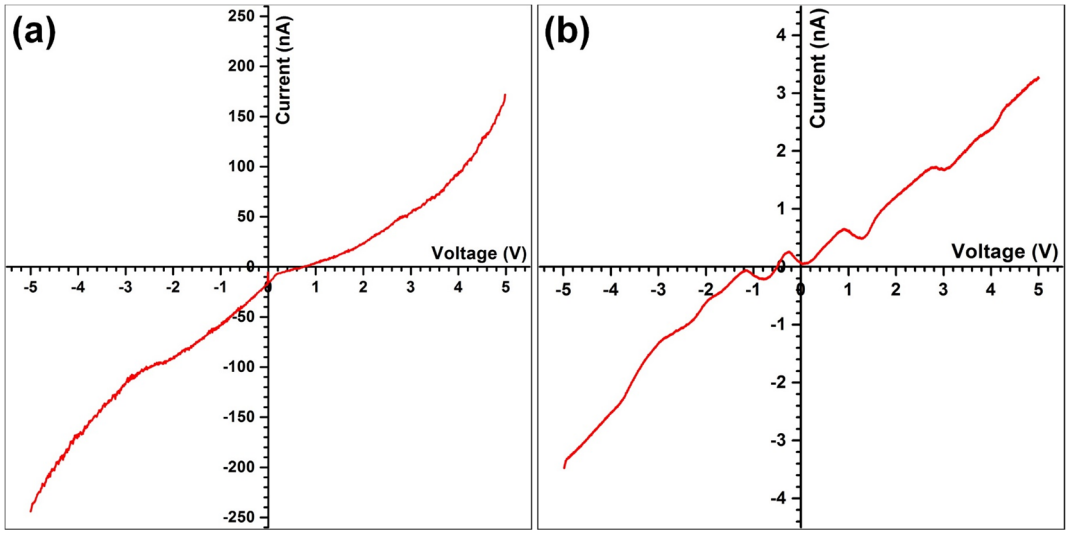

Figure 4.10: (a) I-V curve of the conventional electrical MEMS device, (b) I-V curve of the electrical MEMS device with high resistivity.

4.2.5 Interfaces roughness

The preparation of a battery pellet from powders by simple mechanical pressing of the electrode and electrolyte materials typically results in a fairly high interface roughness. The roughness of the interfaces is critical for the micron-sized battery with a thin electrolyte layer, resulting in local thickness variations (Figure 4.11a-d). The electrolyte thickness extends from a few microns to tens of microns. In contrast, for the typical bulk battery pellets with an electrolyte thickness of 700-800 μm, this difference is negligible.

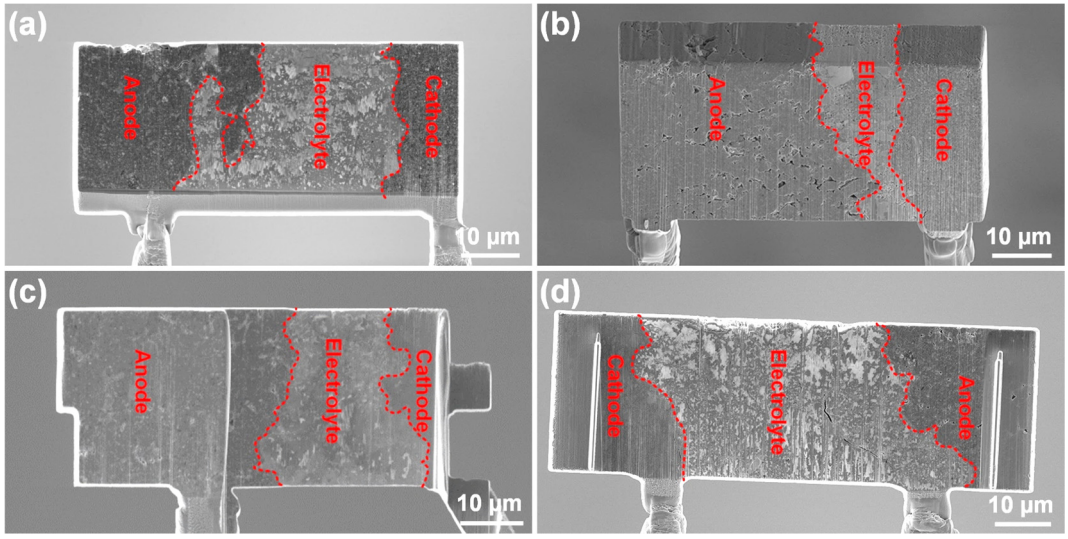

Figure 4.11: (a-d) SEM images of different micron-sized batteries prepared from the same battery pellet.

The reduction of the electrolyte thickness reduces its resistance, so the variation in the electrolyte thickness from one area to another, leads to a variation of the current density. As a result, some areas of the electrodes undergo faster charging/discharging than the other areas, which will ultimately lead to cell failure. Moreover, rapid self-discharge will occur in places where the electrolyte thickness is reduced to the nanometre scale [228], ultimately leading to a short circuit without electrolyte.

4.3 Electron beam effects on the micron-sized battery

Before performing the sample preparation for the *in situ* studies, the as-prepared components of the fluoride ion battery and *ex situ* cycled fluoride ion batteries were investigated to study the effect of the electron beam on the material. The results confirmed that the fluoride ion battery materials are stable under normal operation conditions, so that standard TEM techniques can be used for imaging and analytical TEM of the fluoride ion battery components.

In addition, the effect of the electron beam current on the measured current in the electrochemical circuit was measured by positioning the electron beam in the TEM on the electron transparent thinned areas, the thick areas and the Pt contacts of the MEMS (Protochips E-AEK11) device. For these measurements, a DC voltage between 0 and 180 mV was applied to the micron-sized battery and the corresponding areas illuminated by an electron beam with a current of 9.16 nA. The thickness of the thin and thick areas was approx. 100 nm and 6 μm, while the thickness of the Pt contacts was around 4 μm. The measured current of the electron beam adding to the charging was approx. 0.5 nA, 1-2 nA and 1-1.5 nA on the electron transparent area, the thick area and the Pt contacts, respectively. These currents are negligible compared to the operating currents of the fluoride ion battery.

All of the above indicates that the all-solid-state fluoride battery is a suitable system for demonstration of *in situ* TEM electrochemical measurements.

5 *In situ* TEM studies of fluoride ion batteries

5.1 Introduction

Two fluoride ion battery systems, a Bi/$La_{0.9}Ba_{0.1}F_{2.9}$ half-cell and a Cu/$La_{0.9}Ba_{0.1}F_{2.9}$/MgF_2 full cell, are investigated here to study the processes during electrochemical cycling by fluoride ion transfer through the $La_{0.9}Ba_{0.1}F_{2.9}$ solid-state electrolyte inside the TEM in detail. The optimized preparation of the required micron-sized battery lamella is described in detail in chapters 3 & 4. The *in situ* electrochemical measurements were performed inside an aberration corrected FEI Titan 80-300 transmission electron microscope with an Aduro single tilt sample holder and a Keithley 2611A source meter. The structural and chemical modifications of the electrodes before, during and after cycling were characterized using TEM, STEM, SAED, and EDX to understand the structural changes and relate them to the electrochemical performance of the fluoride ion battery.

5.2 *In situ* TEM study of a Bi/$La_{0.9}Ba_{0.1}F_{2.9}$ half-cell

5.2.1 Electrochemical study

The cathode half-cell consisted of $La_{0.9}Ba_{0.1}F_{2.9}$ as electrolyte and a Bi composite (Bi/$La_{0.9}Ba_{0.1}F_{2.9}$/C) as a cathode. Figure 5-1 shows the SEM/STEM images of the micron-sized half-cell battery contacted on the MEMS device.

The working principle of this half-cell fluoride ion battery is based on a reduction of $La_{0.9}Ba_{0.1}F_{2.9}$, which is acting both as anode and electrolyte (metal fluoride) and oxidation of the discharged Bi cathode (metal) via transport of fluoride ions through the electrolyte. Bi is oxidized forming BiF_3 during charging, releasing three electrons that provide the current for reducing some of the $La_{0.9}Ba_{0.1}F_{2.9}$ in the electrolyte to form metallic La and Ba, releasing the fluoride ions. The released fluoride ions are transported to the electrode, closing the circuit of the cell. The conversion reactions during charging are:

$$Bi + 3F^- \rightarrow BiF_3 + 3e^- \quad \text{(at the cathode)} \quad 5.1$$

$$10\ La_{0.9}Ba_{0.1}F_{2.9} + 29\ e^- \rightarrow 9\ La + Ba + 29\ F^- \quad \text{(at the electrolyte)} \quad 5.2$$

During discharging, the conversions reactions are:

$$BiF_3 + 3e^- \rightarrow Bi + 3F^- \quad \text{(at the cathode)} \qquad 5.3$$

$$9\,La + Ba + 29\,F^- \rightarrow 10\,La_{0.9}Ba_{0.1}F_{2.9} + 29\,e^- \quad \text{(at the electrolyte)} \qquad 5.4$$

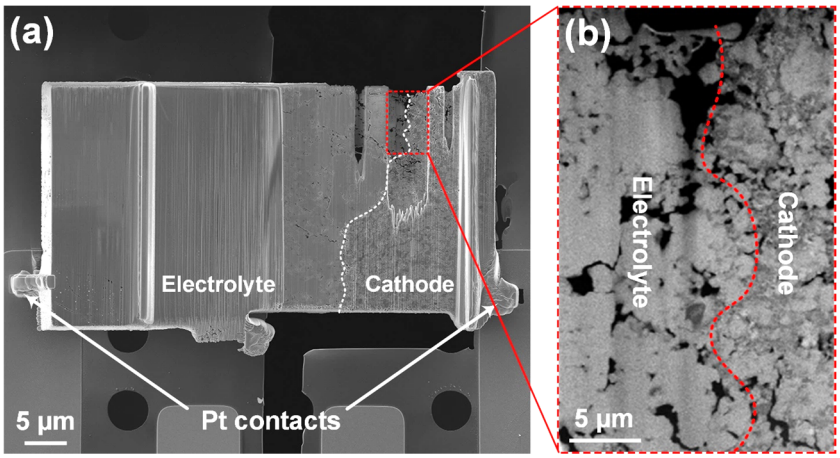

Figure 5-1: (a) SEM image of the micron-sized half-cell mounted on the MEMS device, (b) STEM image of the thin area at the cathode-electrolyte interface.

Cyclic voltammetry has been used to charge and discharge the cathode half-cell. For charging a voltage sweep starting from 0 V to 3 V over 1 h (0.833 mV/s scan rate) has been applied. The voltage was held for 15 min at 3 V to enable more detailed TEM investigations. Afterwards, discharging was performed by applying a voltage sweep from 3 V to 0 V over 1 h. All *in situ* CV measurements were performed at RT. Figure 5-2 shows the cell voltage plotted against the current for the first charge/discharge. During charging, as the voltage sweep starts a current is beginning to flow, which starts to increase significantly around 2.1 V and reaches a maximum at 2.33 V. This peak has been attributed to the formation of BiO_xF_{3-2x} by fluorination of Bi_2O_3 and Bi [192]. Above 2.4 V, the current dropped and then increased again reaching a second maximum at 2.85 V with some fluctuations. This can be attributed to the oxidation of bismuth forming bismuth fluoride (BiF_3). However, that potential is slightly higher than the theoretical potential value 2.687 V of the Bi/BiF_3 redox couple vs. La/LaF_3, indicating a slight overpotential. Similar potentials were observed in the *ex situ* study of $Bi/La_{0.9}Ba_{0.1}F_{2.9}/CeF_3$ full battery system using the same composite cathode [192] (the reduction potentials of La^{3+} and Ce^{3+} are very similar with -2.379 V and -2.336 V). After holding the voltage, discharging was not working properly in the half-cell as no reduction peaks could be observed. Instead, only a straight line dominated by leakage currents is observed. During discharge, only the BiF_3 can be converted back into Bi metal, while the formation of $BiO_{0.1}F_{2.8}$ is irreversible. This could explain the absence of reduction peaks during discharge, where the main phase formed during charge was $BiO_{0.1}F_{2.8}$.

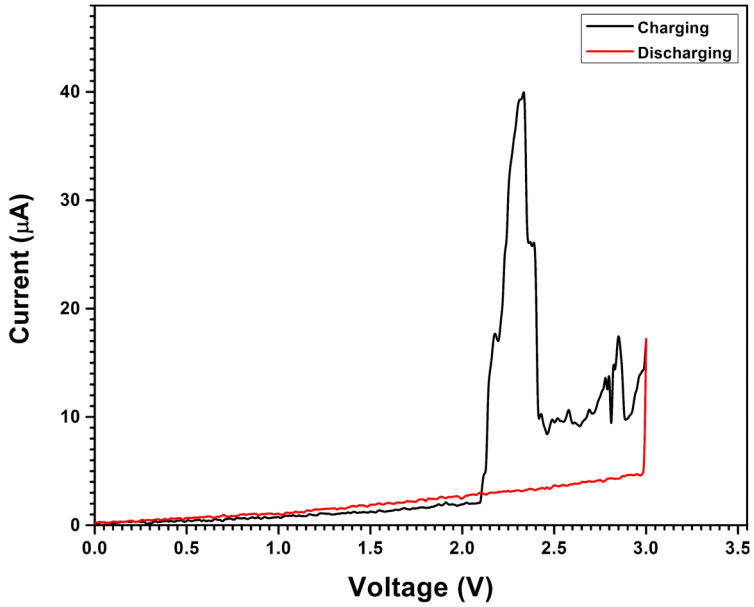

Figure 5-2: Cyclic voltammetry curve of Bi/$La_{0.9}Ba_{0.1}F_{2.9}$ half-cell.

5.2.2 Selected area electron diffraction analysis

The SAED patterns of the as-prepared electrolyte, after charging and after discharging are shown in Figure 5-3 (a-c). The profiles of the SAED patterns compared to the XRD for the as-prepared electrolyte and the references for LaF_3, LaOF, and La are shown in Figure 5-3d. The intensities of the SAED profiles were normalized using the peak at 4.86 nm^{-1}.

The overlap between the strong peak of the different reference patterns and the broad signals make a discrimination of the phases after charging and discharging difficult. However, the intensity of the strongest LaF_3 reflection (-121) is reduced after charging, and mostly recovering after discharging, indicating a (partially) reversible conversion reaction of LaF_3 (equation 5.4). The intensity of the LaF_3 (002) and the LaF_3 (-120) reflections are decreased after charging and even further after discharging, while the intensities of La (011) and La (110) reflections are increased. This would fit to a reduction of the LaF_3 to form metallic La (equation 5.2). In addition to the electrochemical reduction of the electrolyte, the electron beam could also contribute to the reduction of LaF_3 to form metallic La [153, 154, 158], as explained in chapter 2, interpreting the increased intensity of the La (011) and La (110) reflections and decreased intensity of the LaF_3 (002) and the LaF_3 (-120) reflections after discharging. Furthermore, the signal at 3.05 nm^{-1} is split after charging. This is presumably the result of the decreasing intensity of the LaF_3 (-121) reflection and the presence of LaOF (011) in the electrolyte. EDX analysis of the electrolyte powder (Figure 5-4) indicates a significant amount of oxygen in the as-prepared material, which probably stems from the sample preparation,

where the electrolyte has been prepared by ball milling in air. With the partial reduction of the $La_{0.9}Ba_{0.1}F_{2.9}$ during charging, the signal of the oxyfluoride becomes more dominant in the powder pattern. After discharging, the relative intensity of the LaOF (011) peak increased indicating the formation of additional LaOF as also seen in the *ex situ* studies described in chapter 6. The LaF_3 also partially reformed explaining why the (-121) reflection recovered and, hence, the splitting mostly disappeared.

Figure 5-5 (a-c) shows the SAED patterns of the Bi composite cathode before cycling, after charging and after discharging together with the profiles of the SAED patterns compared to the XRD of the as-prepared electrolyte and the references for Bi, Bi_2O_3, BiF_3, $BiO_{0.1}F_{2.8}$, LaOF, and La (Figure 5-5d). The SAED pattern of the cathode before cycling (Figure 5-5a) is in agreement with a polycrystalline material consisting of $La_{0.9}Ba_{0.1}F_{2.9}$ and Bi metal. However, a detailed analysis of the different materials present is difficult, because of the strong peak overlap of the materials and the broad signals. However, the as-prepared cathode exhibits unique reflections at 4.27 nm^{-1} (-114), 4.43 nm^{-1} (-120) and 6.13 nm^{-1} (024) for metallic Bi only overlapped by some weaker Bi_2O_3 reflections, which mostly disappear after charging, indicating a high conversion of Bi and Bi_2O_3 forming BiF_3 and $BiO_{0.1}F_{2.8}$. The formation of BiF_3 after charging can be seen from the SAED profiles (Figure 5-5d), where the charged cathode exhibits unique reflections for BiF_3 at 3.81 nm^{-1} (121) and 6.23 nm^{-1} (141). This indicates that the fluorination of metallic Bi during *in situ* TEM charging of the battery was successful as described in equitation 5.1 and additional oxyfluoride formation. After the discharging, the intensity of these unique BiF_3 reflections is reduced, indicating a partially reversible behavior of this fluoride ion battery even though no proper discharging could be seen in the CV measurements. Moreover, the SAED profiles (Figure 5-5d) reveal increasing of intensities of the two broad peaks around 4.9 nm^{-1} and 5.7 nm^{-1} after charging. These two peaks correspond to reflections of LaOF and $BiO_{0.1}F_{2.8}$ in addition to reflections of the electrolyte. These reflections are 4.87 nm^{-1} (112) and 5.73 nm^{-1} (121) for LaOF, and 4.9 nm^{-1} (-120), 4.98 nm^{-1} (013), 5.6 nm^{-1} (-122), and 5.83 nm^{-1} (021) for $BiO_{0.1}F_{2.8}$. The intensities of these two broad peaks only slightly decrease after discharging, indicating that the LaOF and $BiO_{0.1}F_{2.8}$ formations are non-reversible. Furthermore, the single diffraction peak at 3.05 nm^{-1} in the as-prepared state is split after charging. This signal is presumably a combination of LaF_3 (-121), Bi_2O_3 (211), LaOF (011), $BiO_{0.1}F_{2.8}$ (011) and BiF_3 (111). After charging, the intensities of the LaF_3 (-121) and Bi_2O_3 (211) reflections are decreased, while the intensities of the BiF_3 (111) and LaOF (011) are increased indicating local reactions in the Bi composite. After discharging, the peak splitting disappeared and the single peak is partially recovered.

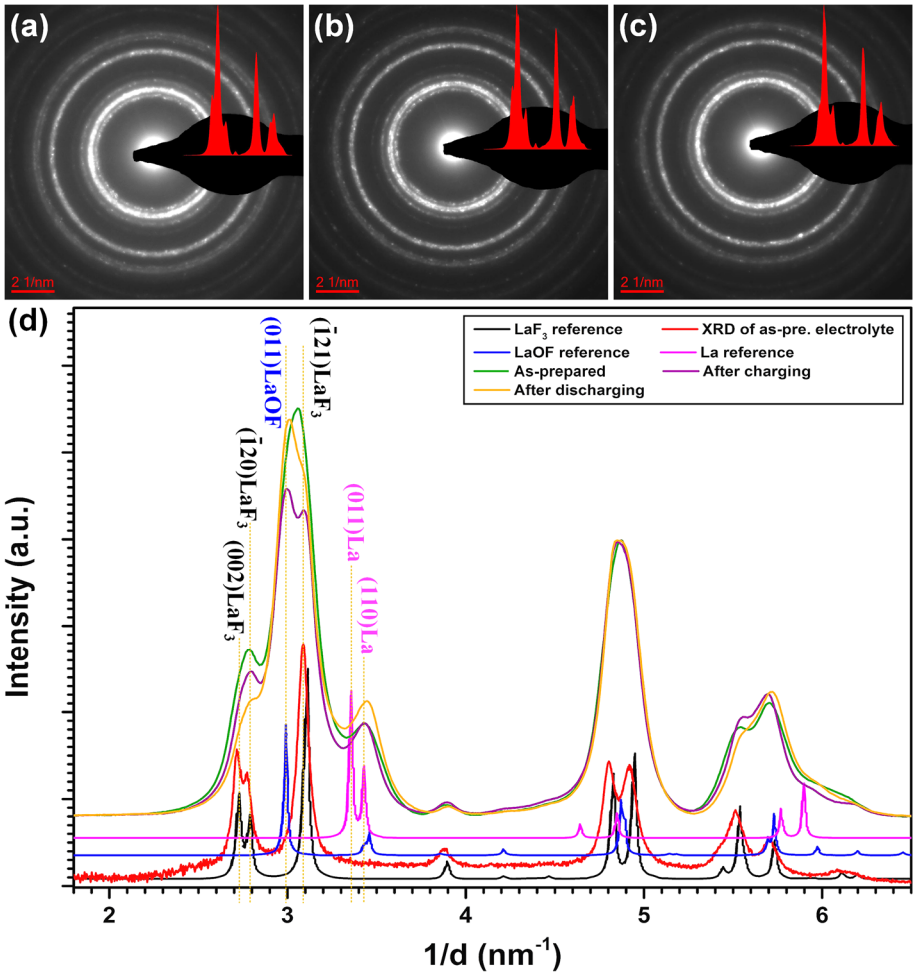

Figure 5-3: SAED pattern of (a) as-prepared electrolyte, (b) electrolyte after charging, (c) electrolyte after discharging, and (d) profiles of the SAED patterns compared to the XRD powder pattern of the as-prepared electrolyte and calculated patterns based on the single crystal structures of LaF_3, LaOF, and La.

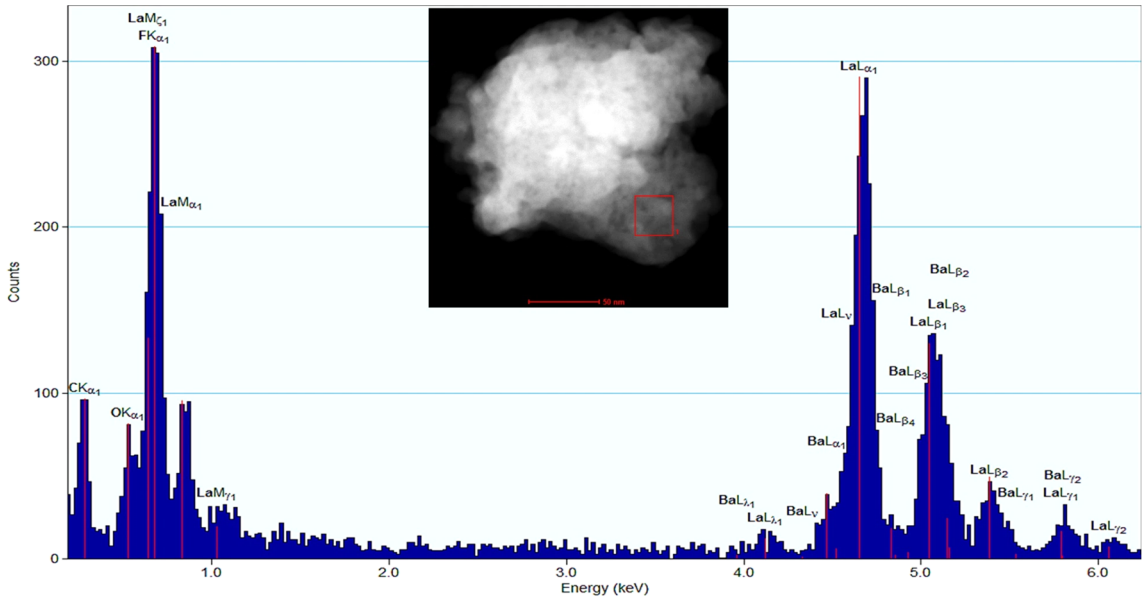

Figure 5-4: EDX analysis of the as-prepared electrolyte powder.

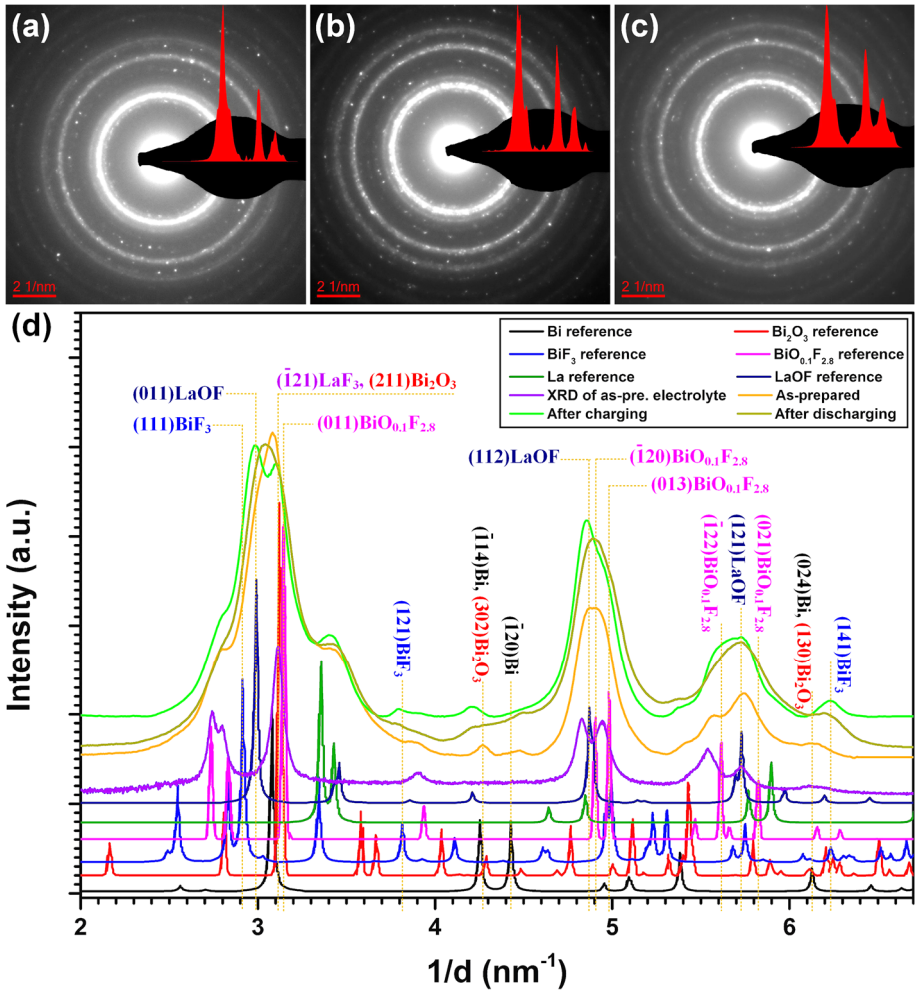

Figure 5-5: SAED pattern of (a) as-prepared cathode, (b) cathode after charging, (c) cathode after discharging, and (d) profiles of the SAED patterns compared to the XRD powder pattern of the as-prepared electrolyte and calculated patterns based on the single crystal structures of Bi, Bi_2O_3, BiF_3, $BiO_{0.1}F_{2.8}$, La, and LaOF.

5.2.3 Bright field and high resolution transmission electron microscopy analysis

BF-TEM and HRTEM images have been used to characterize the morphology and crystal structure of the cathode and the electrolyte. BF-TEM and HRTEM images of the as-prepared cathode (Figure 5-6) reveal a nanocrystalline structure of the cathode. Crystallites in the range of 5-35 nm are observed in good agreement with a previous work by C. Rongeat et. al. [192]. A small particle size and fine mixture of the electrode materials is essential for the electrochemical performance of the battery as a high contact area and good ion and electron diffusion pathways are required for fast and complete conversion reactions [229–232]. Figure 5-6b shows a HRTEM image of a Bi nanoparticle in the composite cathode before cycling identified by the corresponding fast Fourier transform (FFT). The lattice spacings are in good agreement with the hexagonal phase of bismuth (a=b=4.548 Å, c=11.852 Å, α=β=90.0,

γ=120.0) [ICSD-53797]. In addition to Bi metal, the presence of bismuth oxide (Bi_2O_3) in the bismuth composite cathode before cycling is confirmed by HRTEM (Figure 5-6c). The lattice spacings of the Bi_2O_3 particle calculated from FFT are in good agreement with the orthorhombic phase of bismuth oxide (a=12.732 Å, b=4.955 Å, c=5.582 Å, α=β=γ=90.0) [ICSD-261777]. Table 5-1 contains the measured lattice spacings for metallic Bi and Bi_2O_3 compared to the reference structures.

Figure 5-7 shows a BF- and HRTEM images of the composite cathode after charging. The HRTEM images confirm the presence of both BiF_3 and $BiO_{0.1}F_{2.8}$ phases. The lattice spacings of BiF_3 measured from the corresponding FFT match well with the orthorhombic phase of bismuth fluoride (a=6.5614 Å, b=7.0153 Å, c=4.8414 Å, α=β=γ=90.0) [ICSD-1269]. This confirms fluorination of the Bi metal electrode to form BiF_3 in the cathode during charging. While the lattice spacings of the $BiO_{0.1}F_{2.8}$ phase are in good agreement with the hexagonal phase of bismuth oxyfluoride (a=b=4.083 Å, c=7.323 Å, α=β=90.0, γ=120.0) [ICSD-24056]. This emphasizes the fluorination of the bismuth oxide forming the $BiO_{0.1}F_{2.8}$ phase during charging. Table 5-2 summarizes the measured lattice spacings for BiF_3 and $BiO_{0.1}F_{2.8}$ compared to the reference structures. HRTEM images and the corresponding FFTs of the as-prepared electrolyte are shown in Figure 5-8 confirming a high crystallinity of the material. The lattice spacings measured from the HRTEM image (Figure 5-8b) are close to the hexagonal LaF_3 phase (a=b=7.185 Å, c=7.351 Å, α=β=90.0, γ=120.0) [ICSD-35673], which was already identified as the reference structure for the $La_{0.9}Ba_{0.1}F_{2.9}$ by XRD of the bulk electrolyte [233]. Table 5-3 summarizes the measured lattice spacings for LaF_3 compared to the reference structure.

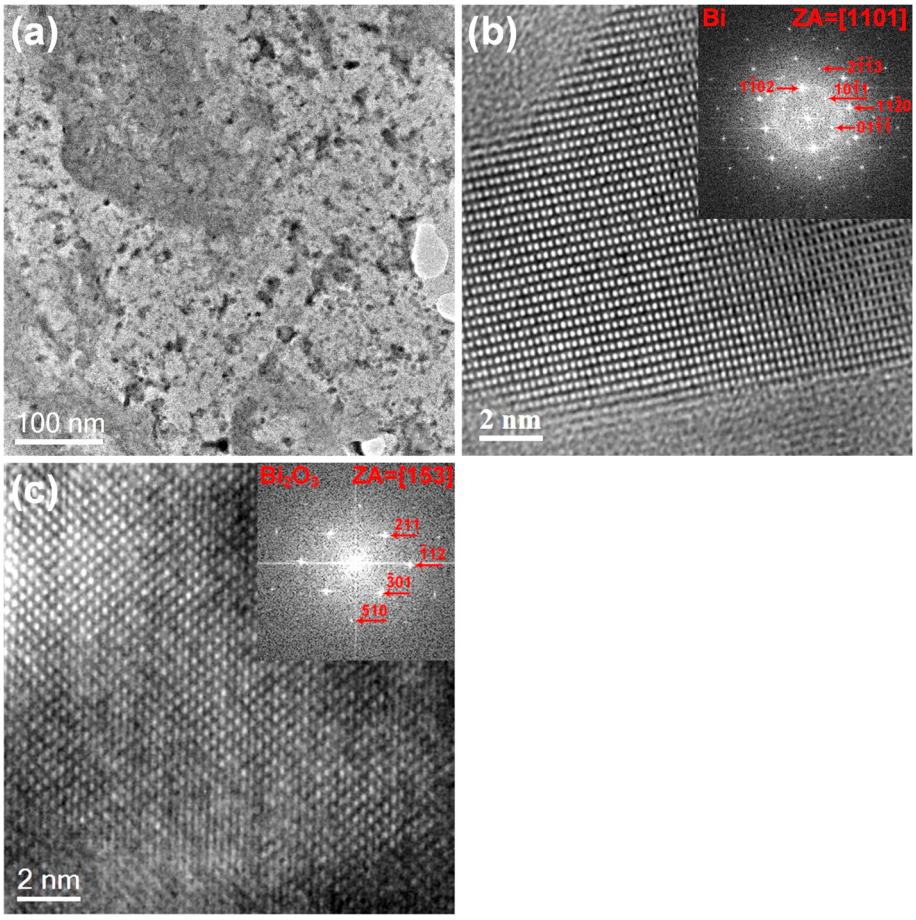

Figure 5-6: (a) Low magnification BF-TEM image of the as-prepared cathode, (b, c) HRTEM images of as-prepared cathode showing the presence of Bi and Bi_2O_3 phases. The HRTEM images have been filtered using the HRTEM-filter script (D. R. G. Mitchell, v2.0, Jan 14).

Table 5-1: Lattice spacings of the Bi & Bi_2O_3 references and the values measured from FFTs.

Lattice plane	**Bi reference [Å]**	**Measured d-spacings [Å]**	**Reference angles [˚]**	**Measured angles [˚]**
1-102	3.28	3.27	(1-102) & (10-11)=55.27	(1-102) & (10-11)=54.7
10-11	3.74	3.75	(1-102) & (01-1-1)=124.73	(1-102) & (01-1-1)=124.2
01-1-1	3.74	3.75	(01-1-1) & (10-11)=69.46	(01-1-1) & (10-11)=69.5
Lattice plane	**Bi_2O_3 reference [Å]**	**Measured d-spacings [Å]**	**Reference angles [˚]**	**Measured angles [˚]**
211	3.2	3.2	(211) & (-112)=44.91	(211) & (-112)=45.2
-112	2.39	2.4	(211) & (-301)=93.05	(211) & (-301)=92.5
-301	3.38	3.3	(-301) & (-112)=48.14	(-301) & (-112)=47.3

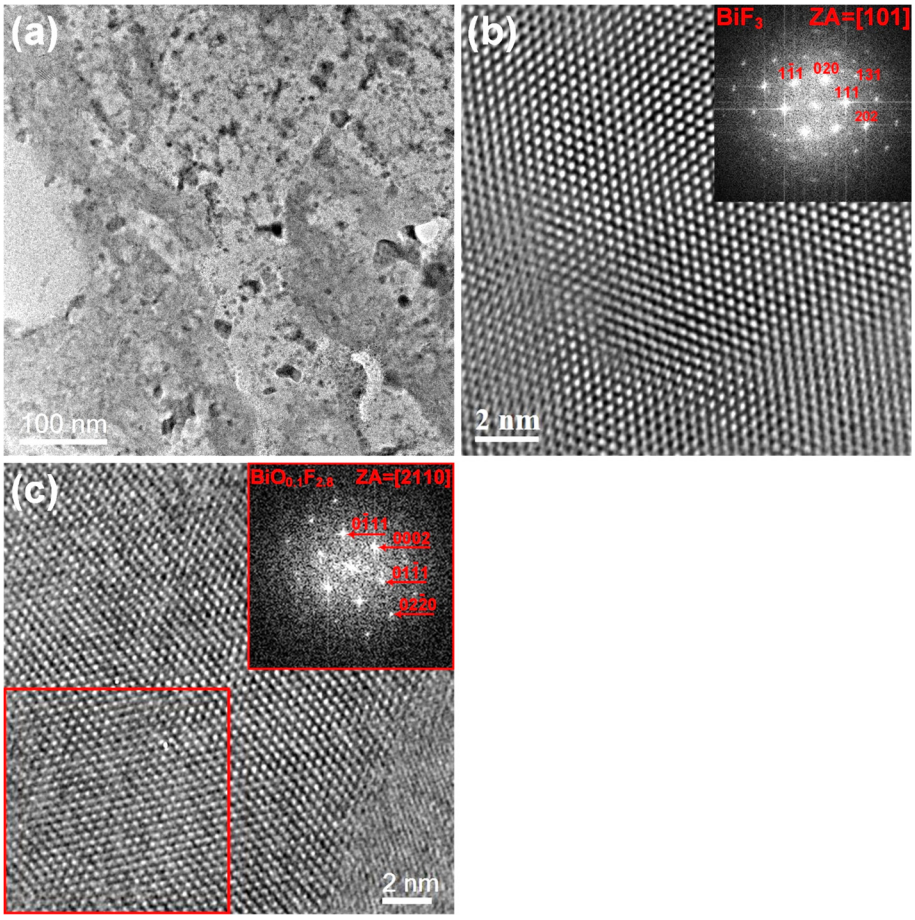

Figure 5-7: (a) Low magnification BF-TEM image of cathode after charging, (b, c) HRTEM images of cathode after charging showing the formation of BiF_3 & $BiO_{0.1}F_{2.8}$ phases. The HRTEM images have been filtered using the HRTEM-filter script (D. R. G. Mitchell, v2.0, Jan 14).

Table 5-2: Lattice spacings of the BiF_3 & $BiO_{0.1}F_{2.8}$ references and the values measured from FFTs.

Lattice plane	**BiF_3 reference [Å]**	**Measured d-spacings [Å]**	**Reference angles [˚]**	**Measured angles [˚]**
1-11	3.4	3.24	(1-11) & (020)=119.04	(1-11) & (020)=118.50
020	3.51	3.52	(1-11) & (111)=58.09	(1-11) & (111)=57.00
111	3.4	3.24	(111) & (020)=60.96	(111) & (020)=61.50
Lattice plane	**$BiO_{0.1}F_{2.8}$ reference [Å]**	**Measured d-spacings [Å]**	**Reference angles [˚]**	**Measured angles [˚]**
0-111	3.18	3.2	(0-111) & (0002)=64.23	(0-111) & (0002)=64.00
0002	3.66	3.64	(0-111) & (01-11)=128.45	(0-111) & (01-11)=128.10
01-11	3.18	3.2	(01-11) & (0002)=64.23	(01-11) & (0002)=64.10

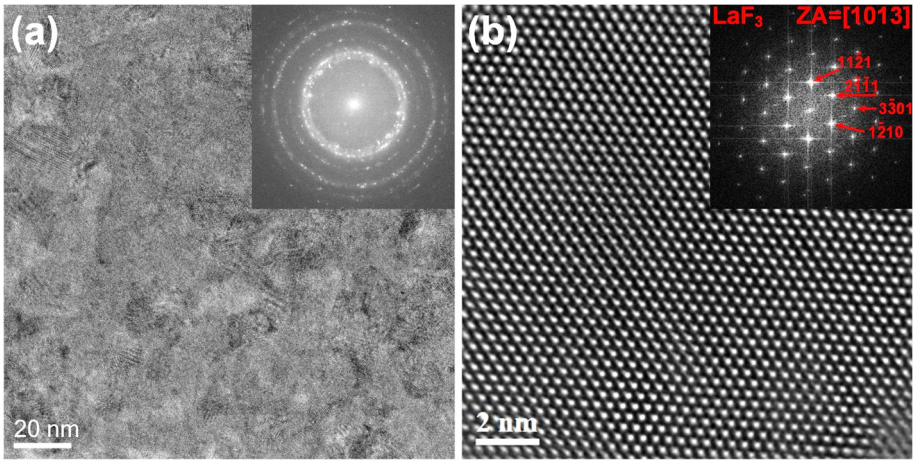

Figure 5-8: HRTEM images and the corresponding FFTs of the as-prepared electrolyte. The image (b) has been filtered using the HRTEM-filter script (D. R. G. Mitchell, v2.0, Jan 14).

Table 5-3: Lattice spacings of LaF_3 and the values determined from HRTEM.

Lattice plane	LaF_3 reference [Å]	Measured d-spacings [Å]	Reference angles [°]	Measured angles [°]
11-21	3.23	3.21	(11-21) & (2-1-11)=53.39	(11-21) & (2-1-11)=53.5
2-1-11	3.23	3.21	(11-21) & (1-210)=116.69	(11-21) & (1-210)=117
1-210	3.59	3.55	(1-210) & (2-1-11)=63.31	(1-210) & (2-1-11)=63.5

5.2.4 Scanning transmission electron microscopy analysis

STEM images of the cathode of the half-cell before and after cycling are provided in Figure 5-9. The STEM images reveal that the cathode and electrolyte are porous. The porosity of the cathode is desirable for a good battery performance to compensate the volumetric changes during fluorination. However, especially in our micron-sized thin batteries, the high porosity is critical as it degrades the mechanical stability [234, 235] and the fluorination and charging pathways between particles. Furthermore, the STEM images reveal inhomogeneities of the cathode materials, where some areas consist of accumulated electrolyte particles whereas other regions are dominated by a Bi/C mixture (Figure 5-9a). Therefore, the concentration of active material varies from one area to another. This non-uniform distribution of the active material leads to a non-uniform current distribution in the electrode parts that is expected to enhance the internal stresses during charging/discharging.

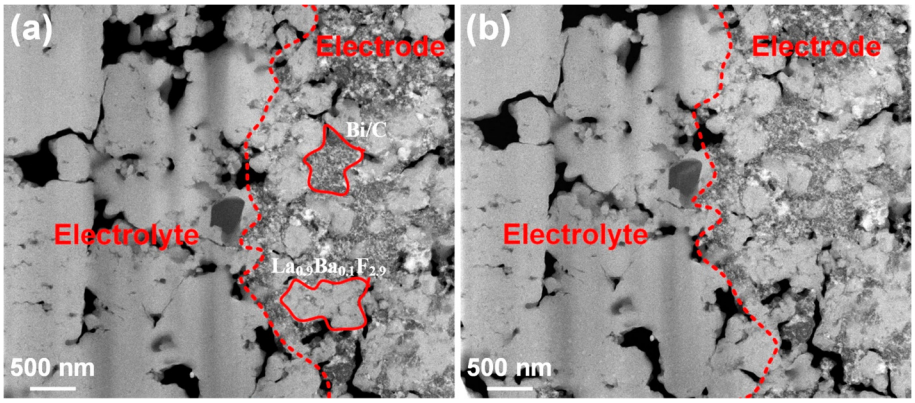

Figure 5-9: STEM images of the half-cell (a) before cycling and (b) after cycling.

The poor reversibility of the half-cell can be attributed to different factors. The main reason is the presence of bismuth oxide in the composite cathode before charging that fluorinate after charging to irreversibly form bismuth oxyfluoride phase ($BiO_{0.1}F_{2.8}$). Based on the electrochemical charging curve, this irreversible phase is the main phase formed during charging. Moreover, the reversibility of battery redox reactions depends on the ionic conductivity. BiF_3 has poor fluoride ion conductivity and is thus limiting further charging/discharging, which is the reason why the electrolyte was mixed into the cathode. Furthermore, the reduction of $La_{0.9}Ba_{0.1}F_{2.9}$ leading to the formation of metallic La and Ba by releasing fluoride will change the nanostructured $La_{0.9}Ba_{0.1}F_{2.9}$ solid electrolyte. The limited conductivity is further enhanced, as the measurement was done at RT where the fluoride ionic conductivity of the electrolyte is very low ($\sim 2\times10^{-6}$ S cm^{-1}). Typically, this solid electrolyte is used at a high temperature of 150 °C to increase its ionic conductivity to around 2.8×10^{-4} S cm^{-1} [48]. The bulk fluoride ion batteries are known not to operate at RT. The only reason, why we have been able to properly charge and partially discharge the battery at all, are the reduced dimensions of the battery, drastically reducing the migration length for the fluoride ions during cycling. In addition to the partial reversibility, the fact that we do not see a discharging current in the CV measurements is presumably related to short circuits in the system leading to a self-discharge. Part of this is due to the limited resistivity of the devices and the low charges accumulated in the miniaturized battery. This could be further enhanced by electromigration of Pt from the two deposited electrical contacts toward the interface during charging [236].

5.3 Study of a Cu/$La_{0.9}Ba_{0.1}F_{2.9}$/MgF_2 full cell

In addition to the half-cell experiments, *in situ* studies on a Cu/$La_{0.9}Ba_{0.1}F_{2.9}$/MgF_2 full cell fluoride ion battery were performed in the TEM. The full cell is based on $La_{0.9}Ba_{0.1}F_{2.9}$ as electrolyte, Cu/C composite as a cathode, and a MgF_2/Mg/$La_{0.9}Ba_{0.1}F_{2.9}$/C composite as an anode. Cu has been chosen as cathode material because of the high theoretical capacity of the Cu/CuF_2 couple (528 mAh g^{-1} [237]) and the high potential vs. Mg/MgF_2 (2.71 V). The composite anode was prepared with equal amounts (typically 20 wt%) of Mg and MgF_2 ball milled with 50 wt% of electrolyte and 10 wt% of carbon black. Even when stored under Ar, Mg metal is sensitive to surface oxidation and hence, rapid performance degradation occurs when used as anode [192]. Therefore, Mg as an anode for the fluoride ion battery was used in the discharged state (MgF_2) [192]. However, the poor reactivity and the low ionic conductivity of MgF_2 prevented its direct us as anode. Therefore, a mixture between Mg and MgF_2 was used to enhance the reactivity [238]. FIB was used to prepare a micron-sized battery from that system as described in chapters 3 & 4. A SEM image of the micron-sized battery after contacting on the MEMS device is shown in Figure 5-10.

The working principle of the Cu/$La_{0.9}Ba_{0.1}F_{2.9}$/MgF_2 fluoride ion battery is the oxidation of the Cu cathode to CuF_2 via transport of fluoride ions through the electrolyte from the MgF_2 anode, which is reduced to form Mg metal. The oxidation of Cu to form CuF_2 will release electrons that travel via the external circuit to the anode.
The conversion reactions of Cu during charging are as follows:

Cathode reaction:	$Cu + 2F^- \rightarrow CuF_2 + 2e^-$	5.5
Anode reaction:	$MgF_2 + 2e^- \rightarrow Mg + 2F^-$	5.6
Cell:	$Cu + MgF_2 \rightarrow CuF_2 + Mg$	5.7

While during discharging, the conversion reactions are as follows:

Cathode reaction:	$CuF_2 + 2e^- \rightarrow Cu + 2F^-$	5.8
Anode reaction:	$Mg + 2F^- \rightarrow MgF_2 + 2e^-$	5.9
Cell:	$CuF_2 + Mg \rightarrow Cu + MgF_2$	5.10

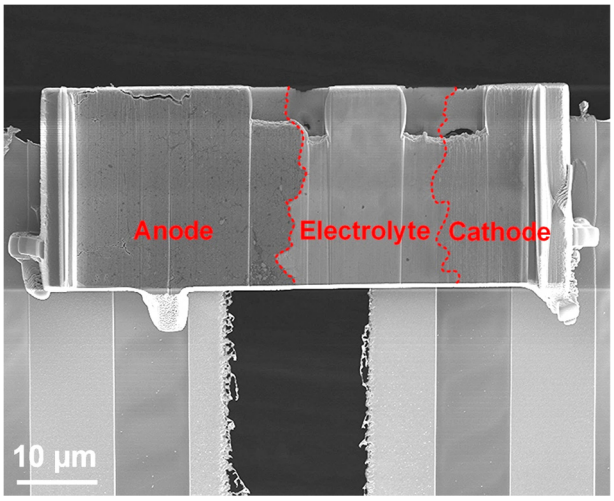

Figure 5-10: SEM image of the micron-sized full cell mounted on the MEMS device.

5.3.1 *Ex situ* cycling of micron-sized full cell

Before performing the *in situ* TEM study, a micron-sized Cu/$La_{0.9}Ba_{0.1}F_{2.9}$/MgF_2 full cell fluoride ion battery was studied *ex situ*. This cell was mounted on a Protochips MEMS device and cycled *ex situ* under vacuum (~10^{-7} mbar) at RT. A Keithley 2611A source meter and the Keithley control software has been used to charge the cell by applying a voltage sweep from 0 to 3.5 V over 4h (with 0.243 mV/s scan rate). Subsequently, the discharging was performed by sweeping the voltage from 3.5 V to 0 V over 4 h. The cell voltage vs. current for the charging and discharging is shown in Figure 5-11. During the voltage sweep, the current slowly increased until it reached a first maximum around 2 V. This peak can be attributed to the formation of copper (I) oxide [192], probably due to the oxygen detected in the electrolyte and electrodes from the bulk sample preparation. A second maximum started from around 2.77 V and continued to 3.5 V, which can be attributed to the copper (II) fluoride formation. This potential is slightly higher than the theoretical potential of 2.71 V for the Cu/CuF_2 redox couple vs. Mg/MgF_2. During discharging, the reverse reaction was observed until the battery failed at 2.85 V, thereafter, the I-V curve showed ohmic behaviour indicating a short circuit between cathode and anode. However, as only the CuF_2 can be converted back to metallic Cu, this reaction is fairly complete, based on the measured conversion charge, while the Cu_2O formation is irreversible anyway [192].

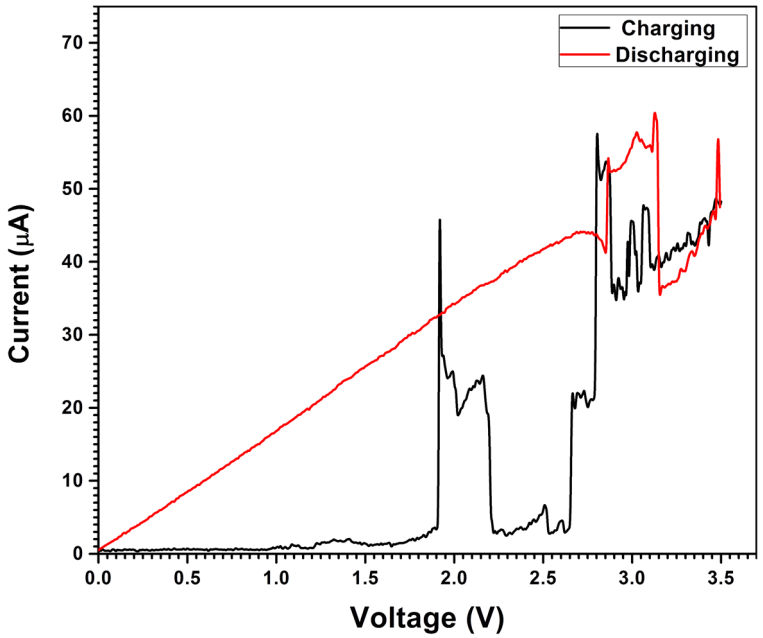

Figure 5-11: *Ex situ* cyclic voltammetry curves of Cu/$La_{0.9}Ba_{0.1}F_{2.9}$/MgF_2 full cell.

5.3.2 *In situ* TEM study of a Cu/$La_{0.9}Ba_{0.1}F_{2.9}$/MgF_2 full cell

5.3.2.1 Electrochemical study

Analogously to the Bi half-cell, the electrochemical measurement was performed by CV at RT *in situ* inside the TEM using an Aduro single tilt sample holder and a Keithley 2611A source meter. The Cu/$La_{0.9}Ba_{0.1}F_{2.9}$/MgF_2 full cell was charged by applying a voltage sweep from 0 V to 3.5 V over 2 h (0.27 mV/s scan rate). The voltage was held at 3.5 V over 30 min for TEM investigation. Afterwards, discharging was performed by sweeping the voltage from 3.5 V to 0 V over 2 h. Using the same conditions, a second cycle was started.

The cell voltage vs. current for the first charging/discharging and the second charging is shown in Figure 5-12. The basic redox steps observed during charging are comparable to the *ex situ* investigation. However, unfortunately, the charging curve is on top of a strong background current, due to a short circuit between cathode and anode, probably due to residual contamination during FIB preparation. However, the two peaks in the charging curve indicate that the electrochemical reaction is still occurring. During the holding period at 3.5 V, the current initially slightly decreased and then suddenly jumped from ~33 μA to ~100 μA indicating a stronger short circuit formed in the cell, which may be due to Pt migration from the contacts [236]. Therefore, a strong self-discharge has to be expected during further cycling of the battery.

During discharging, the current is dominated by the short circuit, but a slight peak around 2.7 V can be seen, indicating some driven discharging of the battery. During the second charging, no characteristic CV peaks could be observed until the micron-sized battery fractured at the cathode-electrolyte interface at a voltage where the electrochemical reaction should have occurred again. The ohmic I-V curve could be due to the short circuit that has developed. However, also in *ex situ* studies, the capacity faded very strongly from 390 mAh g^{-1} to only 33 mAh g^{-1} after the first discharge [192], suggesting a very limited reversibility and thus hardly any recharging should be observed during the second cycle. Nevertheless, the fracture around 3.1-3.5 V suggests that some electrochemical reactions still occurred, presumably causing the fracture because of volumetric expansion of the Cu during fluorination.

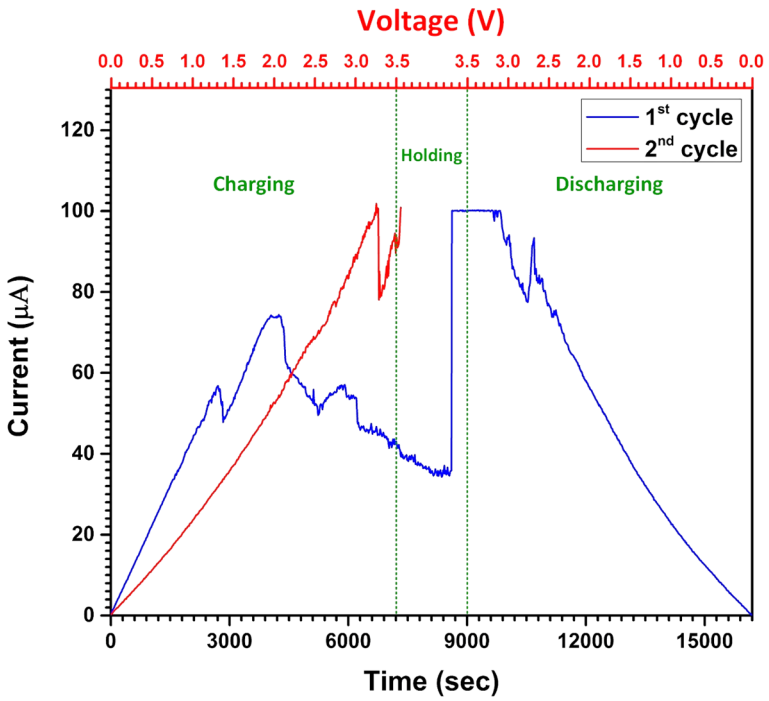

Figure 5-12: Plotted current vs. voltage and time for the first and second cycles of Cu/$La_{0.9}Ba_{0.1}F_{2.9}$/MgF_2 full cell.

5.3.2.2 STEM and SEM analysis

STEM images of the full cell before cycling, after the first cycle, and after failure during the second cycle are given in Figure 5-13 and Figure 5-14. From the STEM images, one can see that the Cu/C cathode contains nanocrystalline Cu surrounded by carbon black. The Cu crystallite size is in the range of 40-250 nm. Comparing the STEM images of the cathode before and after the 1st cycle reveals some coarsening of the Cu. In addition, the formation of voids in the cathode is visible, to some extend after the first cycle, and more clearly after failure. In this

area, the formation of CuF_2 was confirmed by HRTEM as discussed in section 5.3.2.4. Finally, a new phase can be seen as a bright line at the interface, identified as Mo enrichment at the interface as discussed in section 5.3.2.3. In contrast, on the anode side, no significant changes were observed in the thin area of the anode-electrolyte interface, Figure 5-14.

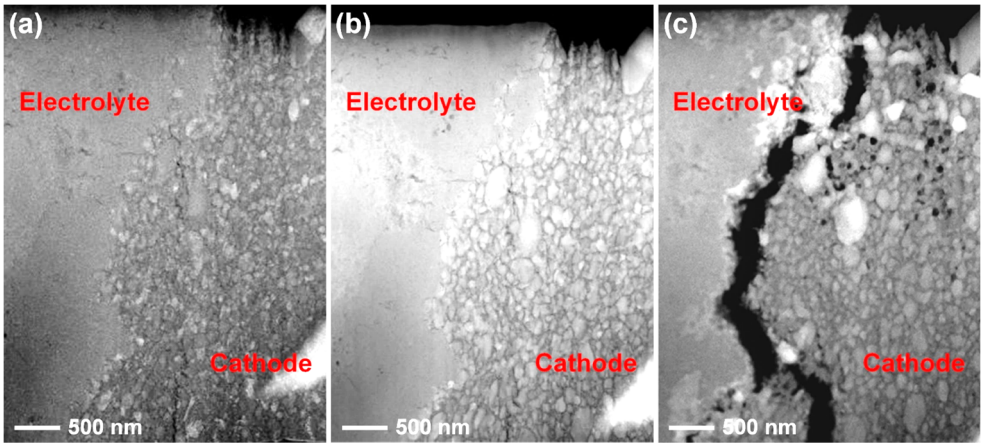

Figure 5-13: Electrolyte-cathode interface (a) as-prepared, (b) after 1st cycle, (c) after 2nd charging.

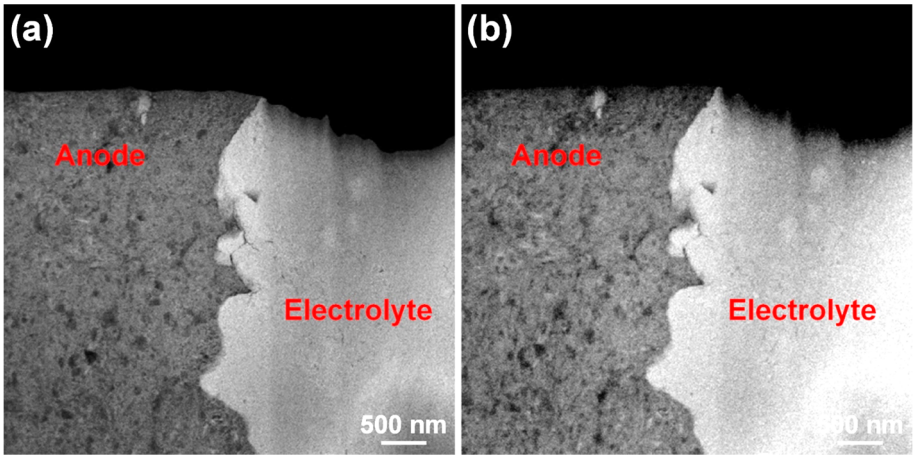

Figure 5-14: The thin area at anode-electrolyte interface (a) before cycling (b) after failure.

The morphological changes are more pronounced at the thick part of the cathode (Figure 5-15c/f). The new phase at the interface is clearer compared to the thin area. Moreover, the new phase and the Cu particles are slightly protruded out of the cathode due to the local volume change during charging. The volumetric change in the cathode attributed to the fluorination of Cu to form CuF_2 [192] is also leading to fracture at the interfaces (Figure 5-15f). The fracture is particularly noticeable in these *in situ* samples as the porosity was reduced compared to batteries cycled *ex situ*, thus providing less free volume to compensate for the volumetric changes.

On the anode side, some volumetric changes are visible as small cracks in the $Mg/MgF_2/La_{0.9}Ba_{0.1}F_{2.9}/C$ composite and at the interfaces with the electrolyte (Figure 5-15a/d). However, more noticeable, the surface of the cycled anode (Figure 5-15d) is remarkably different from the pristine anode (Figure 5-15a). After cycling, the anode surface is covered by small particles in agreement with previously reported *ex situ* results where "snowflake-like" particles were formed on the anode surface [239]. It was found that these particles are MgF_2 sticking out of the anode surface [239, 240]. The formation of these particles on the anode surface has been suggested to be the result of the low ionic conductivity of the electrolyte, leading to preferential fluoride migration on the surface [241]. If the MgF_2 formation on the anode surface is due to fast fluoride ion migration on the surface, this would significantly impact the *in situ* TEM measurements, where the surface to volume ratio of the electron transparent regions is extreme. In addition to the 20 times reduction of the electrode thickness compared to the bulk battery, surface migration could partially explain why it is possible to cycle the micron-sized fluoride ion battery at RT, whereas elevated temperatures are needed to increase the conductivity sufficiently for the bulk battery. However, we did not observe any MgF_2 formation on the surface of the electron transparent part of the battery (only on the thicker part), which suggests that the formation of the MgF_2 surface decoration requires a more complex explanation.

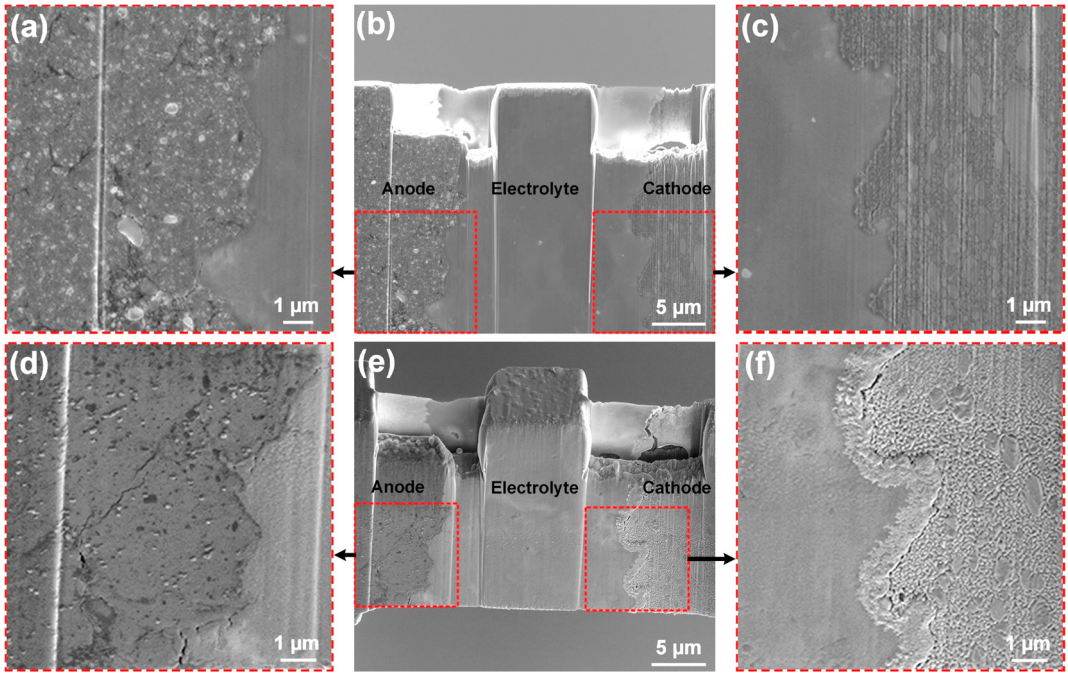

Figure 5-15: SEM images of (a) thick area at anode-electrolyte interface before cycling, (b) full cell before cycling, (c) thick area at electrolyte-cathode interface before cycling, (d) thick area at anode-electrolyte interface after cycling, (e) full cell after cycling, (f) thick area at electrolyte-cathode interface after cycling.

5.3.2.3 STEM-EDX analysis

The STEM-EDX map of a cross-section of an as-prepared cathode-electrolyte interface is shown in Figure 5-16. Even though the cathode consists of 90 wt% copper and 10 wt% carbon black, the O-map reveals significant amounts of oxygen in the cathode. The origin of oxygen in the cathode materials can be clearly attributed to the carbon black, whereas the copper particles do not show significant oxidation. Small amounts of oxygen can also be observed in the electrolyte, which more stable against oxidation. The La, Ba, and F-maps reveal the good homogeneity of the electrolyte materials. Moreover, the interface between the cathode and electrolyte has no Cu diffusion into the electrolyte. The STEM-EDX map of the cathode-electrolyte interface after failure is shown in Figure 5-17. The migration of the fluoride into the Cu/C cathode can be observed from the F distribution. Moreover, diffusion of Cu into the electrolyte can also be seen. This diffusion is probably related to the strong volumetric change accompanying the Cu/CuF_2 reaction in combination with the porosity of the ball milled electrolyte [192]. The local increase of volume during charging leads to the Cu diffusion into the pores of the electrolyte to compensate this volume change.

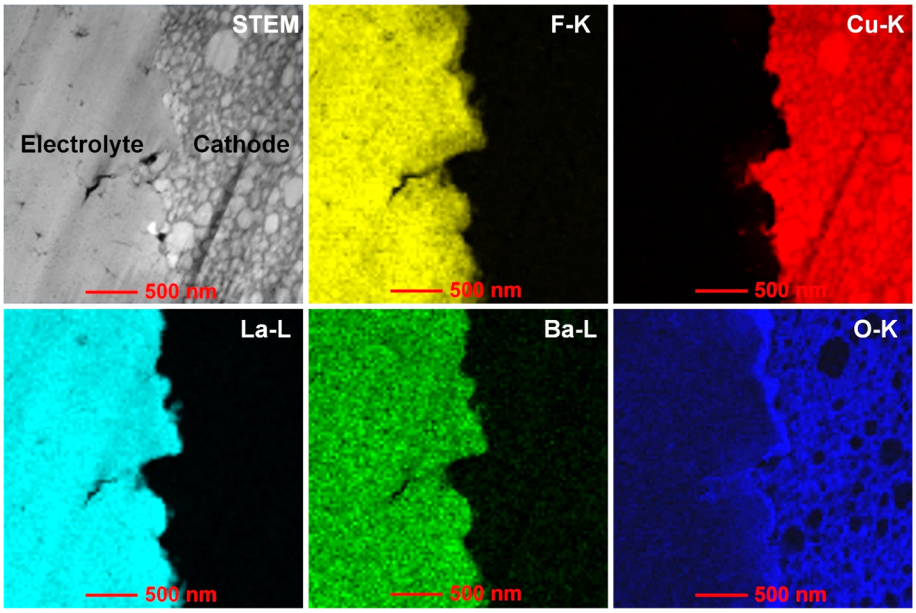

Figure 5-16: STEM-EDX map of an as-prepared cross-section of the cathode-electrolyte interface.

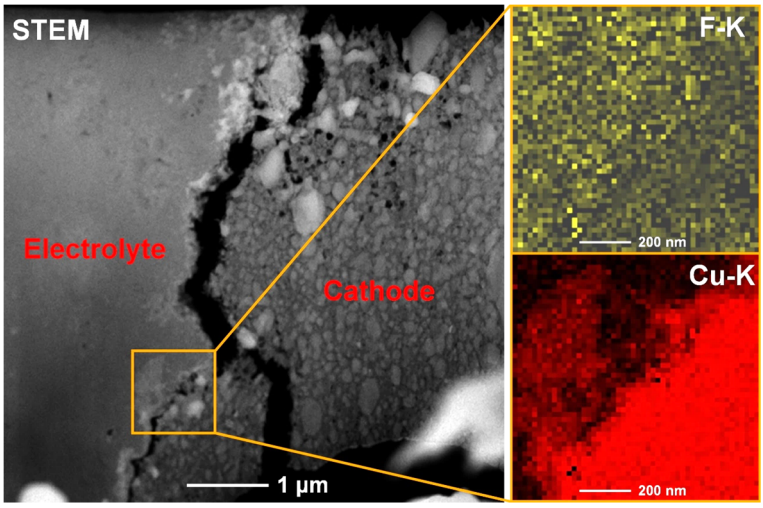

Figure 5-17: STEM-EDX map at cathode-electrolyte interface after failure.

From the thick part of the sample cycled *in situ*, a fresh thin area was prepared at the cathode-electrolyte interface after cycling to investigate potential thickness effects during *in situ* cycling. For this, the micron-sized battery was mounted on a molybdenum TEM grid in the FIB and a fresh area cut close to the original area investigated (Figure 5-18). The morphological changes observed in this thick part and in the thin area investigated *in situ* are comparable, confirming that the sample thickness does not significantly influence the morphological changes observed *in situ* even though surface effects might change the fluoride ion conductivity. A STEM-EDX map from this area is shown in Figure 5-19. The fluoride migration into the Cu/C cathode can be seen more clearly compared to the initially thinned area, which could be because of the limited diffusion pathways in the thin part of the sample. Similar to the thin part, diffusion of Cu into the electrolyte was also observed in the thick part of the sample. Moreover, the new phase, which is formed at the interface and closer to it, can be clearly seen and it was confirmed as copper fluoride by HRTEM. In addition to the effects of the volumetric changes associated due to fluorination that could lead to Cu diffusion from the cathode into the electrolyte [242], formation of Cu oxide may lead to an inhomogeneous distribution of the current density through the cathode and hence, a localized overheating that favors voids formation. Furthermore, the Mo-map reveals Mo contamination at the interface, where the new phase formed, which could be a failure mode due to impurities.

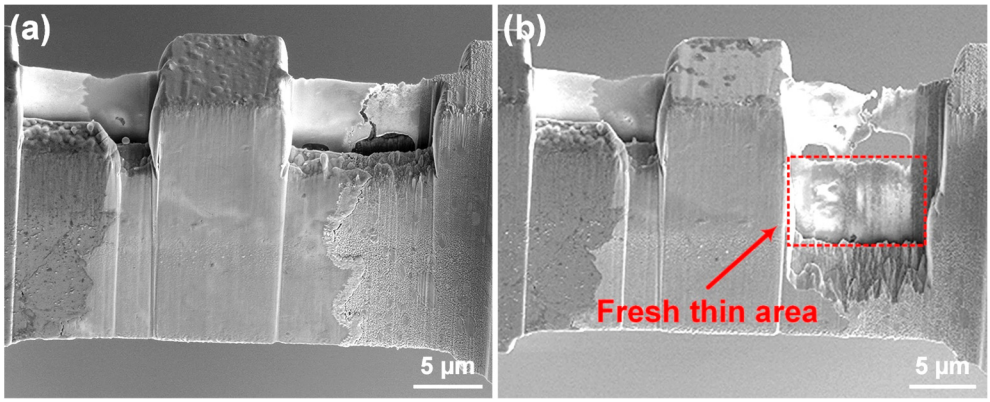

Figure 5-18: SEM images of the cycled micron-sized battery (a) after failure (b) after preparing a fresh thin area at the cathode-electrolyte interface.

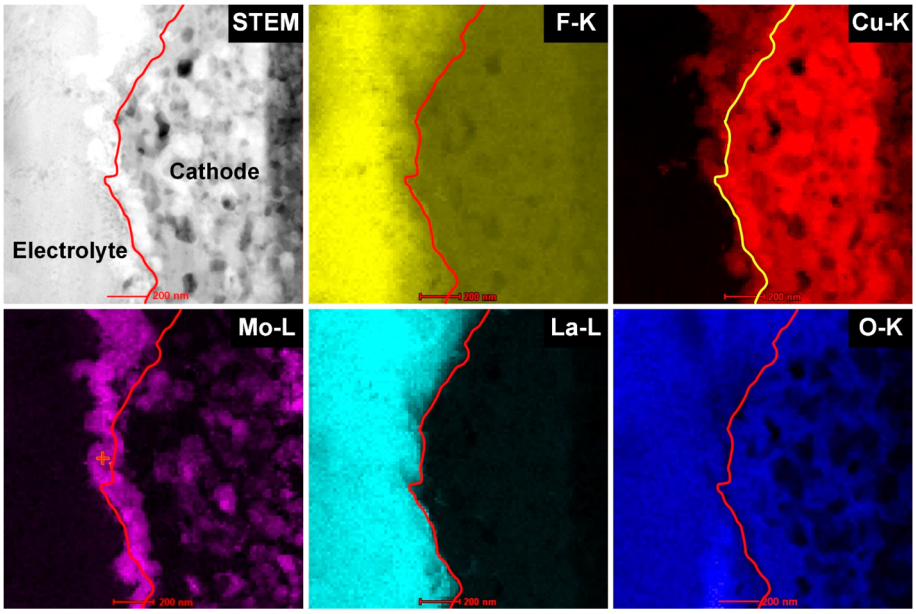

Figure 5-19: STEM-EDX map of the fresh thin area at the cathode-electrolyte interface.

5.3.2.4 TEM and HRTEM study

BF-TEM imaging is used to determine the particles size of Cu/C cathode and to investigate the cathode-electrolyte interface before cycling (Figure 5-20a). The TEM images reveal that the Cu/C cathode material consists of nanoparticles in the size range from 40-250 nm, while the electrolyte consists of denser and smaller nanoparticles. As discussed in section 5.2.3, the small particle size in the electrodes is necessary for good electrochemical performance. HRTEM image has been used to characterize the crystal structure of the cathode materials. Figure 5-20b shows the HRTEM image and the corresponding FFT of cathode material of the as-prepared cell. The HRTEM image confirm the crystallinity of the cathode and

the presence of Cu. The lattice spacings of a Cu particle calculated from the FFT are in good agreement with the tetragonal phase of copper metal (a=b=2.892 Å, c=2.708 Å, α=β=γ=90.0) [ICSD-248435].

TEM and HRTEM images of the Cu/C cathode after cycling (after failure) and the corresponding FFTs are shown in Figure 5-21(a, b, c), confirming the presence of CuF_2 after cycling. The measured lattice spacings fit well to the monoclinic phase of copper (II) fluoride (a=3.309 Å, b=4.569 Å, c=5.362 Å, α=90.0, β=121.11, γ=90.0) [ICSD-9788]. In addition to CuF_2 formation, the presence of Cu_2O is confirmed by HRTEM. The lattice spacings of the Cu_2O crystal are in good agreement with copper (I) oxide, which is a cubic phase (a=b=c=4.27 Å, α=β=γ=90.0) [ICSD-173982]. Table 5-4 contains the measured lattice spacings for Cu, CuF_2 and Cu_2O compared to the reference structures.

Furthermore, TEM images of the cathode-electrolyte interface after failure are shown in Figure 5-22(a, b, c). The images reveal the formation of spherical particles at the interface (Figure 5-22a) in addition to amorphous carbon (Figure 5-22c). The formation of spherical particles would fit the hypothesis that the localized overheating has occurred due to an inhomogeneous current density in the cathode, as a result of Cu oxide and fluoride formation and their inhomogeneous distribution within the conductive matrix. These spherical particles were assumed to be copper (II) fluoride, but, the lattice spacings would also fit to MoO.

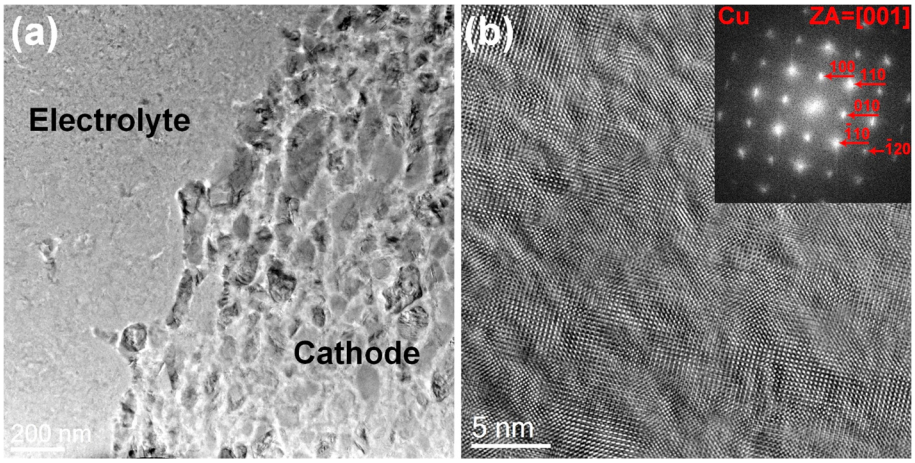

Figure 5-20: (a) TEM image of the cathode-electrolyte interface before cycling, (b) HRTEM image of the cathode before cycling and the corresponding FFT. The HRTEM Image has been filtered using the HRTEM-filter script (D. R. G. Mitchell, v2.0, Jan 14).

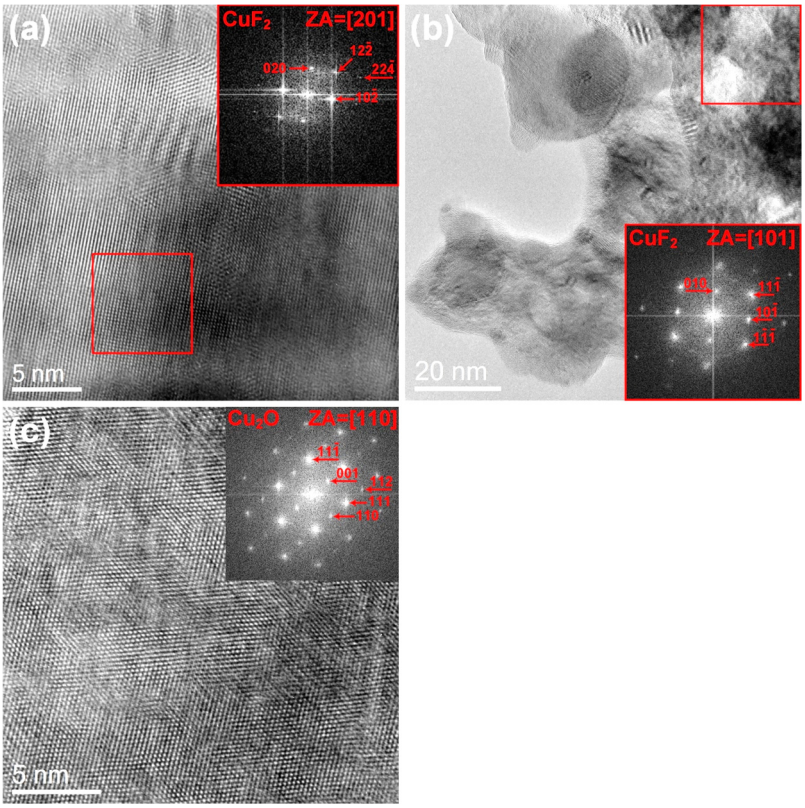

Figure 5-21: HRTEM images of the cathode after cycling and the corresponding FFTs. The image (a) has been filtered using the HRTEM-filter script (D. R. G. Mitchell, v2.0, Jan 14).

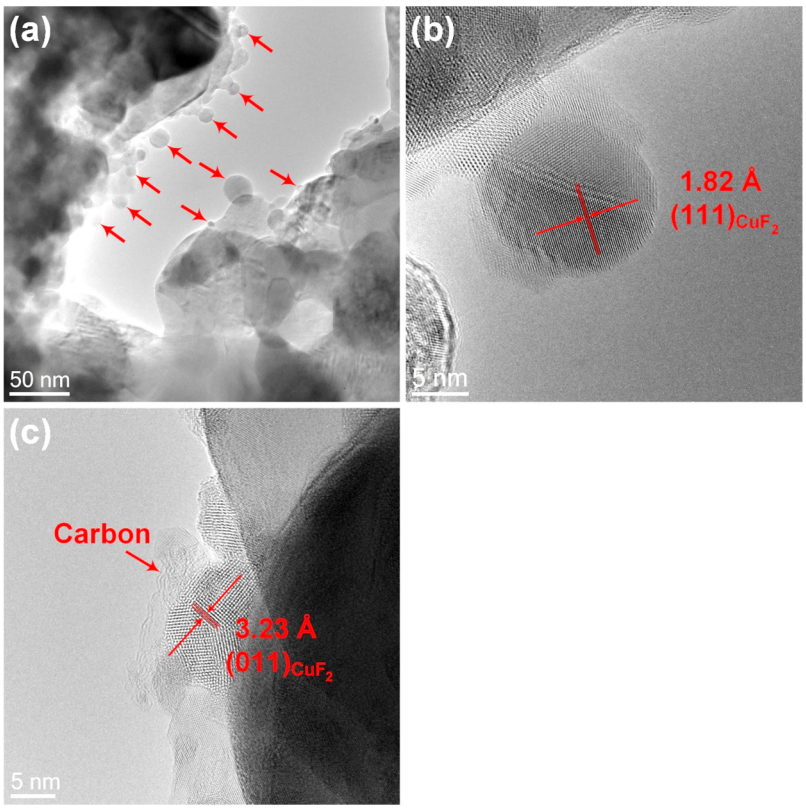

Figure 5-22: TEM and HRTEM images of cathode-electrolyte interface after failure.

Table 5-4: Lattice spacings of the Cu, CuF_2 and Cu_2O references and the values measured from FFTs.

Lattice plane	**Cu reference [Å]**	**Measured d-spacings [Å]**	**Reference angles [˚]**	**Measured angles [˚]**
100	2.89	2.87	(100) & (110)=45.00	(100) & (110)=44.80
110	2.05	2.06	(100) & (010)=90.00	(100) & (010)=90.30
010	2.89	2.87	(010) & (110)=45.00	(010) & (110)=45.50
Lattice plane	**CuF_2 reference [Å]**	**Measured d-spacings [Å]**	**Reference angles [˚]**	**Measured angles [˚]**
020	2.28	2.24	(020) & (12-2)=42.01	(020) & (12-2)=42.7
12-2	1.68	1.7	(020) & (10-2)=90	(020) & (10-2)=90.2
10-2	2.54	2.5	(10-2) & (12-2)=47.99	(10-2) & (12-2)=47.5
Lattice plane	**CuF_2 reference [Å]**	**Measured d-spacings [Å]**	**Reference angles [˚]**	**Measured angles [˚]**
010	4.57	4.5	(010) & (11-1)=54.27	(010) & (11-1)=54.7
11-1	2.67	2.56	(010) & (10-1)=90	(010) & (10-1)=89.9
10-1	3.28	3.16	(10-1) & (11-1)=35.73	(10-1) & (11-1)=35.2
Lattice plane	**Cu_2O reference [Å]**	**Measured d-spacings [Å]**	**Reference angles [˚]**	**Measured angles [˚]**
11-1	2.46	2.46	(11-1) & (001)=125.26	(11-1) & (001)=125.20
001	4.27	4.2	(11-1) & (111)=70.53	(11-1) & (111)=70.50
111	2.46	2.43	(111) & (001)=54.74	(111) & (001)=54.70

5.3.3 Discussion

The micron-sized fluoride ion batteries were prepared using a FIB system from Cu/$La_{0.9}Ba_{0.1}F_{2.9}$/MgF_2 full cell to study the electrochemical cycling *in situ* in the TEM. Before starting the *in situ* study, a micron-sized battery was cycled *ex situ*. The first charging curve of the *ex situ* studies of the micron-sized battery revealed two maxima. The first one around 2 V can be attributed to the formation of copper (I) oxide. The source of oxygen could be the carbon black added to the composite as well as performing most of the bulk battery preparation in air. The second maximum (or plateau) started at 2.77 V to 3.5 V and can be attributed to copper (II) fluoride formation. The potential is slightly higher than the theoretical potential of 2.71 V for the Cu/CuF_2 redox couple vs. MgF_2/Mg. Similar potentials were observed *ex situ* for the Cu/$La_{0.9}Ba_{0.1}F_{2.9}$/CeF_3 full battery system [192]. The initial discharging showed I-V characteristics for the reduction of the CuF_2 very similar to the charging and the total

conversion charge indicates a fairly complete reaction. However, at 2.85 V a short circuit developed, which prevented further controlled discharging of the battery.

The CV peaks measured during the *in situ* studies occur at voltages comparable to the *ex situ* studies. Two peaks were observed during the first *in situ* charging at around 2 V and 2.85 V on top of a strong background that could be due to a higher residual contamination during FIB preparation compared to the *ex situ* studied cell. Pt migration from the contacts cannot be ruled out, where the current was dominated by the short circuit during discharging with a minor peak around 2.7 V. During the second *in situ* charging, no characteristic CV peaks could be observed until the micron-sized battery fractured at the cathode-electrolyte interface. The fracture at the interface suggests an electrochemical reaction of the battery despite the strong leakage current. The fracture at the interface can be attributed to: 1) the volumetric change accompanied to the CuF_2 formation [6] and 2) the reduced free volume available to compensate the volume changes compared to the normal batteries due to the high pressure used in sample preparation. STEM-EDX and HRTEM analysis of the cathode-electrolyte interface confirmed the fluoride migration into the composite cathode forming copper (II) fluoride. Moreover, diffusion of Cu into the electrolyte was observed after cycling, presumably due to the volumetric changes associated with the copper fluorination. In addition, the HRTEM analysis confirmed the formation of Cu_2O after cycling. Formation of Cu oxide could lead to an inhomogeneous current density distribution in the cathode and, hence, a localized overheating that would favor the formation of voids and spherical particles. The same morphological changes and Cu diffusion into the electrolyte were observed for the thick part of the cathode-electrolyte interface as in the thin part indicating that the *in situ* observations are not strongly affected by the sample thickness.

On the other hand, no significant changes could be observed at the thin area of anode-electrolyte interface. Only, some volumetric changes leading to small cracks in the anode composite and at the anode-electrolyte interface were observed at the anode in the thick part. Moreover, the surface of the cycled anode was covered by small particles in agreement with previous reported *ex situ* results [239]. In those papers, the particles were identified as MgF_2 [240], considered to be formed as a result of the low ionic conductivity of the electrolyte leading to the fluoride migration on the surface [241].

Based on these observations, the development of an electrolyte with higher fluoride ion conductivity would be critical for solid-state fluoride batteries operating at RT. However, the protection of the electrode materials from oxidation could already lead to a significantly enhancement of the performance of the fluoride ion battery.

6 *Ex situ* TEM studies of fluoride ion battery

6.1 Introduction

A fluoride ion battery consisting of $CuF_2/La_{0.9}Ba_{0.1}F_{2.9}/C$ as a cathode, $La_{0.9}Ba_{0.1}F_{2.9}$ as an electrolyte, and a metallic La sheet as an anode was prepared. The morphology, structure, and composition were subsequently studied using *ex situ* TEM analysis. The working principle of the $CuF_2/La_{0.9}Ba_{0.1}F_{2.9}/La$ fluoride ion battery is oxidation of La during discharging resulting in the formation of LaF_3 via transport of fluoride ions through the electrolyte from the CuF_2 cathode. At the same time, the CuF_2 cathode is reduced to Cu metal. During charging, the reactions should be reversed with the Cu cathode oxidized to form CuF_2 while the fluorinated anode will be reduced La metal again.

The conversion reactions during discharging are:

Cathode reaction:	$CuF_2 + 2e^- \rightarrow Cu + 2F^-$	6.1
Anode reaction:	$La + 3F^- \rightarrow LaF_3 + 3e^-$	6.2
Cell:	$3\,CuF_2 + 2\,La \rightarrow 3\,Cu + 2\,LaF_3$	6.3

and during charging

Cathode reaction:	$Cu + 2F^- \rightarrow CuF_2 + 2e^-$	6.4
Anode reaction:	$LaF_3 + 3e^- \rightarrow La + 3F^-$	6.5
Cell:	$3\,Cu + 2\,LaF_3 \rightarrow 3\,CuF_2 + 2\,La$	6.6

The battery system has been studied in three different states: as-prepared, discharged, and recharged. The electrochemical cells were prepared as three-layer pellets by compacting the powders for the cathode and the electrolyte with a La sheet as anode. Fabrication of all electrode materials and construction of the electrochemical cells was carried out inside an argon-filled glove box. The electrolyte thickness was around 450 μm, the cathode thickness about 30-45 μm and the La sheet thickness around 180 μm (Figure 6-1). The as-received La foil was manually polished to remove the oxide layer covering the surface prior to the assembly in the cell. The cells were compacted using a Perkin Elmer desktop hand-press. The resulting battery pellets had a diameter of 10 mm and a thickness of approx. 0.7 mm. These samples were used for *ex situ* TEM analysis. One battery was only discharged, while another pellet was discharged and then charged (one complete cycle). The discharging and charging was

controlled galvanometrically to evaluate the electrochemical performance of the cells. The third battery remained in the as-prepared charged state.

The Strata FIB was used for the preparation of two TEM lamellae from each battery across both electrode-electrolyte interfaces using the standard preparation techniques described in chapter 3. The FEI Titan 80-300 microscope with aberration corrector (for imaging) operated at an accelerating voltage of 300 kV was used for TEM analysis. The structure and chemistry of the electrodes before cycling, after discharging and after recharging were characterized using TEM, STEM, SAED, and EDX to understand the changes and relate them to the electrochemical performance of the fluoride ion battery.

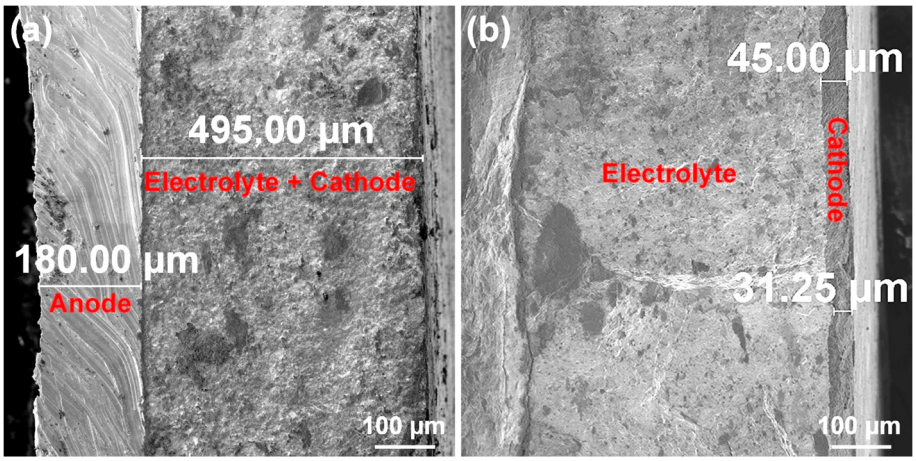

Figure 6-1: SEM images of the cell cross-section focusing on (a) anode side & (b) cathode side.

6.2 Electrochemical study

Galvanometric discharging and recharging of the fluoride ion batteries was performed at an elevated temperature of 150 °C to enhance the ionic conductivity of the electrolyte from approx. 2×10^{-6} S cm^{-1} at RT to approx. 2.8×10^{-4} S cm^{-1} [233]. The group of Maximilian Fichtner performed the electrochemical studies at the KIT. As the cathode consists of CuF_2, the as-prepared cells are in the charged state. Therefore, cycling was started by discharging the as-prepared cell. The discharging was done by applying a current density of -4 mA g^{-1} (10 mA cm^{-2}) with a 1 V cut off potential and for charging current density of +4 mA g^{-1} was applied at a voltage up to 3.6 V. The specific capacity was calculated based on the limiting active material, in this case the CuF_2 cathode.

Figure 6-2 shows the cell voltage plotted vs. the specific capacity for the first discharge, first recharge, and second discharge. The open circuit voltage (OCV) of the as-prepared cell was

measured to be 2.9 V, and the voltage decreased slowly during discharging. The discharge process seems to be characterized by a single voltage plateau corresponding to the reduction of Cu^{2+} to Cu^{0} in the cathode. The specific capacity obtained for the first discharge to 1 V was 360 mAh g^{-1}. This value is below the theoretical specific capacity of the Cu/CuF_2 cathode (528 mAh g^{-1} [237]), indicating an incomplete reaction. The specific capacity obtained for the first recharging to 3.6 V was only 270 mAh g^{-1}. The charging curve exhibits two slightly separated voltage plateaus, suggesting two reactions. The first voltage plateau around 3.25 V may correspond to the reaction of Cu^{0} to Cu^{1+}, while the second plateau around 3.55 V probably corresponds to the reaction of Cu^{1+} to Cu^{2+}. The specific capacity was strongly reduced in the second cycle, where the capacity of the second discharge to 1 V was only 165 mAh g^{-1} (only 46% of the first discharge capacity). The significant decrease of the capacity indicates significant irreversible reactions. TEM analysis was performed to understand the reactions during the first discharging and first recharging and to identify some of the reasons for the capacity fading.

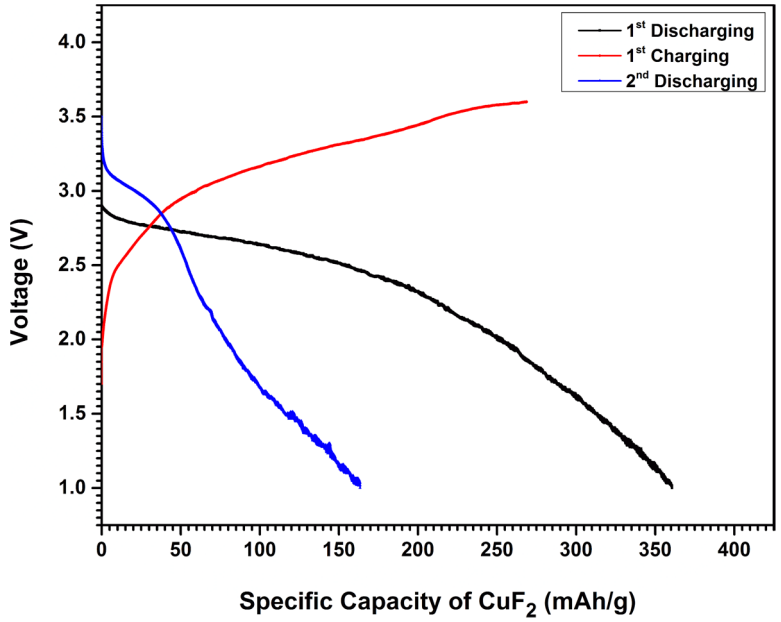

Figure 6-2: Specific capacity of the $CuF_2/La_{0.9}Ba_{0.1}F_{2.9}/La$ battery during galvanostatic testing. The voltage/capacity plots were obtained at 150 °C with a current density of 10 mA cm^{-2}.

6.3 Cathode-electrolyte interface

6.3.1 Scanning transmission electron microscopy-energy dispersive X-ray analysis

STEM images and STEM-EDX maps at the cathode-electrolyte interface of the as-prepared, discharged and recharged cells are shown in Figure 6-3, Figure 6-4, and

Figure 6-5. The STEM-EDX maps reveal that the cathode composite consists of finely disperse nanosized particles. Moreover, the Cu particles are homogeneously distributed in the cathode composite. This homogeneity is the result of using ball milling for a long time of 12h. Rietveld refinement of the XRD analysis of the $La_{0.9}Ba_{0.1}F_{2.9}$ revealed an average particles size of around 19 nm. For the CuF_2 composite mixed with $La_{0.9}Ba_{0.1}F_{2.9}$ electrolyte and carbon black, the pattern looks similar to that of $La_{0.9}Ba_{0.1}F_{2.9}$, but the peaks are slightly broader than those of $La_{0.9}Ba_{0.1}F_{2.9}$ due to the formation of smaller crystallites.

The fluoride maps reveal the fluoride distribution around the interface and in the cathode composite. While the fluoride signal in the cathode composite cannot be separated into the CuF_2 (30 wt%) and the electrolyte (60 wt%) contribution, the overall fluoride signal clearly decreased after discharging compared to the as-prepared charged cell. This decreased fluoride signal is a confirmation for the migration of fluoride ions from the cathode to the anode through the electrolyte, and hence the formation of Cu metal in the cathode and lanthanum fluoride at the anode sheet. After recharging, the fluoride concentration in the cathode increased, indicating some reversible reaction (equation 6.6). However, the extracted EDX profiles from the cathode side reveal that the fluoride intensity in the recharged cell is lower compared to the as-prepared cell (Figure 6-6). This fits to the electrochemical characterization, where the reduced capacity during recharging indicated already that the reactions are not completely reversed. As will be discussed in detail for the anode-electrolyte interface, one of the reasons for the irreversible reaction and hence the capacity fading are oxides at the cathode and their reactions.

Even though the cathode consists of 60 wt% electrolyte ($La_{0.9}Ba_{0.1}F_{2.9}$), 30 wt% CuF_2 and 10 wt% carbon black, the O-map reveals significant amounts of oxygen in the cathode. The origin of oxygen in the cathode materials can presumably be attributed to minor amounts of water in the carbon black that was added to the cathode composite to enhance the electronic conductivity [192] and/or oxidation during ball milling of the composite that has been performed outside the glove box. This significant oxide formation is probably one of the reasons for the reduced capacity during initial discharging compared to the theoretical capacity.

The Cu-maps of the as-prepared (Figure 6-3) and the discharged cells (Figure 6-4) only exhibit Cu in the cathode itself. However, Cu diffusion from the cathode into the electrolyte is noticeable in the Cu-map of the recharged cell (Figure 6-5). This diffusion is presumably related to the strong volume change accompanying the Cu/CuF_2 reaction in combination with the porosity of the ball milled electrolyte [192]. During discharging, where the fluoride ions migrate from the CuF_2 cathode to the La anode, the volume shrinks and hence there is no Cu diffusion

into the electrolyte. However, during charging the volume will increase again locally leading to Cu diffusion into the pores of the electrolyte to compensate this volume change. Diffusion of Cu cations into the electrolyte may increase the electronic conductivity of the electrolyte [243] and could be partially responsible for the performance degradation of the cell. More Cu diffusion into the electrolyte is expected during the following cycles and, hence, fading in the discharge capacities.

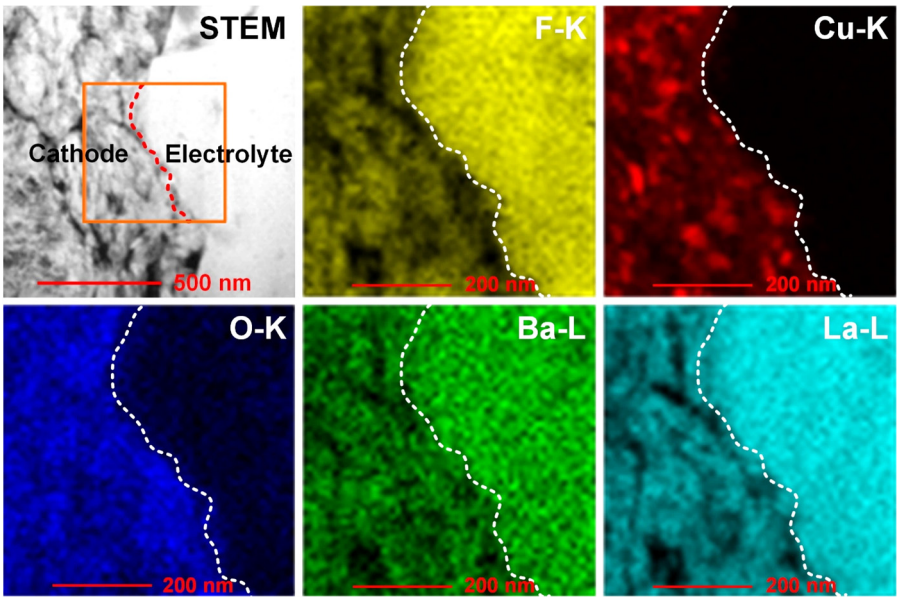

Figure 6-3: STEM-EDX map of the cathode-electrolyte interface of the as-prepared cell.

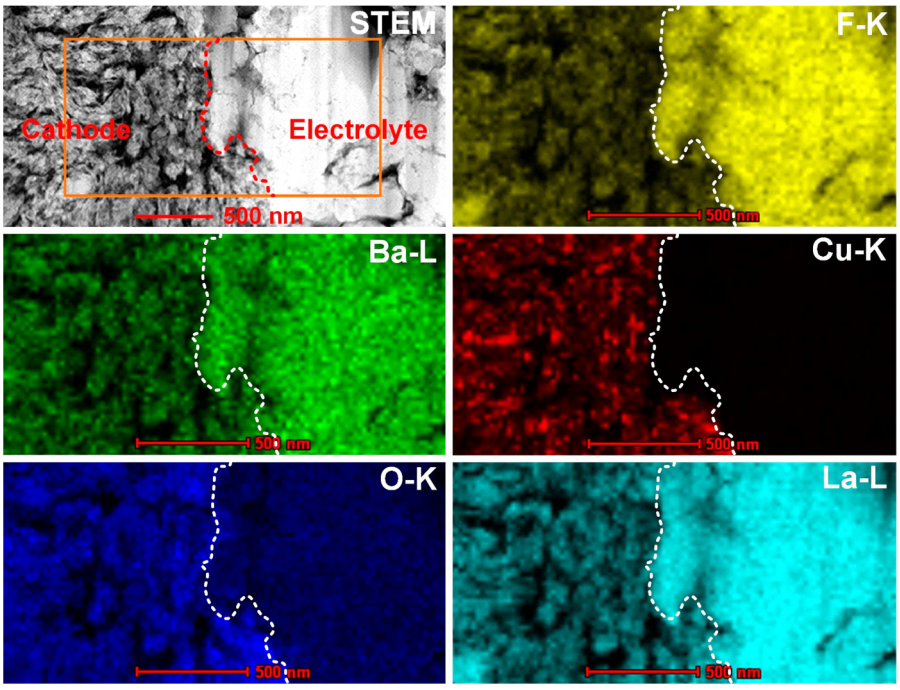

Figure 6-4: STEM-EDX map of the cathode-electrolyte interface after discharging.

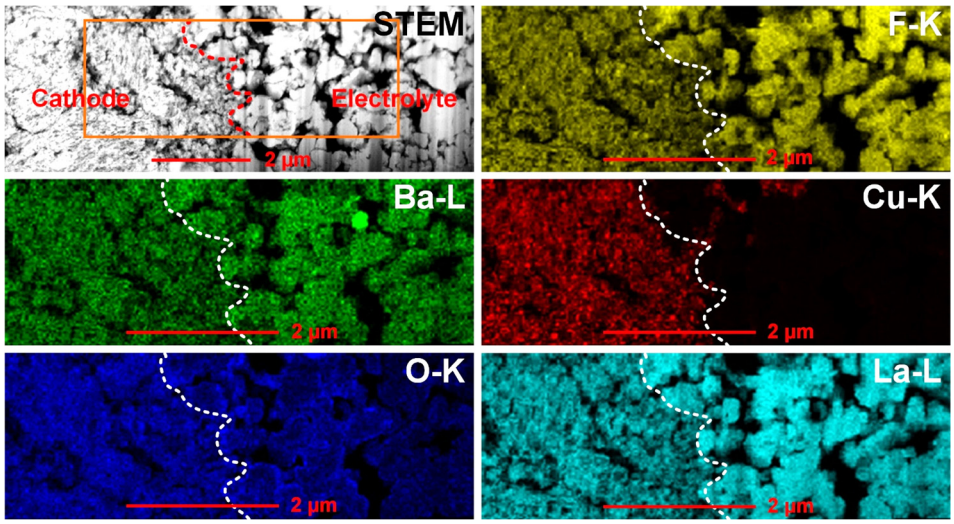

Figure 6-5: STEM-EDX map of the cathode-electrolyte interface after recharging.

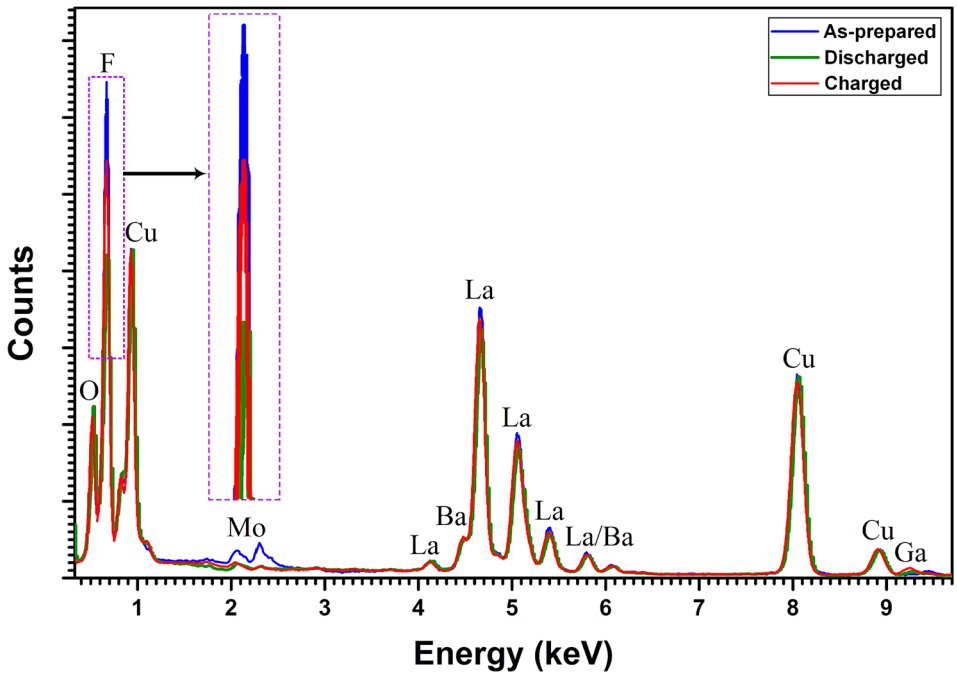

Figure 6-6: Integrated EDX spectra of the cathode.

6.3.2 Bright field and high resolution transmission electron microscopy analysis

BF-TEM images have been used to characterize the crystal structure of as-prepared electrolyte and as-prepared cathode composite materials. Figure 6-7a shows a low magnification TEM image of the as-prepared electrolyte, revealing that the electrolyte materials consist of nanocrystallites of 10-20 nm size range. The cathode composite consists of slightly smaller nanocrystallites (Figure 6-7b), in good agreement with the XRD results.

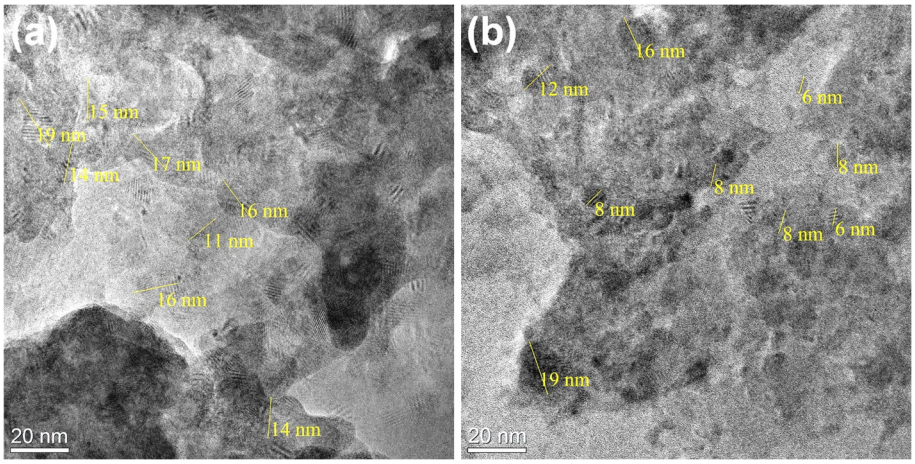

Figure 6-7: BF-TEM images of (a) as-prepared electrolyte and (b) as-prepared cathode.

HRTEM images have been used to further characterize the crystal structure of the materials in the cathode. Figure 6-8 shows the HRTEM images and the corresponding FFTs of cathode material of the as-prepared cell. The TEM images confirm the high crystallinity of the cathode. The presence of CuF_2 and $La_{0.9}B_{0.9}F_{2.9}$ can be confirmed from the HRTEM images. The lattice spacings of a CuF_2 particle calculated from the FFT are in good agreement with the monoclinic phase of copper fluoride (a=3.309 Å, b=4.569 Å, c=5.362 Å, α=90.0, β=121.11, γ=90.0) [ICSD-9788], in the specific case in Figure 6-8a imaged in a [212] zone axis. While the lattice spacings of the electrolyte phase ($La_{0.9}B_{0.9}F_{2.9}$) are in good agreement with the hexagonal LaF_3 phase (a=b=7.185 Å, c=7.351 Å, α=β=90.0, γ=120.0) [ICSD-35673]. The measured lattice spacings for CuF_2 and $La_{0.9}B_{0.9}F_{2.9}$ are compared to reference values in Table 6-1. Moreover, copper oxide crystals were also detected by HRTEM. The HRTEM images reveal two different copper oxide phases, CuO and Cu_4O_3. Figure 6-9 shows the HRTEM images and the corresponding FFT of CuO and Cu_4O_3. The lattice spacings of the CuO particle calculated from FFT are in good agreement with the monoclinic phase of copper (II) oxide (a=4.7162 Å, b=3.3582 Å, c=5.1126 Å, α=90.0, β=100.53, γ=90.0) [ICSD-628618]. The lattice spacings of the Cu_4O_3 crystal are in good agreement with Paramelaconite copper oxide, which it is a tetragonal phase (a=b=5.837 Å, c=9.932 Å, α=β=γ=90.0) [ICSD-100566]. Table 6-2 contains the measured lattice spacings for CuO and Cu_4O_3 compared to the reference structures.

The Paramelaconite Cu_4O_3 phase is a metastable copper oxide with an intermediate stoichiometry between copper (II) oxide (CuO) and copper (I) oxide (Cu_2O) [244, 245], where half of the Cu ions are in the "+1" oxidation state while the other half are in the "+2" oxidation state (Cu_2^{1+} Cu_2^{2+} O_3) [246]. Oxidation of Cu_2O can lead into the formation of Paramelaconite.

However, pure Cu_4O_3 is hard to synthesize in bulk form. Otherwise, it is also known that decomposition of copper (II) oxide (CuO) under the electron beam can produce Cu_4O_3 in small amounts [247]. The group of Maximilian Fichtner has used XPS to analyse the electrode and confirmed the presence of both Cu^{1+} and Cu^{2+}.

The formation of copper oxide is negatively affecting the specific capacity, which is calculated with the assumption of all copper present as copper fluoride in the cathode. Furthermore, the metallic copper formed after discharging can react with additional copper (II) oxide to form copper (I) oxide.

$$CuO + Cu \rightarrow Cu_2O \qquad 6.7$$

The formation of copper oxide after discharging will decrease the available copper for fluorination during recharging and hence result in a fading of the cell capacity. This is contributing to the capacity fading from 360 mAh g^{-1} for the first discharge to only 165 mAh g^{-1} for the second discharge.

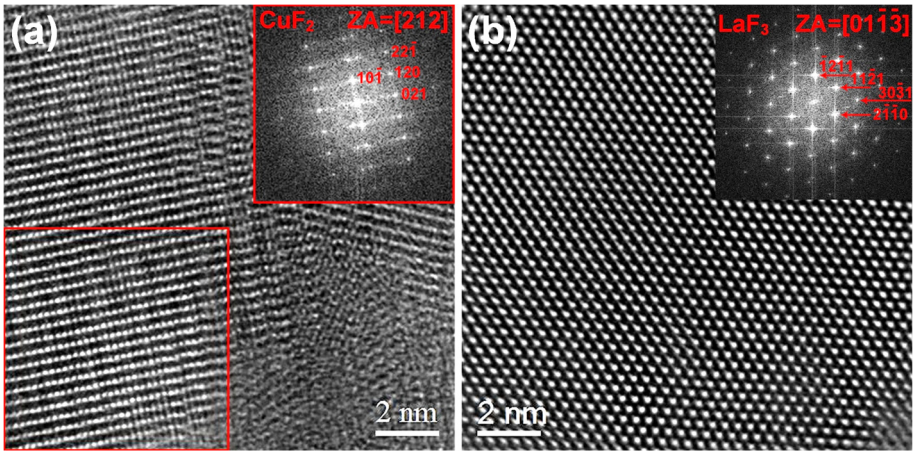

Figure 6-8: HRTEM images and the corresponding FFTs of fluorides in the as-prepared cathode. The images have been filtered using the HRTEM-filter script (D. R. G. Mitchell, v2.0, Jan 14).

Table 6-1: Lattice spacings of the CuF_2 & LaF_3 references and the values measured from FFTs.

Lattice plane	**CuF_2 reference [Å]**	**Measured d-spacings [Å]**	**Reference angles [˚]**	**Measured angles [˚]**
10-1	3.29	3.30	(10-1) & (021)=92.98	(10-1) & (021)=90
021	2.05	2.06	(10-1) & (120)=60.27	(10-1) & (120)=60
120	1.78	1.80	(021) & (120)=32.71	(021) & (120)=30
Lattice plane	**LaF_3 reference [Å]**	**Measured d-spacings [Å]**	**Reference angles [˚]**	**Measured angles [˚]**
-12-11	3.23	3.22	(-12-11) & (11-21)=53.39	(-12-11) & (11-21)=54
11-21	3.23	3.24	(-12-11) & (30-31)=83.15	(-12-11) & (30-31)=84
30-31	1.996	2.00	(11-21) & (30-31)=29.76	(11-21) & (30-31)=30

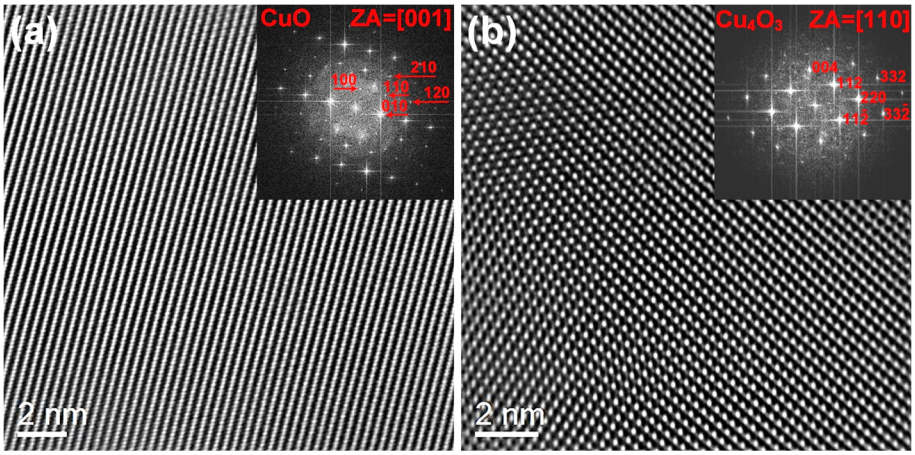

Figure 6-9: HRTEM images and the corresponding FFTs of copper oxides in the as-prepared cathode. The images have been filtered using the HRTEM-filter script (D. R. G. Mitchell, v2.0, Jan 14).

Table 6-2: Lattice spacings of the CuO & Cu_4O_3 references and the values measured from FFTs.

Lattice plane	**CuO reference [Å]**	**Measured d-spacings [Å]**	**Reference angles [˚]**	**Measured angles [˚]**
100	4.64	4.58	(100) & (110)=54.09	(100) & (110)=53.5
110	2.72	2.77	(100) & (010)=90	(100) & (010)=90
010	3.36	3.4	(110) & (010)=35.91	(110) & (010)=36.5
Lattice plane	**Cu_4O_3 reference [Å]**	**Measured d-spacings [Å]**	**Reference angles [˚]**	**Measured angles [˚]**
004	2.48	2.52	(004) & (112)=50.27	(004) & (112)=51
112	3.17	3.23	(004) & (11-2)=50.27	(004) & (11-2)=50
11-2	3.17	3.23	(112) & (11-2)=79.46	(112) & (11-2)=79

HRTEM image of the cathode after discharging and the corresponding FFT are shown in Figure 6-10. The HRTEM image confirm the fluoride migration by the formation Cu metal. The lattice spacings calculated from the FFT (Table 6-3) are in good agreement with fcc copper metal (a=b=c=3.61 Å, α=β=γ=90.0) [ICSD-53755]. The calculated unit cell volume of Cu is 47.05 $Å^3$, while the calculated unit cell volume of CuF_2 is 69.41 $Å^3$. Therefore, the defluorination process of CuF_2 is accompanied by a strong volume shrinkage in the cathode, whereas the fluorination is accompanied by the corresponding increase. Figure 6-11 shows HRTEM images of the cathode after recharging and the corresponding FFTs patterns. The images indicate the formation of monoclinic CuF_2 after recharging (Table 6-4), but some unreacted CuF_2 from the as-prepared cathode cannot be excluded.

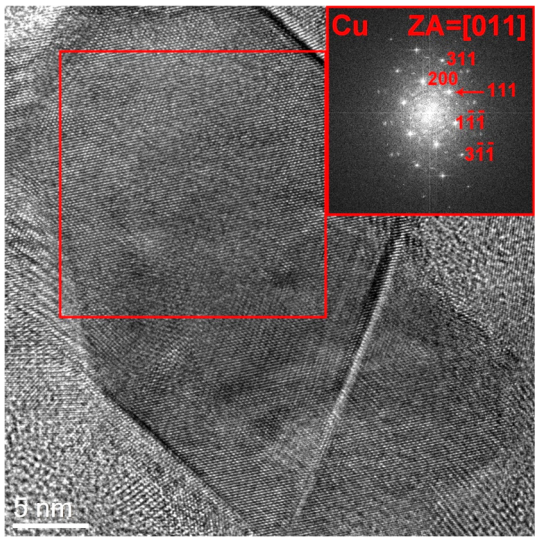

Figure 6-10: HRTEM images and the corresponding FFT of the discharged cathode.

Table 6-3: Lattice spacings of the Cu reference and the values measured from FFT.

Lattice plane	Cu reference [Å]	Measured d-spacings [Å]	Reference angles [°]	Measured angles [°]
200	1.81	1.8	(200) & (111)=54.74	(200) & (111)=54.5
111	2.08	2.1	(200) & (1-1-1)=54.74	(200) & (1-1-1)=55.5
1-1-1	2.08	2.1	(111) & (1-1-1)=70.53	(111) & (1-1-1)=70

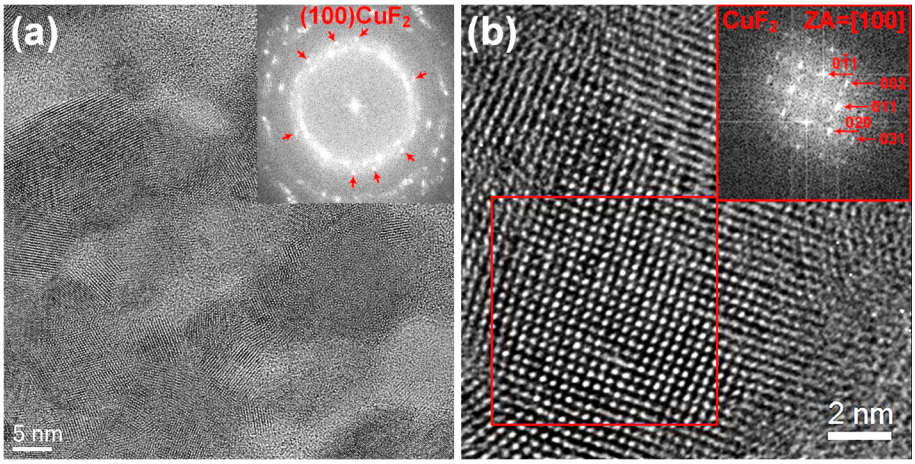

Figure 6-11: HRTEM images and the corresponding FFTs of the recharged cathode.

Table 6-4: Lattice spacings of the CuF_2 reference and the values measured from FFT.

Lattice plane	CuF_2 reference [Å]	Measured d-spacings [Å]	Reference angles [˚]	Measured angles [˚]
0-11	3.24	3.3	(0-11) & (002)=45.14	(0-11) & (002)=43.5
002	2.3	2.4	(0-11) & (011)=90.28	(0-11) & (011)=91
011	3.24	3.3	(002) & (011)=45.14	(002) & (011)=47.5

6.4 Anode-electrolyte interface

While the analysis of the cathode close to the electrolyte interface revealed a partially reversible fluorination reaction during cycling, no side reaction leading to the observed capacity fading were detected at the cathode. The anode-electrolyte interface is studied to see if reasons leading to the observed capacity fading can be detected there.

6.4.1 As-prepared cell

Figure 6-12 shows a STEM image of the as-prepared anode-electrolyte interface. The STEM image reveals the formation of an intermediate layer between the La sheet anode and the $La_{0.9}Ba_{0.1}F_{2.9}$ electrolyte (referred to as (1)). The thickness of this layer is around 1–2 μm. STEM-EDX compositional analysis of this layer (Figure 6-13) shows that it consists of La, O and some F. The fluoride concentration is gradually decreasing from the electrolyte to the anode while the oxygen concentration in this layer is fairly homogeneous. The absence of Ba in this layer shows that it is part of the original La sheet, presumably an oxide layer present on the

surface, which was not fully removed prior to cell assembly. The decreasing F concentration indicates that already during assembly of the cell fluoride diffuses from the electrolyte into the anode.

A SAED pattern taken from layer (1) is shown in Figure 6-14a. The SAED profile of layer (1) is compared to reference patterns for La, La_2O_3, and LaF_3 in Figure 6-14b. It is difficult to confirm the different materials present, because of the strong peak overlap of the reference patterns and the broad signals. Nevertheless, the pattern matches reasonably well with a mixture of La, La_2O_3 and LaF_3. Local HRTEM analysis (Figure 6-15) confirms the presence of La_2O_3 and LaF_3. For example, the measured lattice spacings in Figure 6-15a match well to the hexagonal LaF_3 while the measured lattice spacings in Figure 6-15b fit well to the cubic La_2O_3 phase (a=b=c=11.327 Å, α=β=γ=90.0) [ICSD-641600]. Table 6-5 compares the measured lattice spacings with LaF_3 and La_2O_3 references. This means that fluoride ions diffused into the partially oxidized layer and reacted with the residual La to form LaF_3. Furthermore, the presence of some oxyfluorides cannot be excluded.

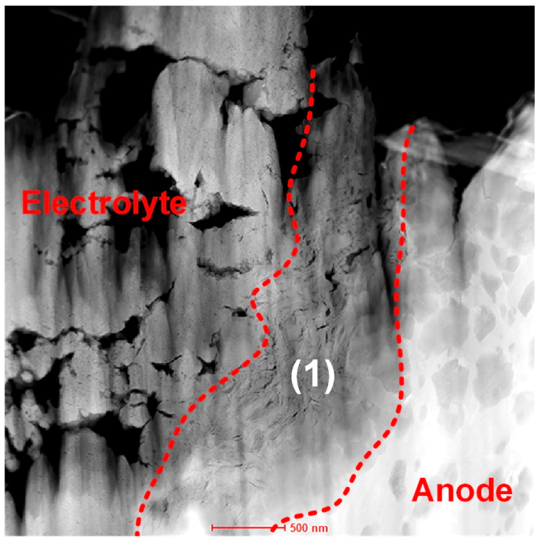

Figure 6-12: HAADF-STEM image of the anode-electrolyte interface of the as-prepared cell.

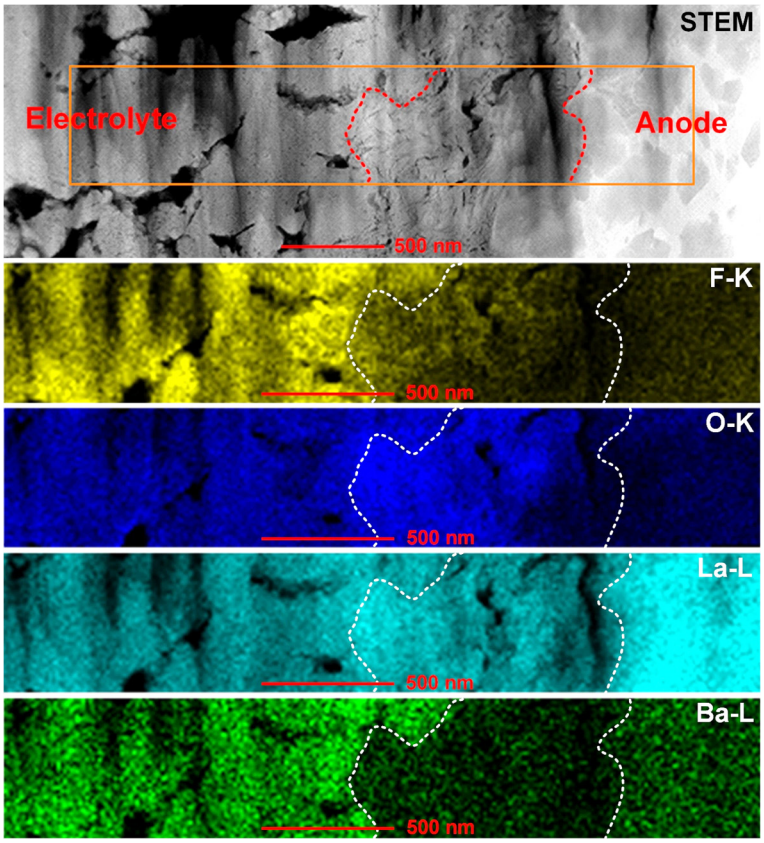

Figure 6-13: STEM-EDX map of the anode-electrolyte interface of the as-prepared cell.

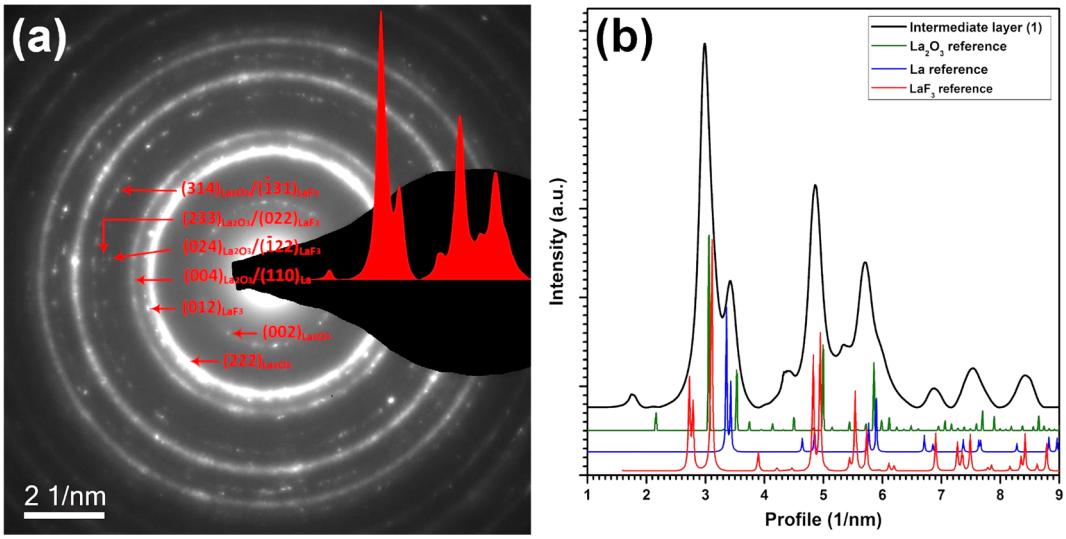

Figure 6-14: (a) SAED pattern of the intermediate layer (1) of the as-prepared cell and (b) corresponding SAED profile vs. the references.

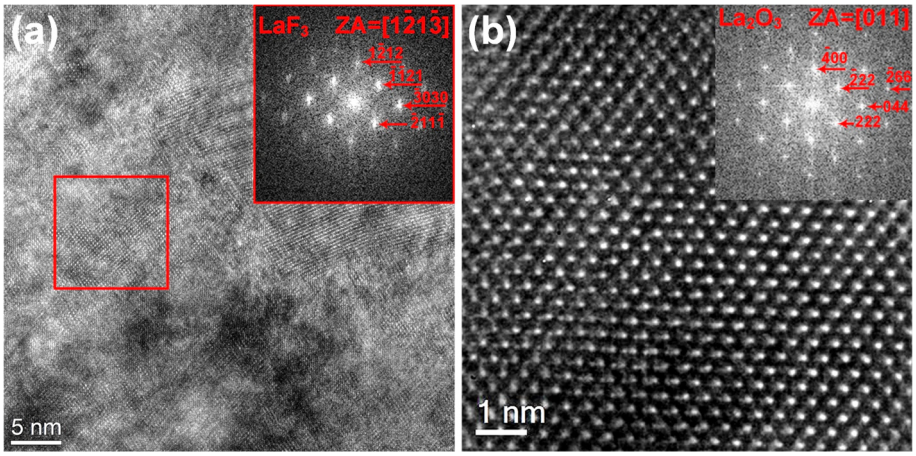

Figure 6-15: HRTEM images and corresponding FFTs at the intermediate layer of the as-prepared cell. The images have been filtered using the HRTEM-filter script (D. R. G. Mitchell, v2.0, Jan 14).

Table 6-5: Lattice spacings of the LaF_3 & La_2O_3 references and the values measured from FFTs.

Lattice plane	**LaF_3 reference [Å]**	**Measured d-spacings [Å]**	**Reference angles [˚]**	**Measured angles [˚]**
1-212	2.57	2.46	(1-212) & (-1-121)=51.09	(1-212) & (-1-121)=51.00
-1-121	3.23	3.2	(1-212) & (-211-1)=51.09	(1-212) & (-211-1)=50.50
-211-1	3.23	3.2	(-211-1) & (-1-121)=77.83	(-211-1) & (-1-121)=78.50
Lattice plane	**La_2O_3 reference [Å]**	**Measured d-spacings [Å]**	**Reference angles [˚]**	**Measured angles [˚]**
-400	2.83	2.88	(-400) & (-222)=54.74	(-400) & (-222)=54.5
-222	3.27	3.3	(-400) & (222)=54.74	(-400) & (222)=54
222	3.27	3.3	(-222) & (222)=70.53	(-222) & (222)=71.5

6.4.2 Discharged cell

A STEM image of the anode-electrolyte interface of the discharged cell is shown in Figure 6-16. The STEM image reveals the formation of a new layer between the electrolyte and the La-sheet anode, referred to as (2) in Figure 6-16. The thickness of the newly formed layer is similar to the thickness of layer (1) that was formed during cell fabrication.

STEM-EDX analysis (Figure 6-17) reveals that layer (2) contains fluoride and oxygen beside La. In contrast of the first layer, the oxygen and fluoride distribution is patchy, with the fluoride distribution representing the local electrochemical reactions. The variation of the oxygen in layer (2) might be due to some variation of the original oxide thickness. Surprisingly, the fluoride concentration in layer 1 did not increase during cycling, indicating that this layer

is not participating in the electrochemical cycling. Nevertheless, the fluoride ion mobility of the La/LaF_3/La_2O_3 composite in layer (1) is apparently sufficiently high to allow the electrochemical reaction with the La sheet underneath leading to the locally high fluoride concentration in layer (2). The thickness of the fluorinated layer differs significantly from one area to another in the same discharged cell as shown in Figure 6-16. A layer thickness of around 7 μm would be expected for the experimentally measured 68% conversion during the first discharging based on the composition and thickness of the as-prepared CuF_2 electrode. This fits to the thicker experimentally observed layer (Figure 6-18), but a detailed comparison is not possible with the strong local variations and the limited statistics in the TEM. However, with the La sheet as anode the missing porosity and the limited ionic and electric conductivity of the formed lanthanum fluoride layer have to be expected to limit the electrochemical reaction [248–250].

A SAED pattern taken from the oxygen rich part of layer (2) is shown in Figure 6-19a. The SAED corresponds to a larger La_2O_3 single crystal, imaged in [011] orientation. Table 6-6 compares the measured lattice spacings from Figure 6-19a with the La_2O_3 reference. A SAED pattern taken from an area containing both oxygen and fluoride (Figure 6-19b) fits the presence of La_2O_3, LaF_3 and potentially also LaOF, but because of the similar lattice spacings of the materials, it is not possible to clearly identify the different phases by SAED. Table 6-7 compares the measured lattice spacings from Figure 6-19b with the La_2O_3, LaF_3 and LaOF references. HRTEM images from different parts in layer 2 confirmed the presence of cubic La_2O_3 and hexagonal LaF_3 after discharging (Figure 6-20). The measured lattice spacings of LaF_3 match well to the hexagonal phase ($a=b=7.185$ Å, $c=7.351$ Å, $\alpha=\beta=90.0$, $\gamma=120.0$) [ICSD-35673]. Table 6-8 summarizes the observed reflections of La_2O_3 and LaF_3 from the area containing both oxygen and fluoride.

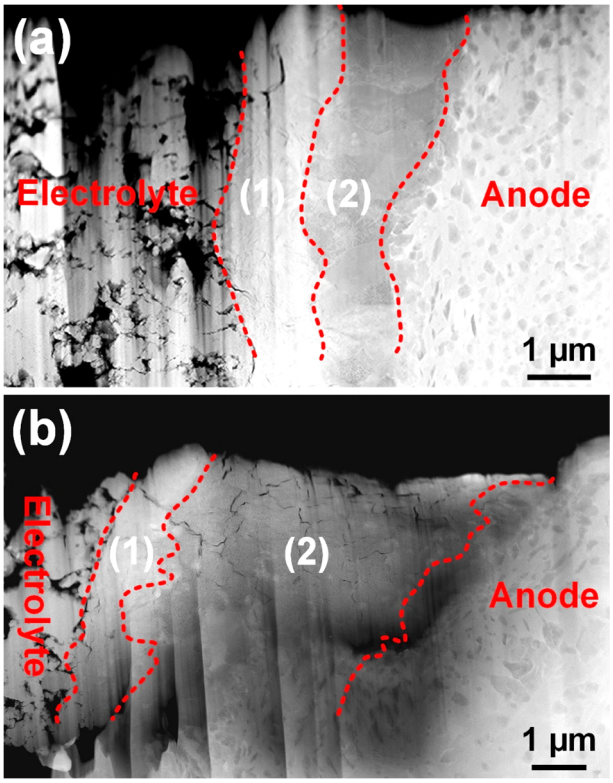

Figure 6-16: HAADF-STEM images of the anode-electrolyte interface of the discharged cell: (a) thin fluorinated layer, (b) thick fluorinated layer.

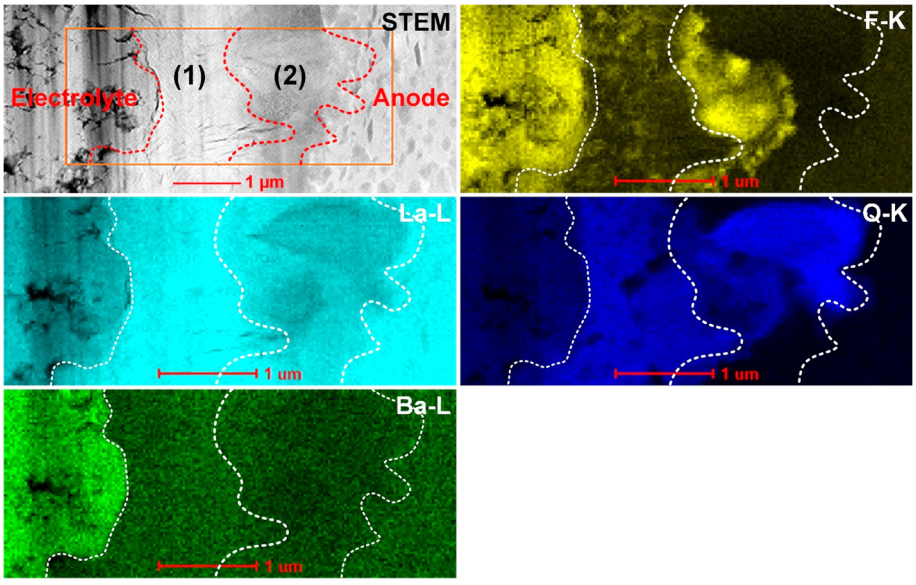

Figure 6-17: STEM-EDX map of the anode-electrolyte interface of the discharged cell.

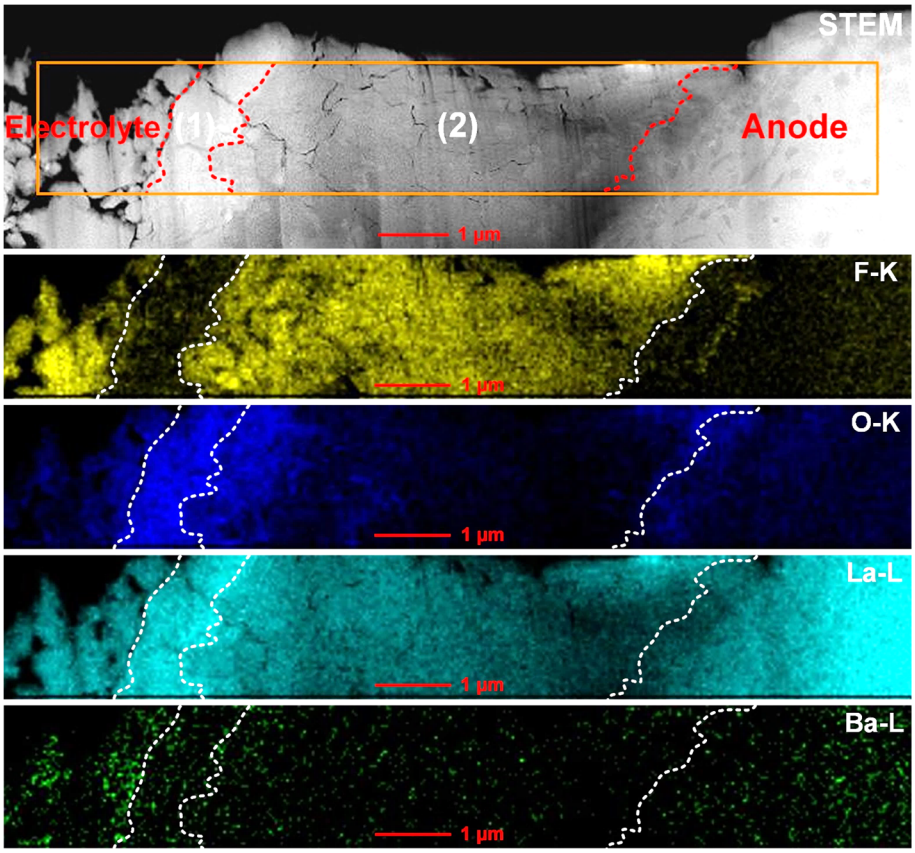

Figure 6-18: STEM-EDX map of the anode-electrolyte interface of the discharged cell (another lamella).

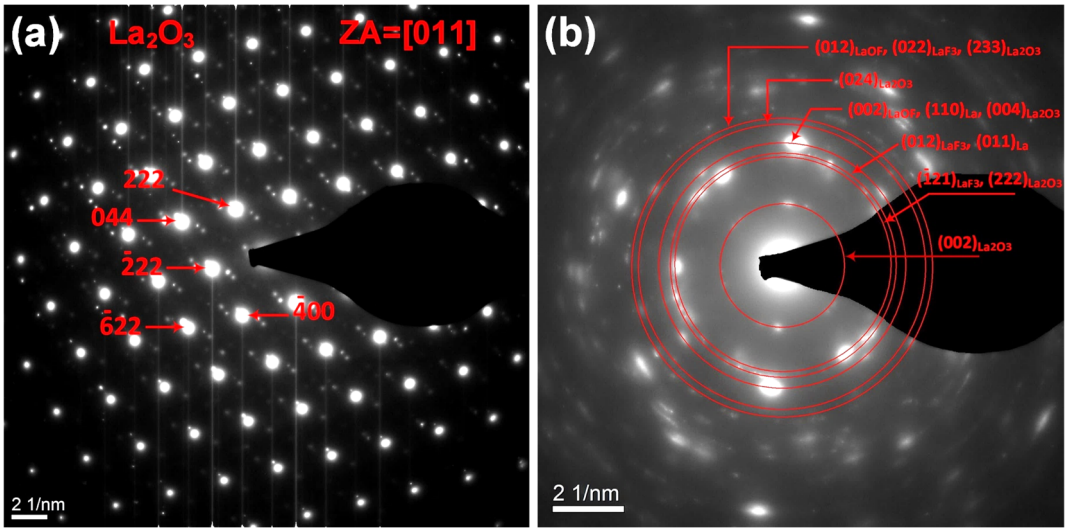

Figure 6-19: SAED patterns of layer (2) after discharging, (a) from area with high oxygen content, and (b) from area with a both oxygen and fluoride present.

Table 6-6: Lattice spacings of the La_2O_3 reference and the values measured from SAED pattern (Figure 6-19a) of layer (2) after discharging.

Lattice plane	La_2O_3 reference [Å]	Measured d-spacings [Å]	Reference angles [˚]	Measured angles [˚]
222	3.27	3.22	(222) & (044)=35.26	(222) & (044)=35.5
044	2	1.98	(222) & (-222)=70.53	(222) & (-222)=71
-222	3.27	3.22	(044) & (-222)=35.26	(044) & (-222)=35.5

Table 6-7: Lattice spacings of the LaF_3, LaOF & La_2O_3 references and the values measured from SAED pattern (Figure 6-19b) of layer (2) after discharging.

Lattice plane	References [Å]	Measured d-spacings [Å]
$(002)_{La2O3}$	$5.66_{(La2O3)}$	5.64
$(-121)_{LaF3}$, $(222)_{La2O3}$	$3.23_{(LaF3)}$, $3.27_{(La2O3)}$,	3.29
$(012)_{LaF3}$, $(011)_{La}$	$3.16_{(LaF3)}$, $3.15_{(La)}$	3.15
$(004)_{La2O3}$, $(110)_{La}$, $(002)_{LaOF}$	$2.83_{(La2O3)}$, $2.92_{(La)}$, $2.92_{(LaOF)}$,	2.90
$(024)_{La2O3}$	$2.53_{(La2O3)}$	2.48
$(233)_{La2O3}$, $(022)_{LaF3}$, $(012)_{LaOF}$	$2.41_{(La2O3)}$, $2.37_{(LaF3)}$, $2.37_{(LaOF)}$,	2.36

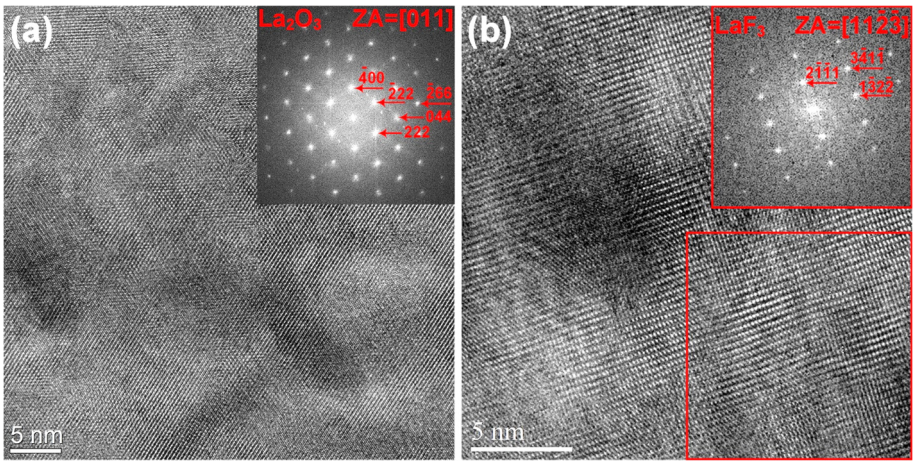

Figure 6-20: HRTEM images and corresponding FFTs of layer (2) after discharging from an area with a both oxygen and fluoride present. The images have been filtered using the HRTEM-filter script (D. R. G. Mitchell, v2.0, Jan 14).

Table 6-8: Lattice spacings of the La_2O_3 & LaF_3 references and the values measured from FFTs.

Lattice plane	**La_2O_3 reference [Å]**	**Measured d-spacings [Å]**	**Reference angles [˚]**	**Measured angles [˚]**
-400	2.83	2.92	(-400) & (-222)=54.74	(-400) & (-222)=56
-222	3.27	3.34	(-400) & (222)=54.74	(-400) & (222)=54
222	3.27	3.34	(-222) & (222)=70.53	(-222) & (222)=70
Lattice plane	**LaF_3 reference [Å]**	**Measured d-spacings [Å]**	**Reference angles [˚]**	**Measured angles [˚]**
2-1-11	3.23	3.24	(2-1-11) & (1-32-2)=89.37	(2-1-11) & (1-32-2)=89.5
1-32-2	1.98	2.00	(2-1-11) & (3-41-1)=58.00	(2-1-11) & (3-41-1)=58.5
3-41-1	1.68	1.72	(1-32-2) & (3-41-1)=31.37	(1-32-2) & (3-41-1)=32

6.4.3 Recharged cell

A STEM image of the anode-electrolyte interface of the recharged cell is shown in Figure 6-21. The STEM image reveals only one layer at the anode-electrolyte interface. The thickness of that layer varies around 1.5-3 μm, which is approximately the sum of layers 1 and 2 in the discharged cell, indicating that the electrochemical reaction resulted in the formation of a combination of the two layers. However, STEM-EDX analysis (Figure 6-22) still reveals significant compositional difference in this layer. The area corresponding to layer (1) in the discharged state has a high fluoride content, whereas the area corresponding to layer (2) in the discharged state has a low fluoride concentration with local patches with a high oxygen concentration. This indicates that the LaF_3 formed during discharging (as evident by the high fluoride concentration observed in layer 2) has been (partially) reduced to La with the fluoride migrating towards the cathode during recharging. However, the fluoride content in layer 1 is increased, indicating a chemical reaction in this region during recharging. SAED patterns and HRTEM images were acquired to better understand the reaction in this region during recharging. A SAED pattern taken from that area is shown in Figure 6-23. It can be indexed as LaOF, indicating that the lanthanum oxide reacted with the fluoride initially present as LaF_3 to form an oxyfluoride. In addition, Figure 6-24 shows HRTEM images acquired from that layer, which reveal that there is also still some LaF_3 and La_2O_3 present in addition to LaOF. The LaOF phase is a tetragonal phase with a=b=4.091 Å, c=5.836 Å [ICSD-76427]. The formation of lanthanum (III) oxyfluoride during recharging and any LaF_3 trapped at the anode decrease the amount of fluoride available at the copper cathode and hence, (partially) explains the fading of the cell capacity from 360 mAh g^{-1} for the first discharge to only 165 mAh g^{-1} for

the second discharge. Table 6-9 compares the lattice spacings of LaOF phase measured from SAED and the lattice spacings of LaF_3, LaOF, and La_2O_3 measured from FFTs with the references.

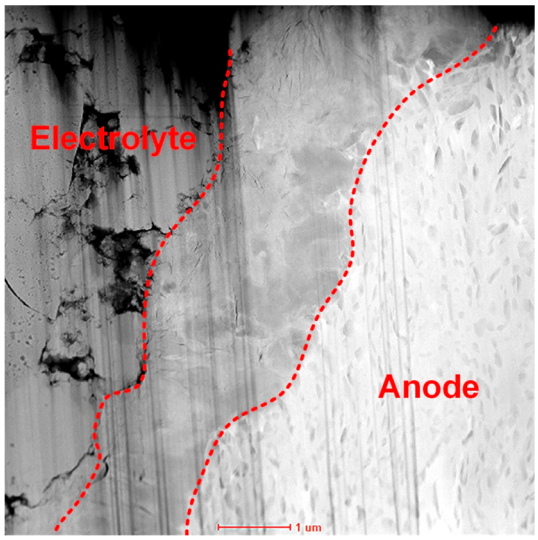

Figure 6-21: STEM image of the anode-electrolyte interface of the recharged cell.

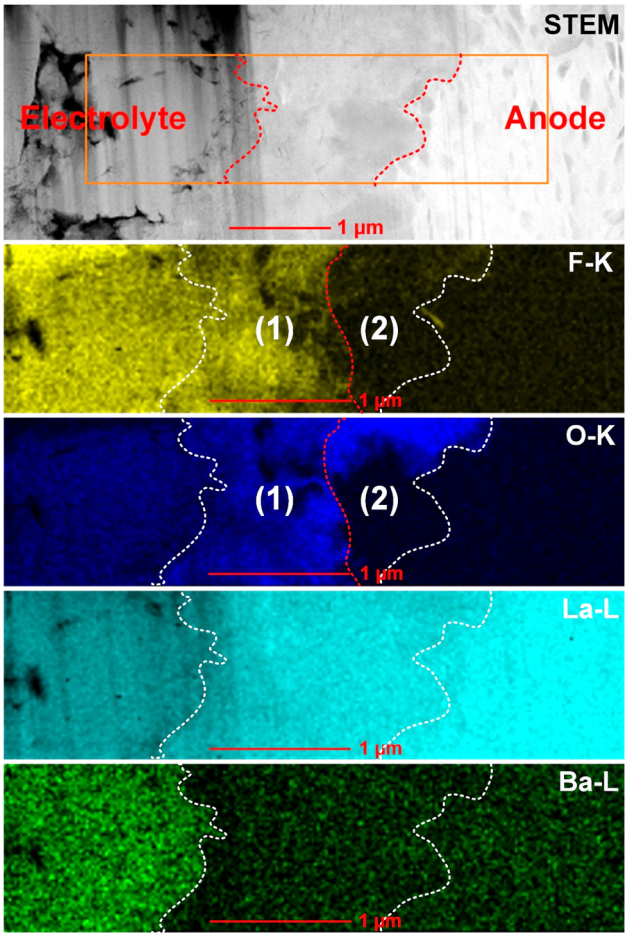

Figure 6-22: STEM-EDX map at the anode-electrolyte interface of the recharged cell.

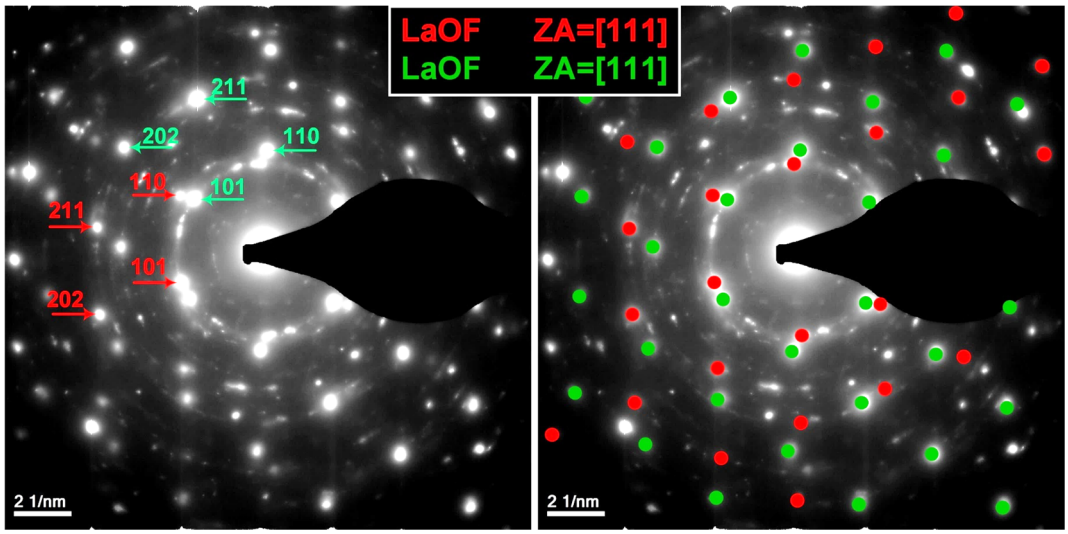

Figure 6-23: SAED pattern taken from region (1) (near the electrolyte).

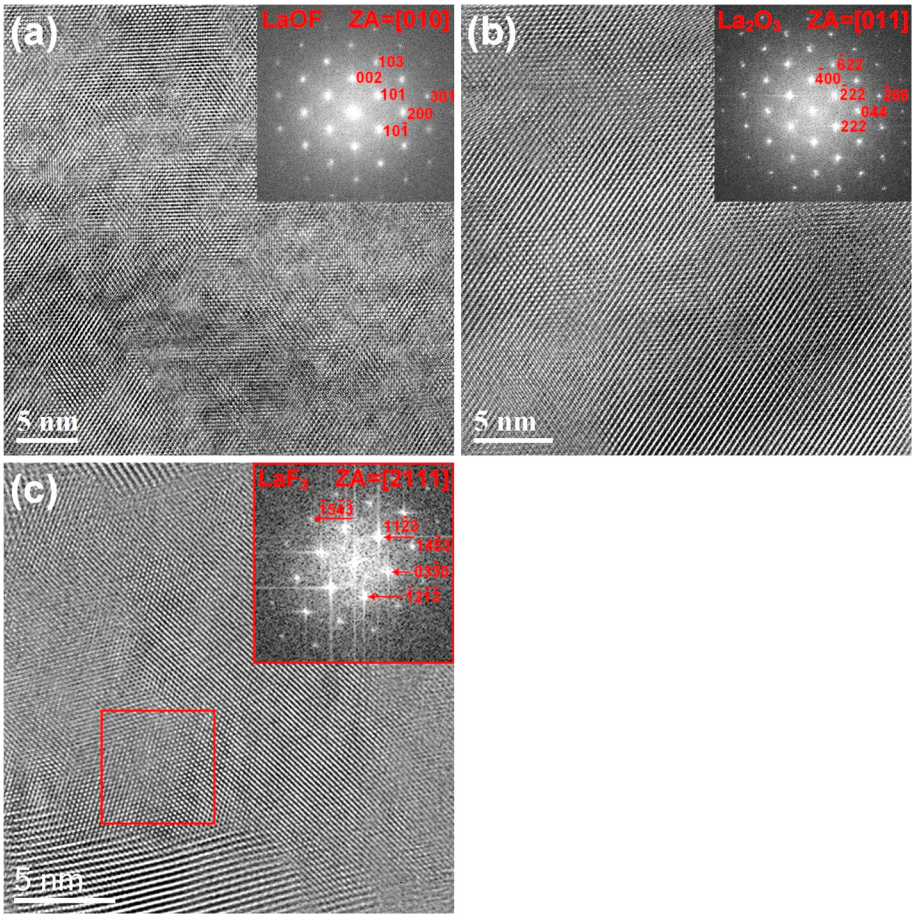

Figure 6-24: HRTEM images and corresponding FFTs from layer (1) in the recharged cell. The images have been filtered using the HRTEM-filter script (D. R. G. Mitchell, v2.0, Jan 14).

Table 6-9: Lattice spacings of the LaOF, La_2O_3 & LaF_3 references and the values measured from SAED pattern & FFTs.

Lattice plane	**LaOF reference [Å]**	**d-spacings SAED [Å]**	**Reference angles [˚]**	**Measured angles [˚]**
101	3.35	3.33	(101) & (110)=54.62	(101) & (110)=54.5
110	2.89	2.86	(101) & (211)=29.47	(101) & (211)=29.5
211	1.75	1.73	(110) & (211)=25.14	(110) & (211)=25
Lattice plane	**LaOF reference [Å]**	**Measured d-spacings [Å]**	**Reference angles [˚]**	**Measured angles [˚]**
002	2.92	2.94	(002) & (101)=54.97	(002) & (101)=56.5
101	3.35	3.3	(002) & (10-1)=54.97	(002) & (10-1)=54
10-1	3.35	3.3	(101) & (10-1)=70.06	(101) & (10-1)=69.5
Lattice plane	**La_2O_3 reference [Å]**	**Measured d-spacings [Å]**	**Reference angles [˚]**	**Measured angles [˚]**
-222	3.27	3.3	(-222) & (044)=35.26	(-222) & (044)=35.5
044	2	2	(-222) & (222)=70.53	(-222) & (222)=70
222	3.27	3.3	(044) & (222)=35.26	(044) & (222)=34.5
Lattice plane	**LaF_3 reference [Å]**	**Measured d-spacings [Å]**	**Reference angles [˚]**	**Measured angles [˚]**
11-23	2.02	2.08	(11-23) & (03-30)=60.79	(11-23) & (03-30)=61
03-30	2.07	2.08	(11-23) & (-12-1-3)=58.42	(11-23) & (-12-1-3)=60
-12-1-3	2.02	2.02	(03-30) & (-12-1-3)=60.79	(03-30) & (-12-1-3)=59

7 Summary and outlook

7.1 Summery

Reversible batteries based on a fluoride ion shuttle have great potential to be an alternative to the commercial systems, because of the high electronegativity and comparable low atomic weight of the fluorine, theoretically resulting in higher energy densities compared to LIBs, above 5000 WhL^{-1}. However, research in the field of fluoride ion batteries is at an early stage of development needing large improvement to meet practical requirements for applications. Understanding the electrochemical reactions occurring at the battery electrodes during cycling was the main objective of this work, which is a basis to develop fluoride ion batteries with improved performance.

TEM is well established as a powerful characterization tool that can provide structural information of various materials down to the atomic level, including local compositional information, and electronic structure information. Numerous *ex situ* TEM studies have been performed to understand the compositional, structural and morphological changes of battery materials at selected states during cycling. However, real-time observations of the structural evolution during electrochemical cycling is very challenging to obtain. Therefore, attempts to perform *in situ* studies became very popular in the past few years.

In the present study, TEM has been chosen to study all-solid-state fluoride ion batteries *in situ* and *ex situ* TEM. Prior to *in situ* studies, the as-prepared components of the fluoride ion batteries were investigated to study the effect of the electron beam on the materials. The results confirmed that the fluoride ion battery materials are stable under normal imaging conditions, so that standard TEM techniques can be used for imaging and analytical work of the fluoride ion battery components. Different all-solid-state fluoride ion battery systems were studied. In all cases, $La_{0.9}Ba_{0.1}F_{2.9}$ was used as solid-state electrolyte, prepared by ball milling a $(1-y)$ LaF_3 and (y) BaF_2 mixture. FIB as a common method for preparing TEM samples has been used to prepare the micron-sized batteries for *in situ* TEM studies. However, development of reliable preparation and contacting methods for all-solid-state micron-sized batteries was an essential task to enable *in situ* TEM studies during electrochemical biasing. Major challenges that had to be overcome were:

- **Porosity**

Although, porosity is required in bulk batteries to enable compensation of volumetric changes during electrochemical cycling, porosity poses a huge problem for *in situ* TEM

measurements affecting both the mechanical stability and the interface connectivity. Therefore, the initially assembled powder-based batteries were further compressed at a pressure of ~5 GPa to produce a stable, dense battery with good contact between neighboring grains as well as between the electrodes and electrolyte.

- **Metal contamination**

Contamination due to metal deposition in the beam tails during FIB sample preparation and contacting could create an electrical short circuit between the electrodes preventing *in situ* cycling. It was observed that the contamination area around the contacts was smaller for EBID (~1 μm for Pt & W) compared to IBID (~17 μm for Pt, ~3.5 μm for W). Preventing this contamination was a prerequisite to obtain a functional battery. So, two Pt-protection walls of 300 nm wide and 7 μm high were deposited vertically on the cathode and anode before performing the initial thinning to reduce the contamination during the contacting stage. Moreover, new MEMS devices with a wide separation between the Pt contacts (50 μm) have been used instead of the standard MEMS devices (20 μm).

- **Contact resistance**

The resistivity of the metal contacts should be sufficiently low to prevent significant losses at the contacts during the charging/discharging process of the micron-sized battery. Therefore, the resistance of Pt and W wires deposited by EBID and IBID was measured. The resistivity was calculated to be 7.5×10^{-2} Ω.m for Pt-EBID and 6.2×10^{-6} Ω.m for Pt-IBID, while it was 5.4×10^{-3} Ω.m for the W-EBID and 3.8×10^{-6} Ω.m for W-IBID. The resistance difference between IBID and EBID is related to differences in the carbon content incorporated from the precursor system, changing the structure from a percolating Pt (or W) network to isolated metal nanoparticles and, hence, switching the conductivity from a metallic conductivity to a 'hopping' process. Therefore, IBID has been used for contacting the electrodes even though the metal contamination area was larger.

- **Leakage currents**

Low leakage currents of the MEMS device are essential to avoid high charging currents, fast discharge and loss of energy stored in the charged battery. Therefore, the standard MEMS devices (Protochips E-AEL11) with ~30 MΩ resistance were replaced by new high resistance MEMS devices (Protochips E-AEK11) of ~1.5 GΩ resistance, which led to a decrease in the leakage current from ~55 nA to ~1.75 nA at 3 V. As a result, based on the theoretical specific capacity and the weight of active material (Cu/CuF_2 for the full cell), the time for discharging by leakage current increased from only ~13 min to ~6 h with the new high resistance MEMS device.

Furthermore, the effect of electron beam current on the measured current in the electrochemical circuit was measured by positioning the electron beam in the TEM on the electron transparent thinned areas, thick areas and the Pt contacts of the MEMS device. The measured current of the electron beam adding to the charging was approx. 0.5 nA, 1-2 nA and 1-1.5 nA on the electron transparent area, thick area and the Pt contacts respectively, while the electron beam current was 9.16 nA. These currents were negligible compared to the operating currents of the fluoride ion battery.

After optimizing the FIB sample preparation, the FIB was used to prepare two different micron-sized fluoride ion batteries for *in situ* TEM characterization, a Bi cathode half-cell and a $Cu/La_{0.9}Ba_{0.1}F_{2.9}/MgF_2$ full cell. The micron-sized batteries were milled from the as-prepared fluoride ion batteries incorporating all interfaces. The areas of interest around the interfaces were thinned for TEM investigation. Then, the micron-sized batteries were contacted by local Pt-deposition between the electrical contacts of the MEMS device and the cell electrodes allowing the electrochemical cycling *in situ* inside the TEM.

The Bi cathode half-cell was cycled *in situ* TEM at RT by applying a sweep voltage between 0 V and 3 V over 1 h. During charging, an I-V peak was observed at a voltage of 2.33 V attributed to the formation of BiO_xF_{3-2x} by fluorination of Bi_2O_3 and Bi. The current reached to a second maximum at 2.85 V, which was attributed to the oxidation of bismuth forming bismuth (III) fluoride. However, no reduction peaks were observed in the discharging process, instead, a straight line dominated by leakage currents. Formation of BiF_3 and BiO_xF_{3-2x} after charging was confirmed by HRTEM analysis. Moreover, unique reflections of BiF_3 were observed in SAED pattern of the charged cathode while unique reflections of Bi metal disappeared after charging. The intensities of the BiF_3 unique reflections were reduced after discharging, partially reversible behaviour. On the other hand, the intensity of the strongest LaF_3 peak of electrolyte was reduced after charging and then mostly recovered after discharging. The poor reversibility of the Bi cathode half-cell was attributed to:

1) Presence of bismuth (III) oxide in the as-prepared composite cathode, which was fluorinated after charging irreversibly forming a bismuth (III) oxyfluoride phase ($BiO_{0.1}F_{2.8}$). Based on the electrochemical charging curve, that irreversible phase was the main phase formed during charging.
2) Presence of oxygen in the electrolyte in form of lanthanum (III) oxyfluoride and probably lanthanum (III) oxide. The oxygen content of the electrolyte was presumably formed during ball milling of the electrolyte outside the glove box. As a result, the partial reduction of the electrolyte during charging increased the amount of LaOF phase.

3) Poor fluoride ion conductivity of the BiF_3 formed after charging, limiting the charging/discharging processes.
4) Probably a short circuit between electrode and electrolyte caused by Pt electromigration from the two deposited electrical contacts towards the interface and, hence, a high self-discharge.

In addition, an *in situ* study of a Cu/$La_{0.9}Ba_{0.1}F_{2.9}$/MgF_2 full cell fluoride ion battery was performed in the TEM. Initially, a micron-sized battery of a Cu/$La_{0.9}Ba_{0.1}F_{2.9}$/MgF_2 full cell fluoride ion battery was cycled *ex situ* the TEM at RT and under high vacuum. The cycling has been done by sweeping the voltage from 0 to 3.5 V over a time of 4h. The charge process was revealed two current steps corresponding to a two-step reaction. The first one around 2 V was attributed to the formation of Cu_2O, while the second maximum started from 2.77 V to 3.5 V forming a plateau attributed to the CuF_2 formation. The carbon black added to the cathode composite and preparation of the battery materials outside the glove box were probably the oxygen sources. The discharging was partially possible, with the reverse reaction observed until the battery failed at 2.85 V with a short circuit between cathode and anode. The CuF_2 phase can convert back to form Cu metal during discharging while the Cu_2O phase is irreversible.

Similar to the Bi half-cell, the *in situ* electrochemical measurements of the Cu/$La_{0.9}Ba_{0.1}F_{2.9}$/MgF_2 full cell fluoride ion battery were performed by CV at RT inside the TEM. The Cu/$La_{0.9}Ba_{0.1}F_{2.9}$/MgF_2 full cell was cycled *in situ* by sweeping a voltage from 0 V to 3.5 V over a time of 2 h. The basic redox steps observed during charging were comparable to the *ex situ* investigation. Formation of copper (II) oxide and copper (II) fluoride was confirmed by HRTEM analysis. However, the characteristic CV peaks during the first charging were on top of a strong background current, which was attributed to residual contamination during FIB preparation and probably Pt migration from the contacts toward the interfaces. During discharging, the current was dominated by the short circuit with a slight peak around 2.7 V, indicating some driven discharging of the battery. During the second charging, no characteristic CV peaks could be observed until the micron-sized battery fractured at the cathode-electrolyte interface. The fracture at the interface was attributed to the volumetric change accompanied to CuF_2 formation and to the reduced free volume available in the cathode composite compared to a normal battery due to the high pressure used for the sample preparation. As a result of the low free volume and the high volumetric change accompanied to Cu/CuF_2 reaction, copper diffusion into the pores of electrolyte was observed after charging. Moreover, formation of voids in the cathode was visible after the first cycle and became more apparent after failure. Voids

were formed in the cathode composite, which was attributed to electromigration or some recrystallization during cycling. In addition, spherical particles formation at the interface to the electrolyte which seem to consist of CuF_2. This formation of spherical particles was attributed to a local overheating as a result of an inhomogeneous Cu oxide and fluoride formation. To investigate potential thickness effects during *in situ* cycling, a fresh thin area was prepared from the thick part of the cathode-electrolyte interface after cycling. The morphological changes and Cu diffusion into the electrolyte were also noticeable in the thick part of the sample. A comparison of the morphological changes in the thick part and the thin area investigated *in situ* suggests that the sample thickness does not significantly alter the *in situ* study. On the other hand, no significant changes were observed in the thin area at the anode-electrolyte interface. Some volumetric changes visible as small cracks in the anode composite and at the anode-electrolyte interface were observed at the thick part of the anode. However, the surface of the cycled anode was covered by small particles of MgF_2 as a result of the low ionic conductivity of the electrolyte leading to fluoride migration on the surface.

In addition to the *in situ* TEM studies, a fluoride ion battery consisting of a CuF_2 composite as cathode, $La_{0.9}Ba_{0.1}F_{2.9}$ as an electrolyte, and a La sheet as anode was studied by *ex situ* TEM. The electrochemical cycling was performed at an elevated temperature of 150 ˚C to enhance the ionic conductivity of the electrolyte. The cycling was started by discharging the as-prepared cell by applying a current density of -4 mA g^{-1} (10 mA cm^{-2}) until a 1 V cut off potential. A current density of +4 mA g^{-1} was applied for charging until 3.5 V. Three different states of that system have been studied, as-prepared (in the charged state), discharged, and recharged. The FIB was used for lifting-out two lamellae from each pellet at the electrodes-electrolyte interfaces, then, the structural and chemical modifications of the electrodes before cycling, after discharging and after recharging were characterized using TEM. Based on the detailed structural characterization of the anode and cathode in the as-prepared, discharged and recharged states, a partially reversible electrochemical cycling was confirmed by fluoride ion transfer through the $La_{0.9}Ba_{0.1}F_{2.9}$ solid-state electrolyte. The discharge process exhibited a single voltage plateau corresponding to the reduction of Cu^{2+} to Cu^0 in the cathode. The recharging process exhibited two voltage steps corresponding to two-step reaction, oxidation of Cu^0 metal to Cu^{1+}, and oxidation of Cu^0 metal or further oxidation of Cu^{1+} to form Cu^{2+}. The HRTEM analysis of the cathode confirmed the formation of Cu metal after discharging as a result of CuF_2 reduction, while the copper fluoride was formed after recharging, validating the concept of the fluoride ion battery. Moreover, the exported F-maps of the cathode revealed a decrease in the fluorine intensity after discharging, confirming the migration of fluorine from

cathode to anode. However, besides the existence of copper (II) oxide in the cathode composite, the HRTEM images revealed the formation of the metastable paramelaconite copper oxide (Cu_4O_3) with an intermediate stoichiometry between the copper (II) oxide and copper (I) oxide. The formation of paramelaconite was attributed to either oxidation of copper (I) oxide or decomposition of copper (II) oxide under the electron beam. The high oxygen content of the cathode composite, presumably formed during to the ball milling of the composite outside the glove box, can partially explain the difference between the theoretical capacity of Cu/CuF_2 (528 mAh g^{-1}) and the observed capacity during the first discharging of the battery (360 mAh g^{-1}). Furthermore, Cu diffusion from the cathode into the electrolyte was observed in the recharged cell during the *in situ* studies, due to the high volumetric change associated to the Cu/CuF_2 reaction. Furthermore, an intermediate layer of La_2O_3 was observed in the as-prepared cell at the anode-electrolyte interface. The oxide layer was present on the La sheet surface prior to fabrication of the cell. After discharging, a LaF_3 layer formed below the La_2O_3 on the La sheet and as a result of the fluoride migration from the cathode into the anode through the oxide layer. After recharging, these two layers merged into one layer with lower fluorine content, indicating the migration of fluorine from the anode toward the cathode. However, the presence of lanthanum (III) oxide on the anode lead to a side reaction resulting in the formation of LaOF during recharging, which was acting as significant fluoride trap. This partially explains the capacity fading after the first recharging to 270 mAh g^{-1} (75% of the first discharge capacity), while it faded strongly in the second discharging to only 165 mAh g^{-1} at 1 V.

Based on the results obtained from the *in situ* and *ex situ* TEM studies, protection of the electrode's materials from oxidation by using improved inert processing conditions for materials preparation and battery assembly will overcome the problems due to the oxides, which could be a reason for a significant improvement in the performance of all-solid-state fluoride ion batteries. Moreover, development of an electrolyte with higher fluoride ion conductivity at room temperature is essential to improve the overall conductance of the battery. As well, it is helpful to decrease the electrolyte thickness and the interfaces roughness to reduce the internal resistance of the battery. Furthermore, more development for the sample preparation for *in situ* TEM studies is required to avoid any metal contamination during FIB preparation and, hence, prevent the short circuit during *in situ* cycling. New design for the MEMS device may be useful in this case. This will be beneficial to study and understand the changes in the electrodes materials at higher cycling number. Additionally, it is essential to use an optimized porosity of

electrode materials achieve mechanical stability of the micron-sized battery and on the other hand still enable compensation of volumetric changes during fluorination/defluorination.

7.2 Outlook

The work in this thesis is providing the basic developments for *in situ* TEM studies of all-solid-state batteries. Further work will be needed to use these approaches to understand details of the electrochemical processes in the batteries and how morphological and chemical parameters influence the battery performance. However, for successful further studies, several aspects need to be addressed:

- **Improved solid-state electrolytes**

It is known that the bulk fluoride batteries only work at elevated temperatures. With the significantly reduced electrolyte, it was possible construct a partially reversible fluoride ion battery. However, development of an electrolyte with higher fluoride ion conductivity is essential for all-solid-state fluoride ion batteries operating at RT.

- **Preparation of oxygen-free materials**

Oxygen in the electrode materials is one of the main reasons for the limited performance of fluoride ion batteries. Oxygen in the electrode materials prevents fluorination/defluorination of large parts of the active material and, as a result, the specific capacity is fading. Therefore, preparation of oxygen-free materials by using improved inert processing conditions is very important to overcome the problems due to the oxides.

- **Further development of sample preparation**

Additional developments for sample preparation for *in situ* TEM studies will be needed for further experimental work. MEMS devices with a new design enabling thinning of the interested area after mounting the lamella on the MEMS device is required to remove any contamination from the preparation. Although the contamination due to the metal deposition during FIB preparation was significantly reduced by using the Pt-protection walls, thinning the interested areas of the electrodes-electrolyte interfaces after mounting the lamella on the MEMS device would be expected to absolutely remove any metal deposition, preventing the short circuit during cycling.

- **Development of thin-film-type fluoride ion battery**

Development of all-solid-state thin-film-type fluoride ion batteries will be expected to improve the overall conductance due to the decreasing of electrolyte thickness. However, the

roughness of electrodes-electrolyte interfaces has to be improved for thin-film-type batteries compared to the current batteries assembled from powders. As a result, the internal resistance of the battery should drastically decrease.

All these will produce an improvement in the performance of all-solid-state fluoride ion battery.

Curriculum Vitae

Personal:

Name	Mohammed Hammad Mohammed Fawey
Date of Birth	Oct. 1, 1980
Place of Birth	Dar El-Salam, Sohag, Egypt
Nationality	Egyptian
Current address	Max-Planck Str. 16, 76344 Eggenstein-Leopoldshafen, Germany
E-mail	mohammed.fawey@gmail.com mohammed.fawey@kit.edu

Education:

2012-2017	Doctoral studies in Materials Science Joint Research Laboratory for Nanomaterials, Technische Universität Darmstadt and Karlsruhe Institute of Technology, Germany Title of Ph.D. thesis: "*In situ* and *Ex situ* TEM Studies of Fluoride Ion Batteries" supervised by Prof. Dr. Horst Hahn
2005–2007	Master of Science (M.Sc.) in Solid-State Physics Plasma Applications Physics Department, Faculty of Science, Sohag University, Sohag, Egypt. Title of Master's thesis: "Duplex Plasma Treatment of Stainless Steel" supervised by Prof. Dr. Fayez M. EL-Hossary
1998–2002	Bachelor of Science (B.Sc.) in Physics Physics Department, Faculty of Science, South Valley University, Sohag, Egypt

List of publications

1. Magnus Garbrecht, Lars Hultman, **Mohammed H. Fawey**, Timothy D. Sands, and Bivas Saha, “Void-mediated coherency-strain relaxation and impediment of cubic-to-hexagonal transformation in epitaxial metastable metal/semiconductor TiN/$Al_{0.72}Sc_{0.28}N$ multilayers”, Physical Review Materials, 1 (2017) 033402, *DOI: https://doi.org/10.1103/PhysRevMaterials.1.033402*.

2. Harshita Bhatia, Duc Tho Thieu, Alexander Herald Pohl, Venkata Sai K. Chakravadhanula, **Mohammed H. Fawey**, Christian Kübel, and Maximilian Fichtner, "Conductivity Optimization of Tysonite-type $La_{1-x}Ba_xF_{3-x}$ Solid Electrolytes for Advanced Fluoride Ion Battery", ACS Applied Materials & Interfaces, 9 (2017) 23707-23715, *DOI: 10.1021/acsami.7b04936*.

3. Bivas Saha, Magnus Garbrecht, Jaime A. Perez-Taborda, **Mohammed H. Fawey**, Yee Rui Koh, Ali Shakouri, Marisol Martin-Gonzalez, Lars Hultman, and Timothy D. Sands, “Compensation of native donor doping in ScN: Carrier concentration control and p-type ScN”, Applied Physics Letters, 110 (2017) 252104, *DOI: 10.1063/1.4989530*.

4. **Mohammed Hammad Fawey***, Duc Tho Thieu*, Harshita Bhatia, Thomas Diemant, Venkata Sai Kiran Chakravadhanula, Rolf Jürgen Behm, Christian Kübel, and Maximilian Fichtner, "CuF_2 as Reversible Cathode for Fluoride Ion Batteries", Advanced Functional Materials, 27 (2017) 1701051, *DOI: 10.1002/adfm.201701051* (* equal contribution first author).

5. **Mohammed Hammad Fawey**, Venkata Sai Kiran Chakravadhanula, Munnangi Anji Reddy, Carine Rongeat, Torsten Scherer, Horst Hahn, Maximilian Fichtner, and Christian Kübel, "*In situ* TEM Studies of Micron-sized All-solid-state Fluoride Ion Batteries: Preparation, Prospects, and Challenges", Microscopy Research and Technique, 79 (2016) 615–624, *DOI: 10.1002/jemt.22675*.

6. Venkata Sai Kiran Chakravadhanula, Thais Silva Teodoro, Torsten Scherer, Suresh Kumar Garlapati, Aaron Kobler, Krishna Kanth Neelisetty, **Mohammed Hammad Fawey** and Christian Kübel, "Electrochemistry in Liquid Environments: Challenges in the Presence of Accelerated Electrons" Imaging & Microscopy, Aug. 17, 2016, http://www.imaging-git.com/science/electron-and-ion-microscopy/electrochemistry-liquid-environments.

7. Suresh Kumar Garlapati, Tessy Theres Baby, Simone Dehm, **Mohammed Hammad**, Venkata Sai Kiran Chakravadhanula, Robert Kruk, Horst Hahn, and Subho Dasgupta,

"Ink-Jet Printed CMOS Electronics from Oxide Semiconductors", Small, 11 (2015) 3591–3596, *DOI: 10.1002/smll.201403288*.

8. F. M. El-Hossary, N. Z. Negm, A. M. Abed El-Rahman, **M. Hammad**, "Duplex treatment of 304 AISI stainless steel using rf plasma nitriding and carbonitriding", Materials Science and Engineering C, 29 (2009) 1167–1173, *DOI: 10.1016/j.msec.2008.09.049*.
9. F. M. El-Hossary, N. Z. Negm, A. M. Abd El-Rahman, **M. Hammad**, C. Templier, "Duplex treatment of AISI 304 austenitic stainless steel using rf nitriding and dc reactive magnetron sputtering of titanium", Surface & Coating technology, 202 (2008) 1392–1400, *DOI: 10.1016/j.surfcoat.2007.06.066*.

References

[1] F. Schüth, "Chemical Compounds for Energy Storage", *Chemie Ingenieur Technik*, vol. 83, no. 11, pp. 1984–1993, 2011.

[2] G. Ren, G. Ma, and N. Cong, "Review of electrical energy storage system for vehicular applications", *Renewable and Sustainable Energy Reviews*, vol. 41, pp. 225–236, 2015.

[3] C. Veerakumar and A. Sreekumar, "Phase change material based cold thermal energy storage: materials, techniques and applications-a review", *International Journal of Refrigeration*, vol. 67, pp. 271–289, 2016.

[4] C. Tang, Q. Zhang, M. Q. Zhao, G. L. Tian, and F. Wei, "Resilient aligned carbon nanotube/graphene sandwiches for robust mechanical energy storage", *Nano Energy*, vol. 7, pp. 161–169, 2014.

[5] B. Abdi, M. M. Teymoori, H. Gholamrezaei, and A. A. Nasiri, "A simple analog BLDC drive control for electromechanical energy storage system", *Energy Procedia*, vol. 12, pp. 1002–1007, 2011.

[6] X. Han, M. Ouyang, L. Lu, and J. Li, "Cycle Life of Commercial Lithium-Ion Batteries with Lithium Titanium Oxide Anodes in Electric Vehicles", *Energies*, vol. 7, no. 8, pp. 4895–4909, 2014.

[7] A.-I. Stan, M. Swierczynski, D.-I. Stroe, R. Teodorescu, S. J. Andreasen, and K. Moth, "A comparative study of lithium ion to lead acid batteries for use in UPS applications", in *Telecommunications Energy Conference (INTELEC), 2014 IEEE 36th International*, 2014, pp. 1–8.

[8] C. V. Nayar, M. Ashari, and W. W. L. Keerthipala, "A grid-interactive photovoltaic uninterruptible power supply system using battery storage and a back up diesel generator", in *IEEE Transactions on Energy Conversion*, 2000, pp. 348–353.

[9] J. Warner, "Chapter 15 - Lithium-Ion Battery Applications", *The Handbook of Lithium-Ion Battery Pack Design*, pp. 177–209, 2015.

[10] G. Pistoia, "APPLICATIONS – PORTABLE | Portable Devices: Batteries", in *Encyclopedia of Electrochemical Power Sources*, Elsevier, 2009, pp. 29–38.

[11] R. . Marsh, S. Vukson, S. Surampudi, B. . Ratnakumar, M. . Smart, M. Manzo, and P. . Dalton, "Li ion batteries for aerospace applications", *Journal of Power Sources*, vol. 97–98, pp. 25–27, 2001.

[12] R. A. Huggins, *Advanced Batteries: Materials Science Aspects*, vol. 1. Springer, 2009.

[13] D. Linden and T. B. Reddy, *Handbook of Batteries*, Third Edit. McGraw-Hill, New York, 2002.

[14] M. V. Reddy, G. V. S. Rao, and B. V. R. Chowdari, "Metal Oxides and Oxysalts as Anode Materials for Li Ion Batteries", *Chemical Reviews*, vol. 113, no. 7, pp. 5364–5457, 2013.

[15] H. Xia, H. L. Wang, W. Xiao, M. O. Lai, and L. Lu, "Thin film Li electrolytes for all-solid-state micro-batteries", *International Journal of Surface Science and Engineering*, vol. 3, no. 1/2, pp. 23–43, 2009.

[16] G.-L. Xu, Q. Wang, J.-C. Fang, Y.-F. Xu, J.-T. Li, L. Huang, and S.-G. Sun, "Tuning the structure and property of nanostructured cathode materials of lithium ion and lithium sulfur batteries", *Journal of Materials Chemistry A*, vol. 2, no. 47, pp. 19941–19962, 2014.

[17] K. Akiya and B. R. James, *Manganese Dioxide Symposium: Vol. 1, Cleveland, 1975, Band 1*. Electrochemical Society. Cleveland Section. I.C. Sample Office. 1975, 1975.

[18] T. Nagaura and K. Tazawa, "Lithium ion rechargeable battery", *Progress in Batteries &*

Solar Cells, vol. 9, pp. 209–217, 1990.

[19] B. Scrosati, "Recent advances in lithium ion battery materials", *Electrochimica Acta*, vol. 45, no. 15–16, pp. 2461–2466, 2000.

[20] V. Etacheri, R. Marom, R. Elazari, G. Salitra, and D. Aurbach, "Challenges in the development of advanced Li-ion batteries: a review", *International Journal of Electrochemical Science*, vol. 4, no. 9, pp. 3243–3262, 2011.

[21] G.-A. Nazri and G. Pistoia, *Lithium Batteries: Science and Technology*, 1st ed. Springer US, 2003.

[22] B. Scrosati and J. Garche, "Lithium batteries: Status, prospects and future", *Journal of Power Sources*, vol. 195, no. 9, pp. 2419–2430, 2010.

[23] J.-M. Tarascon and M. Armand, "Issues and challenges facing rechargeable lithium batteries", *Nature*, vol. 414, no. 6861, pp. 359–367, 2001.

[24] S. Goriparti, E. Miele, D. A. Francesco, D. E. Fabrizio, P. R. Zaccaria, and C. Capiglia, "Review on recent progress of nanostructured anode materials for Li-ion batteries", *Journal of Power Sources*, vol. 257, pp. 421–443, 2014.

[25] N. Takami, A. Satoh, M. Hara, and T. Ohsaki, "Structural and Kinetic Characterization of Lithium Intercalation into Carbon Anodes for Secondary Lithium Batteries", *Journal of the Electrochemical Society*, vol. 142, no. 2, pp. 371–379, 1995.

[26] W. Xu, J. Wang, F. Ding, X. Chen, E. Nasybulin, Y. Zhang, and J.-G. Zhang, "Lithium metal anodes for rechargeable batteries", *Energy & Environmental Science*, vol. 7, no. 2, pp. 513–537, 2014.

[27] M. C. Smart and B. V. Ratnakumar, "Effects of Electrolyte Composition on Lithium Plating in Lithium-Ion Cells", *Journal of Electrochemical Society*, vol. 158, no. 4, pp. A379–A389, 2011.

[28] C. Brissot, M. Rosso, J.-N. Chazalviel, and S. Lascaud, "Concentration measurements in lithium/polymer-electrolyte/lithium cells during cycling", *Journal of Power Sources*, vol. 94, no. 2, pp. 212–218, 2001.

[29] V. Agubra and J. Fergus, "Lithium ion battery anode aging mechanisms", *Materials*, vol. 6, no. 4, pp. 1310–1325, 2013.

[30] M. Rosso, C. Brissot, A. Teyssot, M. Dollé, L. Sannier, J.-M. Tarascon, R. Bouchet, and S. Lascaud, "Dendrite short-circuit and fuse effect on Li/polymer/Li cells", *Electrochimica Acta*, vol. 51, no. 25, pp. 5334–5340, 2006.

[31] B. J. Landi, M. J. Ganter, C. D. Cress, R. A. DiLeo, and R. P. Raffaelle, "Carbon nanotubes for lithium ion batteries", *Energy & Environmental Science*, vol. 2, no. 6, p. 638, 2009.

[32] J. Hou, Y. Shao, M. W. Ellis, R. B. Moore, and B. Yi, "Graphene-based electrochemical energy conversion and storage: fuel cells, supercapacitors and lithium ion batteries", *Physical chemistry chemical physics*, vol. 13, no. 34, pp. 15384–15402, 2011.

[33] J. Yang, Y. Takeda, N. Imanishi, C. Capiglia, J. . Y. Xie, and O. Yamamoto, "SiO_x-based anodes for secondary lithium batteries", *Solid State Ionics*, vol. 152–153, pp. 125–129, 2002.

[34] M. Ge, J. Rong, X. Fang, and C. Zhou, "Porous Doped Silicon Nanowires for Lithium Ion Battery Anode with Long Cycle Life", *Nano Letters*, vol. 12, no. 5, pp. 2318–2323, 2012.

[35] I.-S. Hwang, J.-C. Kim, S.-D. Seo, S. Lee, J.-H. Lee, and D.-W. Kim, "A binder-free Ge-nanoparticle anode assembled on multiwalled carbon nanotube networks for Li-ion batteries", *Chemical Communications*, vol. 48, no. 56, pp. 7061–7063, 2012.

[36] K. Zhuo, M.-G. Jeong, and C.-H. Chung, "Highly porous dendritic Ni-Sn anodes for lithium-ion batteries", *Journal of Power Sources*, vol. 244, pp. 601–605, 2013.

[37] K. Zaghib, a. Mauger, and C. M. Julien, "Overview of olivines in lithium batteries for green transportation and energy storage", *Journal of Solid State Electrochemistry*, vol. 16, no. 3, pp. 835–845, 2012.

[38] H. Yang and J. Prakash, "Determination of the Reversible and Irreversible Heats of a $LiNi_{0.8}Co_{0.15}Al_{0.05}O_2$/Natural Graphite Cell Using Electrochemical-Calorimetric Technique", *Journal of The Electrochemical Society*, vol. 151, no. 8, pp. A1222–A1229, 2004.

[39] K. M. Shaju, G. V. S. Rao, and B. V. R. Chowdari, "Performance of layered Li $(Ni_{1/3}Co_{1/3}Mn_{1/3})O_2$ as cathode for Li-ion batteries", *Electrochimica Acta*, vol. 48, no. 2, pp. 145–151, 2002.

[40] T. Ohzuku, A. Ueda, M. Nagayama, Y. Iwakoshi, and H. Komori, "Comparative study of $LiCoO_2$, $LiNi_{12}Co_{12}O_2$ and $LiNiO_2$ for 4 volt secondary lithium cells", *Electrochimica Acta*, vol. 38, no. 9, pp. 1159–1167, 1993.

[41] G. Pistoia, D. Zane, and Y. Zhang, "Some Aspects of $LiMn_2O_4$ Electrochemistry in the 4 Volt Range", *Journal of The Electrochemical Society*, vol. 142, no. 8, pp. 2551–2557, 1995.

[42] A. Yamada, S. C. Chung, and K. Hinokuma, "Optimized $LiFePO_4$ for Lithium Battery Cathodes", *Journal of The Electrochemical Society*, vol. 148, no. 3, pp. A224–A229, 2001.

[43] J. Barker, M. Y. Saidi, and J. L. Swoyer, "Electrochemical Insertion Properties of the Novel Lithium Vanadium Fluorophosphate, $LiVPO_4F$", *Journal of The Electrochemical Society*, vol. 150, no. 10, pp. A1394–A1398, 2003.

[44] H. Huang, S.-C. Yin, T. Kerr, N. Taylor, and L. F. Nazar, "Nanostructured Composites: A High Capacity, Fast Rate $Li_3V_2(PO_4)_3$/Carbon Cathode for Rechargeable Lithium Batteries", *Advanced Materials*, vol. 14, no. 21, pp. 1525–1528, 2002.

[45] M. M. Thackeray, C. Wolverton, and E. D. Isaacs, "Electrical energy storage for transportation—approaching the limits of, and going beyond, lithium-ion batteries", *Energy & Environmental Science*, vol. 5, no. 7, p. 7854, 2012.

[46] The-Tesla-Team (2016-08-23), "New Tesla Model S Now the Quickest Production Car in the World", 2017. .

[47] X. Zhao, S. Ren, M. Bruns, and M. Fichtner, "Chloride ion battery: A new member in the rechargeable battery family", *Journal of Power Sources*, vol. 245, pp. 706–711, 2014.

[48] M. Anji Reddy and M. Fichtner, "Batteries based on fluoride shuttle", *Journal of Materials Chemistry*, vol. 21, no. 43, pp. 17059–17062, 2011.

[49] H. D. Yoo, I. Shterenberg, Y. Gofer, G. Gershinsky, N. Pour, and D. Aurbach, "Mg rechargeable batteries: an on-going challenge", *Energy & Environmental Science*, vol. 6, no. 8, pp. 2265–2279, 2013.

[50] F. Sagane, T. Abe, and Z. Ogumi, "Sodium-ion transfer at the interface between ceramic and organic electrolytes", *Journal of Power Sources*, vol. 195, no. 21, pp. 7466–7470, 2010.

[51] X. Zhao, Z. Zhao-Karger, D. Wang, and M. Fichtner, "Metal oxychlorides as cathode materials for chloride ion batteries", *Angewandte Chemie - International Edition*, vol. 52, no. 51, pp. 13621–13624, 2013.

[52] P. G. Bruce, S. A. Freunberger, L. J. Hardwick, and J.-M. Tarascon, "Li–O_2 and Li–S batteries with high energy storage", *Nature materials*, vol. 11, pp. 19–29, 2012.

[53] C. Rongeat, M. A. Reddy, R. Witter, and M. Fichtner, "Nanostructured Fluorite-type Fluorides as Electrolyte for Fluoride Ion Batteries", *The Journal of Physical Chemistry C*, vol. 117, no. 10, pp. 4943–4950, 2013.

[54] J. S. Lee, J. Y. Bae, H. Lee, N. D. Quan, H. S. Kim, and H. Kim, "Ionic Liquids as Electrolytes for Li Ion Batteries", *Journal of Industrial and Engineering Chemistry*, vol. 10,

no. 7, pp. 1086–1089, 2004.

[55] J. B. Goodenough and Y. Kim, "Challenges for rechargeable Li batteries", *Chemistry of Materials*, vol. 22, no. 3, pp. 587–603, 2010.

[56] Q. Wang, P. Ping, X. Zhao, G. Chu, J. Sun, and C. Chen, "Thermal runaway caused fire and explosion of lithium ion battery", *Journal of Power Sources*, vol. 208, pp. 210–224, 2012.

[57] A. Hammami, N. Raymond, and M. Armand, "Lithium-ion batteries: Runaway risk of forming toxic compounds", *Nature*, vol. 424, no. 6949, pp. 635–636, 2003.

[58] S. F. Lux, I. T. Lucas, E. Pollak, S. Passerini, M. Winter, and R. Kostecki, "The mechanism of HF formation in $LiPF_6$ based organic carbonate electrolytes", *Electrochemistry Communications*, vol. 14, no. 1, pp. 47–50, 2012.

[59] D. A. Stevens and J. R. Dahn, "High Capacity Anode Materials for Rechargeable Sodium-Ion Batteries", *Journal of The Electrochemical Society*, vol. 147, no. 4, pp. 1271–1273, 2000.

[60] V. Palomares, P. Serras, I. Villaluenga, K. B. Hueso, J. Carretero-González, and T. Rojo, "Na-ion batteries, recent advances and present challenges to become low cost energy storage systems", *Energy & Environmental Science*, vol. 5, no. 3, pp. 5884–5901, 2012.

[61] S. W. Kim, D. H. Seo, X. Ma, G. Ceder, and K. Kang, "Electrode materials for rechargeable sodium-ion batteries: Potential alternatives to current lithium-ion batteries", *Advanced Energy Materials*, vol. 2, no. 7, pp. 710–721, 2012.

[62] D. Aurbach, I. Weissman, Y. Gofer, and E. Levi, "Nonaqueous magnesium electrochemistry and its application in secondary batteries", *Chemical Record*, vol. 3, no. 1, pp. 61–73, 2003.

[63] R. Mohtadi and F. Mizuno, "Magnesium batteries: Current state of the art, issues and future perspectives", *Beilstein Journal of Nanotechnology*, vol. 5, pp. 1291–1311, 2014.

[64] A. Eftekhari, "Potassium secondary cell based on Prussian blue cathode", *Journal of Power Sources*, vol. 126, no. 1–2, pp. 221–228, 2004.

[65] M. P. Paranthaman, H. Liu, X.-G. Sun, S. Dai, and G. M. Brown, "Aluminum-ion batteries for medium- and large-scale energy storage", in *Advances in Batteries for Medium and Large-Scale Energy Storage*, Elsevier, 2015, pp. 463–474.

[66] R. Baskaran, S. Selvasekarapandian, N. Kuwata, J. Kawamura, and T. Hattori, "Structure, thermal and transport properties of PVAc-$LiClO_4$ solid polymer electrolytes", *Journal of Physics and Chemistry of Solids*, vol. 68, no. 3, pp. 407–412, 2007.

[67] S. Ohta, S. Komagata, J. Seki, T. Saeki, S. Morishita, and T. Asaoka, "All-solid-state lithium ion battery using garnet-type oxide and Li_3BO_3 solid electrolytes fabricated by screen-printing", *Journal of Power Sources*, vol. 238, pp. 53–56, 2013.

[68] J. Auvergniot, A. Cassel, D. Foix, V. Viallet, V. Seznec, and R. Dedryvère, "Redox activity of argyrodite Li_6PS_5Cl electrolyte in all-solid-state Li-ion battery: An XPS study", *Solid State Ionics*, vol. 300, pp. 78–85, 2017.

[69] C. R. Stoldt and S.-H. Lee, "All-solid-state lithium metal batteries for next generation energy storage", in *2013 Transducers & Eurosensors XXVII: The 17th International Conference on Solid-State Sensors, Actuators and Microsystems (TRANSDUCERS & EUROSENSORS XXVII)*, 2013, pp. 2819–2822.

[70] Y. Kato, K. Kawamoto, R. Kanno, and M. Hirayama, "Discharge Performance of all-Solid-State battery Using a Lithium Superionic Conductor $Li_{10}GeP_2S_{12}$", *Electrochemistry*, vol. 80, no. 10, pp. 749–751, 2012.

[71] M. Tatsumisago, M. Nagao, and A. Hayashi, "Recent development of sulfide solid electrolytes and interfacial modification for all-solid-state rechargeable lithium

batteries", *Journal of Asian Ceramic Societies*, vol. 1, no. 1, pp. 17–25, 2013.

[72] H. Aono, "Ionic Conductivity of Solid Electrolytes Based on Lithium Titanium Phosphate", *Journal of The Electrochemical Society*, vol. 137, no. 4, p. 1023, 1990.

[73] J. Fu, "Fast Li^+ ion conducting glass-ceramics in the system $Li_2O–Al_2O_3–GeO_2–P_2O_5$", *Solid State Ionics*, vol. 104, no. 3–4, pp. 191–194, 1997.

[74] M. Itoh, Y. Inaguma, W.-H. Jung, L. Chen, and T. Nakamura, "High lithium ion conductivity in the perovskite-type compounds $Ln_{1/2}Li_{1/2}TiO_3$(Ln=La,Pr,Nd,Sm)", *Solid State Ionics*, vol. 70–71, pp. 203–207, 1994.

[75] X. Yu, J. B. Bates, G. E. Jellison, Jr., and F. X. Hart, "A Stable Thin-Film Lithium Electrolyte: Lithium Phosphorus Oxynitride", *Journal of The Electrochemical Society*, vol. 144, no. 2, pp. 524–532, 1997.

[76] R. Murugan, V. Thangadurai, and W. Weppner, "Fast Lithium Ion Conduction in Garnet-Type $Li_7La_3Zr_2O_{12}$", *Angewandte Chemie - International Edition*, vol. 46, no. 41, pp. 7778–7781, 2007.

[77] C. Cao, Z.-B. Li, X.-L. Wang, X.-B. Zhao, and W.-Q. Han, "Recent Advances in Inorganic Solid Electrolytes for Lithium Batteries", *Frontiers in Energy Research*, vol. 2, pp. 1–10, 2014.

[78] N. Kamaya, K. Homma, Y. Yamakawa, M. Hirayama, R. Kanno, M. Yonemura, T. Kamiyama, Y. Kato, S. Hama, K. Kawamoto, and A. Mitsui, "A lithium superionic conductor", *Nature materials*, vol. 10, pp. 682–686, 2011.

[79] Y. Seino, T. Ota, T. Jyunke, and K. Yanagi, "Extend Abstracts of the 36th Symposium on Solid State Ionics in Japan", 2010, pp. 116–117.

[80] P. Knauth, "Inorganic solid Li ion conductors: An overview", *Solid State Ionics*, vol. 180, no. 14–16, pp. 911–916, 2009.

[81] "European Patent Application", International application number: PCT/RU2006/000196, 2008.

[82] C. Rongeat, M. Anji Reddy, T. Diemant, R. J. Behm, and M. Fichtner, "Development of new anode composite materials for fluoride ion batteries", *J. Mater. Chem. A*, vol. 2, no. 48, pp. 20861–20872, 2014.

[83] C. Rongeat, M. Anji Reddy, T. Diemant, R. J. Behm, and M. Fichtner, "Development of new anode composite materials for fluoride ion batteries", *Journal of Materials Chemistry A*, vol. 2, no. 48, pp. 20861–20872, 2014.

[84] W. Xing, J. S. Xue, T. Zheng, A. Gibaud, and J. R. Dahn, "Correlation Between lithium Intercalation Capacity and Microstructure in Hard Carbons", *Journal of The Electrochemical Society*, vol. 143, no. 11, pp. 3482–3491, 1996.

[85] M. Dumont, L. Commin, I. Morfin, F. Degeuser, F. Legendre, and P. Maugis, "Chemical composition of nano-phases studied by anomalous small-angle X-ray scattering: Application to oxide nano-particles in ODS steels", *Materials Characterization*, vol. 87, pp. 138–142, 2014.

[86] Y. C. K. Chen-Wiegart, P. Shearing, Q. Yuan, A. Tkachuk, and J. Wang, "3D morphological evolution of Li-ion battery negative electrode $LiVO_2$ during oxidation using X-ray nano-tomography", *Electrochemistry Communications*, vol. 21, no. 1, pp. 58–61, 2012.

[87] G. T.-K. Fey, P. Muralidharan, Y.-D. Cho, P.-C. Chang, and H.-M. Kao, "Electrochemical performance and ^{7}Li NMR studies on an inverse spinel $LiNi_{1/3}Co_{1/3}Mn_{1/3}VO_4$ for Li-ion batteries", *Journal of Power Sources*, vol. 174, no. 2, pp. 1142–1146, 2007.

[88] S. Vierrath, L. Zielke, R. Moroni, A. Mondon, D. R. Wheeler, R. Zengerle, and S. Thiele, "Morphology of nanoporous carbon-binder domains in Li-ion batteries—A FIB-SEM study", *Electrochemistry Communications*, vol. 60, pp. 176–179, 2015.

[89] M. Wagemaker, W. J. H. Borghols, E. R. H. van Eck, A. P. M. Kentgens, G. J. Kearley, and F. M. Mulder, "The Influence of Size on Phase Morphology and Li-Ion Mobility in Nanosized Lithiated Anatase TiO_2", *Chemistry - A European Journal*, vol. 13, no. 7, pp. 2023–2028, 2007.

[90] T. Sui, B. Song, J. Dluhos, L. Lu, and A. M. Korsunsky, "Nanoscale chemical mapping of Li-ion battery cathode material by FIB-SEM and TOF-SIMS multi-modal microscopy", *Nano Energy*, vol. 17, pp. 254–260, 2015.

[91] Y. Lin, J. A. McCarthy, K. R. Poeppelmeier, and L. D. Marks, "Applications of Electron Microscopy in Heterogeneous Catalysis", in *Catalysis by Materials with Well-Defined Structures*, Elsevier Inc., 2015, pp. 193–238.

[92] K. H. Kim, T. Hirayama, C. A. J. Fisher, K. Yamamoto, T. Sato, K. Tanabe, S. Kumazaki, Y. Iriyama, and Z. Ogumi, "Characterization of grain-boundary phases in $Li_7La_3Zr_2O_{12}$ solid electrolytes", *Materials Characterization*, vol. 91, pp. 101–106, 2014.

[93] J. Zhou, N. Lin, W. long Cai, C. Guo, K. Zhang, J. Zhou, Y. Zhu, and Y. Qian, "Synthesis of S/CoS_2 Nanoparticles-Embedded N-doped Carbon Polyhedrons from Polyhedrons ZIF-67 and their Properties in Lithium-Sulfur Batteries", *Electrochimica Acta*, vol. 218, pp. 243–251, 2016.

[94] Y. Shiraishi, I. Nakai, K. Kimoto, and Y. Matsui, "EELS analysis of electrochemically deintercalated $Li_{1-x}Mn_2O_4$ and substituted spinels $LiMn_{1.6}M_{0.4}O_4$ (M=Co, Cr, Ni)", *Journal of Power Sources*, vol. 97–98, pp. 461–464, 2001.

[95] P. K. Nayak, J. Grinblat, M. Levi, Y. Wu, B. Powell, and D. Aurbach, "TEM and Raman spectroscopy evidence of layered to spinel phase transformation in layered $LiNi_{1/3}Mn_{1/3}Co_{1/3}O_2$ upon cycling to higher voltages", *Journal of Electroanalytical Chemistry*, vol. 733, pp. 6–19, 2014.

[96] A. Brazier, L. Dupont, L. Dantras-Laffont, N. Kuwata, J. Kawamura, and J.-M. Tarascon, "First Cross-Section Observation of an All Solid-State Lithium-Ion “Nanobattery” by Transmission Electron Microscopy", *Chemistry of Materials*, vol. 20, no. 6, pp. 2352–2359, 2008.

[97] C. Villevieille, "Electrochemical characterization of rechargeable lithium batteries", in *Rechargeable Lithium Batteries*, Elsevier, 2015, pp. 183–232.

[98] L. Y. Beaulieu, K. W. Eberman, R. L. Turner, L. J. Krause, and J. R. Dahn, "Colossal Reversible Volume Changes in Lithium Alloys", *Electrochemical and Solid-State Letters*, vol. 4, no. 9, pp. A137–A140, 2001.

[99] D. Chen, S. Indris, M. Schulz, B. Gamer, and R. Mönig, "In situ scanning electron microscopy on lithium-ion battery electrodes using an ionic liquid", *Journal of Power Sources*, vol. 196, no. 15, pp. 6382–6387, 2011.

[100] X. H. Liu and J. Y. Huang, "In situ TEM electrochemistry of anode materials in lithium ion batteries", *Energy & Environmental Science*, vol. 4, no. 10, pp. 3844–3860, 2011.

[101] C. R. Fell, M. Chi, Y. S. Meng, and J. L. Jones, "In situ X-ray diffraction study of the lithium excess layered oxide compound $Li[Li_{0.2}Ni_{0.2}Mn_{0.6}]O_2$ during electrochemical cycling", *Solid State Ionics*, vol. 207, pp. 44–49, 2012.

[102] R. Bhattacharyya, B. Key, H. Chen, A. S. Best, A. F. Hollenkamp, and C. P. Grey, "In situ NMR observation of the formation of metallic lithium microstructures in lithium batteries", *Nature materials*, vol. 9, no. 6, pp. 504–510, 2010.

[103] L. J. Hardwick, P. W. Ruch, M. Hahn, W. Scheifele, R. Kötz, and P. Novák, "In situ Raman spectroscopy of insertion electrodes for lithium-ion batteries and supercapacitors: First cycle effects", *Journal of Physics and Chemistry of Solids*, vol. 69, no. 5–6, pp. 1232–1237, 2008.

[104] J. Yano and V. K. Yachandra, "X-ray absorption spectroscopy", *Photosynthesis Research*,

vol. 102, no. 2, pp. 241–254, 2009.

[105] J. E. Penner-Hahn, "X-ray absorption spectroscopy in coordination chemistry", *Coordination Chemistry Reviews*, vol. 190–192, pp. 1101–1123, 1999.

[106] Q. P. McAllister, K. E. Strawhecker, C. R. Becker, and C. A. Lundgren, "In situ atomic force microscopy nanoindentation of lithiated silicon nanopillars for lithium ion batteries", *Journal of Power Sources*, vol. 257, pp. 380–387, 2014.

[107] R. Baddour-hadjean and J.-P. Pereira-Ramos, "Raman Microspectrometry Applied to the Study of Electrode Materials for Lithium Batteries", *Chemical Reviews*, vol. 110, pp. 1278–1319, 2010.

[108] D. Kurouski, "Advances of tip-enhanced Raman spectroscopy (TERS) in electrochemistry, biochemistry, and surface science", *Vibrational Spectroscopy*, vol. In press, 2016.

[109] P. P. R. M. L. Harks, F. M. Mulder, and P. H. L. Notten, "In situ methods for Li-ion battery research: A review of recent developments", *Journal of Power Sources*, vol. 288, pp. 92–105, 2015.

[110] L. Zhou, M. Leskes, A. J. Ilott, N. M. Trease, and C. P. Grey, "Paramagnetic electrodes and bulk magnetic susceptibility effects in the in situ NMR studies of batteries: Application to $Li_{1.08}Mn_{1.92}O_4$ spinels", *Journal of Magnetic Resonance*, vol. 234, pp. 44–57, 2013.

[111] E. Ruska, "Beitrag zur übermikroskopischen Abbildung bei höheren Drucken", *Kolloid-Zeitschrift*, vol. 100, no. 2, pp. 212–219, 1942.

[112] H. Hashimoto, T. Naiki, T. Eto, and K. Fujiwara, "High temperature gas reaction specimen chamber for an electron microscope", *Japanese Journal of Applied Physics*, vol. 7, no. 8, pp. 946–952, 1968.

[113] I. M. Abrams and J. W. McBain, "A closed cell for electron microscopy", *Journal of Applied Physics*, vol. 15, no. 8, pp. 607–609, 1944.

[114] M. J. Williamson, R. M. Tromp, P. M. Vereecken, R. Hull, and F. M. Ross, "Dynamic microscopy of nanoscale cluster growth at the solid-liquid interface", *Nature materials*, vol. 2, no. 8, pp. 532–536, 2003.

[115] E. P. Butler, "In situ experiments in the transmission electron microscope", *Reports on Progress in Physics*, vol. 42, no. 5, pp. 833–895, 1979.

[116] R. Ramachandra, H. Demers, and N. De Jonge, "Atomic-resolution scanning transmission electron microscopy through 50-nm-thick silicon nitride membranes", *Applied Physics Letters*, vol. 98, no. 9, 2011.

[117] N. de Jonge and F. M. Ross, "Electron microscopy of specimens in liquid", *Nature Nanotechnology*, vol. 6, no. 11, pp. 695–704, 2011.

[118] E. A. Ring and N. de Jonge, "Microfluidic System for Transmission Electron Microscopy", *Microscopy and Microanalysis*, vol. 16, no. 5, pp. 622–629, 2010.

[119] T. J. Woehl, C. Park, J. E. Evans, I. Arslan, W. D. Ristenpart, and N. D. Browning, "Direct Observation of Aggregative Nanoparticle Growth: Kinetic Modeling of the Size Distribution and Growth Rate", *Nano Letters*, vol. 14, no. 1, pp. 373–378, 2014.

[120] P. Abellan, B. L. Mehdi, L. R. Parent, M. Gu, C. Park, W. Xu, Y. Zhang, I. Arslan, J.-G. Zhang, C.-M. Wang, J. E. Evans, and N. D. Browning, "Probing the Degradation Mechanisms in Electrolyte Solutions for Li-Ion Batteries by in Situ Transmission Electron Microscopy", *Nano Letters*, vol. 14, no. 3, pp. 1293–1299, 2014.

[121] H.-G. Liao, L. Cui, S. Whitelam, and H. Zheng, "Real-time imaging of Pt_3Fe nanorod growth in solution", *Science*, vol. 336, no. 6084, pp. 1011–1014, 2012.

[122] Z. Zeng, W. Liang, H. Liao, H. L. Xin, Y. Chu, and H. Zheng, "Visualization of Electrode–Electrolyte Interfaces in $LiPF_6$/EC/DEC Electrolyte for Lithium Ion Batteries via in Situ

TEM", *Nano Letters*, vol. 14, no. 4, pp. 1745–1750, 2014.

[123] M. E. Holtz, Y. Yu, D. Gunceler, J. Gao, R. Sundararaman, K. A. Schwarz, T. A. Arias, H. D. Abruña, and D. A. Muller, "Nanoscale Imaging of Lithium Ion Distribution During In Situ Operation of Battery Electrode and Electrolyte", *Nano Letters*, vol. 14, no. 3, pp. 1453–1459, 2014.

[124] F. Wu and N. Yao, "Advances in sealed liquid cells for in-situ TEM electrochemial investigation of lithium-ion battery", *Nano Energy*, vol. 11, pp. 196–210, 2015.

[125] J. Belloni, M. Mostafavi, H. Remita, J.-L. Marignier, and M.-O. Delcourt, "Radiation-induced synthesis of mono- and multi-metallic clusters and nanocolloids", *New Journal of Chemistry*, vol. 22, no. 11, pp. 1239–1255, 1998.

[126] R. F. Egerton, P. Li, and M. Malac, "Radiation damage in the TEM and SEM", *Micron*, vol. 35, no. 6, pp. 399–409, 2004.

[127] T. J. Woehl, K. L. Jungjohann, J. E. Evans, I. Arslan, W. D. Ristenpart, and N. D. Browning, "Experimental procedures to mitigate electron beam induced artifacts during in situ fluid imaging of nanomaterials.", *Ultramicroscopy*, vol. 127, pp. 53–63, 2013.

[128] J. P. Sullivan, J. Huang, M. J. Shaw, A. Subramanian, N. Hudak, Y. Zhan, and J. Lou, "Understanding Li-ion battery processes at the atomic- to nano-scale", in *Proceedings of SPIE*, 2010, vol. 7683, p. 76830B.

[129] Q. Su, G. Du, J. Zhang, Y. Zhong, B. Xu, Y. Yang, S. Neupane, K. Kadel, and W. Li, "In Situ Transmission Electron Microscopy Investigation of the Electrochemical Lithiation–Delithiation of Individual Co_9S_8/Co-Filled Carbon Nanotubes", *ACS Nano*, vol. 7, no. 12, pp. 11379–11387, 2013.

[130] J. Y. Huang, L. Zhong, C. M. Wang, J. P. Sullivan, W. Xu, L. Q. Zhang, S. X. Mao, N. S. Hudak, X. H. Liu, A. Subramanian, H. Fan, L. Qi, A. Kushima, and J. Li, "In Situ Observation of the Electrochemical Lithiation of a Single SnO_2 Nanowire Electrode", *Science*, vol. 330, no. 6010, pp. 1515–1520, 2010.

[131] X. H. Liu, L. Q. Zhang, L. Zhong, Y. Liu, H. Zheng, J. W. Wang, J. H. Cho, S. A. Dayeh, S. T. Picraux, J. P. Sullivan, S. X. Mao, Z. Z. Ye, and J. Y. Huang, "Ultrafast electrochemical lithiation of individual Si nanowire anodes", *Nano Letters*, vol. 11, no. 6, pp. 2251–2258, 2011.

[132] L. Zhong, X. H. Liu, G. F. Wang, S. X. Mao, and J. Y. Huang, "Multiple-Stripe Lithiation Mechanism of Individual SnO_2 Nanowires in a Flooding Geometry", *Physical Review Letters*, vol. 106, no. 24, p. 248302(1-4), 2011.

[133] C.-M. Wang, X. Li, Z. Wang, W. Xu, J. Liu, F. Gao, L. Kovarik, J.-G. Zhang, J. Howe, D. J. Burton, Z. Liu, X. Xiao, S. Thevuthasan, and D. R. Baer, "In Situ TEM Investigation of Congruent Phase Transition and Structural Evolution of Nanostructured Silicon/Carbon Anode for Lithium Ion Batteries", *Nano Letters*, vol. 12, no. 3, pp. 1624–1632, 2012.

[134] A. Nie, L.-Y. Gan, Y. Cheng, H. Asayesh-Ardakani, Q. Li, C. Dong, R. Tao, F. Mashayek, H.-T. Wang, U. Schwingenschlögl, R. F. Klie, and R. S. Yassar, "Atomic-Scale Observation of Lithiation Reaction Front in Nanoscale SnO_2 Materials", *ACS Nano*, vol. 7, no. 7, pp. 6203–6211, 2013.

[135] X. H. Liu, J. W. Wang, S. Huang, F. Fan, X. Huang, Y. Liu, S. Krylyuk, J. Yoo, S. a. Dayeh, A. V. Davydov, S. X. Mao, S. T. Picraux, S. Zhang, J. Li, T. Zhu, and J. Y. Huang, "In situ atomic-scale imaging of electrochemical lithiation in silicon", *Nature Nanotechnology*, vol. 7, no. 11, pp. 749–756, 2012.

[136] Y. Liu, N. S. Hudak, D. L. Huber, S. J. Limmer, J. P. Sullivan, and J. Y. Huang, "In Situ Transmission Electron Microscopy Observation of Pulverization of Aluminum Nanowires and Evolution of the Thin Surface Al_2O_3 Layers during Lithiation–Delithiation Cycles", *Nano Letters*, vol. 11, no. 10, pp. 4188–4194, 2011.

[137] X. H. Liu, S. Huang, S. T. Picraux, J. Li, T. Zhu, and J. Y. Huang, "Reversible Nanopore Formation in Ge Nanowires during Lithiation-Delithiation Cycling: An In Situ Transmission Electron Microscopy Study", *Nano Letters*, vol. 11, no. 9, pp. 3991–3997, 2011.

[138] X. Li, D. Xiao, H. Zheng, X. Wei, X. Wang, L. Gu, Y.-S. Hu, T. Yang, and Q. Chen, "Ultrafast and reversible electrochemical lithiation of InAs nanowires observed by in-situ transmission electron microscopy", *Nano Energy*, vol. 20, pp. 194–201, 2016.

[139] X. H. Liu, L. Zhong, S. Huang, S. X. Mao, T. Zhu, and J. Y. Huang, "Size-dependent fracture of silicon nanoparticles during lithiation", *ACS Nano*, vol. 6, no. 2, pp. 1522–1531, 2012.

[140] Q. Su, J. Zhang, Y. Wu, and G. Du, "Revealing the electrochemical conversion mechanism of porous Co_3O_4 nanoplates in lithium ion battery by in situ transmission electron microscopy", *Nano Energy*, vol. 9, pp. 264–272, 2014.

[141] S. Liu, J. Xie, Q. Su, G. Du, S. Zhang, G. Cao, T. Zhu, and X. Zhao, "Understanding Li-storage mechanism and performance of $MnFe_2O_4$ by in situ TEM observation on its electrochemical process in nano lithium battery", *Nano Energy*, vol. 8, pp. 84–94, 2014.

[142] J. Xie, F. Tu, Q. Su, G. Du, S. Zhang, T. Zhu, G. Cao, and X. Zhao, "In situ TEM characterization of single PbSe/reduced-graphene-oxide nanosheet and the correlation with its electrochemical lithium storage performance", *Nano Energy*, vol. 5, pp. 122–131, 2014.

[143] Q. Su, D. Xie, J. Zhang, G. Du, and B. Xu, "In Situ Transmission Electron Microscopy Observation of the Conversion Mechanism of Fe_2O_3/Graphene Anode during Lithiation-Delithiation Processes", *ACS Nano*, vol. 7, no. 10, pp. 9115–9121, 2013.

[144] Y. Yuan, L. Ma, K. He, W. Yao, A. Nie, X. Bi, K. Amine, T. Wu, J. Lu, and R. Shahbazian-Yassr, "Dynamic study of (De)sodiation in alpha-MnO_2 nanowires", *Nano Energy*, vol. 19, pp. 382–390, 2016.

[145] F. Xu, Z. Li, L. Wu, Q. Meng, H. L. Xin, J. Sun, B. Ge, L. Sun, and Y. Zhu, "In situ TEM probing of crystallization form-dependent sodiation behavior in ZnO nanowires for sodium-ion batteries", *Nano Energy*, vol. 30, pp. 771–779, 2016.

[146] W. Xia, F. Xu, C. Zhu, H. L. Xin, Q. Xu, P. Sun, and L. Sun, "Probing microstructure and phase evolution of -MoO_3 nanobelts for sodium-ion batteries by in situ transmission electron microscopy", *Nano Energy*, vol. 27, pp. 447–456, 2016.

[147] L. Zhong, R. R. Mitchell, Y. Liu, B. M. Gallant, C. V. Thompson, J. Y. Huang, S. X. Mao, and Y. Shao-Horn, "In Situ Transmission Electron Microscopy Observations of Electrochemical Oxidation of Li_2O_2", *Nano Letters*, vol. 13, no. 5, pp. 2209–2214, 2013.

[148] Y. S. Meng, T. McGilvray, M.-C. Yang, D. Gostovic, F. Wang, D. Zeng, Y. Zhu, and J. Graetz, "In Situ Analytical Electron Microscopy for Probing Nanoscale Electrochemistry", *The Electrochemistry Society Interface*, vol. 20, no. 3, pp. 49–53, 2011.

[149] J. D. C. Jr., M. Phaneuf, C. Chandler, M. Megorden, K. E. Noll, R. Schuman, T. J. Gannon, A. Krechmer, D. Monforte, N. Antoniou, N. Bassom, J. Li, P. Carleson, and C. Huynh, "Copper device editing: Strategy for focused ion beam milling of copper", *Journal of Vacuum Science & Technology B*, vol. 20, no. 6, pp. 2682–2685, 2002.

[150] P. J. Goodhew, J. Humphreys, and R. Beanland, *Electrons and their interaction with the specimen*, Third. Taylor & Francis, 2001.

[151] D. Brandon and W. D. Kaplan, *Microstructural Characterization of Materials*. 2008.

[152] D. B. Williams and C. B. Carter, *Transmission Electron Microscopy*. Boston, MA: Springer US, 2009.

[153] R. F. Egerton, P. Li, and M. Malac, "Radiation damage in the TEM and SEM", *Micron*, vol. 35, no. 6, pp. 399–409, 2004.

[154] N. Jiang and J. C. H. Spence, "On the dose-rate threshold of beam damage in TEM", *Ultramicroscopy*, vol. 113, pp. 77–82, 2012.

[155] L. Reimer, "Review of the radiation damage problem of organic specimens in electron microscopy", in *Physical Aspects of Electron Microscopy and Microbeam analysis*, B. M. Siegel and D. R. Beaman, Eds. Wiley, New York, 1975, p. 474.

[156] R. F. Egerton, P. A. Crozier, and P. Rice, "Electron energy-loss spectroscopy and chemical change", *Ultramicroscopy*, vol. 23, pp. 305–312, 1987.

[157] F. Lin, I. M. Markus, M. M. Doeff, and H. L. Xin, "Chemical and Structural Stability of Lithium-Ion Battery Electrode Materials under Electron Beam", *Scientific Reports*, vol. 4, pp. 1–6, 2014.

[158] H. Ota, Y. Sakata, A. Inoue, and S. Yamaguchi, "Analysis of Vinylene Carbonate Derived SEI Layers on Graphite Anode", *Journal of The Electrochemical Society*, vol. 151, no. 10, pp. A1659–A1669, 2004.

[159] T. J. Woehl, J. E. Evans, I. Arslan, W. D. Ristenpart, and N. D. Browning, "Direct in situ determination of the mechanisms controlling nanoparticle nucleation and growth", *ACS nano*, vol. 6, no. 10, pp. 8599–610, 2012.

[160] D. M. Poojary and A. Clearfield, "Application of X-ray Powder Diffraction Techniques to the Solution of Unknown Crystal Structures", *Accounts of Chemical Research*, vol. 30, no. 10, pp. 414–422, 1997.

[161] W. H. Bragg and W. L. Bragg, "The Reflection of X-rays by Crystals", *Proceedings of the Royal Society A: Mathematical, Physical and Engineering Sciences*, vol. 88, no. 605, pp. 428–438, 1913.

[162] B. D. Cullity, *Elements of X-Ray Diffraction*. Addison Wesley, 1956.

[163] S. Amelinckx, D. van Dyck, J. van Landuyt, and G. van Tendeloo, *Electron Microscopy: Principles and Fundamentals*. VCH Verlagsgesellschaft GmbH: Weinheim (Federal Republic of Germany), 1997.

[164] "http://kids.britannica.com/comptons/art-167800.", 2016. [Online]. Available: Encyclopædia Britannica, Inc.

[165] D. B. Murphy and M. W. Davidson, *Fundamentals of Light Microscopy and Electronic Imaging*, Second Edi. Hoboken, New Jersey, USA: John Wiley & Sons, Inc., 2012.

[166] A. Putnis and R. C. Liebermann, *Transmission electron microscopy of minerals and rocks*. 1991.

[167] D. B. Williams and C. B. Carter, *Transmission electron microscopy.*, vol. 13. Springer Science + Business Media, New York, USA, 1996.

[168] D. Tomus and H. P. Ng, "In situ lift-out dedicated techniques using FIB-SEM system for TEM specimen preparation", *Micron*, vol. 44, no. 1, pp. 115–119, 2013.

[169] Wikipedia, "https://en.wikipedia.org/wiki/Transmission_electron_microscopy#/media/File:Scheme_TEM_en.svg", 2016. .

[170] U. Kolb, K. Shankland, L. Meshi, A. Avilov, and W. David, *Uniting Electron Crystallography and Powder Diffraction*. Dordrecht: Springer Netherlands, 2012.

[171] R. G. Newton, *Scattering Theory of Waves and Particles*, 2nd ed. Springer Science+Business Media, LLC, 1982.

[172] J. Goldstein, D. E. Newbury, D. C. Joy, C. E. Lyman, P. Echlin, E. Lifshin, L. Sawyer, and J. R. Michael, *Scanning Electron Microscopy and X-ray Microanalysis*, Third. Springer Science + Business Media, New York, USA, 2003.

[173] R. F. Egerton, "Electron energy-loss spectroscopy in the TEM", *Reports on Progress in*

Physics, vol. 72, no. 1, p. 016502 (25pp), 2009.

[174] R. F. Egerton, *Electron Energy-Loss Spectroscopy in the Electron Microscope*. Plenum Press, New York, 1986.

[175] D. B. Williams and C. B. Carter, "Part 4: spectrometry", in *Transmission electron microscopy*, Springer, 1996, pp. 553–717.

[176] G. Kothleitner, "http://www.microimage.com.cn/uploadfile/xwjs/uploadfile/201009/20100928050148412.pdf". .

[177] R. F. Egerton, *Electron Energy-Loss Spectroscopy in the Electron Microscope*, Third., vol. 53, no. 9. Springer, 2011.

[178] M. J. Lopez-Martinez and E. M. Campo, "Micro-Nano Technologies for Cell Manipulation and Subcellular Monitoring", in *Intechopen.Com*, Prof. Reza Fazel, Ed. 2003, pp. 275–299.

[179] J. Mayer, L. A. Giannuzzi, T. Kamino, and J. Michael, "TEM Sample Preparation and FIB-Induced Damage", *MRS Bulletin*, vol. 32, no. 5, pp. 400–407, 2007.

[180] T. Yaguchi, R. Urao, T. Kamino, T. Ohnishi, T. Hashimoto, K. Umemura, and S. Tomimatsu, *Nonlithographic and Lithographic Methods of Nanofabrication: From Ultralarge-Scale Integration to Photonics to Molecular Electronics*, vol. 636. 2001.

[181] A. J. Bard and L. R. Faulkner, *Electrochemical Methods: Fundamentals and Applications*, 2nd ed. Wiley, 2001.

[182] S.-I. Pyun, H.-C. Shin, J.-W. Lee, and J.-Y. Go, *Electrochemistry of Insertion Materials for Hydrogen and Lithium*. Berlin, Heidelberg: Springer Berlin Heidelberg, 2012.

[183] D. Andrienko, "Cyclic Voltammetry", *http://www2.mpip-mainz.mpg.de/~andrienk/journal_club/cyclic_voltammetry.pdf*, 2008. .

[184] "http://www.ceb.cam.ac.uk/research/groups/rg-eme/teaching-notes/linear-sweep-and-cyclic-voltametry-the-principles", *Department of Chemical Engineering and Biotechnology; University of Cambridge*, 2015. .

[185] C. Rongeat, M. Anji Reddy, R. Witter, and M. Fichtner, "Solid Electrolytes for Fluoride Ion Batteries: Ionic Conductivity in Polycrystalline Tysonite-Type Fluorides", *ACS Applied Materials & Interfaces*, vol. 6, no. 3, pp. 2103–2110, 2014.

[186] "Unpublished results, direct communication with Prof. M. Fichtner group", 2015.

[187] W. Baukal, "Über reaktionsmöglichkeiten in elektroden von festkörperbatterien", *Electrochimica Acta*, vol. 19, no. 11, pp. 687–694, 1974.

[188] J. Meng, Ying S.; McGilvray, Thomas; Yang, M-C; Gostovic, Daniel; Wang, Feng; Zeng, Dongli; Zhu, Yimei; Graetz, "In situ Analytical Electron Microscopy for Probing NanoScale Electrochemistry", *Electrochemical society interface*, vol. 20, no. 3, pp. 49–53, 2011.

[189] M. Jublot and M. Texier, "Sample preparation by focused ion beam micromachining for transmission electron microscopy imaging in front-view", *Micron*, vol. 56, pp. 63–67, 2014.

[190] S. Kuwano, T. Fujita, D. Pan, K. Wang, and M. Chen, "TEM Sample Preparation for Microcompressed Nanocrystalline Ni", *MATERIALS TRANSACTIONS*, vol. 49, no. 9, pp. 2091–2095, 2008.

[191] M. Duchamp, Q. Xu, and D.-B. R. E, "Convenient Preparation of High-Quality Specimens for Annealing Experiments in the Transmission Electron Microscope", *Microscopy and Microanalysis*, vol. 20, pp. 1638–1645, 2014.

[192] C. Rongeat, M. Anji Reddy, T. Diemant, R. J. Behm, and M. Fichtner, "Development of

new anode composite materials for fluoride ion batteries", *Journal of Materials Chemistry A*, vol. 2, no. 48, pp. 20861–20872, 2014.

[193] Q. Su, G. Du, J. Zhang, Y. Zhong, B. Xu, Y. Yang, S. Neupane, K. Kadel, and W. Li, "In Situ Transmission Electron Microscopy Investigation of the Electrochemical Lithiation–Delithiation of Individual Co_9S_8/Co-Filled Carbon Nanotubes", *ACS Nano*, vol. 7, no. 12, pp. 11379–11387, 2013.

[194] Q. Su, L. Chang, J. Zhang, G. Du, and B. Xu, "In Situ TEM Observation of the Electrochemical Process of Individual CeO_2/Graphene Anode for Lithium Ion Battery", *The Journal of Physical Chemistry C*, vol. 117, no. 8, pp. 4292–4298, 2013.

[195] J. Xie, F. Tu, Q. Su, G. Du, S. Zhang, T. Zhu, G. Cao, and X. Zhao, "In situ TEM characterization of single PbSe/reduced-graphene-oxide nanosheet and the correlation with its electrochemical lithium storage performance", *Nano Energy*, vol. 5, pp. 122–131, 2014.

[196] X. H. Liu, Y. Liu, A. Kushima, S. Zhang, T. Zhu, J. Li, and J. Y. Huang, "In Situ TEM Experiments of Electrochemical Lithiation and Delithiation of Individual Nanostructures", *Advanced Energy Materials*, vol. 2, no. 7, pp. 722–741, 2012.

[197] C.-M. Wang, "In situ transmission electron microscopy and spectroscopy studies of rechargeable batteries under dynamic operating conditions: A retrospective and perspective view", *Journal of Materials Research*, vol. 30, no. 3, pp. 326–339, 2015.

[198] M. R. Zamfir, H. T. Nguyen, E. Moyen, Y. H. Lee, and D. Pribat, "Silicon nanowires for Li-based battery anodes: a review", *Journal of Materials Chemistry A*, vol. 1, no. 34, p. 9566, 2013.

[199] L. K. Nan and L. M. Lung, "Study of FIB milling induced damage and contamination on ex-situ lift-out TEM specimen and methodology to reduce the artifacts", in *Proceedings of the 20th IEEE International Symposium on the Physical and Failure Analysis of Integrated Circuits (IPFA)*, 2013, pp. 404–407.

[200] A. Reguer, F. Bedu, D. Tonneau, H. Dallaporta, M. Prestigiacomo, A. Houel, and P. Sudraud, "Structural and electrical studies of conductive nanowires prepared by focused ion beam induced deposition", *Journal of Vacuum Science & Technology B*, vol. 26, no. 1, pp. 175–180, 2008.

[201] D. Brunel, D. Troadec, D. Hourlier, D. Deresmes, M. Zdrojek, and T. Mélin, "Characterization of ion/electron beam induced deposition of electrical contacts at the sub-um scale", *Microelectronic Engineering*, vol. 88, no. 7, pp. 1569–1572, 2011.

[202] A. Botman, M. Hesselberth, and J. J. L. Mulders, "Investigation of morphological changes in platinum-containing nanostructures created by electron-beam-induced deposition", *Journal of Vacuum Science & Technology B*, vol. 26, no. 6, pp. 2464–2467, 2008.

[203] A. Fernández-Pacheco, J. M. De Teresa, R. Córdoba, and M. R. Ibarra, "Metal-insulator transition in Pt-C nanowires grown by focused-ion-beam-induced deposition", *Physical Review B*, vol. 79, no. 17, p. 174204 (12pp), 2009.

[204] J. M. De Teresa, R. Córdoba, A. Fernández-Pacheco, O. Montero, P. Strichovanec, and M. R. Ibarra, "Origin of the Difference in the Resistivity of As-Grown Focused-Ion- and Focused-Electron-Beam-Induced Pt Nanodeposits", *Journal of Nanomaterials*, vol. 2009, pp. 1–11, 2009.

[205] J. J. L. Mulders, "Purity and resistivity improvements for electron-beam-induced deposition of Pt", *Applied Physics A*, vol. 117, no. 4, pp. 1697–1704, 2014.

[206] A. R. Vaz, M. M. da Silva, J. Leon, S. A. Moshkalev, and J. W. Swart, "Platinum thin films deposited on silicon oxide by focused ion beam: characterization and application", *Journal of Materials Science*, vol. 43, no. 10, pp. 3429–3434, 2008.

[207] J.-F. Lin, J. P. Bird, L. Rotkina, and P. A. Bennett, "Classical and quantum transport in

focused-ion-beam-deposited Pt nanointerconnects", *Applied Physics Letters*, vol. 82, no. 5, pp. 802–804, 2003.

[208] N. Kanzaki, P. Wilhite, S. Maeda, T. Yamadal, and C. Y. Yang, "Contact improvement using E-beam and FIB deposited tungsten in carbon nanofiber interconnects", in *IEEE Nanotechnology Materials and Devices*, 2011, pp. 248–251.

[209] E. Horváth, P. L. Neumann, A. L. Tóth, É. Vázsonyi, A. A. Koós, Z. E. Horváth, P. Fürjes, C. Dücső, and L. P. Biró, "Electrical Characterization of Tungsten Nanowires Deposited by Focused Ion Beam (FIB)", *Nanopages*, vol. 1, no. 2, pp. 255–262, 2006.

[210] W. Li, J. C. Fenton, A. Cui, H. Wang, Y. Wang, C. Gu, D. W. McComb, and P. A. Warburton, "Felling of individual freestanding nanoobjects using focused-ion-beam milling for investigations of structural and transport properties", *Nanotechnology*, vol. 23, no. 10, p. 105301 (10pp), 2012.

[211] W. Li and P. A. Warburton, "Low-current focused-ion-beam induced deposition of three-dimensional tungsten nanoscale conductors", *Nanotechnology*, vol. 18, no. 48, p. 485305 (5pp), 2007.

[212] M. Prestigiacomo, L. Roussel, A. Houël, P. Sudraud, F. Bedu, D. Tonneau, V. Safarov, and H. Dallaporta, "Studies of structures elaborated by focused ion beam induced deposition", *Microelectronic Engineering*, vol. 76, no. 1–4, pp. 175–181, 2004.

[213] W. Li, J. C. Fenton, Y. Wang, D. W. McComb, and P. A. Warburton, "Tunability of the superconductivity of tungsten films grown by focused-ion-beam direct writing", *Journal of Applied Physics*, vol. 104, no. 9, p. 093913 (10pp), 2008.

[214] J. Melngailis, "Focused ion beam induced deposition - a review", in *Electron-Beam, X-Ray, and Ion-Beam Submicrometer Lithographies for Manufacturing*, 1991, vol. 1465, pp. 36–49.

[215] P. G. Li, A. Z. Jin, and W. H. Tang, "Pt/Ga/C and Pt/C composite nanowires fabricated by focused ion and electron beam induced deposition", *physica status solidi (a)*, vol. 203, no. 2, pp. 282–286, 2006.

[216] Y. B. Koh, "Characteristics of W films formed by ion beam assisted deposition", *Journal of Vacuum Science & Technology B: Microelectronics and Nanometer Structures*, vol. 9, no. 5, pp. 2648–2652, 1991.

[217] H. Langfischer, B. Basnar, H. Hutter, and E. Bertagnolli, "Evolution of tungsten film deposition induced by focused ion beam", *Journal of Vacuum Science & Technology A*, vol. 20, no. 4, pp. 1408–1415, 2002.

[218] D. W. K. Jenkins, G. C. Allen, P. D. Prewett, and P. J. Heard, "Focused ion-beam assisted deposition of tungsten and carbon", *Journal of Physics: Condensed Matter*, vol. 3, no. S, pp. S199–S206, 1991.

[219] D. Tham, C.-Y. Nam, and J. E. Fischer, "Microstructure and Composition of Focused-Ion-Beam-Deposited Pt Contacts to GaN Nanowires", *Advanced Materials*, vol. 18, no. 3, pp. 290–294, 2006.

[220] T. Hu and B. I. Shklovskii, "Theory of hopping conductivity of a suspension of nanowires in an insulator", *Physical Review B*, vol. 74, no. 5, p. 054205(1-5), 2006.

[221] C. J. Adkins, "Conduction in granular metals-variable-range hopping in a Coulomb gap?", *Journal of Physics: Condensed Matter*, vol. 1, no. 7, pp. 1253–1259, 1989.

[222] J.-F. Lin, J. P. Bird, L. Rotkina, A. Sergeev, and V. Mitin, "Large effects due to electron–phonon-impurity interference in the resistivity of Pt/C-Ga composite nanowires", *Applied Physics Letters*, vol. 84, no. 19, pp. 3828–3830, 2004.

[223] P. C. Hoyle, J. R. A. Cleaver, and H. Ahmed, "Ultralow-energy focused electron beam induced deposition", *Applied Physics Letters*, vol. 64, no. 11, p. 1448, 1994.

[224] K. T. K. Platen, L.-M. Buchmann, H.-C. Petzold, and W. H. Brünger, "Electron-beam induced tungsten deposition: Growth rate enhancement and applications in microelectronics", *Journal of Vacuum Science & Technology B*, vol. 10, no. 6, pp. 2690–2694, 1992.

[225] P. C. Hoyle, M. Ogasawara, J. R. A. Cleaver, and H. Ahmed, "Electrical resistance of electron beam induced deposits from tungsten hexacarbonyl", *Applied Physics Letters*, vol. 62, no. 23, p. 3043, 1993.

[226] H. Hiroshima and M. Komuro, "High Growth Rate for Slow Scanning in Electron-Beam-Induced Deposition", *Japanese Journal of Applied Physics*, vol. 36, no. Part 1, No. 12B, pp. 7686–7690, 1997.

[227] I. Utke, P. Hoffmann, and J. Melngailis, "Gas-assisted focused electron beam and ion beam processing and fabrication", *Journal of Vacuum Science & Technology B*, vol. 26, no. 4, pp. 1197–1276, 2008.

[228] D. Ruzmetov, V. P. Oleshko, P. M. Haney, H. J. Lezec, K. Karki, K. H. Baloch, A. K. Agrawal, A. V. Davydov, S. Krylyuk, Y. Liu, J. Y. Huang, M. Tanase, J. Cumings, and A. A. Talin, "Electrolyte stability determines scaling limits for solid-state 3D Li ion batteries", *Nano Letters*, vol. 12, no. 1, pp. 505–511, 2012.

[229] B. Hu, X. Wang, H. Shu, X. Yang, L. Liu, Y. Song, Q. Wei, H. Hu, H. Wu, L. Jiang, and X. Liu, "Improved electrochemical properties of BiF_3/C cathode via adding amorphous $AlPO_4$ for lithium-ion batteries", *Electrochimica Acta*, vol. 102, pp. 8–18, 2013.

[230] E. Pohjalainen, T. Rauhala, M. Valkeapää, J. Kallioinen, and T. Kallio, "Effect of $Li_4Ti_5O_{12}$ Particle Size on the Performance of Lithium Ion Battery Electrodes at High C-Rates and Low Temperatures", *The Journal of Physical Chemistry C*, vol. 119, pp. 2277–2283, 2015.

[231] T. V. S. L. Satyavani, B. Ramya Kiran, V. Rajesh Kumar, A. Srinivas Kumar, and S. V. Naidu, "Effect of particle size on dc conductivity, activation energy and diffusion coefficient of lithium iron phosphate in Li-ion cells", *Engineering Science and Technology, an International Journal*, vol. 19, no. 1, pp. 40–44, 2015.

[232] S.-M. Lee, S.-T. Lee, D.-H. Lee, S.-H. Lee, S.-S. Han, and S.-K. Lim, "Effect of particle size on the density and ionic conductivity of $Na_3Zr_2Si_2PO_{12}$ NASICON", *Journal of Ceramic Processing Research*, vol. 16, no. 1, pp. 49–53, 2015.

[233] M. Anji Reddy and M. Fichtner, "Batteries based on fluoride shuttle", *Journal of Materials Chemistry*, vol. 21, no. 43, pp. 17059–17062, 2011.

[234] Z. Chen, I. Belharouak, Y.-K. Sun, and K. Amine, "Titanium-Based Anode Materials for Safe Lithium-Ion Batteries", *Advanced Functional Materials*, vol. 23, no. 8, pp. 959–969, 2013.

[235] D. Antartis, S. Dillon, and I. Chasiotis, "Effect of porosity on electrochemical and mechanical properties of composite Li-ion anodes", *Journal of Composite Materials*, vol. 49, no. 15, pp. 1849–1862, 2015.

[236] T. KOZLOVA, "In situ transmission electron microscopy investigations of electromigration in metals", 2015.

[237] F. Badway, A. N. Mansour, N. Pereira, J. F. Al-Sharab, F. Cosandey, I. Plitz, and G. G. Amatucci, "Structure and electrochemistry of copper fluoride nanocomposites utilizing mixed conducting matrices", *Chemistry of Materials*, vol. 19, no. 17, pp. 4129–4141, 2007.

[238] W. Baukal, "Über reaktionsmöglichkeiten in elektroden von festkörperbatterien", *Electrochimica Acta*, vol. 19, no. 11, pp. 687–694, 1974.

[239] F. Gschwind and J. Bastien, "Parametric investigation of room-temperature fluoride-ion batteries: assessment of electrolytes, Mg-based anodes, and BiF_3-cathodes", *Journa of Materials Chemistry A*, vol. 3, no. 10, pp. 5628–5634, 2015.

[240] K. Aarstad, G. Tranell, G. Pettersen, and T. A. Engh, "Various techniques to study the surface of magnesium protected by SF_6", *Magnesium Technology 2003*, pp. 5–10, 2003.

[241] F. Gschwind, G. Rodriguez-Garcia, D. J. S. Sandbeck, A. Gross, M. Weil, M. Fichtner, and N. Hörmann, "Fluoride ion batteries: Theoretical performance, safety, toxicity, and a combinatorial screening of new electrodes", *Journal of Fluorine Chemistry*, vol. 182, pp. 76–90, 2016.

[242] C. Julien and Z. Stoynov, *Materials for Lithium-Ion Batteries*, vol. 85. Dordrecht: Springer Netherlands, 2000.

[243] S. S. Penner, "Assessment of Research Needs for Advanced Fuel Cells", Oak Ridge, TN, 1985.

[244] M. O'Keeffe and J.-O. Bovin, "The crystal structure of paramelaconite, Cu_4O_3", *American Mineralogist*, vol. 63, pp. 180–185, 1978.

[245] C. Frondel, "Paramelaconite: a tetragonal oxide of copper", *American Mineralogist*, vol. 26, no. 11, pp. 657–672, 1941.

[246] L. Debbichi, M. C. M. de Lucas, and P. Krüger, "Electronic structure, lattice dynamics and thermodynamic stability of paramelaconite Cu4O3", *Materials Chemistry and Physics*, vol. 148, no. 1–2, pp. 293–298, 2014.

[247] N. J. Long and A. K. Petford-Long, "In-situ electron-beam-induced reduction of CuO: A study of phase transformations in cupric oxide", *Ultramicroscopy*, vol. 20, no. 1–2, pp. 151–159, 1986.

[248] B. Suthar, P. W. C. Northrop, D. Rife, and V. R. Subramanian, "Effect of Porosity, Thickness and Tortuosity on Capacity Fade of Anode", *Journal of the Electrochemical Society*, vol. 162, no. 9, pp. A1708–A1717, 2015.

[249] G. Sikha, B. N. Popov, and R. E. White, "Effect of Porosity on the Capacity Fade of a Lithium-Ion Battery", *Journal of The Electrochemical Society*, vol. 151, no. 7, pp. A1104–A1114, 2004.

[250] C. Jo, Y. Park, J. Jeong, K. T. Lee, and J. Lee, "Structural Effect on Electrochemical Performance of Ordered Porous Carbon Electrodes for Na-ion Batteries", *ACS Applied Materials & Interfaces*, vol. 7, pp. 11748–11754, 2015.